γ-Titanium Aluminide Alloys for Aircraft and Automotive Engine Components Applications Processed by Electron Beam Melting

By

Giorgio Baudana

******

Politecnico di Torino
2018

Declaration

I hereby declare that, the contents and organization of this dissertation constitute my own original work and does not compromise in any way the rights of third parties, including those relating to the security of personal data.

Giorgio Baudana

2018

* This dissertation is presented in partial fulfillment of the requirements for **Ph.D. degree** in the Graduate School of Politecnico di Torino (ScuDo).

Acknowledgment

Last but not least, my loved family, all my friends for the encouragement and support and a very warm thanks to Giorgia for all her love and for everything she did for me also in the most critical periods.

Abstract

γ-TiAl alloys are a family of intermetallic compounds which, thanks to their excellent physical and mechanical properties, are arousing big interest in the aerospace and automotive industries. In particular, they are considered an attractive alternative to nickel-based superalloys due to a lower density (about 4 g/cm3 for γ-TiAl alloys and 8 g/cm3 for Ni-based superalloys) that makes their specific mechanical properties comparable to those of nickel-based superalloys. The low weight of these materials allows to reduce the overall weight of the aircraft engine component or automotive engine component. As a result, it is possible to enhance the components performances and reduce fuel consumption and emissions. The low weight of γ-TiAl alloys, it will also contribute to achieve the targets for fuel-burn and emission reduction proposed by the European Commission and NASA.

The most applied conventional industrial scale processing routes for titanium aluminides include ingot casting, ingot forging, hot-rolling sheet production, investment and permanent mold casting and powder metallurgy processing. The processing of titanium aluminide via these conventional manufacturing methods can be complex due to the low ductility and fracture toughness of the material and casting process is an expensive solution and presents several problems such as the reactivity of the molten material with ceramics. The Electron Beam Melting (EBM) additive manufacturing technology is well known and considered for the processing of TiAl alloys, in particular for the aerospace application. This additive manufacturing technology uses an electron beam to generate parts by selectively melting the powder layer by layer according to CAD data. EBM technology allows to produce lighter and complex-shape components with a minimum material and energy waste.

The goal of this thesis was to investigate and characterize both γ-TiAl specimens and components produced by EBM and the heat treatments set-up in order to optimize the material properties. Since the starting material for the EBM process is the pre-alloyed powder, the characterization and the optimization of the

powders was a fundamental preliminary step in order to guarantee a successful production of the final parts.

The experimental activities are related to four different TiAl alloys, three of which for aircraft engine application that are the 48-2-2 alloy (Ti-48Al-2Cr-2Nb (at.%)), the High-Niobium alloy (Ti-(45-47)Al-2Cr-8Nb (at.%)) and the TNM alloy (Ti-43.5Al-4Nb-1Mo-0.1B (at.%)) and one of automotive interest that is the so called RNT650 alloy (Ti-48Al-2Nb-0.7Cr-0.3Si (at.%)).

The TiAl 48-2-2 powder reuse investigation has demonstrated the possibility to reuse the powder up to six EBM cycles without a significant pick-up of contaminants, modification of particle size distribution, flowability and apparent density during the subsequent EBM jobs. This achievement means that, by reusing the powders for several cycles it is possible to obtain a considerable advantage in terms of cost and material saving. However, it is important to specify, that it is possible to mix the recycled powder with new powder between different cycles in order to maintain the proper powder characteristics.

The effect of the EBM processes parameters on the TiAl 48-2-2 material properties has been investigated by varying certain building parameters according to a Design Of Experiment (DOE) matrix. The study has shown that i) there is a parameters combination window in which the amount of process defects in the built material is very limited, ii) inside this window it is possible to perform a further fine parameters tuning in order to obtain an homogeneous microstructure and limit the evaporation of low-melting elements such as aluminum. In fact, this study has confirmed that the aluminum content and microstructure are very sensitive to the parameters variation.

Regarding the 3rd generation TNM alloy for aircraft engine application, it has been demonstrated the possibility to process it by EBM obtaining fully densified parts and, after a proper heat treatment, it has been possible to obtain the desired

microstructures in order to improve the mechanical properties of the material according to the application.

The RNT650 alloy for the automotive application has been successfully processed by EBM and both massive specimens and lightweight hollow turbocharger wheels have been produced and characterized. Also in this case, a proper microstructure for the application has been obtained by means of a proper heat treatment. In addition, the characterization of a turbocharger wheel-shaft assembly prototype has been performed and it has shown a promising junction quality with a complete adhesion and without the presence of any defects at the interface.

Regarding the aircraft engine application of γ-TiAl, big part of the research activity was done in collaboration with AvioAero, within some European and Regional research projects. In particular, the 48-2-2 alloy as well as new generation alloys such as High Niobium alloy and TNM alloy produced by Electron Beam Melting were investigated in the frame of the European project E-BREAK.

Considering the automotive application, the part of the work on the RNT650 alloy was done within the European project TIALCHARGER.

Table of Contents

List of Figures

List of Tables

Chapter 1

Introduction

1.1 Materials for high temperature structural application: development and present status

Since the beginning of civilization, the knowledge and use of materials, together with energy, represented the most important instrument to improve the quality of life. Materials are all around us, because all the products that we use are made with them.

The continuous progress in engineering constantly requires an improvement of material properties, especially to operate in extreme conditions. For this reason, material science and engineering are playing a key role to develop new high-performance materials with properties that allow the realization of technologically advanced objects, devices and vehicles. The challenge is to push the materials properties to increase components performance.

For some specific applications, one of the most limiting condition at which materials have to resist is temperature. Considering the aerospace and automotive industry, there is a simultaneous need for lower weight and higher temperature resistance in order to obtain a better engine efficiency. To increase the efficiency of an engine, higher temperatures are needed and a suitable material for this application must have good physical and mechanical properties at such temperatures. Unfortunately, most of the conventional materials such as steel and aluminum alloys cannot satisfy the requirements to work in such conditions.

However, there is a group of materials that can be defined as "high-temperature materials" that, thanks to their chemical composition and atomic structure, presents excellent properties at high temperatures [1][2].

Commonly, materials are not characterized or classified in terms of their temperature capabilities, in fact, the materials for high-temperature applications can be metals and alloys, ceramics or composites depending on the requirements for the specific application. On the other hand, for the materials scientist or material engineer can be very useful characterizing materials according to how they perform under certain thermal conditions because it is a way of narrowing the field of possible candidates suitable for a particular application. However, what is the temperature that divides low and high temperature materials? Even though, there is not a universally accepted temperature, most scientists consider materials that maintain structural integrity above 600°C as high temperature materials [2].

1.2 The new challenge: Greening the propulsion. Environmental and energy-saving politics and EU projects

According to the Intergovernmental Panel on Climate Change (IPCC), the airline industry is responsible for an estimated 2% of the global man-made carbon dioxide (CO_2) emissions. For the road transport, the estimated percentage is around 15% for cars and vans and around 6% for heavy-duty vehicles of total EU emission of CO_2. Nowadays, the aircraft and road-transport emissions are regulated. However, the huge increase in traffic over the intervening period, forces to reduce local chemical pollutants, specifically nitrogen oxides (NOx) [3][4].
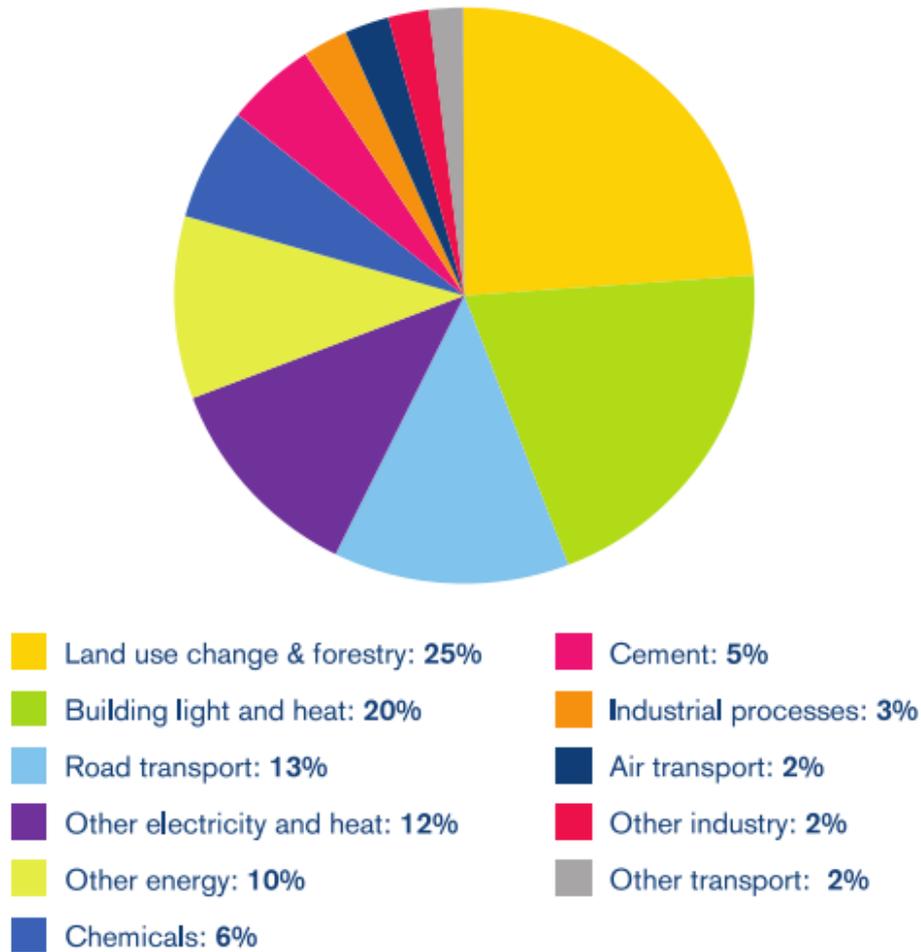
Figure 1: Contributions of various industry sectors to man-made CO_2 emissions [4].

In 2001 the Advisory Council for Aviation Research and Innovation in Europe (ACARE) published a "vision" for 2020; this set targets of 50% reductions in fuel-burn and perceived noise, and 80% in landing/take-off NO_x emissions compared to the year 2000 levels [5]. Furthermore, with the program "FlightPath 2050", in 2011 the European Commission established the reductions of fuel-burn, noise and NO_x emission of 75%, 65% and 90% respectively by 2050 [6]. In the U.S., similar goals have been proposed by NASA for the "N+2" (service-entry 2025) and "N+3" (service-entry 2030-35) generations of aircraft [7]. The ACARE and NASA goals are summarized in **Table 1** [8].

Table 1: Fuel-burn and emission reduction goals put forward by ACARE and NASA [8].

Category	ACARE		NASA	
	Vision 2020	**FlightPath 2050**	**N+2 (2025)**	**N+3 (2030-35)**
Fuel	50%	75%	50%	60%
	Relative to year-2000 aircraft		Relative to year-2005 best-in-class	
NO$_x$	80%	90%	75%	80%
Noise	50%	65%	42 EPNdB	71 EPNdB
	Relative to year-2000 aircraft		Cumulative, relative to Stage 4	

Regarding the road transport, the EU legislation sets binding emission targets for the new car and van fleets. As the automotive industry works towards meeting these targets, average emissions are falling each year and the targets for 2015 (for cars) and 2017 (for vans) were achieved already in 2013. By the other hand, for heavy-duty vehicles the emissions are still rising, mainly due to increasing road freight traffic. The Commission is working on a comprehensive strategy to reduce CO_2 emissions from heavy-duty vehicles in both freight and passenger transport [9][10].

In order to achieve these goals, the European Commission is funding several research projects where the collaboration between industries, research centers and universities, it is already providing huge results in emissions reduction and vehicles efficiency [11][12].

In this thesis, part of the described activities, where conducted within two European Projects funded by the Seventh Framework Program of the European Commission:

- **E-BREAK - Engine BREAKthrough components and subsystems**

    Related to the Aircraft sector, started on October 2012, and ended in March 2017, the aim of this project is to reducing air traffic emissions by adapting sub-systems to new constraints of temperature and pressure. E-BREAK will target sub-systems breakthrough, through improvements regarding mass reduction, material resistance, sealing

technologies, oil systems, abradable coatings, tip clearance control, stability of the engine in off-design operations and health monitoring.

This project will contribute a reduction of CO_2 of between 1.6% and 1.9% (depending on the engine architecture), which, together with the results of previous and current European projects, could enable a reduction of up to 32% in CO_2 emissions over the Year 2000 status.

The E-BREAK consortium consists of 41 partners from 10 different countries, in particular 12 industrial companies, 4 SMEs, 18 academic institutes and 7 research institutes. Just to name a few partners: Safran Turbomeca, Safran Snecma, MTU Aero Engines, Avio Aero, Rolls-Royce, DLR, Onera, Politecnico di Torino, Politecnico di Milano, University of Oxford and many more [13]. The part of the project related to the works described in this thesis is the SP5 "Lightweight materials for breakthrough components".

- **TiAlCharger – Titanium Aluminide Turbochargers**

  This project is related to the automotive sector. In particular, the purpose of TiAlCharger is the development of production processes for turbocharger wheel-shaft assemblies made of titanium aluminide alloys. The combination of the use of this light-weight high-temperature materials and the Electron Beam Melting (EBM) as manufacturing technique, will brings to an improvement of vehicle efficiency by 5% and a reduction of CO_2 emissions by 8%.

  The partners of this project are TWI, CVE, Cogeme, TLS Technik, Arcam AB, Josh, Politecnico di Torino, IHI charging systems international and Fraunhofer IFAM [14].

In both projects, the efficiency improvement, the emission reduction and, consequently, the reduction of environmental impact of the aircraft and automotive propulsion is obtained thanks to the use of titanium aluminide and the electron beam melting additive manufacturing technology.

The use of heat-resistant and light-weight materials such as titanium aluminides in low-pressure turbine blades and in turbocharger wheels, allows high operating temperatures, higher engine performances with a considerable reduction in fuel consumption and emissions. In the following chapters, the comparison between

titanium aluminides and conventional materials will be considered and the advantages obtained by the use of this material will be discussed.

The achievement of the goals is also possible thanks to an alternative manufacturing method based on the additive manufacturing technologies. As it will be highlighted in this thesis, the electron beam melting (EBM) is an extremely advantageous technology in terms of cost and material saving [15][16][17].

1.3 Aircraft engine and automotive application

In this section, two important applications for high temperature structural materials and titanium aluminides are briefly described: the aircraft engine and the automotive engine application.

The main reason why these two industrial field are considered is because there is a continuous need for materials capable to maintain the integrity of the mechanical properties and environmental resistance to overcome the stresses in operation. Another reason to consider these fields is because this thesis focuses on Titanium aluminides, a class of materials, that from few decades, is attracting a big interest for the aircraft engine and automotive engine application.

In particular, to fully understand the potentiality of titanium aluminides, can be useful to describe the gas turbine of aircraft engine and, regarding the automotive application, the turbocharger.

1.3.1 Gas turbine: principles and components

In the aircraft application, there are different forces involved. Some forces act in an opposite way respect the others and, in order to allow an aircraft to fly and obtain the maximum efficiency, is extremely important to maximize some forces and, of consequences, overcome the other forces. The driving forces created by the engine propulsion is the thrust, and the drag is its opposite force resulting by the air resistance. Another force in act that allow a vehicle to fly is the lift; on the other hand, the lift is opposed by an inevitable downward force caused by gravity: the weight. In few words, maximize the propulsion and minimize the weight is the way to reach a good efficiency.
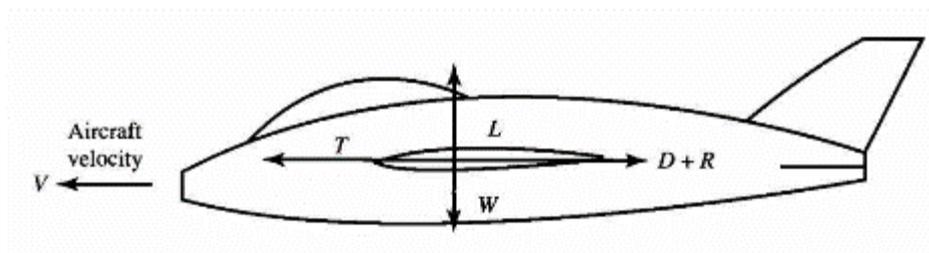
Figure 2: Forces on aircraft

Methods devised to produce a thrust force for the propulsion of a vehicle in flight are based on the principle of jet propulsion, which can be defined as the momentum change of a fluid by the propulsion system. The fluid used by the

vehicle may be stored in it and carried during the flight as in rocket, may be the gas used by the engine itself or may be a fluid available in the surrounding environment [18].

The different type of aircraft engines or spacecraft engines, create propulsion force in different ways, using different principles and the jet propulsion systems can be subdivided into two broad categories: the rocket propulsion (or non-air breathing) and the air-breathing propulsion [19]. While rocket propulsion is used for rocket motors, nuclear propulsion systems and electric propulsion systems, air-breathing propulsion is the method used by the aircraft engine.

Once this first distinction has been made, it is fundamental to further distinguish the air-breathing aircraft engines in turbojet, turbofan, ramjet, turboprop and turboshaft. The thrust of the turbojet and ramjet results from the action of a fluid jet leaving the engine; the turbofan, turboprop and turboshaft engines supply thrust using fans, propellers, and shaft.

High-temperature and high-pressure gas is the fluid needed by the engine, and for this reason, the core of the gas turbine engine is the gas generator. The gas generator is composed by the compressor, the combustor and the turbine. The principle is based on the Brayton thermodynamic cycle: air is aspirated into the engine and compressed. The compression increases the pressure and reduces the volume causing an increase in temperature. Then, fuel is mixed with high-pressured air the combustion occurs. During combustion, the temperature and volume increase while the pressure remains stable because the generated exhaust gas expands through the turbine to drive the compressor. At the turbine and nozzle stage, the temperature and pressure decrease which leads the volume to increase [20].
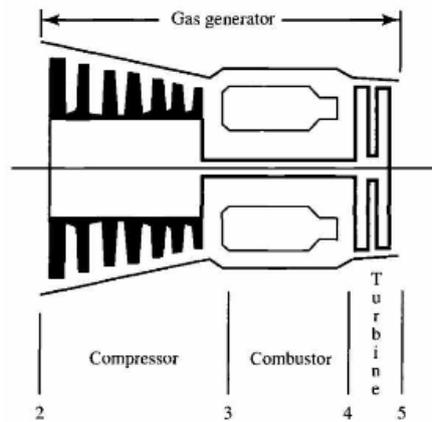
Figure 3: Schematic diagram of gas generator.

The schematic drawings of the different gas turbine engine and some engine examples are represented in **Figure 3**, **Figure 4, Figure 5, Figure 6, Figure 7, Figure 8, Figure 9** [21][22][23][24]**.**
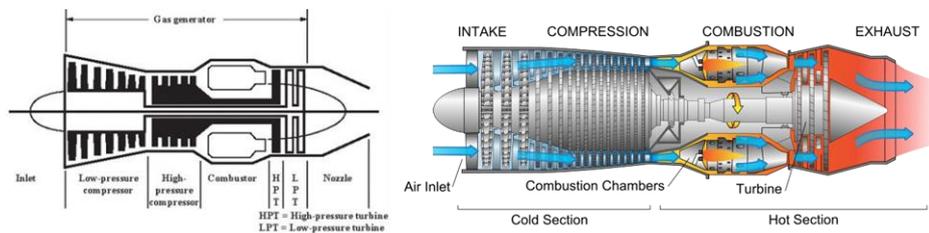
Figure 4: Schematic diagram of a turbojet.

Figure 5: General Electric J79 turbojet.
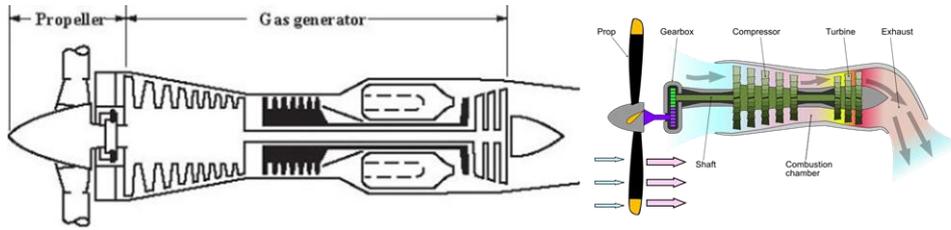
Figure 6: Schematic diagram of a turboprop.
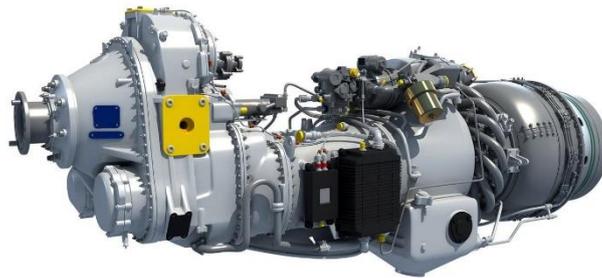
Figure 7: Pratt & Whitney Canada PW100 turboprop.
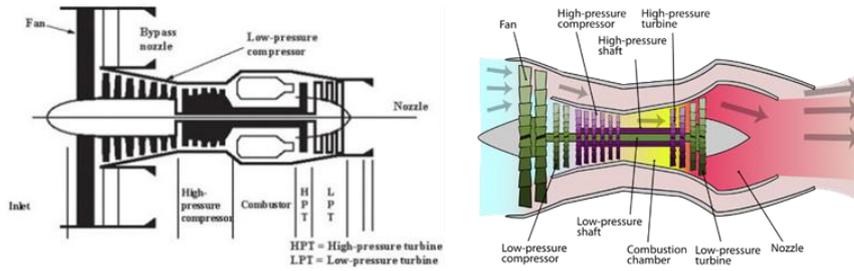
Figure 8: Schematic diagram of a high-bypass-ratio turbofan.
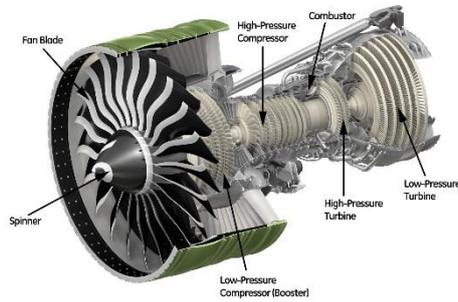
Figure 9: General Electric GE90 turbofan.

Each engine type will operate within a certain range of altitudes and velocities (corridor of flight). **Figure 10** shows the velocity and altitude operation limits for the different airlift vehicles.
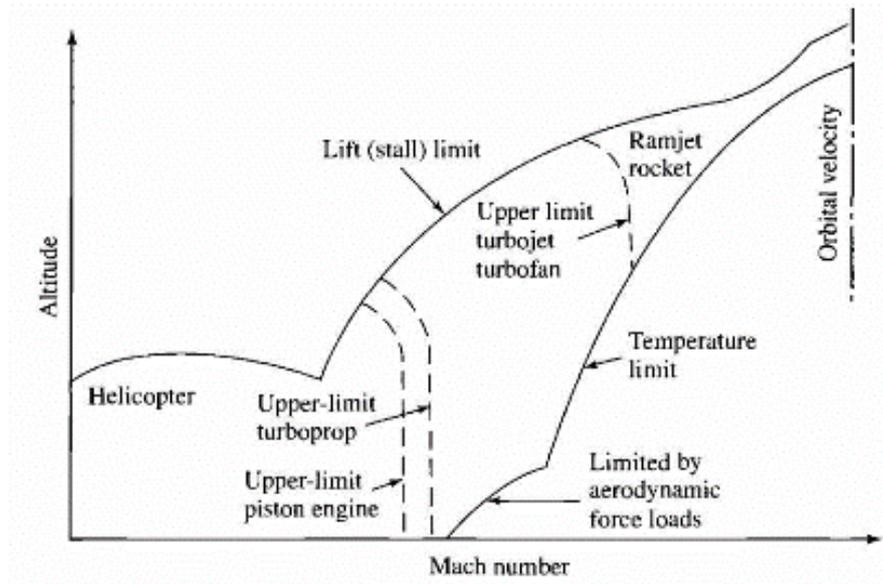
Figure 10: Flight limits [18].

The corridor is bounded by a lift limit, a temperature limit and an aerodynamic force limit. The temperature limit is settled by the structural thermal limits of the materials used.

The operational limits of each propulsion system are determined by limitations of the used components [18].
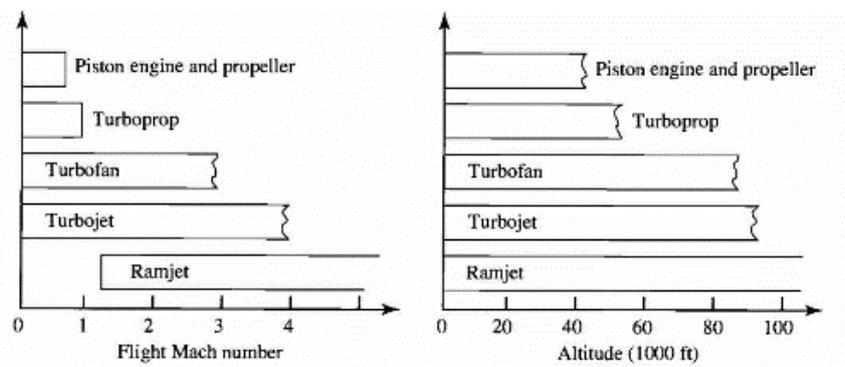
Figure 11: Engine operational limits [18].

In **Figure 12**, the specific thrust characteristics of the different typical aircraft engines are reported and in **Figure 13**, the typical aircraft engines are compared in terms of thrust-specific fuel consumption. These characteristics give the general trends of the performance parameters with flight velocity for the different propulsion systems.
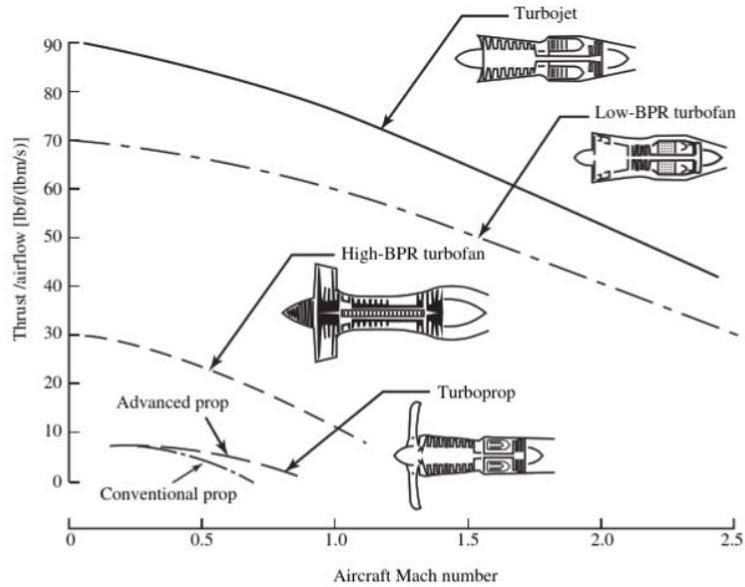
Figure 12: Specific thrust characteristics of typical aircraft engine [18].
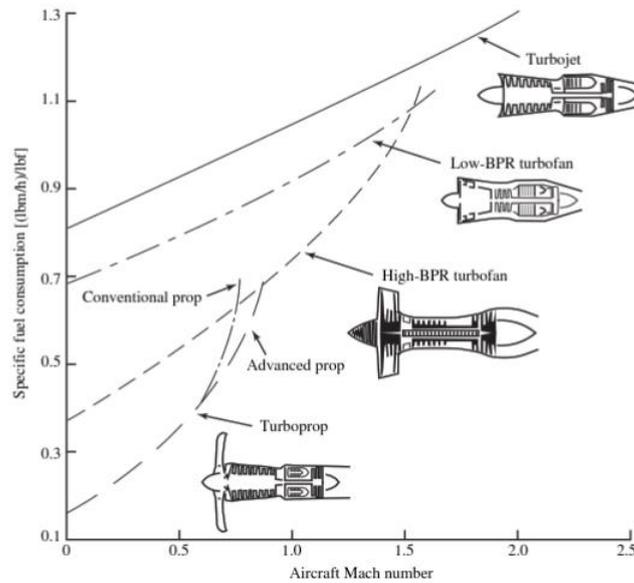
Figure 13: Thrust-specific fuel consumption characteristics of typical aircraft engines [18].

Nowadays, turbofan engines are probably the most used in civil aviation for different reasons:

- More economical and efficient than a turbojet;
- Better aerodynamic performance than turboprops at high speed.

On the other hand, the frontal area of a turbofan is quite large compared to that of a turbojet resulting in more drag and more weight [25].

1.3.2 Turbofan main components

Even if every model of turbofan engine is different in terms of configuration, fuel consumption and technology, the design and the manufacturing process of the components are similar. From a material point of view, all types of turbofans are similar because the temperature and pressure range for the different section are similar.

In this section, the attention is mainly focussed on two important components: Turbines and compressors. Turbines and compressor belong to the *turbomachinery* category defined by Dixon (1998) as:

We classify as *turbomachinery* all those devices in which energy is transferred either to, or from, a continuously flowing fluid by the dynamic action of one or more moving blade rows. The word turbo or turbines is of Latin origin and implies that which spins or whirls around. To narrow the range of machines we usually look at enclosed machines in which a finite amount of air passes through.
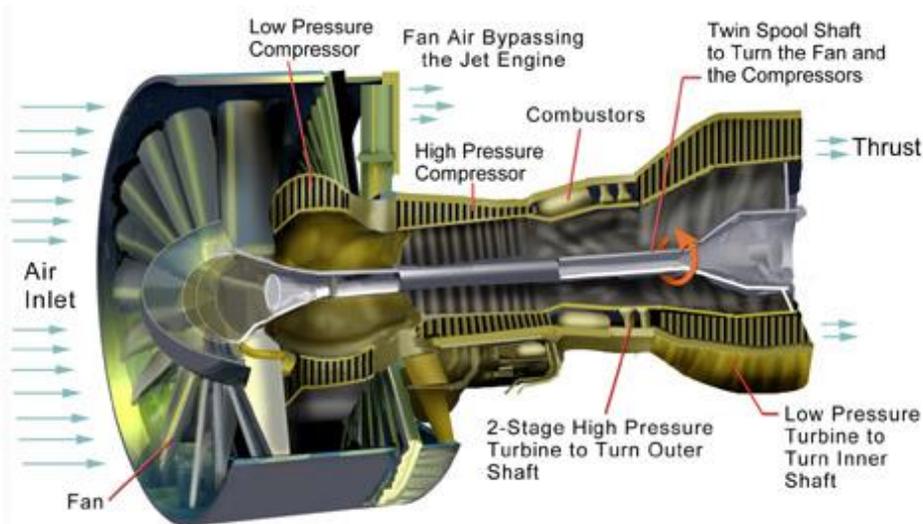
Figure 14: Schematic of High Bypass Ratio Turbofan Engine [26].

The main components and operations of the turbofan engine can be explained as follow:

- **The fan module**

The most of the thrust is produced by the fan and the low pressure compressor (booster). The aim of this module is to provide the airflow to the engine. In the case of the high bypass ratio turbofan, 80% of the air flow by-pass the core of the engine (secondary air flow) and 20% of the air flow is directed towards the core of the engine.

- **The core module**

The gas generator is composed by the HPC high-pressure compressor, the HPT high-pressure turbine and the combustor.

The compressor supplies the air at high static pressure to the turbine. The compressor is composed by several stages that are formed by a set of rotor blades attached to a rotating followed by a stator vanes attached to a stationary

ring. The role of the compressor rotor blades is to convert mechanical energy into gaseous energy by expanding the hot and high-pressure gases. The temperature of the air at the compressor outlet can reach 700°C.

The hot and high-pressure air enters the combustor where is mixed with fuel and burnt.

The HPT converts the gaseous energy of the mixture of air and burnt fuel into mechanical energy, expanding the hot compressed gases to a lower temperature and pressure, in order to drive the compressor [27].

- **The low-pressure turbine module**

The low-pressure turbine (LPT) converts the gaseous energy into mechanical energy by expanding the hot and high-pressure gases. This allows the LPT module to drive the fan and produce the thrust.

Each stage of the LPT consists of stationary vanes and rotating blades organized in rows and in a reverse order compared to the compressor.

In this module, the gas velocity is increased by the stator vanes end the energy in extracted by the rotor blades. The temperature at the turbine outlet can reaches 700°C.

At the end of the cycle, the gas is discharged through the exhaust. The exhaust gas contains a significant amount of not-converted energy that can be used to produce jet thrust accelerating the gas through the convergent duct or exhaust nozzle [28][29].

(e)
Legend
1. Spinner cone
2. Fan blades (7 of 38)
3. Fan forward case
4. Low-pressure compressor (LPC) booster stator
5. LPC booster rotor
6. Fan shaft
7. Fan frame, aft case, and outlet guide vanes
8. High-pressure compressor (HPC) stator
9. HPC rotor
10. Compressor rear frame
11. Combustor
12. High-pressure turbine (HPT) stage 1 nozzle
13. HPT rotor
14. HPT stage 2 nozzle
15. Low-pressure turbine (LPT)
16. Turbine rear frame
17. Accessory gearbox and fire shield

Figure 15: General Electric CF6 80C2 engine

1.3.3 Turbocharger: principle and components

The power output of an engine basically depends on the amount of energy, in the form of a fuel, that can charge the cylinders, but this amount of fuel is limited by the mass of air that can be introduced. In a naturally aspirated engine, the air is forced in by the atmospheric pressure but, because of throttling by components and viscous drag in the induction system, the pressure of the air and its density ultimately in the cylinder is lower than atmospheric. The amount of air actually inspired, compared to the theoretical amount if the engine could maintain atmospheric pressure, is called "volumetric efficiency" [30]. Consequently, any measure such as supercharging, turbocharging or cooling the charge to increase its density must be the key to increasing power output per unit of size and weight of the engine. These measures can be used also to modify the torque characteristic, generally to help to increase the torque over a broad speed range [31].

A turbocharger consists of a single-stage radial-flow compressor (left-hand side in **Figure 16**) which is driven by a single-stage radial-flow turbine (right-hand side in **Figure 16**). Basically, the turbine extracts wasted kinetic and thermal energy from the high temperature exhaust gas flow and produces the power to drive the compressor. In other words, the turbine recovers some of the energy which is lost in the thermodynamic cycle [32][33].
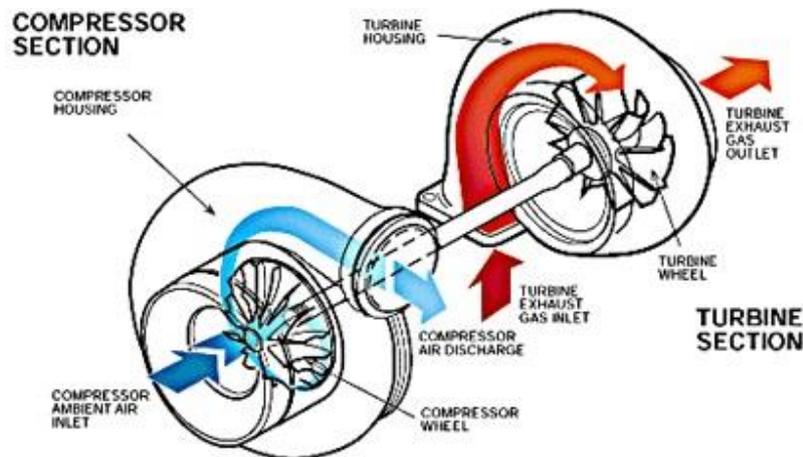
Figure 16: schematic view of a turbocharger [32].

The advantage of compressing the air is that it lets the engine squeeze more air into a cylinder, and more air means that more fuel can be added. Therefore, you get more power from each explosion in each cylinder. A turbocharged engine produces more power overall than the same engine without the charging. This can

significantly improve the power-to-weight ratio for the engine. Incrementing the inlet pressure allows downsizing the engine; this brings to reduce the fuel consumption and pollutants emission.

The turbocharger performance has a huge impact on engine and vehicle performance. In **Figure 17**, it is represented an example of turbocharger maps that are used to specify the performance of compressors (left) and turbines (right). Maps contain information about how pressure ratio, rotational speed, mass flow, and efficiency are connected [34][31].
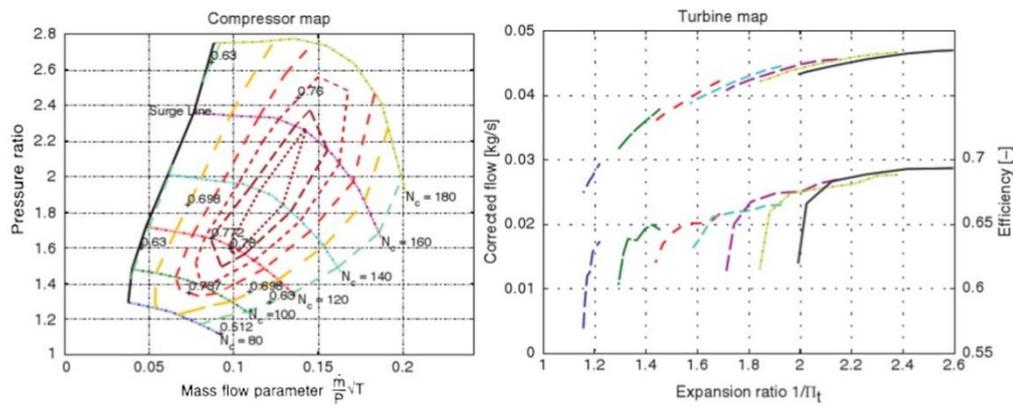
Figure 17: Turbocharger maps [34].

A common lack of turbocharging is what is termed *turbocharger lag*. This phenomenon is caused by the need, as the demand of torque fluctuates, to accelerate and decelerate the rotor to and from extremely high speeds. Because of the inertia of the rotating assembly, of which about 60% is generally attributable to the rotor of the turbine, it can take several seconds to respond to such changes. This can be overdue thanks to modern designs allowing much shorter response times.

The operating range can be improved by the development of suitable variable geometry or variable nozzle systems. In such systems, the geometry of ring of vanes or the nozzle can varying as mass flows change. Improving the operating range means greater efficiencies and higher compressor pressure ratio [35].

Twin-turbo or twin-scroll turbochargers are other advanced schemes used to improve efficiency and reduce turbocharger dimensions in larger engines.

Another way to improve turbocharging is the pulsating flow approach that can be obtained directly from the exhaust gases or by using a rotating valve [36][37].

Intercooling systems avoid the reduction of volumetric efficiency due to the excessive intake air temperature. In fact, the warmer is the intake air, the lower is its density.

It is also important to minimize the heat flow effect using several approaches. The external heat flow can be reduced by using a thermal insulation.

In order to obtain high mass flow rates and thus to convert as much energy as possible into torque, speeds over 100000 rpm are necessary. The temperatures of gas are about 1000 K on diesel engines, and up to 1200 K on spark ignition engines. In automotive application, torques generally is around 10 Nm [31].

1.4 High Temperature Materials for Aircraft Engine and Automotive

Progresses in gas turbine engines and automotive engines technology have led to engines with higher power ratings and efficiency levels. Improvements in component design have been possible thanks to advancements made in the field of materials. Materials with higher capability to withstand elevated temperature service conditions allow the engine efficiency to increase. The high specific properties, such as strength to weight ratio at elevated temperature of certain materials, help to reduce component weight and further increase the engine efficiency. Another advantage obtained thanks to the weight reduction is the decrease of carbon and nitrogen oxides emissions and noise.

An aircraft gas turbine is composed by thousands of structural component with different function and operating at different environmental conditions. Due to the condition range at which components are subjected, a wide spectrum of high performance materials is used in gas turbines design. The main material used are special steels, titanium alloys, super alloys. Big interest is growing for other major group of materials like ceramics, composites and intermetallics, that are under intense research and development for the gas turbine engine application [38].
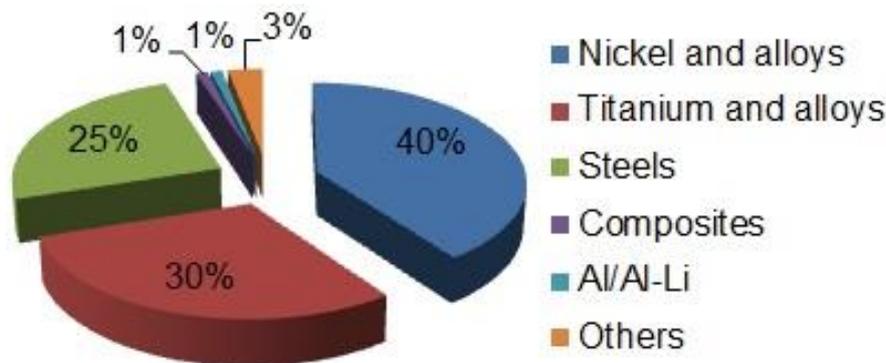
Figure 18: Material composition in Turbofan engines by total weight [38].

The first requirement for materials for gas turbine engine and turbocharger application is the high temperature tensile strength. Obviously, this requirement depends on the operating temperature. The components must also have the proper stress rupture life, creep properties and fatigue resistance.

The materials choice criteria for the different components are based on the capability of the material to withstand static, fatigue and creep loading at which the components are subjected during their operating life. At high temperature and critical environmental conditions, also oxidation and hot-corrosion resistance are crucial for components and the used materials have to satisfy also these properties, in many cases with the aid of coating technologies. Advanced processing methods are usually involved in the manufacturing of these materials [39][40][41][15].

As reported in **Table 2**, a particular component having peculiar function in the gas turbine engine is made of a material or material class that has to satisfy certain requirements for the application [38].

Table 2 schematic representation of the status for aero engine materials [38].

Component	Characteristics	Materials
Suction Fan	It should extremely strong so that it doesn't fracture when birds or other debris are sucked into the blades	Titanium alloys
Intermediate Compressor	Experiences very high pressure	Titanium and Nickel alloys (Inconel 625)
Combustion Chamber	Ability to withstand very high temperature	Nickel and Titanium alloys with ceramic coatings.
Turbine blades	Must endure the intense heat of the engine.	Titanium and Single Crystal castings of Nickel alloys with ceramic coatings.
Exhaust Systems a. Inner duct b. Outer duct	Should possess very high strength and resist to high temperature.	a. Titanium alloys b.Composites-Synthetic Fibers held together with resins.

In **Figure 19** it is reported a schematic diagram of a turbofan aircraft engine. The operating temperature ranges and an example of commonly used material are indicated in the image [42].

e.g.	Ti-64	Ti-6246	Ti-834	Ni-based Superalloys	Titanium Aluminides
Operating temperature [°C]	up to 230	up to 430	up to 730	1,230 - 730	up to 730
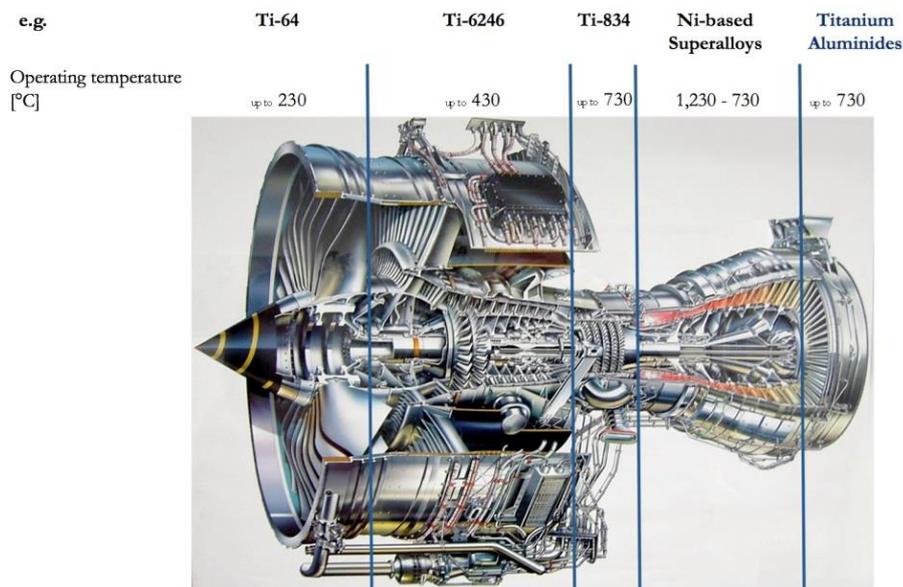
Figure 19: Representative turbofan engine section. The operating temperatures and the used materials are reported [42].

In a similar way, the hostile environmental conditions at which turbochargers are subjected, lead to an accurate choose of heat-resistant materials. Candidate materials for turbocharger turbines have to meet the necessary requirements such as high strength, fatigue, creep and oxidation resistance. Other important properties are resistance to erosion and foreign object damage [43][44][45].

Ni-based superalloys are commonly used for the turbine wheels as they retain high strength values at high temperatures. Turbines are typically manufactured by investment casting from Inconel 713 C or 713 LC. The Hot Isostatic Pressing (HIP) is then used to improve the wheels structure and minimize the presence of cast defects such as pores. Afterwards, the required strength level is obtained performing a proper heat treatment. **Table 3** lists the different superalloys commonly used nowadays in turbochargers.

Table 3: Superalloys currently used in turbochargers.

Chemistry of Certain Superalloys
Nominal Percentages of Alloying Elements

Material	Ni	Co	W	Cr	Al	Mo	Ti	C	Fe	Mn	Si	B	Nb	Hf	Zr
AMS 5844 (MP35N)	34.0	33.0		20.0		9.8	1.0	0.03	1.0	0.2	0.2	0.1			
CustomAge 625+	61.0			21.0	0.35	8.0	1.3	0.03	5.0	0.2	0.2		3.4		
Inconel 713LC	76.0			9.3	6.5	4.7	0.8	0.1					2.1		0.1
Mar-M-247	61.0	9.2	9.5	8.2	5.6	0.6	1.0	0.07		0.10	0.25	0.015		1.5	

Al = Aluminum	Cr = Chromium	Mo = Molybdenum	Ta = Tantalum
B = Boron	Fe = Iron	Nb = Niobium	Ti = Titanuim	GREEN numbers
C = Carbon	Hf = Hafnium	Ni = Nickel	W = Tungsten	are max values
Co = Cobalt	Mn = Manganese	Si = Silicon	Zr = Zirconium

The primary property required for a turbine wheel material is endurance against centrifugal stress generated during rotation. Since the centrifugal stress is proportional to specific gravity, specific strength is an appropriate measure. Ni-based superalloys present a specific gravity of about 8, for this reason, lightweight metallic materials should improve the response ability of turbochargers. However, as turbines are subjected to long-term exposure to high temperature exhaust gases of at least 850°C, conventional lightweight materials such as aluminum or Ti-based alloys cannot be used. As highlighted in this thesis, the development and application of high-performance TiAl alloy, together with innovative manufacturing technologies, will increase the performance of turbochargers such as the response ability and the reduction of the turbo-lag effect. In fact, the specific gravity of intermetallic TiAl-base alloys is roughly half that of Ni-based superalloys and that makes their specific mechanical properties extremely interesting [46].

As shown in **Figure 20**, the response ability of a particular TiAl turbocharger is higher than that of conventionally used turbocharger made of Inconel 713C. This means an improvement of the vehicles acceleration and drivability [32].

Resistance to high temperature oxidation and hot corrosion is also important, in fact, there are several studies about environmental resistance of all the used materials at highest application temperatures (850-1030°C). There has been a significant effort to develop coating solutions, in particular for TiAl, to enable operation at higher temperatures.
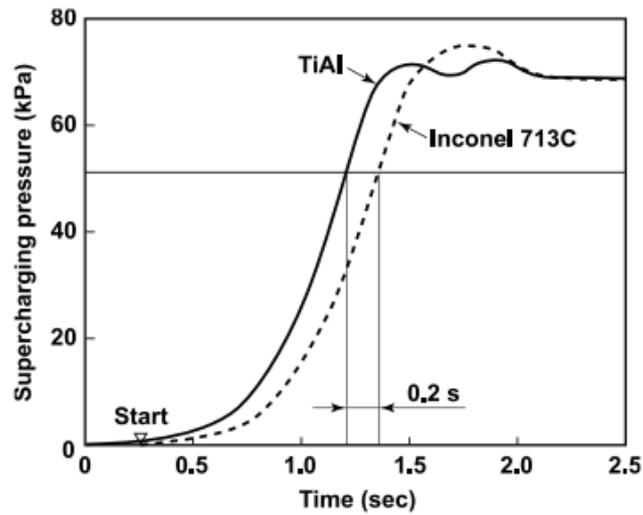
Figure 20: Comparison of response ability of a TiAl turbocharger and an Inconel 713C turbocharger [32].

In the following part, the most used classes of materials for the aircraft engine and turbochargers are briefly described.

1.4.1 Titanium Alloys

About one third of the structural weight of modern turbine engines is made of titanium; in particular, titanium alloys are used for most structural parts of the high-pressure compressor. Thanks to the high strength to weight ratio of titanium alloys, they satisfy the requirements for components working at medium range temperature and where oxidation is not an issue.

As it is possible to observe in **Table 4**, the maximum temperature limit of titanium alloys can reach about 600°C for the most advanced alloys [47].

Table 4: Titanium alloys used for compressor parts in aircraft engines – chemical composition and maximum service temperature [47].

Grade designation	Chemical composition	Maximum service temperature (°C)
Ti64	Ti-6Al-4V	315
Ti811	Ti-8Al-1Mo-1V	400
Alloy 685	Ti-6Al-5Zr-0.5Mo-0.25Si	520
Alloy 829	Ti-5.5Al-3.5Sn-3Zr-1Nb-0.25Mo-0.3Si	550
Alloy 834	Ti-5.8Al-4Sn-3.5Zr-0.7Nb-0.5Mo-0.35Si-0.06C	600
Ti1100	Ti-6Al-2.8Sn-4Zr-0.4Mo-0.4Si	600
Ti6242	Ti-6Al-2Sn-4Zr-2Mo	
Ti6242S	Ti-6Al-2Sn-4Zr-2Mo-0.2Si	540

The higher temperature resistance for titanium alloys has been achieved thanks to proper alloy composition modifications and optimized processing routes. Using these strategies, the microstructures can be set in order to increase the mechanical properties [48][49].

Since the hottest stages of the high-pressure compressor may exceed this temperature, the materials used for this part are Ni-based or Co-based superalloalloys.

1.4.2 Superalloys

Superalloys are probably the most studied and advanced structural materials for high temperature gas turbine engine application. Superalloys, typically Ni-based or Co-based alloys, constitute about 40% of a modern aeroengine total weight, in particular for combustor and turbines. In turbocharger application also, Ni-based superalloys represent the currently most used material [50][51].

Regarding the aircraft engine, the combustor parts in a gas turbine are exposed to very high temperatures and Ni-based superalloys represent the best option thanks to their high creep and oxidation and hot corrosion resistance. Traditionally, combustor components have been fabricated using sheet Ni-base superalloys. From 1960s to 1980s, the Hastelloy X was used, than, Nimonic 263 was subsequently introduced for it higher creep strength. In the new gas turbine models, cobalt base superalloys has been adopted for some combustion system components to improve

creep rupture strength at higher temperature. In **Table 5** the chemical compositions of combustor materials are reported [47].

Table 5: Combustor sheets superalloys [47].

Grade	Chemical composition
Hastelloy X	Ni-22Cr-1.5Co-1.9Fe-0.7W-9Mo-0.07C-0.005B
Nimonic 263	Ni-20Cr-20Co-0.4Fe-6Mo-2.1Ti-0.4Al-0.06C
HA188	Co-22Cr-22Ni-1.5Fe-14W-0.05C-0.01B
617	54Ni-22Cr-12.5Co-8.5Mo-1.2Al
230	55Ni-22Cr-5Co-3Fe-14W-2Mo-0.35Al-0.10C-0.015B

In turbine stages, the combined effects of high temperature and centrifugal forces, makes creep strength a primary requirement for turbine vanes and blades materials.

The manufacturing routes for producing superalloys for the different engine parts components have to be considered because from them, depend the particular properties of the different types of superalloys. Originally, conventional ingot metallurgy routs were adopted to manufacture turbine disks using for example IN100 and Rene95. Anyway, these alloys are sometimes difficult to forge by conventional methods and for this reason, casting and Powder Metallurgy processing (PM) offered many advantages. The main advantage was the possibility to produce alternative alloys. Another big vantage of PM processes is the enhancement of the properties of the parts thanks to a better control of the microstructure. In addition, PM manufacturing allows to produce near-net-shape parts with an advantageous reduction of material waste and post processing operation. In **Table 6** details of disc superalloys for aircraft engines are reported.

Table 6: Disc superalloys for aircraft engines [47].

Grade	Chemical composition	Remarks
A286	Fe-15Cr-25Ni-1.2Mo-2Ti-0.3Al-0.25V-0.08C-0.006B	Iron-base superalloy; ingot metallurgy
718	Ni-19Cr-18.5Fe-3Mo-0.9Ti-0.5Al-5.1Cb-0.03C	Nickel-iron-base superalloy; ingot metallurgy
IN 100	60Ni-10Cr-15Co-3Mo-4.7Ti-5.5Al-0.15C-0.015B-0.06Zr1.0V	Nickel-base superalloy; PM
Rene 95	61Ni-14Cr-8Co-3.5Mo-3.5W-3.5Nb-2.5Ti-3.5Al-0.16C-0.01B-0.05Zr	Nickel-base superalloy; PM
LC Astroloy	56.5Ni-15Cr-15Co-5.25Mo-3.5Ti-4.4Al-0.06-C-0.03B-0.06Zr	Nickel-base superalloy; PM
MERL-76	54.4Ni-12.4Cr-18.6Co-3.3Mo-1.4Nb-4.3Ti-5.1Al-0.02C-0.03B-0.35Hf-0.06Zr	Nickel-base superalloy; PM
Rene88 DT	56.4Ni-16Cr-13Co-4Mo-4W-0.7Nb-3.7Ti-2.1Al-0.03C-0.015B-0.03Zr	Nickel-base superalloy; PM
Udimet 720	55Ni-18Cr-14.8Co-3Mo-1.25W-5Ti-2.5Al-0.035C-0.033B-0.03Zr	Nickel-base superalloy; ingot metallurgy / PM

The first stage turbine blades or buckets are subjected to the most severe conditions in gas turbine engines. Conventional equiaxed investment casting was originally used to produce turbine parts in the most demanding gas turbine engines. The casting process produce a coarse microstructure that ensure good high temperature mechanical properties in all directions. Using the equiaxed investment casting, rotating turbine blades made of IN713 were early produced. It is also important to remind that at extreme operation conditions, about 15% below the absolute temperature melting point, the microstructure of a superalloy can quickly change also in terms of constitution phases and their composition. By optimizing the chemical composition and post process treatment, the materials capabilities have been enhanced. In particular $\gamma^{'}$-Ni$_3$ (Al, Ti) precipitates volume fraction was

increased to improve the creep strength in IN100 and Rene100. In order to increase temperature capabilities, higher amount of refractory solid solution strengtheners, like W and Mo, were added. Other alloying elements were added to improve ductility (Hf) and increase corrosion resistance (Cr).

The Directional Solidification (DS) was developed with the intent to eliminate nucleation and growth of cavities along transverse grain boundaries, which represent the major fracture mechanism for gas turbine airfoils. DS increased the creep resistance and rupture strength and also the temperature capability could be increased by about 14°C with respect to conventionally cast superalloys. Another advanced casting manufacturing routes is the Single Crystal (SC) blade technology. SC allowed to increase the temperature capability of turbine blades of about 30°C eliminating all grain boundaries from the microstructure. Whit this technique, the airfoil blade consist entirely of a single crystal with a controlled orientation. Since in SC alloys no grain boundary strengtheners are necessary, the elimination of these elements helped in raising the melting temperature increasing the high temperature strength. **Figure 21** shows the improvement in creep strength of a cast superalloy produced by equiaxed polycrystalline investment casting, by DS casting and SC casting. In **Figure 22** turbine blades fabricated by conventional, DS and SC are shown [52][41].
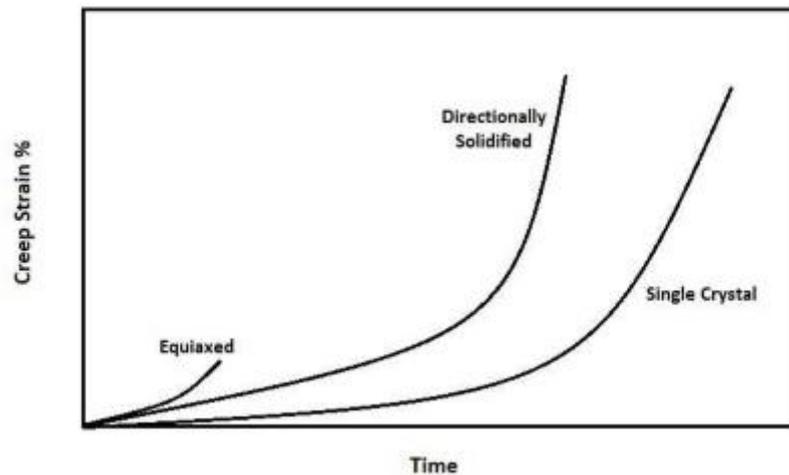
Figure 21: Relative creep deformation of equiaxed, DS and SC superalloy castings [52].
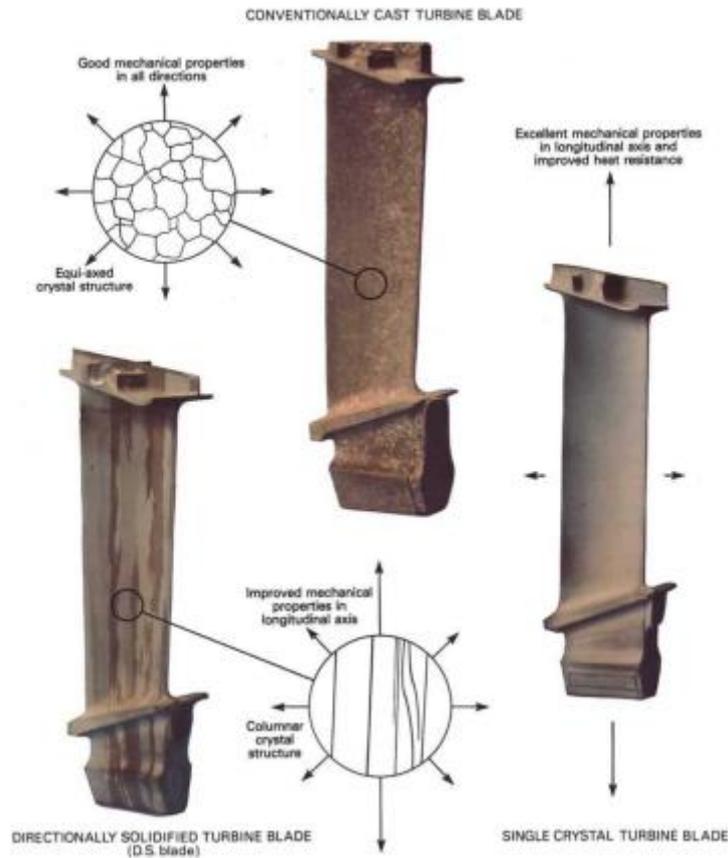
Figure 22: Different Ni-based superalloys turbine blades: polycrystal (center), directionally solidified alloy (left), single crystal (right) [41].

According to E. Campo [53], the superalloys used for the different applications in aeroengines, produced using different manufacturing processes and having different chemical composition, can be grouped in the following six classes:

Class A – solid solution strengthened alloys;

Class B – Co-base cast alloys;

Class C – Ni-base precipitation hardened wrought alloys;

Class D – Ni-base cast alloys;

Class E – 1st generation single crystal alloys;

Class F – 2nd generation single crystal alloys.

Table 7 shows some examples of these alloys belonging to the different classes with the relative manufacturing processes and in **Table 8** it is represented a summary of ranges for ultimate tensile strengths and elongations at 850°C. For material selection and for the very preliminary design, fatigue behavior can be described through the tensile characteristics because the low cycle fatigue resistance in terms of strain range is related to the tensile elongation of the material, whereas the high cycle fatigue resistance in terms of stress range is proportional to the ultimate tensile strength.

Table 7: Different groups of superalloys [53].

GROUP	PROCESS	ALLOY
A	Ni & Co sheets	Hastelloy X, Haynes 186, Nimonic 86
B	Cast Co	X 40, X 45, FSX 414, ECY 768
C	Wrought Ni	Inconel X740, Nimonic 105, Udimet 500, Inconel 700, Nimonic 115, Udimet 710, Udimet 720
D	Cast Ni	Udimet 500, Inconel 713LC, Renè 77, IN 100, Renè 80
E	SC Ni	PWA 1480, Renè N4, SRR 99
F	SC Ni II	PWA 1484, CSM X4, Renè N5

Table 8: Tensile properties at 870°C [53].

GROUP	UTS [MPa]	El. [%]
A	310 - 420	50 – 85
B	310 – 410	16 – 22
C	640 – 830	15 – 30
D	660 – 900	5 - 18
E	980 -1020	10 - 20

Thanks to their high temperature strength resistance, Ni-base superalloys, in particular Inconel713C, are currently the most used materials for turbocharger turbines too. Casting processes are the most used manufacturing technique for the production of conventional turbocharger turbines and compressors.

1.4.3 Intermetallics and Titanium Aluminides

Intermetallics are a family of compounds formed by two metallic elements, having properties that are different from those of the constituent metals. A peculiar characteristic of intermetallic compounds is the limited deformation caused by the formation of long-range ordered crystal structure below T_c, which is the critical ordering temperature. This brings to an increased yield strength at high temperatures but also to poor room ductility and low fracture toughness at room temperature. The brittleness of intermetallics is usually due to the lack of dislocation mobility and it is the more limiting characteristic for the application of these materials.

Since the mechanical properties of intermetallics are strictly related to their crystal structures, it is important to underline that many intermetallics compounds change different ordered structures when subjected to temperature below the melting point. In particular, γ-TiAl alloys maintain ordered structure until the melting temperature that is around 1440°C. By varying the chemical composition range from the stoichiometric ratio, the structure tends to become less ordered [54].

Intermetallics have been deeply studied and developed during the last 30 years for application in aircraft gas turbine engine and in automotive application. The primary purpose was to replace Ni-based superalloys with a density of 8-8.5 g/cm^3 with lower density materials (about 4 g/cm^3). Titanium aluminides represent the most intensively investigated intermetallics for these applications.

In particular, titanium aluminides phases of technical interest are the α_2-Ti$_3$Al and γ-TiAl. The latter alloys are usually also two-phase $\alpha_2 + \gamma$ or multi-phase alloys depending on the alloying elements. The TiAl phase diagram and the effects of the different alloying element used are described in details in section 1.5 The binary Ti-Al phase diagram" of this thesis.

Further advantages of TiAl intermetallics are high melting temperature, high strength, good oxidation resistance and good creep properties in a selected temperature range. On the other hand, these materials exhibit low room temperature ductility and low fracture toughness. Big efforts have been done in order to optimize the composition and the microstructure of TiAl in order to overcome these drawbacks.

As can be observed from **Table 9**, Ni-based superalloys present superior properties compared to those of γ-TiAl. However, since the density of the γ-TiAl is about one half of that of Ni-based superalloys, the specific properties are significantly higher for γ-TiAl [55].

Table 9: Comparison between cast γ-TiAl alloys and cast Ni-based superalloys [55].

Property	γ-TiAl alloys	Ni superalloys
Density [g/cm^3]	3.7-3.9	8.3
Yeld Strength [MPa]	400-650	1000
Ultimate Tensile Strength [MPa]	450-800	1200
Ductility [%]	1-4	15
Modulus of elasticity [GPa]	160-175	206
Poisson's Ratio	0.27	0.29
Coefficient of Thermal Expansion [10^{-6}/°C]	10.8	14.8
Thermal Conductivity [W/m*K]	22	11
Maximum Use Temperature [°C]	900	1000

TiAl alloys with an appropriate composition and microstructure have shown outstanding specific strength compared to currently used superalloys in the considered temperature range (**Figure 23)** [56]**.**
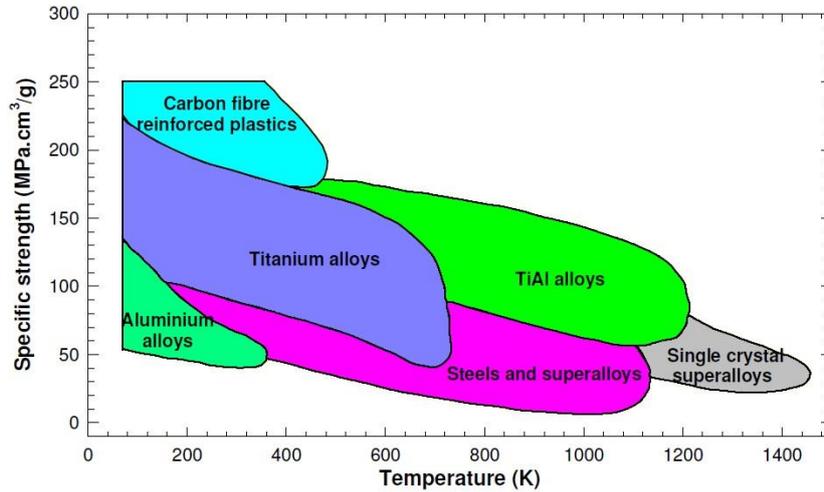
Figure 23: Temperature dependence of specific strength of various groups of alloys [56].

Other specific properties that are higher for γ-TiAl are shown in **Figure 24** [57]. The good specific mechanical and physical properties of TiAl-based alloys make them suitable for applications as rotating medium-high-temperature structural components [58][59].
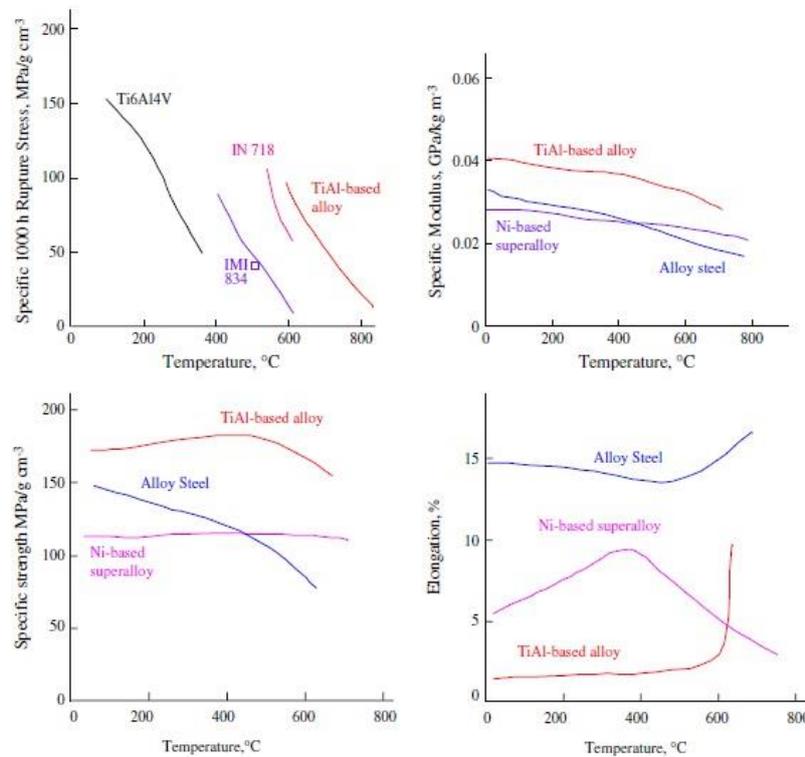
Figure 24: Specific properties comparison between TiAl-based alloys, Ni-based superalloys, alloy steel and Ti alloys [59].

A very explanatory example regarding the aircraft engine application is the use of TiAl alloy in a large and advanced turbofan engine like the GE9X. In particular, TiAl is going to replace Ni-based superalloys for the production of blades at some stage of the low-pressure turbine. TiAl blades are only about 55% the weight of a conventional Ni-based superalloy blade. This weight reduction means a significant drop in fuel consumption and emission of the engine and it also enable an even lighter weight design of the entire turbine due to the lower centrifugal forces imposed on the disc [22].

Generally, the production cost of TiAl is higher than that of Ni-based superalloys. This is due to the difficulty to process it using conventional manufacturing methods because the fairly low ductility of TiAl alloys. Due to the low fracture toughness, post-processing and machining without damaging the material is also a challenge.

Popular techniques that have been used to produce TiAl parts are investment casting, ingot metallurgy (IM), and powder metallurgy (PM). Direct rolling, laser

forming, mechanical alloying, spark plasma sintering are other more recently and advanced manufacturing techniques that have been used to forming TiAl [60][61][62].

Additional costs are due to a series of post processing steps, like hot-isostatic pressing, ageing, annealing and hot working, that are necessary to reach the desired mechanical properties of TiAl products after their manufacturing by investment casting, ingot metallurgy and powder metallurgy technology.

Casting routes bring to a microstructure characterized by large columnar grains with a non-homogeneous chemistry and segregation. This particular microstructure results in a drop of mechanical properties, in particular strength and fatigue resistance. Significant improvements in chemical homogeneity and microstructure refinement can be achieved by thermos-mechanical processing, by the optimization of the alloy composition and also by using other servo-mechanical routes such as hot-rolling, forging and extrusion [55][59][56].

Powder metallurgy can be an alternative. This manufacturing technique generally consists of gas atomization of pre-alloyed powder followed by hot isostatic pressing (HIP) of the powder. The advantages of hot isostatic pressing are a low porosity in the final part and a homogeneous microstructure. By the other hand, HIP requires exposure to high temperatures for several hours and this leads to a big grain size [63][64].

Other powder metallurgy methods, which allow to produce near-net shape parts are metal injection molding (MIM) and spray forming [65].

Additive Manufacturing (AM) is considered an advanced and cost-saving manufacturing technique for TiAl alloys. The main advantages of AM is the possibility to obtain near-net shape parts with homogeneous and fine microstructure and the possibility to re-use the powder with a considerable enhance of processing costs [17][66][67].

In **Figure 25** the industrial scale processing routes established for wrought γ-TiAl-based alloys during the last two decades are summarized [68].
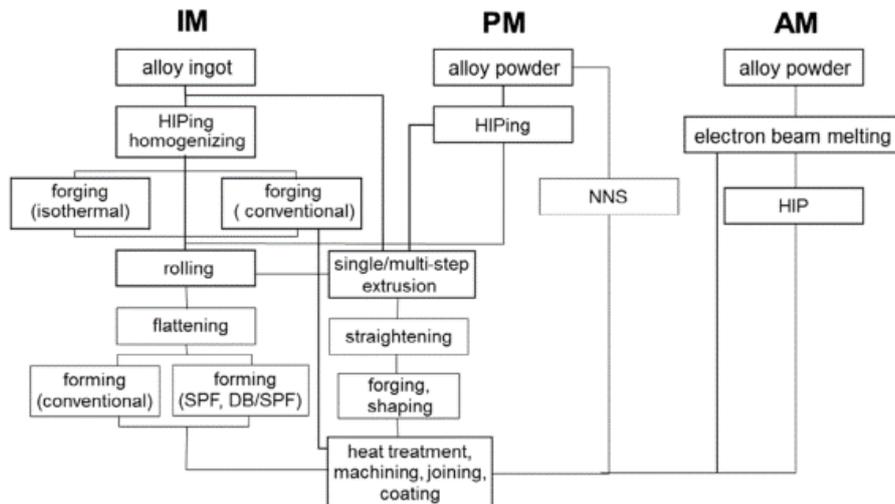
Figure 25: Manufacturing and processing routes established for wrought γ-TiAl-based alloys on an industrial scale [68].

Taking into account all the consideration done about these advanced high temperature alloys, in **Table 10** it is possible to compare the properties of titanium alloys, superalloys and gamma titanium aluminides [56].

Table 10: Properties profiles of advanced high temperature alloys for jet engines [56].

Property	Near-α-Ti	Ni superalloys	γ-TiAl alloys
Density	+	-	++
Specific tensile strength	+	-	+/-
High temperature Young's modulus	+/-	+	++
Room-temperature ductility	+	+	-
Formability	+	+	-
Creep	-	++	++
Room-temperature fracture toughness	+	++	-
Room-temperature crack growth	+	+	-
Specific fatigue strength	+	-	+/-
Oxidation	-	++	++
High-temperature embrittlement	-	+	+/-

1.5 The binary Ti-Al phase diagram

The binary phase diagram shown in **Figure 26** contains several intermetallic compounds for example Ti_3Al (α_2), TiAl (γ), $TiAl_2$ and $TiAl_3$.

From the application point of view, the α_2 - Ti_3Al phase and the γ – TiAl phase are the mainly considered compound for structural applications.

The α_2 - Ti_3Al phase and the γ – TiAl phase are characterized by a very good specific strength at high temperatures and better oxidation resistance compared to the other phases. The high-temperature creep properties are enhanced by limited dislocation and atomic diffusion at high temperatures in the ordered superlattice crystal structure.
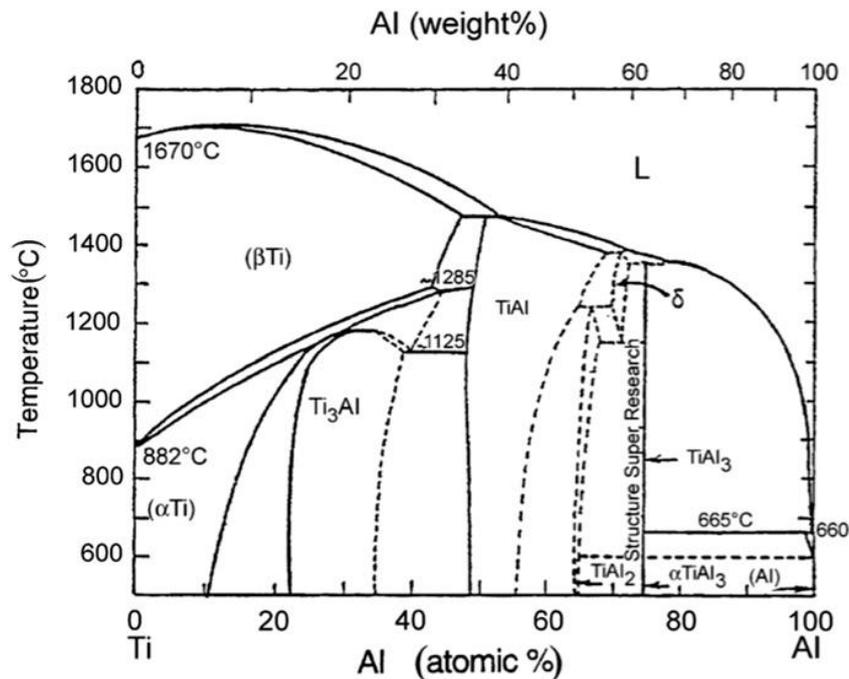
Figure 26: Ti-Al phase diagram [55]

In particular, the interest is focused on γ – TiAl alloys containing minor fraction of the α_2 - Ti_3Al phase. For this reason, hereafter, the phase diagram is cut in the range between 25% and 65% (at.%) as suggested by McCullough et al (**Figure 27**) [69] [70].
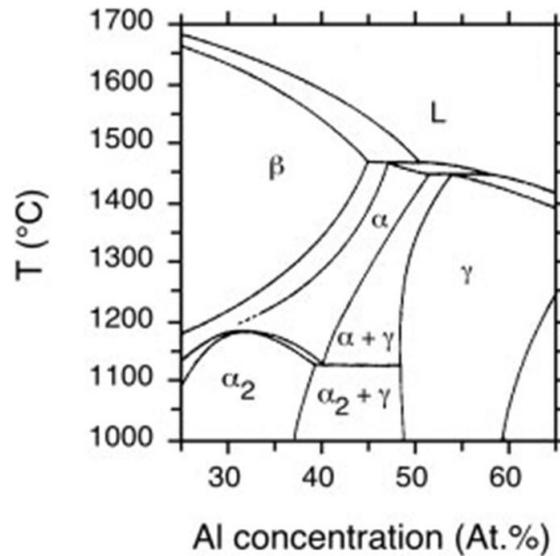
Figure 27: Binary phase diagram proposed by McCullough et al. [69]

In this central portion of the Ti-Al phase diagram in **Figure 27** three phase reactions can be observed: the peritectic reactions L + α → γ and L + β → α and a eutectoid reaction α → α₂ + γ [70].

1.5.1 α₂-Ti₃Al

The crystal structure of the α_2 phase, having stoichiometric composition Ti_3Al, is an ordered hexagonal closed packed $D0_{19}$ according to the Struktubericht designation (**Figure 28**). The atomic stacking sequence is ABAB.

This phase presents an Al composition between 22% an 35% (at.%) depending on temperature [70]. At a temperature of 1180°C and Al content of 32% (at.%) it transforms into a disordered hcp structure.
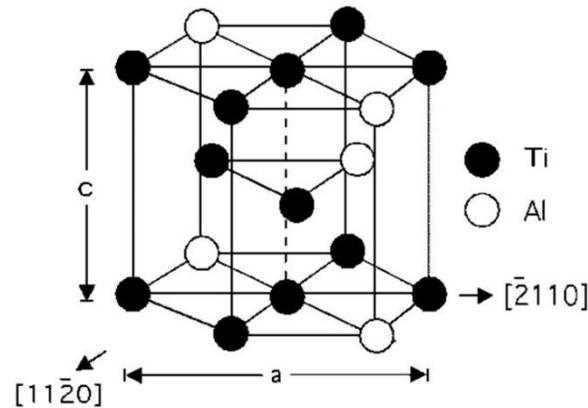
Figure 28: Crystal structure for α_2 – TiAl [49]

The space group is P6$_3$/mmc and the lattice parameters are: a = 0,5782 nm, c = 0,4629 nm (c/a ratio = 0,8). The planes (0002) are closed packed [49].

The properties of this phase are good high temperature strength and low ductility.

1.5.2 γ-TiAl

The γ phase with stoichiometric composition TiAl presents an ordered face centered tetragonal L1$_0$ crystal structure (**Figure 29**) existing between 48% and 58% (at.%) of Al. In the cases of non-stoichiometric composition, the Ti or Al atoms in excess create vacancies since they are placed as anti-site atoms [70].

The stacking sequence is ABCABC…(closed packed {111} planes), the space group is P4/mmm and the lattice parameters are: a = 0.4005 nm, c = 0.4070 nm (c/a ratio = 1.02). The c/a ratio can increases up to 1.03 (increased tetragonality) if the Al content increase, and decreases to 1 if the Al decrease. In the case of c/a = 1 the structure becomes ordered fcc.

The low mobility of dislocations, due to the strong covalent atomic bonds, brings to good high temperature strength and creep resistance but also to poor room temperature ductility.
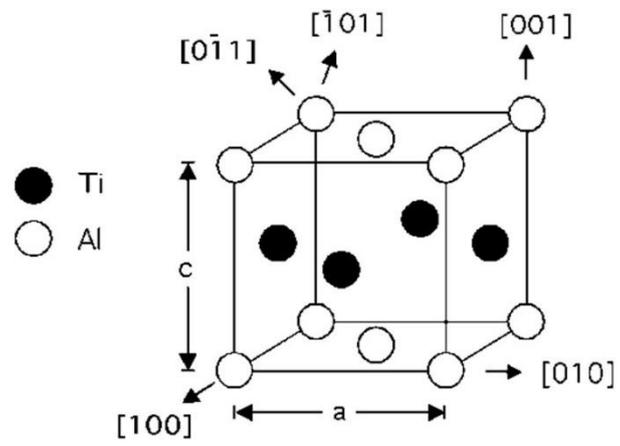
Figure 29: Crystal structure for γ – TiAl [49]

1.6 TiAl microstructures and phase transformations

One of the main parameters controlling the microstructure is the aluminum content. For Al amount larger than 48 (at.%) the γ phase is the stable one in the phase diagram. For an Al amount between 35% and 48% (at.%) it is possible to obtain combined microstructure depending on the heat treatment. For Al amount lower than 35% (at.%) single phase α_2, α and β compounds are obtained.

Since the single α_2 phase cannot be considered for application, two phased α_2 + β structural alloys are developed and they present a considerable higher strength compared to the single α_2 phase alloy. The β phase has a disordered centered cubic structure and presents an Al content between 0 and 47.5% (at.%).

The β phase is generated by the addition of certain β stabilizing elements such as Molybdenum, Chromium and Tantalum [71][72]. These elements are added in addition to Niobium that can be present between 11% and 18% (at.%) because of its positive effect on the material properties [73][74]. The effect of the different alloying elements is described in 1.9 Effect of chemical composition.

The single phase γ-TiAl and the α_2-Ti$_3$Al phase, or their two-phase system (see phase diagram), combine to form different microstructures. The four microstructures that can be obtained are equiaxed, duplex, near lamellar and fully lamellar. The microstructures are dependent of the thermal history of the material, so that are influenced by the processing route and, by the heat treatments and cooling rate applied to the material [75][62].

The mechanical properties of γ-TiAl alloys strongly depend on microstructure.

When γ-TiAl alloys are heated in the single α phase region above the α-transus temperature, there is the formation of the hexagonal closed-packed phase. This can be considered the starting point for all the further phase transformations and different microstructures formation.

Binary γ-TiAl alloys pass through the single-phase field of the α solid solution after solidification. With further cooling, the α solid solution decomposes according to the reaction $\alpha \rightarrow \alpha + \gamma \rightarrow \alpha_2 + \gamma$. For all the engineering γ-TiAl alloys, also the eutectoidic transformation $\alpha \rightarrow \alpha_2 + \gamma$ should be considered [76].

After cooling below the α-transus temperature, different phase transformations occur and depend on the cooling rate. At high cooling rates, α phase grains precipitate lamellar α_2 and γ phases.

Regarding this lamellar reaction, it is possible to consider:

- formation of Widmannstätten colonies in lamellar colonies;
- "feathery structures" formation, consisting of γ lamellae with misorientation of 2° - 15°.
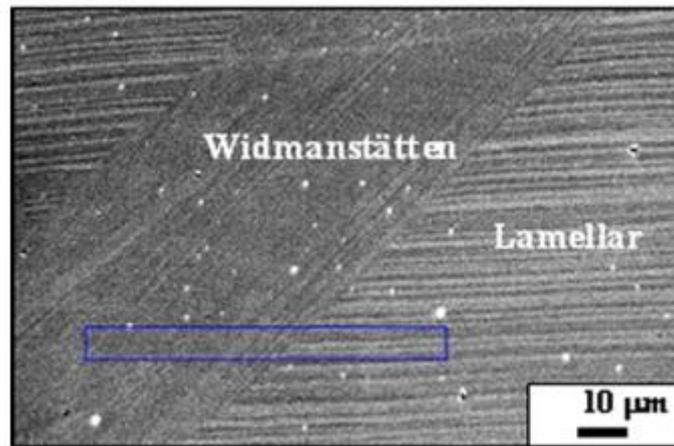
Figure 30: SEM image of Widmannstätten lath embedded inside lamellar structure [77].

At high cooling rate, the massive transformation of the existing α into γ structure takes place. This can be obtained at cooling rate sufficiently high to avoid the Widmanstätten and primary lamellar structure formation. The massively transformed γ-TiAl microstructure is fine grained and presents the so-called "feathery-like" microstructure shown in **Figure 31** [77] [78]. Some studies have demonstrated that the hcp to $L1_0$ massive transformation takes place via the f.c.c. as intermediate phase. The γ_m phase develops with the same orientation relationship from γ lamellae that intersect a grain boundary and diffuse in the adjacent grain [79].
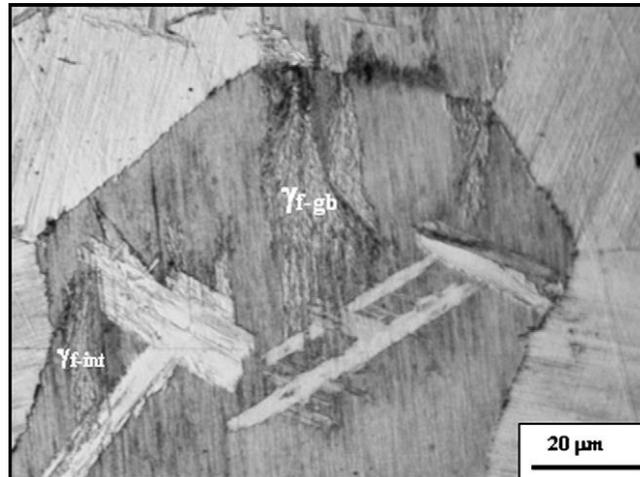
Figure 31: Feathery-like lamellar microstructure obtained with air-cooling [77].

The first stage of the lamellar formation is the formation of the fcc γ grains within the hcp α grains. Then, the nucleation of γ phase through diffusion at the α grain boundaries occurs. The residual α phase is ordered into α$_2$. The γ lamellae formation from α follows the transformation through the movement of the Shockley partial dislocation (**Figure 32**).
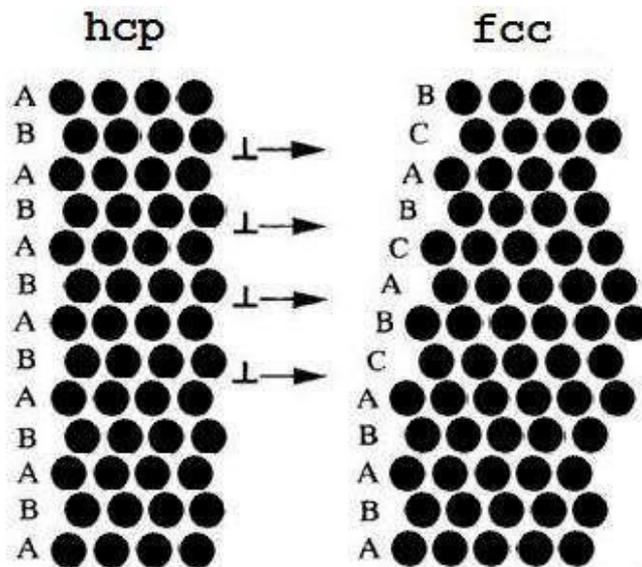
Figure 32: Movement of the Shockley parts transferring from hcp to fcc.

The lamellae formed having the Blackburn Orientation Relationship: $\{111\}_\gamma//(0001)_{\alpha_2}$ and $>110]_\gamma//<1120>_{\alpha_2}$ present fully coherent interfaces with low internal energy. They are parallel to the basal planes of α_2 and the $\{111\}$ planes of γ. When the γ phase precipitates from the α phase, the $L1_0$ structure can be formed in six orientations, called variants, corresponding to the six possible orientation of the [110] direction along a reference <1120> direction of the α and α_2 phases [80][81].

At lower cooling rates, the formation of γ grains are observed [77][82].

In the case of a microstructure containing both γ grains and $\alpha_2+\gamma$ lamellae, the microstructure formation can be followed by a discontinuous coarsening reaction during the annealing in the $\alpha_2+\gamma$ phase field. The low temperature in this phase field slow down diffusion and this makes the coarsening evolution a slow process.

Considering the mechanical properties, the combination giving the best performances is achieved with fine lamellar spacing and small colony size lamellar microstructures.

The microstructure obtained using typically applied cooling rate are not stable at service temperatures of around 700°C. This is because, for alloy compositions that deviate from the eutectoidic composition, these cooling rates do not allow thermodynamic equilibrium. In order to stabilize microstructure for the application temperature range, it is important to consider proper cooling conditions or an equilibration treatment.

The microstructures formation through heat treatment are described more in detail in the following section 1.7 Heat treatments and microstructure evolution.

In the following part, the four different γ-TiAl microstructures are described.

1.6.1 Equiaxed Microstructure

The equiaxed microstructure (**Figure 33a**) consists of equiaxed γ-TiAl grains with a small amount of α_2 phase at the equiaxed γ grains boundaries. This microstructure is characterized by an average grain size between 30µm and 50µm. This phase is formed in the $\alpha_2 + \gamma$ phase region above the eutectoid temperature T_e.

The equiaxed microstructure presents good specific high-temperature properties and high elastic modulus. On the other hand, it shows poor room-temperature properties such as low ductility and fracture toughness that make it not desired for structural application [70] [75][83].

1.6.2 Duplex Microstructure

The duplex microstructure is composed by both equiaxed γ-TiAl grains and fine lamellar colonies (**Figure 33b)**. This microstructure is obtained by heat-treating the material in the middle of the $\alpha + \gamma$ phase region. During the formation of this microstructure, the α_2 grains and the new α precipitates coarsen into α plates and α grains. At the same time, the predominant γ phase is decreased by dissolution to reach the equilibrium volume fraction. By increasing the temperature in this region, the amount of lamellar grains increases and vice versa. The finer duplex microstructure presents an average grain size around 10µm.

Since this microstructure is a combination of equiaxed and lamellar phases, the mechanical properties of duplex TiAl are a combination of the mechanical properties of these single microstructures making it desirable for structural applications. One of the most enhanced material property is ductility: the interfaces between lamellar colonies and equiaxed grains increase the ductility of the material. Moreover, is possible to enhance creep, high-temperature strength and fracture toughness by increasing the volume fraction of lamellar colonies [70][83][75][56].

1.6.3 Near Lamellar Microstructure

The near lamellar microstructure is obtained with heat treatments at temperatures near the α transus (T_α), that is between the fully lamellar and duplex formation temperatures, and it consists of predominantly coarse lamellar grains with only a low amount of fine γ-TiAl grains (**Figure 33c**). The average grain size ranges between 150µm and 200µm. In comparison to the equiaxed microstructure, the near lamellar brings to a higher ductility thanks to the interlamellar spacing and to the γ-grains – lamellar colonies interfaces.

1.6.4 Fully Lamellar Microstructure

Heat treatments in the pure α phase region, above the T_α produce the formation of fully lamellar microstructures (FL) (**Figure 33d**). During the cooling at room temperature, the lamellar morphology is formed by the precipitation of the α-Ti phase into alternate α_2 and γ plates (**Figure 34**). FL microstructures are characterized by coarse lamellar grains having average grain size up to 1000µm.

The high temperature strength, creep resistance and fracture toughness are enhanced thanks to the dislocations and twinning formed at the lamellae interfaces. On the other hand, TiAl materials with FL microstructures present a poor room temperature ductility. The mechanical properties of FL microstructure are also dependent to the grain size; in fact, fine-grained FL microstructures bring to excellent mechanical properties and sufficient ductility.
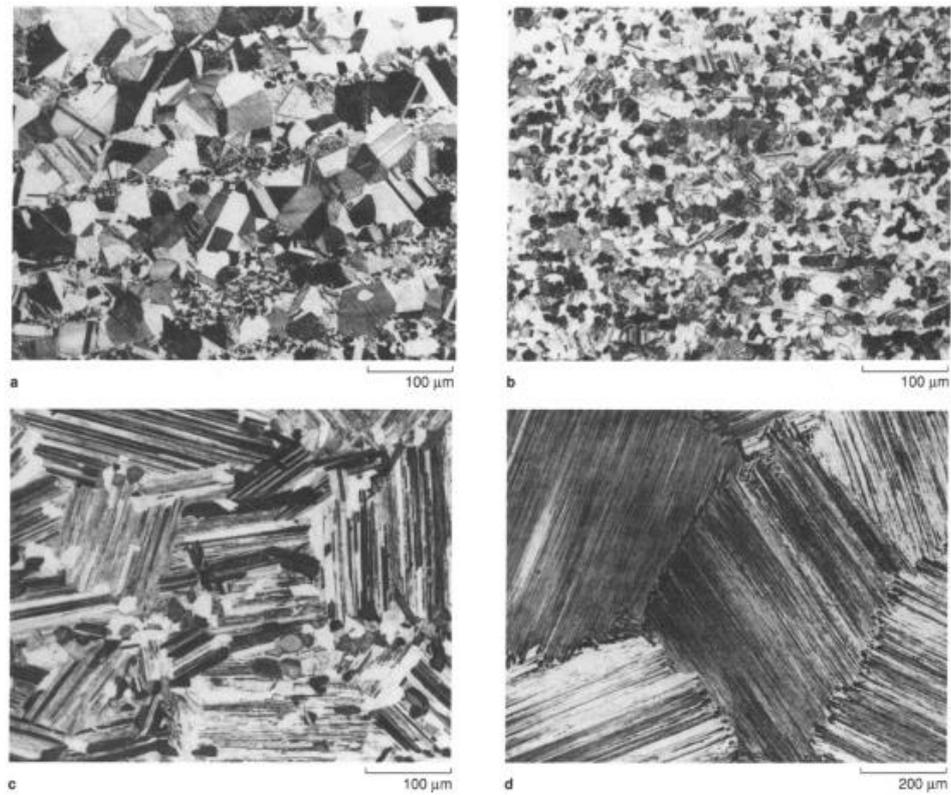
Figure 33: γ -TiAl alloys typical microstructures. a) Equiaxed or near-gamma; b) Duplex; c) Near Lamellar; d) Fully Lamellar [70].
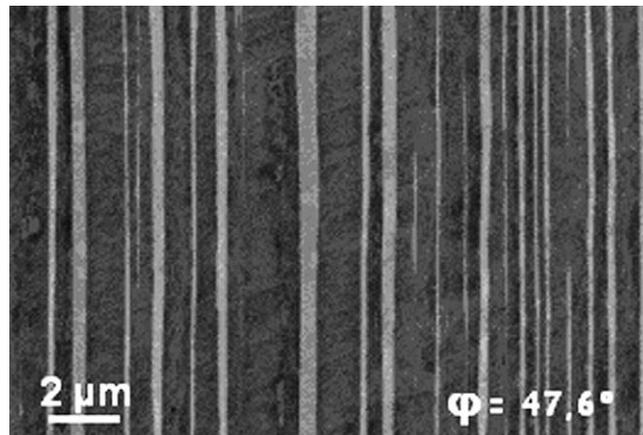
Figure 34: Typical scanning electron microscopy image of $\alpha_2 + \gamma$ lamellar structure; γ phase dark and α_2 bright [76]

1.7 Heat treatments and microstructure evolution

Depending on the manufacturing method and type of product, the microstructure of the as-produced TiAl material can be of different type. The manufacturing method has an influence on the microstructure due to the different cooling ways other parameters such as melt dimension [84][85].

Some manufacturing methods produce microstructure segregation, in particular for the casting process, the central part of the material results to be more segregated due to the slow cooling. On the contrary, powder metallurgy manufacturing techniques result in more homogeneous and less segregated microstructures thanks to the lower size of the melt.

In order to improve the mechanical properties of the final product it is necessary to obtain the desired mechanical properties by exposing the material to different types of heat treatments.

1.7.1 Hot Isostatic Pressing (HIP)

Hot Isostatic Pressing (HIP) is mainly a processing technology considered for the powder metallurgy manufacturing. With the HIP method, it is possible to produce near-net-shape parts starting from the material powder by applying and maintaining for a certain time both heat and high pressure. HIP is also considered as post processing in order to decrease the amount of porosity and/or to homogenize the microstructure in a component [84][86][87].

During the HIP process, the component or powders are placed inside a vessel, heated and an inert gas is used to increase the pressure.

Regarding the use of HIP as post-process technology, it is particularly useful for as-produced additive manufacturing parts such as TiAl components. In this case, the temperature used shall be in the two-phase field of the phase diagram in order to close residual pores without produce significant microstructural modifications. More precisely, at such conditions, recrystallization and grain growth append.

For TiAl material, it has been demonstrated that the ideal HIP condition to increase ductility and shrink the residual pores is obtained by HIPping the material at a temperature around 1200°C [87].

1.7.2 Heat Treatment

Considering TiAl alloys with an aluminium amount of 48 at.%, for the solidification, three primary solidification phases and two peritectic reaction during the cooling down from liquid state are possible. According to the central zone of the TiAl phase diagram, the phase transformation steps during cooling is:

$$L \rightarrow \beta + L \rightarrow L + \alpha \rightarrow \alpha \rightarrow \alpha + \gamma \rightarrow \alpha_2 + \gamma$$
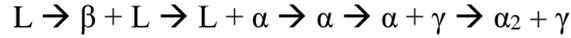
Thanks to the β-stabilizing effect of Cr, for the Ti-48Al-2Cr-2Nb alloy, it is possible to obtain a small amount of β phase during cooling from liquid phase.

The hexagonal closed-packed α phase is the starting point for microstructure transformation and it is obtained by heating the material above the α transus temperature in the single α phase region (T_1 in **Figure 35**).
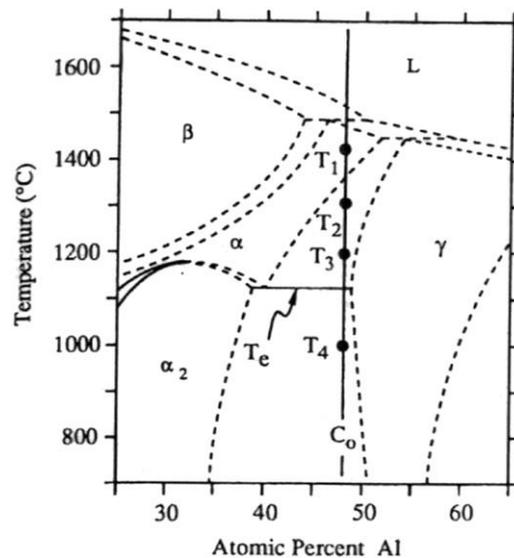
Figure 35: Central region of the Ti-Al phase diagram [55].

By heating in the α phase region a material with γ phase segregated with α, the microstructure is homogenized, the created α grains grow and the γ grains dissolve through a diffusion-controlled growth and dissolution [88].

To overcome grain growth phenomena at these temperatures it is possible to perform recrystallization by hot working or re-nucleation. In re-nucleation, during the $\alpha_2 + \gamma \rightarrow \alpha$ reaction, the γ phase dissolves and there is the nucleation of new grains.

Considering the heat treatment of the γ-TiAl alloy in the $\alpha_2 + \gamma$ phase region, it is possible to compare the phase transformation reaction $\alpha \rightarrow \alpha + \gamma \rightarrow \alpha_2 + \gamma$ with the cooling reaction $\gamma \rightarrow \alpha + \gamma \rightarrow \alpha_2 + \gamma$.

The dimensions of the lamellae created with the first reaction are the same of the pre-existing α grains produced in the α phase region.

In the second reaction, the α phase start to precipitate during cooling at the {111} plane of the tetragonal γ phase already present.

The near gamma or equiaxed microstructure is obtained with heat treatment of a material with fine γ microstructure just above the eutectoid temperature (T_e) in the $\alpha + \gamma$ region (T_3 in **Figure 35**). During cooling the α transfers into α_2 phase and at the grain boundaries between γ grains. It is possible to determine the amount of each phase by the lever rule. The duplex microstructure is obtained with a higher heat treatment temperature in the $\alpha + \gamma$ region (between T_2 and T_3 in **Figure 35**). The Al content and the cooling rate have an influence on the lamellar volume fraction.

The near lamellar microstructure is than obtained by rising the heat treatment temperature just around the α transus temperature (T_2 in **Figure 35**). During the heat treatment at such temperatures, coarsening of the predominant phase occurs. [55][89][77][90][91].

Some alloying elements, such as Nb, Mo and Ta act as β phase stabilizers and are used in third-generation alloys in order to improve mechanical and workability properties. The effect of these elements and these third-generation alloys, named as TNM and based on the nominal composition of Ti-43.5Al-4Nb-1Mo-0.1B (at.%) are deeply described in the following sections 1.9 Effect of chemical composition and 1.10 Alloy development and generations of γ-TiAl alloys.

In β-solidifying multi-phase γ-TiAl alloys, it is possible to obtain a microstructural homogeneity and a desired amount of the β phase, starting from the cast/HIP condition, by means of a simple short-term annealing within the single β phase field region combined with a subsequent stabilization treatment near service temperature.

Thanks to the alloy composition, the solidification pathway via the β-phase $L \rightarrow L+\beta \rightarrow \beta \rightarrow \beta+\alpha \rightarrow \beta+\alpha+\gamma \rightarrow \alpha+\beta+\beta_0+\gamma \rightarrow \alpha+\beta_0+\gamma \rightarrow \alpha+\alpha_2+\beta_0+\gamma \rightarrow \alpha_2+\beta_0+\gamma$ is

ensured instead of a peritectic solidification according to **Figure 36a** (L$\rightarrow$L+β$\rightarrow$α$\rightarrow$…) [92].

Studies have demonstrated that ordering reaction β-Ti(Al) (bcc structure) $\rightarrow$ $β_0$-TiAl (B2 structure) at about 1415°C ($T_{β,ord}$) take place and this significantly affect the hot-workability of TNM alloy and cause embrittlement at ambient temperature and creep issues [68].

In order to avoid grain coarsening effect during the microstructural tuning, it is necessary to avoid a single phase region at elevated temperatures. For instance, α+γ$\rightarrow$α transitions must be supressed. It is also possible to reduce the α-phase region and in this case, the α-field can be passed without coarsening because the β-phase is stabilized by alloying elements with low diffusivity [71].
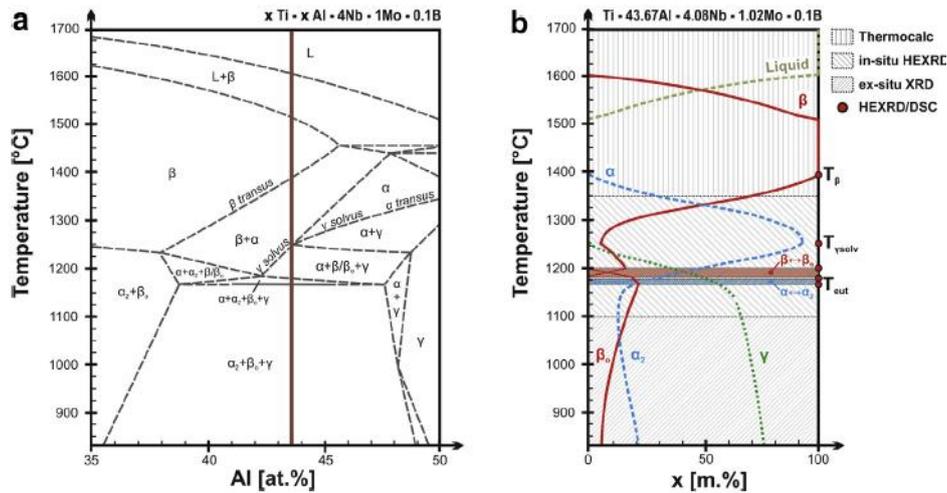
Figure 36: a) Experimental quasi-binary section through the TNM alloying system. The Al-content of the investigated alloy is indicated as a vertical line. b) Course of phase fractions with temperature for the investigated alloy composition Ti-43.67Al-4.08Nb-1.02Mo-0.1B [92]

1.8 Mechanical properties of TiAl alloys and influence of microstructure

TiAl-based alloy are considered promising for certain structural application because of their interesting specific mechanical properties that, thanks to the low density of these alloys, are comparable to the properties of other well studied materials for aircraft and automotive engine such as Ni-based superalloys.

By replacing the Ni-based superalloy in gas turbine engines with γ-TiAl it is possible to increase up to two time the thrust to weight ratio. Newly developed γ-TiAl alloys with small additions of Nb, Cr and B present the same specific strength of Ni-based superalloys, but lack room temperature ductility (<3%) and fracture toughness (<35 MPa m$^{1/2}$). On the other hand, the high temperature creep and fatigue behaviours of γ-TiAl alloys can be considered equivalent to that of superalloys at temperatures up to 750°C [62].

It is demonstrated that there is a strictly relationship between structure and properties of some TiAl-based alloys processed via different manufacturing techniques. The processing route is very effective in controlling the microstructure because of the solid state phase transformation from a hexagonal single phase to a ordered hexagonal and ordered tetragonal two phase structure.

It is also demonstrated that, in general, high and low temperature properties cannot be optimized simultaneously and the processing route, alloy composition and heat treatment shall be optimized in order to obtain an acceptable compromise between these properties [85]. The microstructure of the dual ($\alpha_2 + \gamma$) phase γ-TiAl alloys can hence be engineered to exhibits a proper set of mechanical properties for the desired application. In particular, as it will be deeply described in the following part, the duplex and fully lamellar microstructures present the best combination of mechanical properties.

The type of microstructure is not the only factor controlling the mechanical properties of these alloys but it is also important to control and optimize certain microstructural parameters such as grain size and lamellar spacing. These parameters have a strong influence on certain mechanical properties and it has been reported that fracture toughness is inversely proportional to the lamellar spacing and directly proportional to grain size. At the contrary, ductility decrease with increasing grain size [62][83][70].

The general properties of γ-TiAl alloys are reported in **Table 11** and in the following sections, each property and the effect of microstructure will be analysed and described.

Table 11: General properties of L10/D019 γ-TiAl alloys [75][93][54][94].

Density	3.7-4.0 g/cm^3
Young's modulus at Room Temperature	160-180 GPa
Yeld strength at Room Temperature	400-650 MPa
Tensile strength at Room Temperature	450-800 MPa
Tensile strain to rupture at Room Temperature	1-4%
Tensile strain to rupture at High Temperature	10-60%
Fracture toughness K_{th} at Room Temperature	10-20 MPa m$^{1/2}$
Temperature limit due to creep	900-1000°C
Temperature limit due to oxidation	900°C
Thermal conductivity	22 W m^{-1} K^{-1}

1.8.1 Deformation mechanisms

The brittleness of TiAl alloys is due to their low dislocation density or absence of mobile dislocation. The dislocation mobility and the material behaviour under mechanical load are two important factors controlling the strength and fracture behaviour of these alloys. In order to predict the material properties it is essential to understand the micro-mechanisms that control the multiplication and mobility of dislocations.

Ordinary dislocations, ordered twinning and superdislocations are the deformation modes present in the γ phase. These deformations are closely related to the slip planes in the L1$_0$.

Slip and twinning dislocation modes operate on the close-packed {1 1 1} plane. Slip occurs on the close-packed {1 1 1} plane because of the face-centered cubic structure of the γ phase. Ordinary dislocations and superdislocations with 1/2<1 1 0> type Burgers vectors on the {1 1 1} plane are due to the layered arrangement of atoms on the (0 0 2) planes and the tetragonality ratio of 1.02.

At low temperatures, <1 0 1] superdislocations are dominant in the single phase γ-TiAl while at high temperatures deformation modes are controlled by twinnings and slip by 1/2<1 1 0] ordinary dislocations. The poor room temperature ductility of single phase γ-TiAl is explained by the very limited mobility of <1 0 1] superdislocations at room temperature due to the covalent nature of Ti-Ti and Ti-Al bonds.

Regarding the lamellar microstructure dual phase TiAl, at low temperatures twinning and glide 1/2<1 1 0] ordinary dislocations are predominant and at high temperatures glide of superdislocations are significant. For lamellar microstructures, mechanical properties depend on different factors such as lamellar orientation respect to the loading axis and microstructural variables (grain size, thickness and lamellar spacing) [95] [96]. The mobility of dislocations with 1/2<1 1 0] Burger vector is also improved by reducing the interstitials and impurities in γ-TiAl. The effect of α$_2$-Ti$_3$Al phase in a dual phase TiAl is to get interstitial impurities in its laths from adjacent laths because of the higher solubility of impurities in it [55] [97] [98].
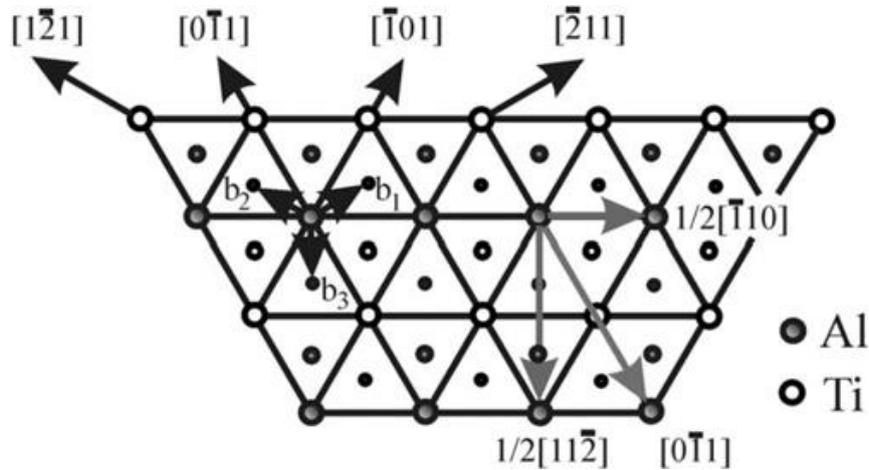
Figure 37: Potential slip and twinning systems in the γ-TiAl {1 1 1} planes [97].

1.8.2 Tensile properties and ductility

The dual phase alloys having a duplex microstructure formed by fine lamellar colonies and equiaxed gamma grains exhibit the best ductility. However, tensile and ductility properties are also strongly influenced by other factors such as alloy production methods, heat treatment, microstructural variables and alloy composition. Considering the microstructural features, the ductility is controlled by grain size, L/γ ratio, variations in lattice dimensions and impurity amount. More in details, the best ductility is achieved with a 0.3 – 0.4 L/γ ratio. Because of the strong dependence of the L/γ ratio from the α_2/ γ ratio, the best ductility is obtained considering the α_2/ γ ratio between 3% and 15%. The influence of alloy composition is mainly due to the effect of Al content on these ratios and different studies have demonstrated that the optimal Al concentration is 48% (at.%). Al amount has also an influence on tetragonality ratio c/a of the lattice and other small ternary or quaternary alloying elements added to the alloy composition, improve ductility by decreasing the unit cell volume of the lattice. As it will be described, an important example of impurities affecting ductility is the presence of oxygen.

Regarding the tensile properties, in general, the ultimate tensile strength at room temperature vary from 300 MPa to 700 MPa, the yield strength between 250-600 MPa and the elongation between 0.3% – 4% [99]. The influence of the microstructure on tensile properties at room temperature is an important factor to keep in account for engineering structural applications.

Materials with fully lamellar structures and duplex structures exhibit different tensile properties as shown in stress – strain curves in **Figure 38** [95]**.** FL microstructure brings to lower tensile strength compared to the duplex microstructure because of the coarser grains, lack of slip and twinning activity.

However, by decreasing the grain size in FL structures, both ductility and strength are expected to increase.

The tensile yield strength is inversely proportional to the grain size and this trend is described by the Hall-Petch relationship that estimates the necessary stress to transmit dislocation through the boundaries:

$$\sigma_y = \sigma_0 + k_y d^{-1/2}$$

d indicates the structural length parameter of the microstructure, σ_0 (intrinsic strength) and k_y are constant depending on the material [62].
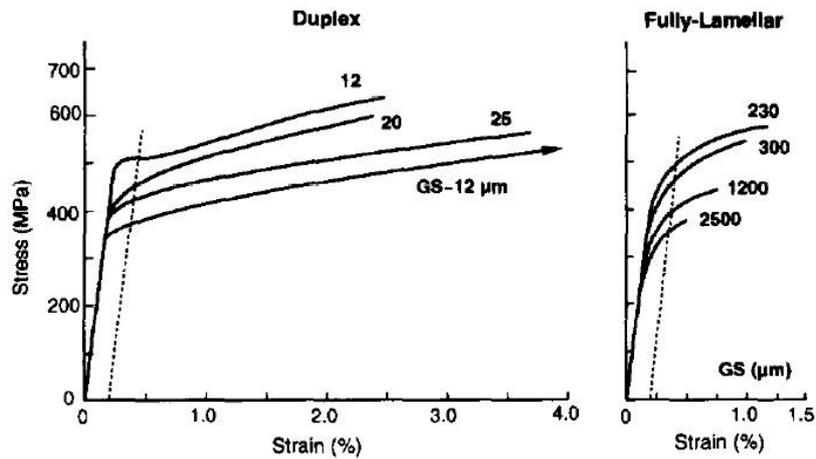
Figure 38: Tensile curve of alloys with different microstructure and grain size [95].

Considering the Ti-48Al-2Cr-2Nb alloy, in the transition from a totally equiaxed microstructure to a duplex and finally to a FL microstructure it is possible to observe a decrease in ultimate tensile strength and yield strength with the appearance of lamellar grains. Tensile properties remain constant between 20% and 80% of lamellar grains and from 80% of lamellar grains to a FL microstructure UTS and YS further decrease (**Figure 39** [100]).
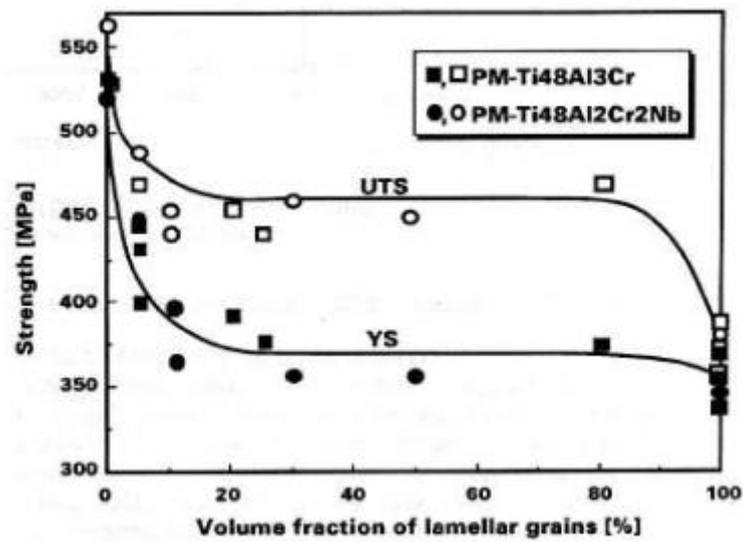
Figure 39: Tensile strength (UTS) and yield strength (YS) as function of volume fraction of lamellar grains [100].

The effect of lamellar spacing on yield strength for a FL material is represented in **Figure 40** [95]**.**
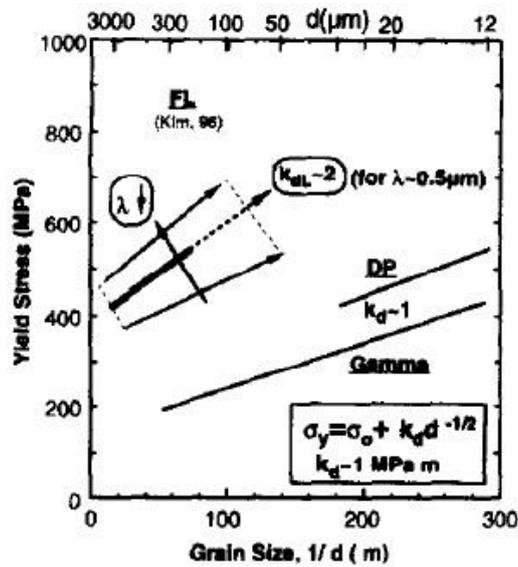
Figure 40: Yield strength, grain size and lamellar spacing relationship for FL microstructure. d: grain size; λ: lamellar spacing [95].

The effect of grain size and type of microstructure on the ultimate tensile strength and elongation is summarized in **Figure 41** [99]**.**
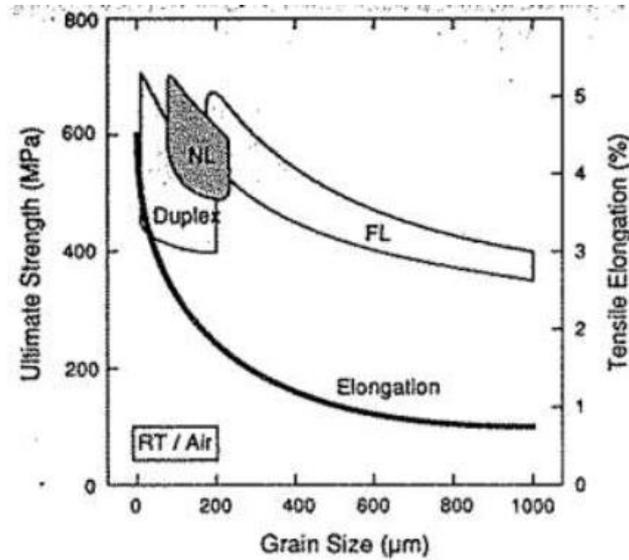
Figure 41: Room temperature tensile strength and ductility of TiAl alloys with different microstructures and different grain size [99].

Figure 42 shows the variations of tensile properties with temperature for γ-TiAl having different microstructures [70].
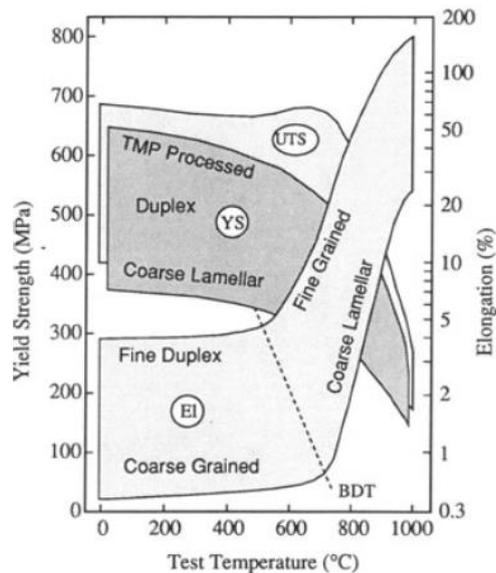
Figure 42: Tensile properties variation with test temperatures for different gamma alloy with different microstructures [70].

The brittle-to-ductile transition (BDT) is a particular characteristic of these alloys affecting the tensile ductility. The BDT temperature can varies from 550°C to 800°C depending on alloy composition and microstructure. Considering the alloy ductility, it slightly increases with temperature up to the BDT then, the ductility rapidly increases because of the activity of twinning and ordinary dislocations. Dynamic recrystallization takes place in the necking area of tensile specimens. As it is possible to observe from **Figure 42**, for single phase γ-TiAl, yield strength gradually decreases up to the BDT and then rapidly decrease at higher temperatures. Ultimate Tensile strength presents a slight increase up to about 600°C, peaks between 600°C and 700°C and then dramatically decrease. This behaviour is characteristics of intermetallics because of their long range ordering.

Dual phase γ-TiAl do not present the anomalous yield strength behaviour observed and the ultimate tensile strength peak appear at slightly lower temperature [70][101][55].

1.8.3 Fatigue behaviour

Fatigue resistance and fatigue crack growth resistance can be an issue for the materials, especially in critical aircraft engine application. There is a need for material scientist and designers to consider the mechanisms governing the fatigue properties in TiAl alloys and consequently optimize the microstructures and develop consistent lifing methods. Fatigue properties are also strictly dependant on environmental factors such as temperature and environmental atmosphere [102].

The different fatigue properties are high-cycle fatigue (HCF), low-cycle fatigue (LCF) and fatigue crack growth resistance (FCG).

A typical HCF diagram showing the S/N curves for a binary lamellar Ti-36.5Al (wt.%) alloy at different temperatures is reported in **Figure 43** [103].
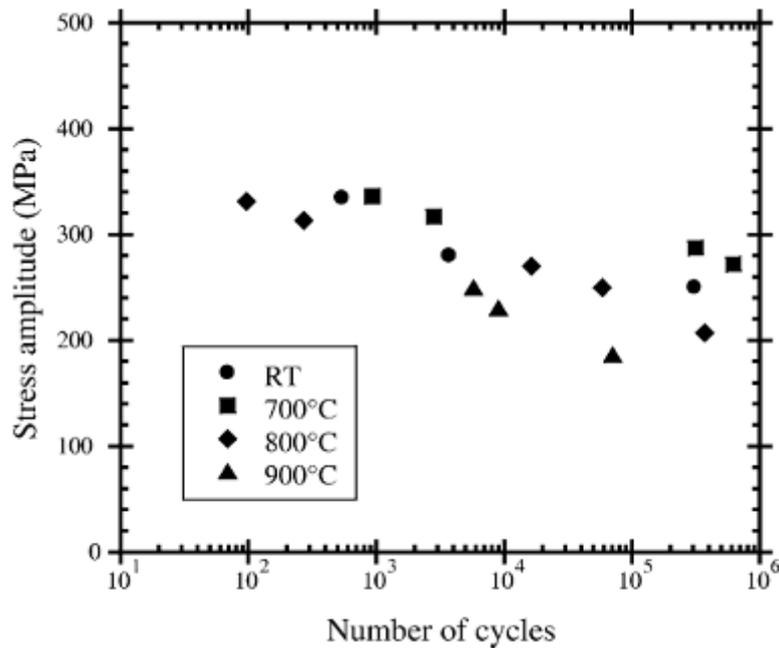
Figure 43: S-N curves for a Ti-36.5Al wt.% alloy at different temperatures [103].

It is possible to notice that a slight applied stress amplitude variation can lead to a significant variation in the number of cycles to failure. Furthermore, the fatigue resistance is not significantly affected by the temperature up to 800°C.

In high-cycle systems, ductile metallic materials exhibit a knee at about 10^6 cycles in the S/N diagram. For higher cycles, the curve is horizontal at a certain stress amplitude that is considered the fatigue limit. TiAl alloys S/N curves continue to decline gradually with increasing number of cycles to failure. For materials with this type of behaviour, the fatigue limit is defined as the stress amplitude corresponding to a certain number of cycles, often 10^7. Duplex and lamellar TiAl alloys exhibit a fatigue strength at 10^7 cycles that is 70-80% of the tensile strength [49].

Regarding the microstructural effects, it is possible to consider that fatigue is affected by the same factors affecting the creep resistance. Both duplex and lamellar structures exhibit good high-cycle fatigue properties up to high temperatures.

Up to 800°C, the fine-grained duplex microstructure increase fatigue life and at higher temperatures, the microstructure bringing to longer fatigue life is the fully

lamellar [55]. In particular, the better fatigue behaviour of duplex microstructures at temperatures lower than the BDTT is due to the finer grain size. At higher temperatures, lamellar structures present higher strength and this lead to a better fatigue resistance.

In **Figure 44** the influence of different microstructures on the room temperature fatigue resistance is represented [83][102] [103][104].
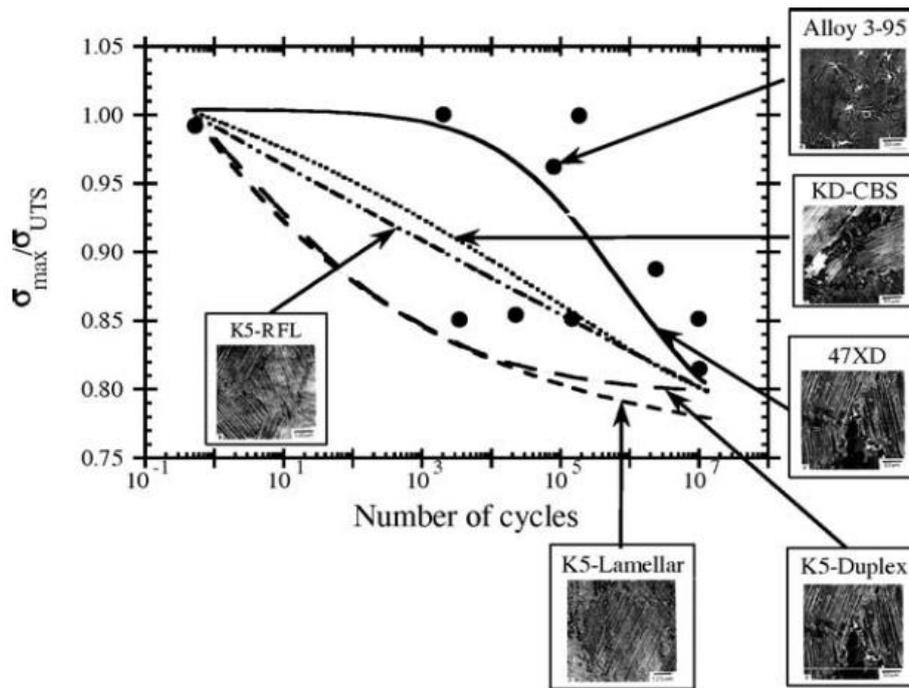
Figure 44: Influence of microstructure on the room temperature fatigue resistance [104].

The microstructure reported by Larsen et al. in **Figure 44** are mainly based on the K5 (Ti-46Al-2Cr-3Nb-0.2W) alloy. The K5-RFL refers to a refined lamellar microstructure and the CBS is a carbon-boron-silicon modified K5 alloy. Other alloys reported in this comparison are the 3-95 alloy (Ti-46Al-2Cr-2Nb-1Mo-0.2B) and the 47XD (Ti-47Al-2Mn-2Nb-0.2W). The microstructure is strongly affecting the shape of the S-N curves [104].

Filippini et al. have demonstrated that the microstructure and the characteristic dimensions of the lamellar colonies are fundamental parameters to determine the fatigue strength of duplex γ-TiAl alloys. For both the studied Ti-48Al-2Cr-2Nb (at.%) and high Nb TiAl, peculiar inherent microstructural features, observed on the fracture surface of the fatigue specimens, act as crack initiation sites controlling

the fatigue strength of the material. In particular, it was observed that fatigue failures by translamellar cleavage originate from lamellae having unfavourable direction respect to the loading direction [105][106].

Because of the high strain in low-cycle fatigue condition, the LCF fatigue resistance is mainly governed by the material yield strength and ductility. For this reason, duplex microstructures bring to longer low-cycle fatigue life respect to lamellar microstructures. Up to the BDTT, low-cycle fatigue resistance is not affected by temperature, in a similar way of strength and ductility properties [102][107][108][109].

Figure 45 represents the LCF behaviour of different TiAl alloys with various microstructures at 600°C. The analysed alloys are the β-solidified XD45 alloy (Ti-45Al-2Mn-2Nb + 0.8% vol. TiB_2) having a random lamellar microstructure, the XD47 alloy (Ti-47Al-2Mn-2Nb + 0.8% vol. TiB_2) duplex microstructure with lamellar colonies elongated along the loading axis, a duplex and lamellar ABB alloy (Ti-48Al-2W-0.5Si) and a GE alloy with a duplex microstructure that is the Ti-48Al-2Cr-2Nb [110].
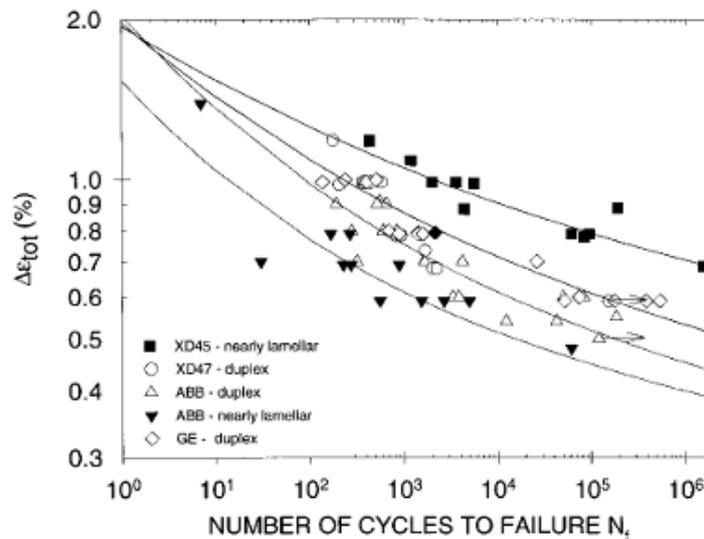
Figure 45: Low-cycle fatigue behaviour of different alloys at 600°C [110].

As it is possible to observe from **Figure 45**, the alloy composition and microstructure are the main material characteristics influencing the LCF resistance. The nearly lamellar XD45 alloy exhibits the higher resistance. This alloy present a lower aluminium content and a fine lamellar structure. It has been established that

the aluminium content, by governing the lamellae width, also controls the flow stress and the LCF resistance. In fact, the lower aluminium content in the XD45 alloy increases the α_2 phase volume fraction lowering the stiffness of the material. The presence of interstitial atoms also increase the LCF resistance. Moreover, by comparing the duplex and near lamellar ABB alloys, the duplex presents the higher LCF resistance [110].

1.8.4 Fracture Toughness and crack propagation resistance

Regarding the crack propagation mechanism, fracture starts from the crystal defects, such as vacancies and dislocations. These defects can evolve into microcracks that may gradually turn into macrocracks or cavities. The first step is named crack initiation and the second is the crack propagation. The total fatigue life (N_f) is controlled by the crack initiation life (N_i) and the crack propagation life (N_p) and the relationship between these two parts is:

$$N_f = N_i + N_p$$

Both the crack nucleation life and microcrack propagation life are included into the crack initiation term (N_i).

Considering the fatigue crack nucleation mechanism for crystalline materials, the crack nucleation is assumed as the result of partially retarded plastic deformation. The alternating stress is the key factor causing fatigue cracks and the prerequisite is the local plastic deformation. In practice, the stress concentration play an important role in the crack initiation process because crack originates from the components surface or from stress concentration area [111].

In order to analyse the influence of crack size on fatigue life, it is possible to consider the extended Kitagawa-Takahashi diagram proposed by Larsen et al [104] [112]. (**Figure 46**)
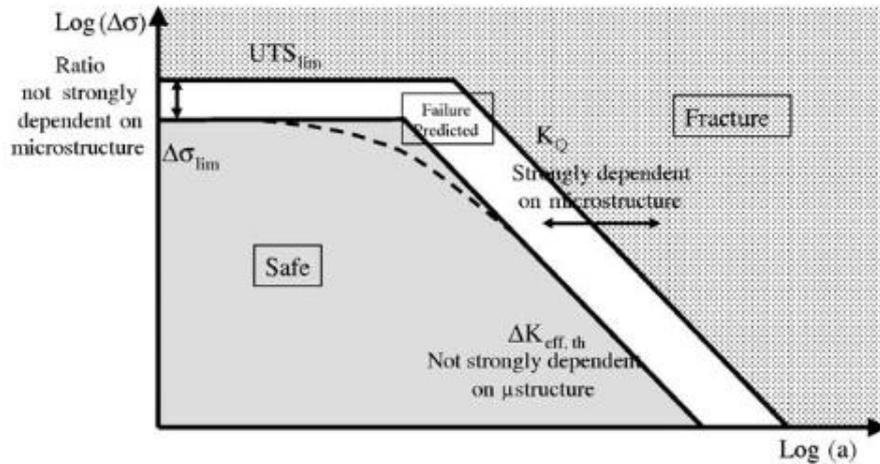
Figure 46: Schematic extended Kitagawa diagram influencing the microstructure of the different regions [104].

In the Kitagawa diagram used to study the surface defect tolerance for a certain TiAl alloy, the safe operation area is under the fatigue limit $\Delta\sigma_{lim}$ and the line for the threshold condition ΔK_{th}. In the extended diagram, the boundary conditions corresponding to fracture within a single cycle are included. These boundaries conditions are the ultimate tensile strength UTS limit and the fracture toughness K_q for fracture controlled by defects. The finite fatigue life between the boundary conditions can be predicted with S/N curves and FCG data. The results obtained with this type of diagram have suggested that the ratio between the fatigue limit and UTS is nearly constant also varying the microstructure. Therefore, an increasing in the fracture strength is expected to cause a fatigue limit improvement. It is also been demonstrated that microstructure does not have a strong influence on the effective threshold value. By the contrary, microstructure strongly influence the fracture toughness and the γ and nearly- γ microstructures exhibit the lower fracture toughness. Considering the effect of small and long cracks, a fine duplex microstructure tends to induce initial cracks with small size, while in lamellar microstructures there is a formation of initial defects with size comparable to the colony dimension. This means that the fatigue propagation life is lower, despite of the superior FCG resistance. The best compromise is given by refined lamellar microstructure having a good balance between crack initiation and defect-tolerance properties [102][103].

In a similar way to other properties, fracture toughness (K_{IC}) of double phase TiAl alloys depends on the microstructure. Fracture toughness can varies from 10 MPa√m to 16 MPa√m for duplex fine-grained microstructures depending on the gamma/lamellar grain ratio. A significant increase is observed for fully lamellar

microstructures, where it increases with lamellar grain size and can ranging from 20 MPa√m to 30 MPa√m [70][101].

Fracture toughness is strongly influenced also by lamellar grain boundary morphology. It has been demonstrated that interlocked grain boundaries present a higher fracture resistance compared to smoot grain boundaries.

It is interesting to compare the fracture behaviors of duplex and fully lamellar microstructures at room temperature and consider the effect of plastic deformation in these two microstructures (**Figure 47**) [99].
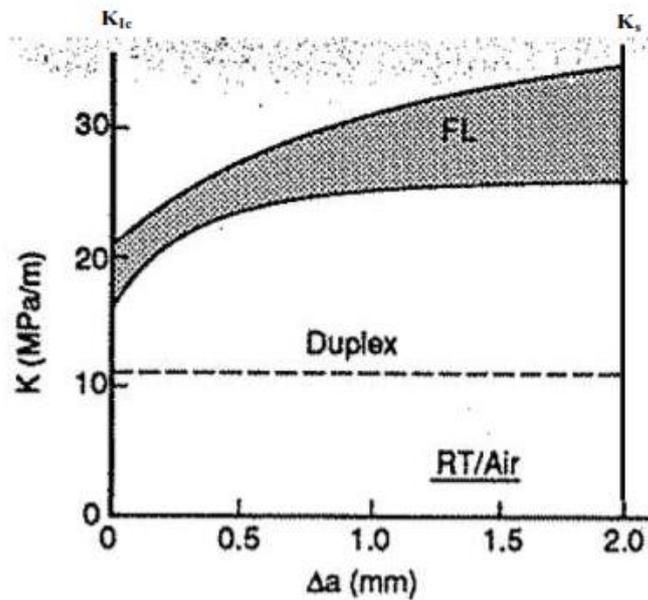
Figure 47: γ-TiAl Toughness for duplex and fully lamellar microstructures [99].

Low plastic strain near the onset of crack extension and no resistance to crack propagation has been observed for duplex microstructures. On the other hand, lamellar microstructures exhibit large plastic strains near crack tip and increased crack propagation resistance with crack length. This behaviour is reported in **Figure 47** where the toughness versus crack extension is represented for both duplex and fully lamellar microstructure. It is possible to notice that for fully lamellar microstructure the toughness value increase from the beginning of the crack propagation to reach a maximum values of toughness saturation (K_s). Duplex microstructures exhibit lower and constant values of toughness. This means that, in duplex microstructures, near the beginning of the crack extension only a small plastic deformation is observed bringing to a constant resistance to its propagation,

whereas, in fully lamellar microstructures, the higher plastic deformation leads to an increased resistance to crack propagation [83].

The anisotropy behaviour of lamellar microstructures is supposed to act as composite reinforcement blocking the crack front growth and, in the case the front is perpendicular to the $\alpha_2 + \gamma$ lamellae, this hindering effect is maximum. The interactions between the crack tip with lamellar boundaries involve crack deflection and crack immobilization creating a more tortuous crack path.

The fracture mechanisms in lamellar alloys are interfacial delamination, translamellar fracture and decohesion of lamellar colonies. For duplex microstructures, the mechanisms are intergranular fracture and cleavage.

Figure 48 shows the temperature dependence of fracture toughness for two different microstructures [49].
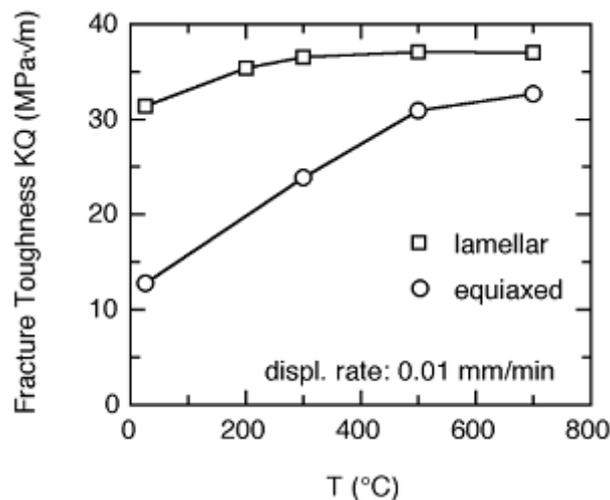
Figure 48: Fracture toughness - Temperature dependence for lamellar and near gamma microstructures [49].

For lamellar microstructures, the crack propagation resistance is mainly controlled by toughening mechanisms related to the lamellar morphology. The near gamma microstructures present a fracture toughness temperature dependence suggesting that the crack tip plasticity can lead to a significant toughening as previously assessed. At high temperature, the high glide resistance of the dislocation is dramatically reduced due to thermal activation and diffusion-assisted climb. At high temperature the glide process can spread within the plastic zone

more easily than at room temperature. Consequently, the fracture mechanism changes from cleavage to an energy absorbing ductile form passing from low temperatures to high temperatures [49].

1.8.5 Creep properties

The operating temperature and the efficiency of many high-temperature applications such as gas turbines are limited by the creep properties of the material. For instance, LPT blades must not creep more than 1% within 10000h at about 700°C under a tensile stress of 100-150MPa [72]. In general, creep properties of γ-TiAl alloys are lower or comparable than nickel-based superalloy, and this deficit limits the replacing of superalloys by titanium aluminides. Since the creep properties are microstructure and alloy composition dependant, it is possible to optimize these two factors in order to improve creep resistance in TiAl alloys.

Considering the effect of the microstructure and the morphology of microstructural phases on creep, it has been demonstrated that fully lamellar microstructures with large lamellar grains brings to enhanced creep properties compared to the duplex microstructures. In particular, if the lamellar grain boundaries are serrated or interlocked the creep resistance is further increased.

As an example, considering the steady state creep rate in air at 760°C and 105 MPa for the Ti-48Al-2Cr-2Nb, it was found to be 3.3 x 10^{-5}/h for a duplex microstructure and 4.0 x 10^{-7}/h for a large-grained fully lamellar microstructure. In lamellar structures ,the α_2 laths act as reinforcement and dislocation movements are inhibited by interfaces with large area and reduced lamellar spacing. By the other hand, duplex structures are characterized by a higher dislocations mobility within the equiaxed γ grains and this causes a drop in creep resistance [83][62][55][70][49][92].

Figure 49a shows the effect of applied stress on the long-term creep of a Ti-48Al-2Cr alloy and the effect of processing conditions of a particular engineering alloy. In **Figure 49b** it is evident that for similar microstructures, the effect of the processing route, HIP and heat treatment causes a significant variation in creep rates [113].
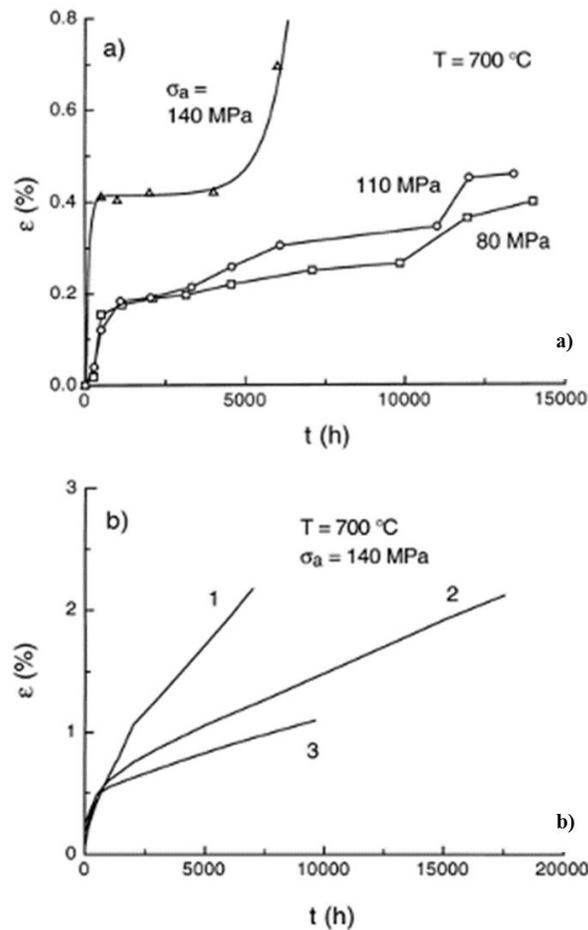
Figure 49: Creep properties of two-phase titanium aluminides. a) Ti-48Al-2Cr, duplex microstructure; b) Ti-47Al-3.7 (Nb, Cr, Mn, Si)-0.5B produced by investment casting with (1) nearly lamellar microstructure and lamellar spacing 0.01-0.5 µm, (2) duplex microstructure and HIPped, (3) HIPped and heat treated near lamellar microstructure, lamellar spacing 10 nm to 0.5 µm [113].

The environmental effect on creep has to be considered for high temperatures. In particular, creep fracture is extremely sensitive to oxygen. The other factor influencing creep resistance is the chemical composition and, as it will be described in more detail in the next section, increases in aluminium content and additions of carbon, nickel and tungsten enhance creep properties [114]. It is also been demonstrated that addition of silicon decreases the primary creep strain and minimum creep rate and also increases the rupture life and elongation to failure [115] [116][44] [117].

1.8.6 Oxidation resistance

The poor oxidation resistance of titanium aluminides at temperature higher than 800°C is one of the factors limiting their application at high temperatures. However, up to this temperature, the oxidation resistance of TiAl alloys is considered acceptable. At temperature up to 800-850°C, titanium aluminides present a more desirable tendency to form a protective alumina (Al_2O_3) layer than rutile (TiO_2) scale, while at higher temperatures the poor oxidation resistance is due to the lack of protective alumina scale and the rapid growth of detrimental rutile [57]. The four different layers formed below 800°C follow a certain order from the γ-TiAl matrix to the outwards. Near the matrix, a thin layer of Ti_3Al can be observed. Adjacent to it, a rich Al_2O_3 layer, than a mixture of TiO_2 and α-Al_2O_3 and an outer layer of TiO_2. From the SEM cross section in **Figure 50** it is possible to observe the different layers formed after exposure for 3000 cycles in air at 800°C for a near-gamma Ti-48Al-2Cr alloy [118].
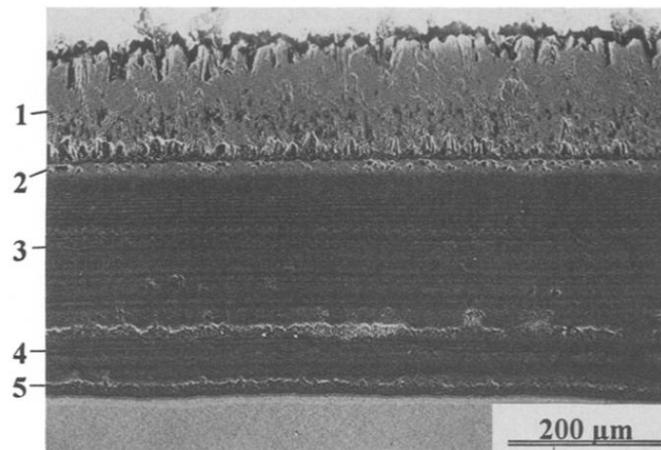
Figure 50: SEM cross-section micrograph of near-gamma Ti-48Al-2Cr alloy after exposure for 3000 cycles in air at 800°C (each cycle 1h at 800°C and 12 min at room temperature) [118].

EDX analysis has demonstrated that the layer (1) contains only Ti and O. the thin layer (2) presents also a small content of Al. Layers (3,4 and 5) contain a higher Al to Ti ratio that the first two layers. At the scale/metal interface an aluminium-depleted zone can be observed and EDX analysis revealed that the aluminium content in the oxide scale near the oxide/matrix interface was higher than in the oxide scale [118].

The detrimental effect of rutile scale is also due to its tendency to do cracking and spallation after a certain number of cycles, especially at edges and corners.

It has been demonstrated that microstructure has only a little influence on the oxidation resistance. **Figure 51** compares the mass change of Ti-48Al-2Cr alloy with different microstructure during exposure at 800°C in air for 150 hours [118].
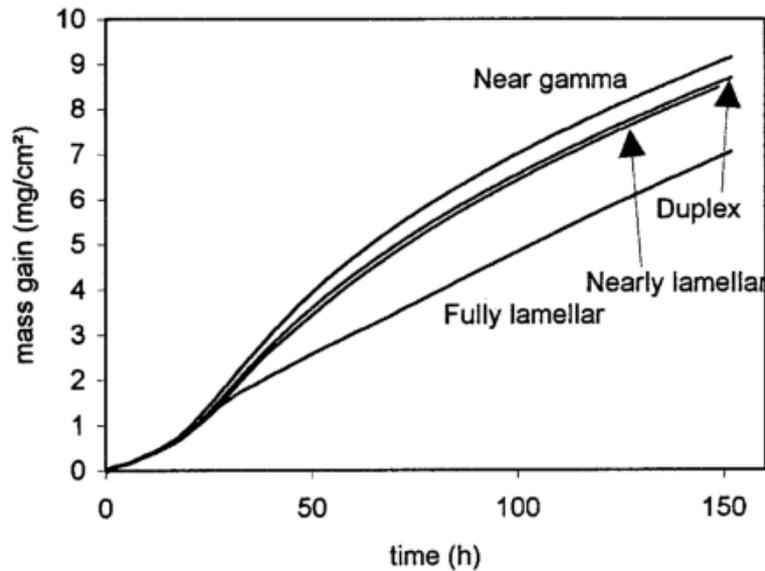
Figure 51: Mass gain vs. time for Ti-48Al-2Cr with different microstructures in air at 800°C [118].

Regarding the effect of alloy chemical composition, a higher concentration of Al is needed to achieve a protective alumina scale. The principle is to decrease oxygen diffusivity and solubility and to increase the aluminium diffusivity. On the other hand, a too high Al concentration is not desired for application because the loss of ductility due to the formation of brittle $TiAl_3$ phase. The addition of ternary and quaternary refractory elements such as Nb, Ta, Mo, W, Zr or Hf is demonstrated to improve the oxidation behaviour of TiAl alloys. The effect of these elements is to prevent the growth of detrimental rutile [119][57]. **Figure 52** shows as an addition of Nb to the alloy composition can improves the oxidation resistance of TiAl alloys [119]. The effect of the different alloying elements on the different properties of γ-TiAl will be analized in more detail in the following chapter.
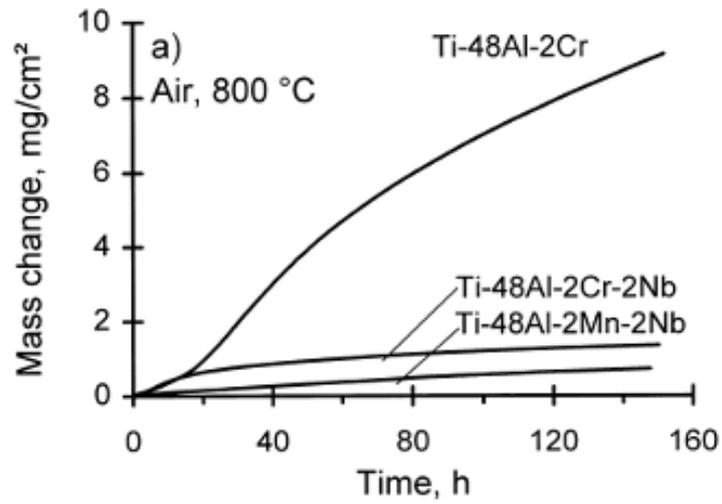
Figure 52: Mass gain vs. time for Ti-48Al-2Cr, Ti-48Al-2Cr-2Nb and Ti-48Al-2Mn-2Nb upon isothermal oxidation in air at 800°C [119].

From the technological point of view, further improvements have been achieved in order to extend the service temperatures of γ-TiAl by using proper thermal barrier coating or surface treatment [120] [121] [122] [123].

1.9 Effect of chemical composition

According to the component requirements, the chemical composition of the alloy shall be optimized and strictly defined in order to achieve the final microstructure and desired mechanical properties for the application. In fact, the chemical composition has a strong influence on the material properties and microstructure, in addition, alloying elements bring to a phase boundaries shift in the alloy phase diagram by altering the path by which microstructures evolve (**Figure 53**) [59].
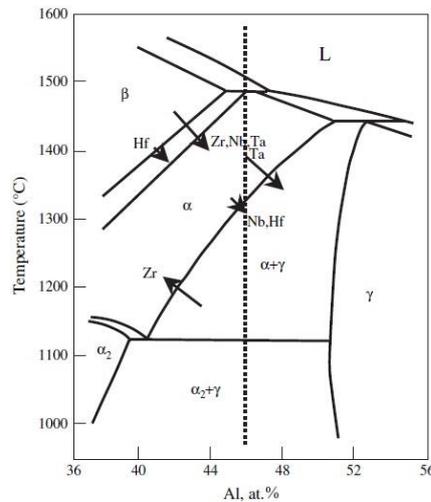
Figure 53: Section of the Ti-Al phase diagram. The shift direction of the phase boundaries for ternary alloying addition is indicated by the arrows. The length of the arrows indicating the magnitude of each element [59].

The phase boundaries shift caused by the ternary alloying addition is an important factor to take into account when the alloy has to be heat treated. The influence of the chemical composition of TiAl-based alloy was the subject of several studies and it is currently considered for new alloys development [55] [44][58] [124] [46] [32] [59] [125] [126] [57] [94] [93] [113] [127].

Table 12 shows the main effects of the chemical composition, with elemental concentration range considered for gas turbine applications, where ductility, high temperature strength, creep and oxidation resistance are extremely important.

Table 12: Effect of chemical composition and main alloying elements [94].

Element	Optimal content (at.%)	Effects
Aluminum (Al)	46 - 48	Insures the highest room temperature ductility
Chromium (Cr)	1.2 - 2	Improves room temperature ductility and corrosion resistance (β-stabilizer)
Niobium (Nb)	6 - 8	Improves oxidation resistance, creep resistance, high-temperature strength and erosion resistance (β-stabilizer)
Silicon (Si)	0.3 – 0.4	Improves creep strength and oxidation resistance
Nickel (Ni)	0.5 – 1.2	Increases internal friction and improves resonance resistance Improves oxidation resistance (β-stabilizer)
Yttrium (Y)	0.1 – 0.3	Increase oxidation resistance Grain size reduction Reduces ductility
Tungsten (W)	0.5	Increase oxidation and creep resistance Grain size reduction
Vanadium (V)	0.5 – 1.1	Improves high temperatures tensile strength and ductility Improves castability Grain size reduction (β-stabilizer)
Boron (B)	0.5 - 1	Grain size reduction Increases room temperature ductility
Zirconium (Zr)	0.2	Increase oxidation resistance (β-stabilizer)
Hafnium (Hf)	0.2	Increase oxidation resistance (β-stabilizer)
Tantalium (Ta)		Improves creep and oxidation resistance Tendency for hot cracking (β-stabilizer)
Molybdenum (Mo)	0.4 – 0.8	Improves creep and oxidation resistance Improves high temperature strength Grain size reduction (β-stabilizer)
Iron (Fe)	0.4 – 0.8	Improves creep resistance Grain size reduction (β-stabilizer)

Carbon (C)	0.05 – 0.12 (wt.%)	Increase creep and oxidation resistance
Manganese (Mn)	0.2 - 4	Grain size reduction Improves ductility (β-stabilizer)
Cobalt (Co)	1 - 3	Increase Creep resistance (β-stabilizer)

Dual ($\alpha_2 + \gamma$) phase alloys can present an Al concentration between 40% and 48.5% (at.%). Ductility of these alloys increases with the increase of Al content up to 48% and, between 48% and 50% of Al the ductility decreases. This can be explained by Al effect upon the microstructure, in fact, the fraction of equiaxed gamma phase increases with the increase of Al concentration (**Figure 54**) [55] [128].
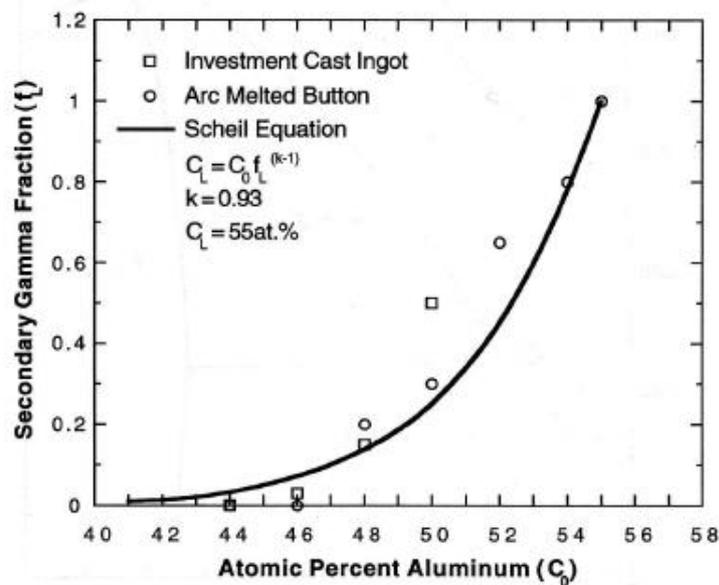
Figure 54: Volume fraction of equiaxed gamma phase as a function of the concentration of Al [128].

The yield strength versus Al content trend is opposite respect to ductility. It has been observed that yield strength increases with decreasing Al content. This is due to the effect of Al on the lamellar thickness. More precisely, a decrease of Al brings to a decrease of the number of thick α_2 lamellae. The decrease of the average thickness of the γ-lamellae leads to a finer lamellar microstructure with a positive effect on the yield strength of the material.

The Al concentration between 46% and 48% is also necessary to insure good oxidation resistance.

Regarding the influence of niobium, it has been found to produce strengthening, in particular at high temperature, for an addition between 5% to 10%. A relatively small solid solution strengthening due to short-range dislocation interactions with solved Nb atoms is observed [113]. Studies have revealed that Nb occupies the Ti sublattice and this leads to an increase of the α_2 volume fraction and to a microstructure refinement [49]. Nb tends to stabilize the lamellar structure and its addition causes a decrease of alloy ductility. The most important advantages of Nb addition is the improvement of oxidation resistance of TiAl alloys at high temperature. Considering the second generation Ti-48Al-2Cr-2Nb, the addition of Nb of 2% (at.%), it is revealed to be sufficient to obtain a significant increase in oxidation resistance for gas turbine application. Moreover, to push the application of TiAl at higher temperature, i.e. higher LPT stages, certain latest developed third generation TiAl alloys, also named TNB alloys, can reach a Nb content up to 10%. An addition of higher amount of Nb is not considered beneficial because it will be increase the alloy density up to the density of Ni-base superalloys. The addition of Nb in the alloy could increase the activity of Al for the formation of the protective Al_2O_3 scale and suppress the growth of TiO_2. Also the addition of Mo or Sb presents a similar effect. On the other hand, the presence of a Nb-enriched phase (Nb_2Al and Nb_3Al) it is demonstrated to decrease the high temperature oxidation resistance due to Nb_2O_5 formation which promote the spallation of the oxide scale [129]. **Figure 55** shows the influence of Nb on the weight gain at different temperatures of an alloy with a constant Al content [130]. **Figure 56** shows the isothermal oxidation behavior comparison at 850°C and 950°C between ternary TiAl alloys with different Al content and 2% and 8% (at.%) of Nb [57].
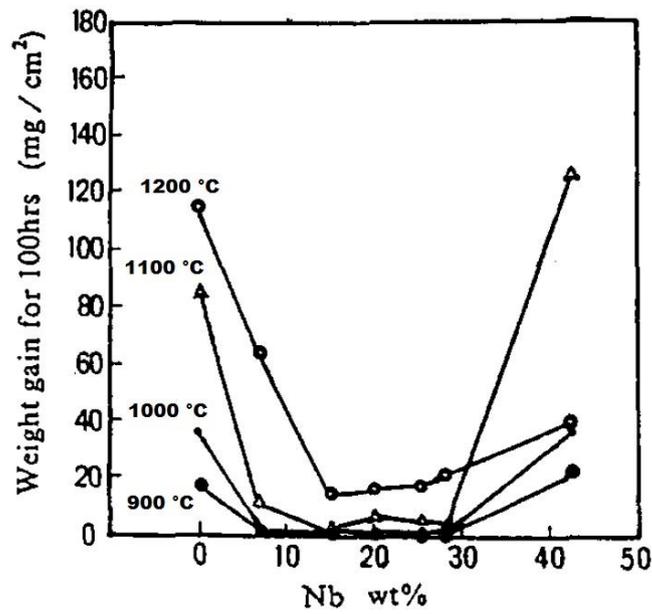
Figure 55: Effect of Nb content on the oxidation behaviour of alloy with 36.5% (wt.%) Al [130].
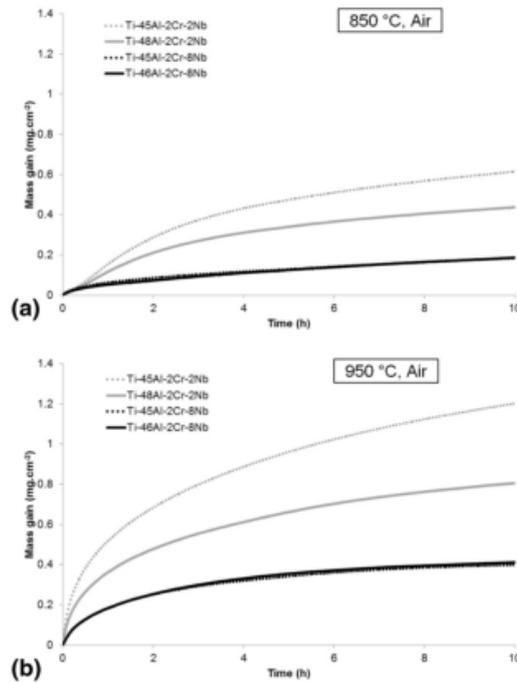
Figure 56: Mass gain vs. time for TiAl45-2, TiAl48-2, TiAl45-8 and TiAl46-8 during 10 h isothermal oxidation in air at a) 850°C and b) 950°C [57].

The exact mechanism of the oxidation protection due to Nb but also Mo and W is object of several studies and many authors support the hypothesis that in TiO_2 formed during oxidation, the oxygen diffusion can be controlled by vacancies. The vacancy concentration should be reduced by ions with valence +5 or +6, such as Nb and W, incorporated in the scale and this brings to the suppression of TiO_2 growth. Moreover, the mixed $(Ti, Nb)O_2$ rich layer is more dense and chemically uniform compared to the pure rutile scale and this prevent the oxygen diffusion through it [73] [74] [131].

It is also demonstrated that the combination of Nb and Si can improve the oxidation resistance of TiAl based alloys. Si modify the oxide scale morphology by promoting the formation of a dense Al_2O_3 in the internal part of the oxide scale. **Figure 57** shows the variation of oxide scale thickness with Nb and Si content [132].
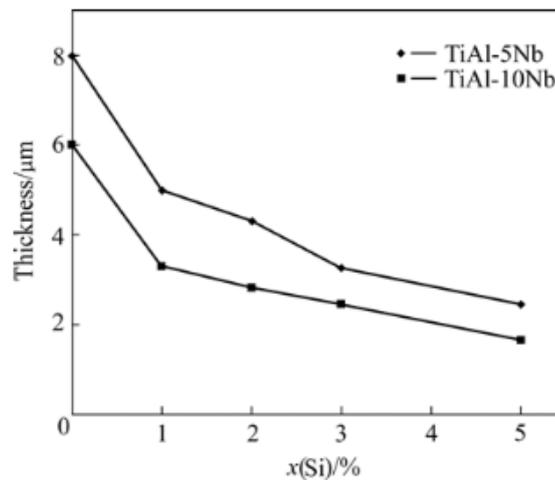
Figure 57: Change of scale thickness with Nb and Si contents [132].

Chromium is commonly present at 2% (at.%) in the alloy composition in order to increase ductility. Its effect it is to slow the kinetics of lamellar phase formation increasing the equiaxed/lamellar grain ratio [114].

Certain alloying elements are added in small amount depending on the processing method, in order to improve the workability or to enhance the microstructural characteristics of the as-processed material. In particular, β-stabilizer elements are added to improve the hot workability in wrought alloys and boron is added in cast material as a grain refiner. Other and advanced manufacturing processes, such as the Electron Beam Melting additive manufacturing technology,

does not requires particular addition of alloying to improve workability as these technologies allow to produce near net-shape components needing a limited post processing. Alloying addition is however considered in TiAl based alloys processed by EBM in order to improve the material properties.

The presence of limited amount of other light elements as contaminants, in particular oxygen, is an inevitable consequence of the processing route. Even if the production process is conducted in a vacuum or inert protective atmosphere, it is common to have an oxygen content of about 1000 wt. ppm in the final TiAl material. However, the oxygen content has to be kept under control because of its detrimental effects on the material properties and microstructure. As it will be described in the following chapter, EBM presents several advantages in terms of controlling impurities because it is a hot process and conducted in high vacuum, therefore, the degassing of impurities takes place. Titanium and titanium alloys present a high affinity to oxygen, and oxygen atoms occupy the octahedral interstitial sites in the closed-packed structures. From the properties point of view, an increasing amount of oxygen lead to a decrease of ductility (**Figure 58**). The microstructural effect of oxygen is the increase and stabilization of lamellar phase formation and lamellar thickness. Oxygen presents an high solubility in the α_2 phase, while in γ the phases the oxygen solubility is low [114].
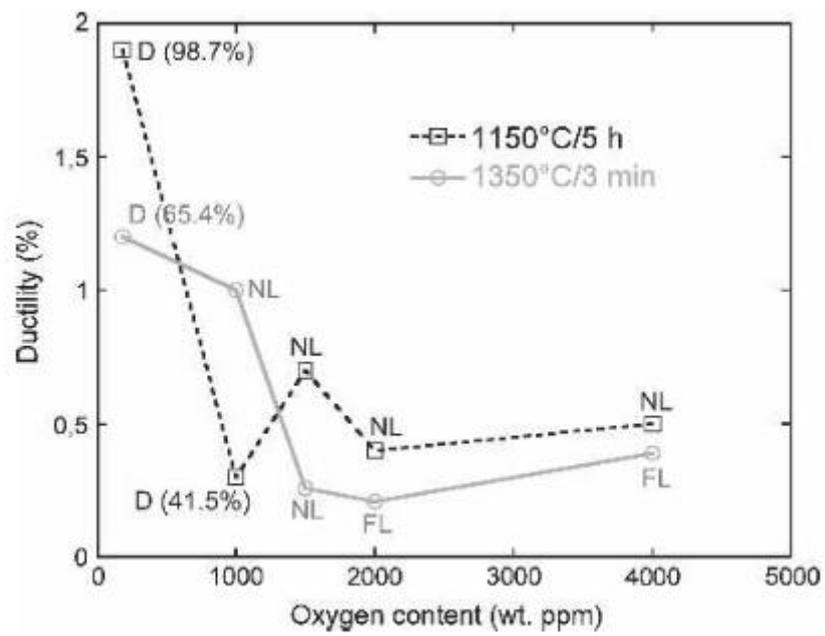
Figure 58: Fracture strain variation with oxygen content as a function of the heat treatment [114].

1.10 Alloy development and generations of γ-TiAl alloys

The optimization of the TiAl based alloys chemistry in order to obtain good material properties and make this family of compounds suitable for applications in aircraft engine and automotive components is nowadays a big challenge for the research. Three generations of TiAl based alloys have been developed over the last 25 years. The first generation of developed γ-TiAl alloys contain between 45% to 50% (at.%) of Al. As described before, by varying the Al content the ductility is significantly changed. The highest ductility is obtained with an Al content of 47-48 at.%.

Since the first generation of TiAl alloys did not fulfilled the requirements for application in gas turbine structural parts in terms of mechanical properties, further improvements were obtained with the development of a second generation of γ-TiAl alloys which presents a substantial addition of alloying elements. In these alloys, the ductility is further improved by a Cr addition up to 2 at.%. In certain alloys the ductility is improved adding Mn or V instead of Cr. High temperature creep and oxidation resistance, that are critical and very limiting for application, were improved by the addition of refractory elements such as Nb, Mo, Ta and W. An addition of B or C can also be considered. In particular, B is used as grain refiner and C to further improve the creep resistance and strength thanks to the precipitation hardening mechanism. One of the most significant example of second generation γ-TiAl alloy is the Ti-48Al-2Cr-2Nb alloy developed by General Electric for application in low pressure turbine blades. This alloy exhibits balanced properties up to the application temperature of 750°C. GE Ti-48Al-2Cr-2Nb casting blades are used for the last two stages of the low pressure turbine of the GEnx next generation engine from 2007 [133] but also in the more recents LEAP engine [134] and GE9X [135].

Third generation γ-TiAl alloys present an increased temperature application limit thanks to the alloying with a higher amount of refractory elements such as Nb, Mo or Ta up to 10 at.%. Alloys like TNB and TNM present a large amount of Nb and this lead to an increasing of the high temperature strength, creep and oxidation resistance. TNM alloys were developed to improve both the hot-workability and the high temperature mechanical properties of TiAl alloys. For these reason, additional alloying elements are added to induce the disordered β-phase at elevated temperatures as ductile phase. It has been demonstrated that the β-phase stabilization can be achieved by Nb, Ta and Mo addition [71] [136]. Also for these third generation alloys, the microstructure and mechanical properties can be further improved by a small addition of B and C. In 2014, forged blades made from TNM

alloy have been implemented in the geared turbofan (GTF) engine equipping the new Airbus 320neo [68].
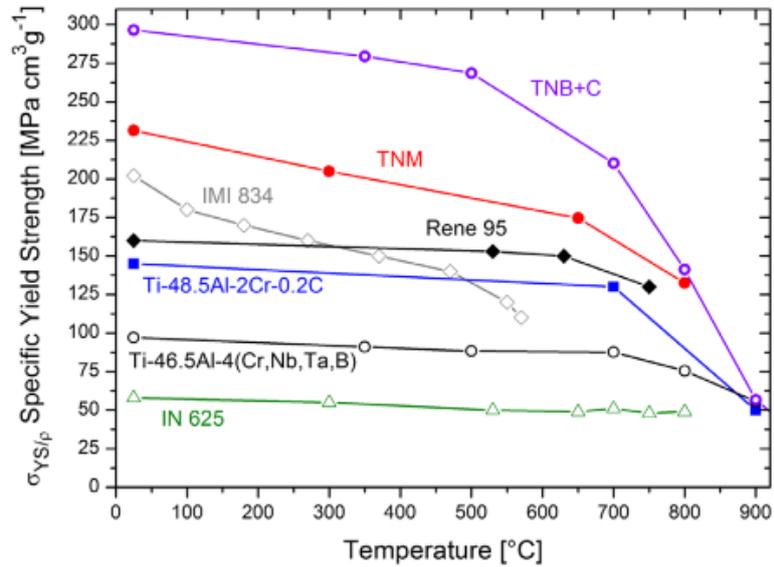
Figure 59: Temperature dependance of specific yield strength of γ-TiAl based alloys in comparison with different structural materials [68].

In **Table 13** different generations alloys described by Kotari et al. in the state of the art of γ-TiAl and other patented γ-TiAl of industrial interest are reported [55].

Table 13: TiAl alloys from the state of the art (2012) with chemical composition and improvements of mechanical properties [55].

Alloy name	Composition (at.%)	Alloy strengths
General Electric, USA. **48-2-2**	Ti-48Al-2Cr-2Nb	Ductility, fracture toughness and oxidation resistance
Plasee, Austria. **γ-MET**	Ti-45Al-(5-10)Nb	High temperature strength, creep, fatigue and oxidation resistance
GKSS Research Center, Germany. **TNB Alloy**	Ti-(45-47)Al-10Nb	High temperature strength, creep and oxidation resistance
Martin Marietta Laboratories, USA. **XD^{TM} TiAl**	Ti-45Al-2Mn-2Nb-0.8B	Ductility, high temperature strength, stiffness, creep and oxidation resistance
Daido Steel Co. Ltd, Japan **RNT004**	Ti-47Al-0.4Nb-0.4Cr-0.7Si	Ductility, creep
Daido Steel Co. Ltd, Japan **RNT650/DAT-TA1**	Ti-48Al-2Nb-0.7Cr-0.3Si	High temperature strength, ductility, stiffness, creep and oxidation resistance
Daido Steel Co. Ltd, Japan **DAT-TA2**	Ti-46Al-3Nb-0.8Cr-0.7Si-0.1C	Higher temperature application limit, high temperature strength, ductility, creep and oxidation resistance.

The development of particular TiAl based alloys for automotive applications such as turbocharger wheels or exhaust valves, takes in consideration the

improvement of certain material properties in order to satisfy the requirements for the automotive components. TiAl-based products are currently used in automotive applications and the alloy design in terms of chemical composition is actually the subject of several studies. Several TiAl based alloys have been patented and used by automotive companies such as Mitsubishi that in 1998 has begun to equip Lancer cars with second generation turbochargers manufactured from Ti-46Al-6.5Nb with other minor additions [56] [59].

Daido Steel has been developed a series of two TiAl based alloys for turbocharger wheel application that have extended the possibility for this alloy to be used at higher service temperature and thus in gasoline engine also (**Figure 60**). These alloys are the DAT-TA1 having a nominal composition of Ti-33.5Al-4.8Nb-1.0Cr-0.2Si (wt.%) and the newest DAT-TA2: Ti-31.5Al-7.5Nb-1.0Cr-0.5Si-0.03C (wt.%). The high mechanical properties of these alloys have improved the characteristics and performance of the turbochargers wheels produced by casting by Daido. In particular creep strength and phase stability at high temperature have been increased thanks to the addition of C and Si (**Figure 61**). The presence of Si together with Nb has led to an improvement of the oxidation resistance (**Figure 62**). DAT-TA2 exhibits an oxidation resistance that is comparable with Ni-based superalloys up to 1000°C [116].
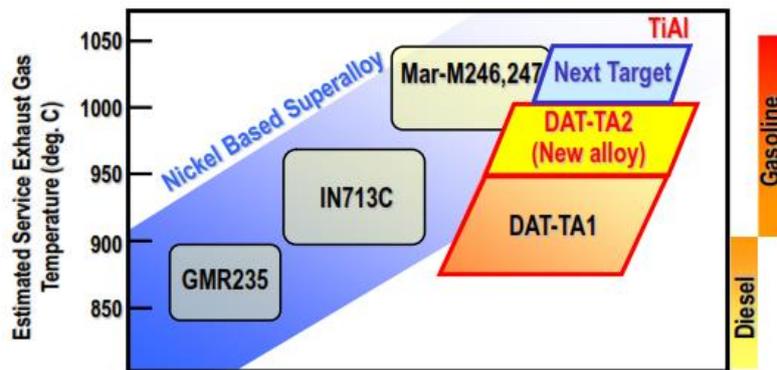
Figure 60: Service temperature of TiAl alloys DAT-TA1 and DAT-TA2 compared to Ni-based superalloys [116].
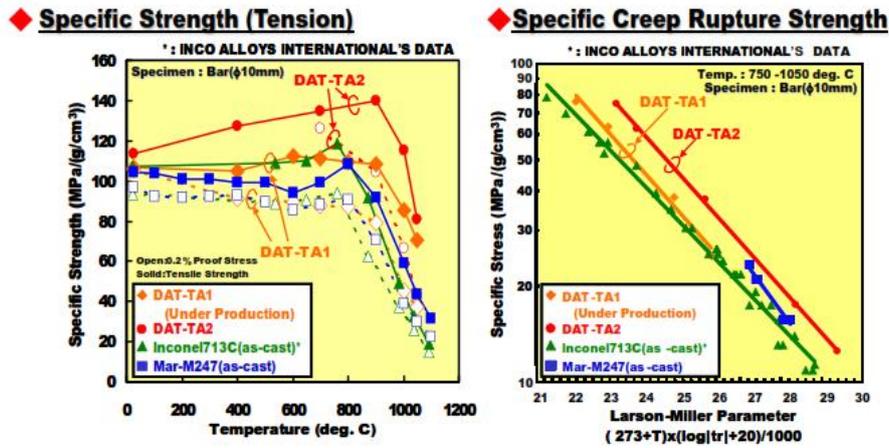
Figure 61: Specific strength vs temperature and specific Creep rupture strength comparisons between DAT-TA1, DAT-TA2 and Ni-based superalloys [116].
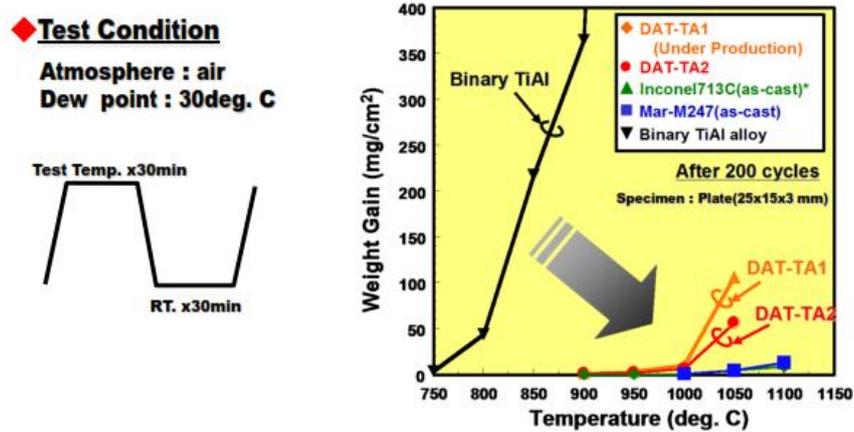
Figure 62: Mass gain vs temperature of DAT-TA1 and DAT-TA2 compared with binary TiAl alloy and Ni-based superalloys [116].

The cast γ-TiAl alloy developed for the automotive applications named RNT650 having the same composition of the DAT-TA1 alloy was already described by Noda in 1995. Another Si containing alloy for exhaust valves application is named RNT004 and have a chemical composition of Ti-33.5Al-1.0Nb-0.5Si (wt.%). This alloys have been designed to present γ/α$_2$ lamellar structure in as-cast condition. For the turbocharger wheel application, this lamellar microstructure brings to a better combination of mechanical properties (**Figure 63**) [44] [127].
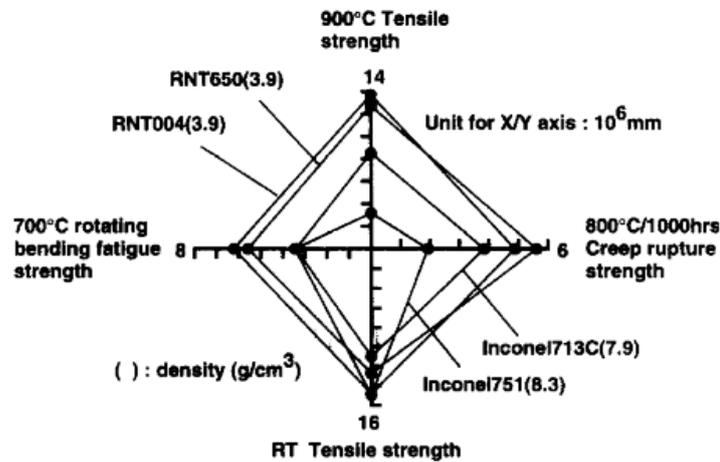
Figure 63: Specific strength of cast RNT004 and RNT650 alloys [44].

The development of TiAl alloys for automotive application was also been studied by Tetsui and Ono from Mitsubishi R&D center in collaboration with Daido Steel and the environmental behavior of alloys with different composition and low and high Nb content has been evaluated [32] [46] [58].

The effect of the presence of Si in the alloy composition on the creep properties have been analyzed by Noda et al. earlier in 1995. It has been demonstrated that the specific strength of Si-containing alloy is better than of a conventional Ni-base cast superalloy. The addition of Si, in an amount of 0.26-0.65 mol.%, generates fine Ti_5Si_3 precipitates that was found to be effective in creep resistance enhancement for a fully lamellar Ti-48Al-1.5Cr (at.%) alloy (**Figure 64**) [115].
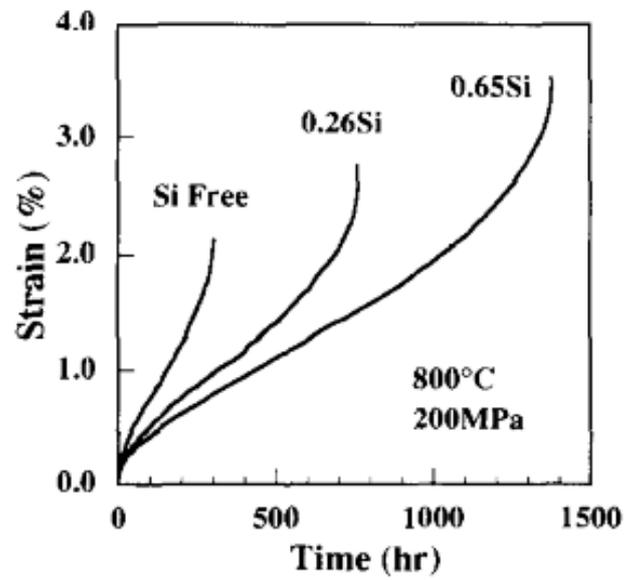
Figure 64: Creep curves of TiAl alloys without Si, with 0.26 and 0.65 mol.% Si under 200 MPa at 800°C in air [115].

1.11 Additive manufacturing and Electron Beam Melting (EBM) technology

As already introduced in section 1.4.3 Intermetallics and Titanium Aluminides, the processing of titanium aluminide via conventional manufacturing methods can be complex due to the low ductility and fracture toughness of the material. In fact, the limited use of TiAl alloys can be related to the difficulty in its production. The most applied conventional industrial scale processing routes include ingot casting, ingot forging, hot-rolling sheet production, investment and permanent mold casting and powder metallurgy processing. Conventional methods for alloying and ingot production are induction scull melting, vacuum arc re-melting and plasma melting.

Casting of TiAl alloys presents different problems to take into account, first is the reactivity of the molten material with ceramics. The use of cold-wall furnaces can in part solve this problem. However, the superheating of TiAl can only be 600°C, and this make difficult to fill the mold properly. Perform the melting in argon overcomes the problem of Al evaporation during the melting in vacuum atmosphere. Further problems with casting is the anisotropic coarse lamellar microstructure and alloying elements segregation phenomena.

Investment casting is successfully used to manufacturing certain TiAl parts such as turbine blades but the high cost of this manufacturing method is an obstacle for some industrial sectors such as the automotive. Permanent mold casting allows to reduce the cost and by increasing the cooling speed of this technique it is possible to obtain TiAl material with fine grained near-γ or duplex microstructures. The low ductility of casted materials are generally due to the coarse structure obtained with these methods.

With wrought methods, it is possible to obtain more ductile and tough materials. In wrought processes, the structure from the ingot is broken and re-crystallization takes place. However, the workability of TiAl material has to be improved by controlling the Al content and by adding some alloying elements such as Cr. The production of a material with fine lamellar structures is desirable in order to obtain good mechanical properties [137] .
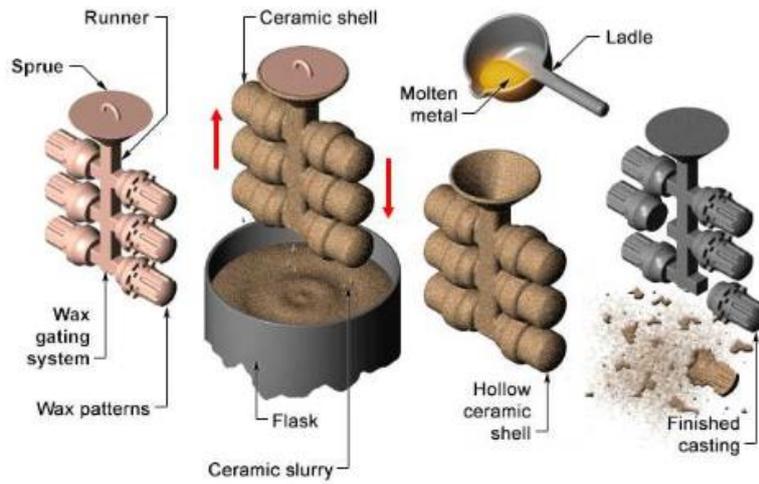
Figure 65: Schematic representation of the investment casting process [138].
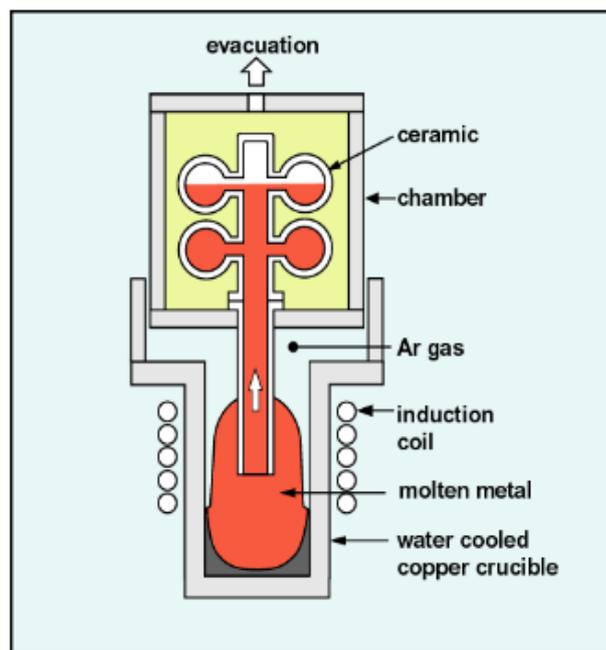
Figure 66: Schematic representation of the LEVICAST process developed by Daido steels [116].
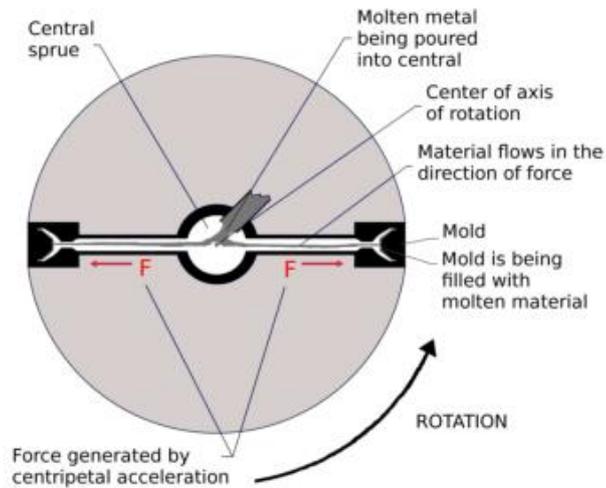
Figure 67: Schematic representation of centrifuge casting [139].

Recently, additive manufacturing technologies already proved to be a promising alternative to casting or forging for titanium aluminides alloys.

Additive manufacturing techniques allow building of parts in a layer-by-layer way according to a computer assisted design (CAD). One of the main advantages of these techniques is the possibility to produce parts with complex shape and geometry. The processing time can be reduced adopting AM technology and the material waste can be considerable reduced if the re-using of the unmelted powders is considered.

AM can be divided into Powder Bed, Material Deposition/Extrusion, Liquid processes and 3D printing according to the way the layers are deposited during the process. In particular, since Electron Beam Melting (EBM) is the AM technique considered in this thesis, the attention is focused on Powder Bed technologies. In these techniques, layers of powder having variable thickness, are deposited and consolidated by melting or sintering using a laser or electron beam, which follows a scan path defined by the sliced CAD model. Once a layer is completed, the building platform is moved down, another powder layer is deposited and the next layer can be consolidated. The process is repeated layer by layer until the part is completed.
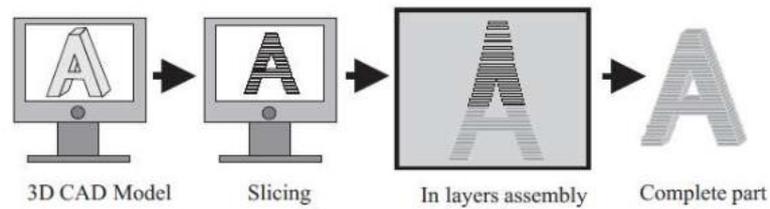
Figure 68: Additive manufacturing process steps [93].

Powder Bed AM technologies are selective laser melting (SLM), selective laser sintering (SLS), direct metal laser sintering (SMLS) and electron beam melting (EBM) [140] [141]. **Figure 69** shows the classification of metal powder-based AM processes and the main suppliers producing these AM machines [142].

Figure 69: Powder-based Metal Additive Manufacturing technologies and suppliers [142].

Among powder bed additive manufacturing (AM) technologies, Electron Beam Melting (EBM) has proved to be the most suitable to produce TiAl parts. Other AM technologies such as laser techniques do not meet the requirements for TiAl production because of the not sufficient pre-heating of the chamber in order to avoid detrimental thermal gradients. Thermal gradients results in the formation of cracks or micro-cracks in the as-produced material. Another problem concerning the laser techniques is the cleanliness of the process. In fact, the chamber atmosphere is an

inert gas and not a high-vacuum environment, like in EBM, capable to avoid any pick-up of contaminants [142].

EBM is a registered mark technology developed by Arcam AB. In 2002 the first EBM machine model starts to be commercially available. The power source used by EBM to melt the powders is a high-energy electron beam. The near-net-shape parts are produced layer-by-layer in a high vacuum chamber resulting in fully dense components. The vacuum environment allows to process parts in reactive materials, in particular titanium that presents a high affinity for oxygen.

Advantageous characteristic of AM technologies like EBM is the fine and homogeneous microstructure obtained in the as-built parts and the possibility to choose the desired chemical composition of the material from the pre-alloyed powder. The schematic of the Arcam A2 and a photo of the Arcam A2X EBM machines are represented in **Figure 70a and b** [143].
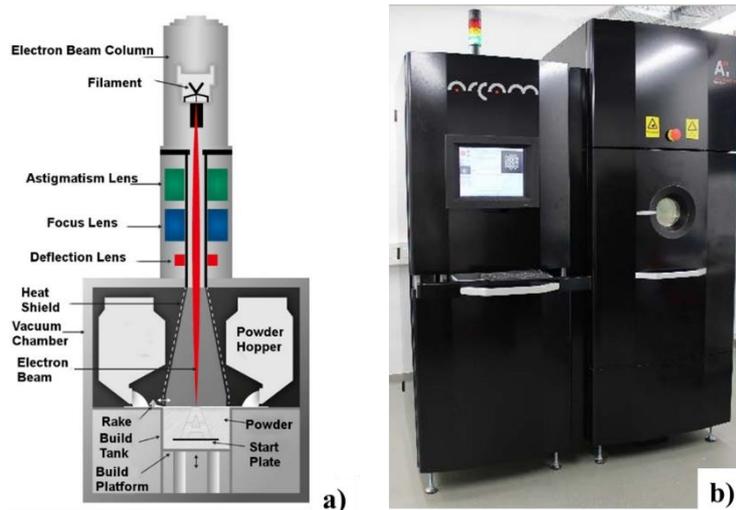
Figure 70: a) schematic of the arcam A2 machine; b) photo of the Arcam A2X [143]**.**

The whole EBM manufacturing process can be briefly resumed as follow and it is represented in **Figure 71:**

- Design of the part → CAD drawing;
- Slicing of 3D part into 2D layers;
- Positioning of part(s) within building space and addition of support structures if they are needed;
- Building of the part(s) layer-by-layer;

- Removal of part(s) from the machine, blow off surplus powder;
- Collection of unmelted power from the chamber and not used powder from the powder recovery system if powder re-use is considered.
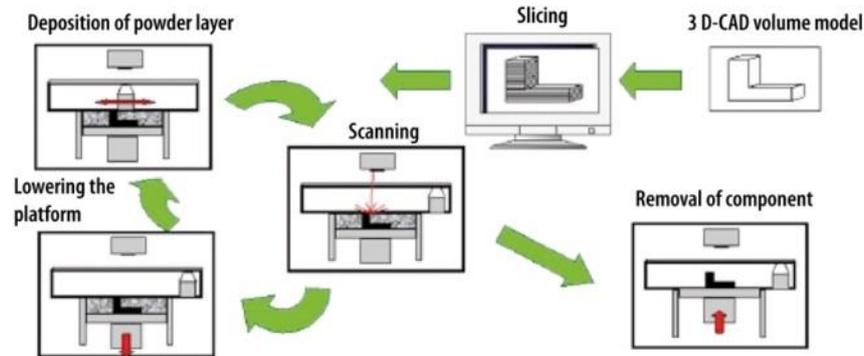
Figure 71: Diagram of the EBM process.

The EBM process uses a high energy focused electron beam and the melting of the metal powder is obtained when kinetic energy from concentrated electron beam is accelerated to a high speed.

The electron beam is generated in the electron gun by a tungsten filament heated to above 2000°C by the filament current. The electrons released by the filament are accelerated within an electrical field generated by a high voltage applied between the filament and an anode. A control electrode is used to control the beam current in the range 1-50mA and an electromagnetic coil focusses the beam down to about 0.1mm. The electron beam can scans the powder layers in a controlled way thanks to electromagnetic lenses named deflection coils.

The energy density that can be obtained with EBM is up to 106 KW/cm^2. The melting of the powder appends when the accelerated electrons impact with the powder particles and their kinetic energy converts into thermal energy sufficient to reach the melting temperature of the powder. At the beginning of the process, the building plate made of a compatible material is heated to a certain temperature.

The metal powder are contained into two powder hopper, by gravity it is fed on the building platform and the layer is distributed by a raking mechanism. After the melting of a layer, the build platform is lowered with each successive layer building. The powder layer thickness is typically between 0.05 and 0.2mm depending on the powder particles dimensions. Spherical powders with an optimized particle size

distribution are used in order to improve the flow and the packing of the powder during the racking.

A preheating and initial sintering of the powder layer is obtained with an initial multiple pass using a strongly defocused beam having a high rate scan and medium beam current. In this phase, the powder is preheated up to 80% of the melting temperature of the metal. The preheating of the entire build region is needed for reducing the thermal gradient and, consequently, the internal stresses within the parts between the last melted layer and the already solidified built material. This step is also useful to give electrical conductivity to the powder layer [144] [145].

The process is carried out under high vacuum and the typical pressures are 10^{-2} Pa in the vacuum chamber and 10^{-4} Pa inside the electron gun. The so-called smoke phenomena due to the electrical charge formation in the powder is avoided adding a small pressure of helium (10^{-2} Pa) to the vacuum chamber. The added helium has also the function to speed up the cooling of the built components inside the chamber.

In **Table 14** the main technical data for the Arcam A2 EBM machine are reported. These data are available on the Arcam AB web page [143].

Table 14: Arcam A2 technical details [143].

Build tank volume (WxDxH)	**250x250x400 mm** **350x350x250 mm**
Maximum build size (WxDxH)	200x200x350 mm ⌀300x200mm
Model-to-Part accuracy long range (100 mm)	± 0.20 mm
Model-to-Part accuracy short range (10 mm)	± 0.13 mm
Surface finish (vertical/horizontal)	Ra25/Ra35
Typical powder size	45 – 180 µm (325 – 80 mesh)
Beam power	50-3500 W
Beam spot size	0.2 mm – 1.0 mm
EB scan speed	8000 m.s^{-1}
Layer thickness	0.05 – 0.2 mm
Build rate	55/80 cm^3.h^{-1} (Ti6Al4V)
N° of beam spots	1 – 100
Vacuum base pressure	≤ 10^{-2} Pa
Size and weight (WxDxH)	1850x900x2200 mm 1420 kg

Regarding the parameters for the processing of a material, it is important to consider the beam parameters during the preheating and melting, the individual scan lines distance/overlap, layer thickness and process temperature. The melt of the powder layer and the re-melt of at least one layer of the underlying consolidated material is necessary to ensure a good interlayer connection. The process temperature is chosen according to the phase transformation in the processed material. Higher temperatures are usually needed to increase the process stability. The deflection speed υ and beam current I are the beam parameters, often combined into one parameter that is the line energy LE according to the following relation:

LE = (I*U)/ υ

U is the acceleration voltage fixed to 60 KV [145].

During the EBM process, it is possible to apply different building path and scanning strategies according to the part to build. These strategies can be, for

example, the use of a certain number of contours from the center to the edge (in-out) or in the opposite direction (out-in) instead of a linear melting path or also the combination of these two. A process performed with not optimized parameters often brings to various typical macroscopic and microscopic/microstructural defects in the final material. Not fully-densified parts with irregular shaped pores, insufficient interlayer connection, micro and macro cracks and microstructural inhomogeneity are the most observed defects coming from not optimized building parameters.

EBM process presents considerable melting pool dimension and this is one of the main factor affecting the surface finishing of the processed parts. In fact, EBM brings to parts having a less refined surface than those obtained by laser technique. In order to improve the surface quality of the components, a surface finishing obtained by sand blasting and subsequent machining is considered after the process. The sand blasting operation is performed using the same powder of the process to avoid contaminations and removes the partially sintered powder from the surface of the part.

It is also necessary to specify that the use of supports made of partially sintered powder during the building is needed to avoid components distortions and to facilitate the removal of the parts from the building platform after the process.

EBM, like other metal powder bed AM techniques, involves several different physical phenomena. In particular the absorption of the electron beam from the powder bed, the melting and solidification, the melt pool dynamics, the wetting of solid powder particles by the melt, the heat conduction within the powder bed by diffusive and radiative mechanisms, the capillary effect, gravity and other (**Figure 72**). The low viscosity of liquid metals combined to the high surface tension drives the movement of the melt pool. This brings to a consolidated surface with a stochastic nature and it is evident from its irregular and corrugated appearance. It might happen that the melt pool disintegrates into spherical droplets resulting in a rough and bead-shaped surface decreasing the density of the processed parts. This phenomenon is commonly named as Rayleigh instability. Another phenomenon that affect the quality of the upper surface of the melt pool is known as Marangoni flow and it arise from the required excess energy. The wetting characteristics of the melt with the powder particles is strongly influencing the shape of the re-solidified melt pool [146] [147] [148].

Evaporation of elements from the molten metal is another common phenomenon in EBM and it is controlled by mass transport of atoms from the inner melt to the surface, liquid to gaseous phase transformation at the surface, mass transport in the gas phase and condensation. The low-pressure environment and high temperature typical of the EBM process facilitate the evaporation of certain lightweight and low-melting metals and alloying elements [145].
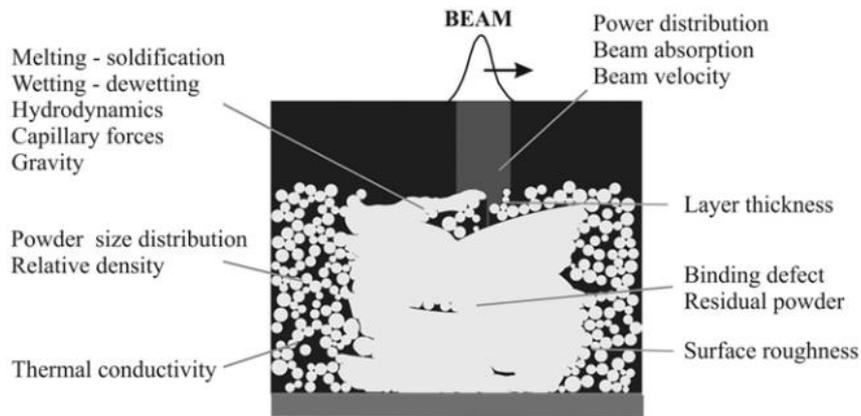
Figure 72: Physical phenomena and aspects in EBM [146].

Experimental activities

In the next chapters, the different experimental activities are described. Because the research activities focused on different TiAl alloys for different applications, this part of the thesis is organized considering each single studied TiAl alloys separately, except for the powders characterization that can be considered a transversal activity.

Since the starting material for the EBM process is the alloy powder, it is fundamental to characterize and optimize the powder in order to guarantee a successful production of the final parts. In fact, the aims of the powders characterization and optimization are i) make the process possible and fast avoiding problems during the fabrication and avoiding defects in the manufactured parts; ii) obtain the desired properties in the final massive parts in terms of chemical composition, microstructure and, consequently, physical and mechanical properties.

The experimental activities are related to four different TiAl alloys, three of which for aircraft engine application that are the 48-2-2 alloy (Ti-48Al-2Cr-2Nb (at.%)), the High Niobium HNb alloy (Ti-48Al-2Cr-8Nb (at.%)) and the TNM alloy (Ti-43.5Al-4Nb-1Mo-0.1B (at.%)) and one of automotive interest that is the so called RNT650 alloy (Ti-48Al-2Nb-0.7Cr-0.3Si (at.%)).

Regarding the aircraft engine application of γ-TiAl, big part of the research activity was done in collaboration with AvioAero, for some European and Regional research projects. In particular, the 48-2-2 alloy as well as new generation alloys such as High Niobium alloy and TNM alloy produced by Electron Beam Melting were investigated in the frame of the European project E-BREAK [13]

Considering the automotive application, a part of the work was done within the European project TIALCHARGER [14], for the evaluation of the feasibility by EBM of turbocharger wheels in a Si-containing alloy.

Chapter 2

Experimental techniques

In this chapter, the techniques used for the material characterization and material treatments are described. In this work, the material properties study was performed on both TiAl alloys powders and massive specimens. For the characterization of the massive specimens, in particular for the morphology characterization and microstructure analysis by means of optical or electron microscopy, a preliminary metallurgical preparation was necessary. However, the specimens preparation techniques, such as cutting, mounting, polishing and etching, are not deeply described in this part.

2.1 Optical microscopy

Optical microscopy analysis was performed on both solid specimens and TiAl powders. This technique was used to analyze the microstructure of TiAl alloys in as-EBM condition and after the heat treatment but also for porosity analysis according to ASTM E2109 [149]. Specimens for optical microscopy analysis were prepared by polishing up to 4000 grit or finer and etching in Kroll's reagent in order to reveal the TiAl microstructure. The Kroll's reagent is composed by 6 vol.% HNO_3, 3 vol. % HF and water. For powders morphological analysis, optical microscopy was used to observe the presence of any pores inside the powder particles.

The optical microscopy used for this work is a Leica DMI5000 M inverted microscope with an integrated camera and Leica LAS software.

Figure 73: Leica DMI5000 M optical microscope.

2.2 Scanning Electron Microscopy (SEM)

The Scanning Electron Microscopy (SEM) technique, and in particular the Field Emission Scanning Electron Microscopy (FE-SEM) technique, was used for the morphological analysis of the TiAl powders, for the microstructural analysis of finer TiAl alloys microstructures (in particular for the TNM alloy) and, thanks to the Energy Dispersion Spectroscopy (EDS) technique, for a semi-quantitative elemental analysis of the used powders and specimens.

The electron microscopy uses accelerated electrons as energy source. The electrons accelerated toward the samples produce an interaction with the material bringing to the emission of both other electrons and X-Rays. The emitted electrons can be elastically or inelastically backscattered, re-emitted with high-energy loss or very low energy (secondary electrons). In SEM the electrons used for the materials analysis are the elastically backscattered electrons (BSE) and the secondary electrons (SE). Different detectors are used according to the type of emitted electrons to reveal.

SE electrons can give morphological information with very high resolution. BSE electrons emerge from deeper locations within the specimen and consequently the resolution of BSE images is generally poorer than SE images. However, BSE images can provide information about the distribution of different elements in the

sample because the intensity of the BSE signal is related to the atomic number of the atoms present in the specimen.

In **Figure 74** a schematic structure of a SEM microscope is reported [150].
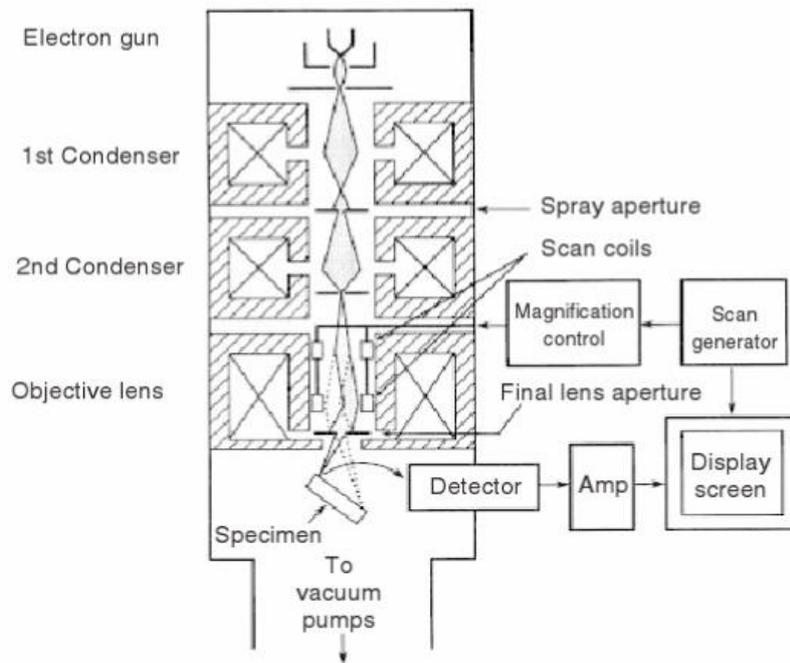
Figure 74: Structure of a scanning electron microscope (SEM) [150].

In **Figure 75** and **Figure 76** the mechanisms for SE and BSE imaging are shown [151].
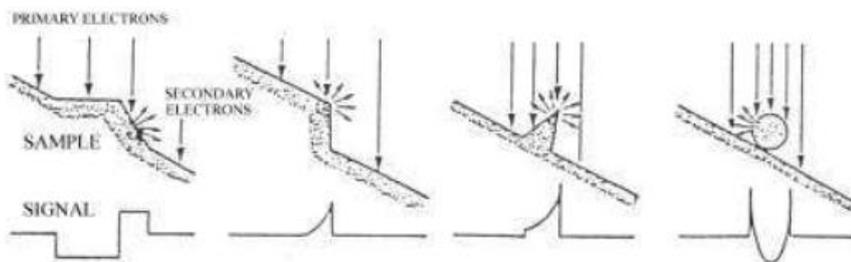
Figure 75: Image formation mechanism for SE revelation [151].
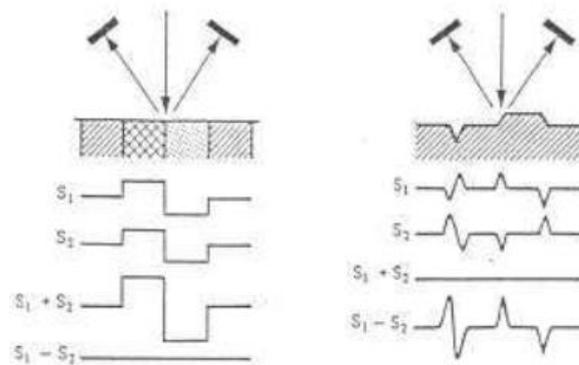
Figure 76: Image formation mechanism in the case of BSE revelation [151].

Figure 77 illustrates the interaction zone where electrons scatter under the specimen surface. The size of this zone increase with the incident electrons energy. Characteristic X-Rays are also generated in the interaction zone, and these are useful for chemical analysis as described in the following sub-section.
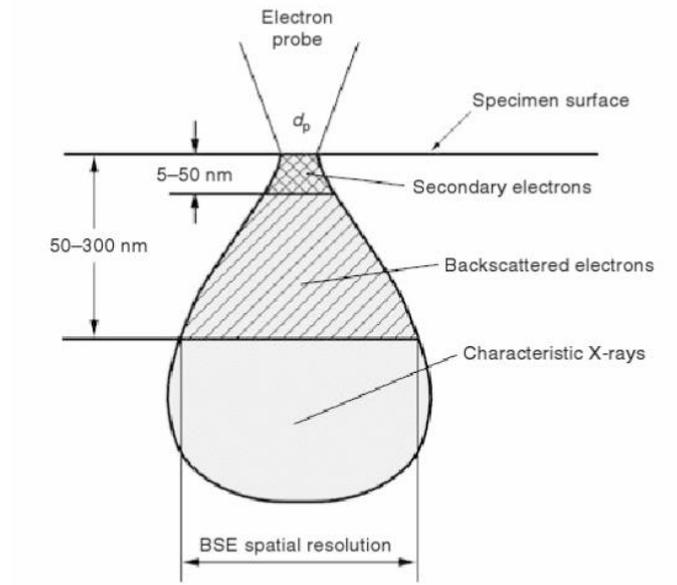
Figure 77: Specimen-electrons interaction zone below a specimen surface [151].

The energy level of inelastically scattered SE is in the order of several electron volts. In the interaction zone, SE can escape only from a depth of 5-50 nm near the specimen surface. By the other hand, elastically scattered BSE have an energy level

close to that of incident electrons. For this reason, they can escape from a much deeper level in the interaction zone, from depths of about 50-300 nm.

During this thesis, a Field Emission Scanning Electron Microscope (FE-SEM) was used. This particular technique provides a higher spatial resolution (down to 1, ½ nanometers) compared to conventional SEM. Other advantages are the possibility to examine with EDS smaller-area spots, lower electrical charging of samples. In FE-SEM a field-emission cathode in the electron gun provides narrower probing beams at low and high electron energy, resulting in improved spatial resolution and minimized sample charging. In this work, a Zeiss MERLIN FE-SEM field emission scanning electron microscope and a SEM Phenom XL were used.

2.2.1 Energy Dispersion Spectroscopy (EDS)

Energy dispersion spectroscopy is an analytical technique that can be integrated in a SEM apparatus in order to perform the elemental analysis of a sample. The EDS microanalyzer uses the primary electron beam of the SEM (or Transmission Electron Microscope TEM) to excite the emission of characteristic X-Ray from the atoms of the sample. The incident high-energy electron beam excite an electron in an inner shell of a sample atom. This causes the ejection of the electron from the shell and creates an electron vacancy. The vacancy is then filled by an electron from an outer, high-energy shell and the energy difference between these two shell levels is released in form of an X-Ray. An energy-dispersive spectrometer can measures the number and energy of the emitted X-Rays. The elemental composition of the sample can be measured because the energy of the X-Rays is characteristic of the atomic structure of the element from which they are emitted. In fact, each element has a unique atomic structure allowing a unique set of peaks on its emission spectrum.
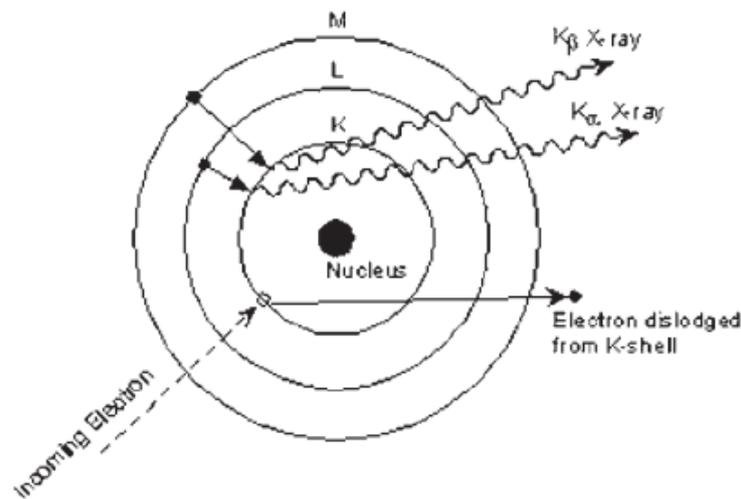
Figure 78: Excitation and emission in an atom.

With EDS, it is possible to examine chemical composition in a microscopic area thanks to the focused electron beam. Moreover, it is also possible to perform elemental composition maps on acquired image of the sample surface thanks to the combination of X-Ray spectroscopy and computer-assisted imaging.

The EDS spectrum is displayed with the X-Ray energy represented on the x-axis (usually in 10 or 20 eV wide channels) and the number of counts per channels on the y-axis. The X-Ray line is consisting of mono-energetic photons but it is broadened by the response of the system, producing a Gaussian profile. The energy resolution of is defined as the full width of the peak at half maximum height and in EDS it is good enough to separate the K lines of neighboring elements.

Accuracy of EDS can be affected by the nature of the sample and by elements with overlapping peaks. For example, inhomogeneous samples and samples with irregular surfaces can results in a reduced accuracy and in particular, low-energy X-Rays, such as the Kα radiation emitted by carbon, nitrogen and oxygen atoms are affected by the sample geometry. Moreover, the low-energy X-Ray produced by these atoms generate a low count rates, making it difficult to detect them at low concentrations [150].

In this work, a Zeiss MERLIN FE-SEM field emission scanning electron microscope and a SEM Phenom XL were used.

2.3 X-Ray Diffraction (XRD)

X-Ray diffraction technique is used for the characterization of crystalline materials.

The XRD techniques is based on the interference between an incident X-Ray beam with the atomic planes of a crystal.

The XRD instrument is called X-Ray diffractometer. In this instrument, a single wavelength X-Ray beam is used to examine polycrystalline specimens. By continuously changing the X-Ray beam incident angle, a spectrum of diffraction intensity versus the angle between incident and diffracted beam is acquired. This technique allows identifying the crystal structure by the analysis and comparison of the spectrum with a database containing several diffraction spectra of crystalline materials. In **Figure 79** a schematic of an XRD apparatus is represented.
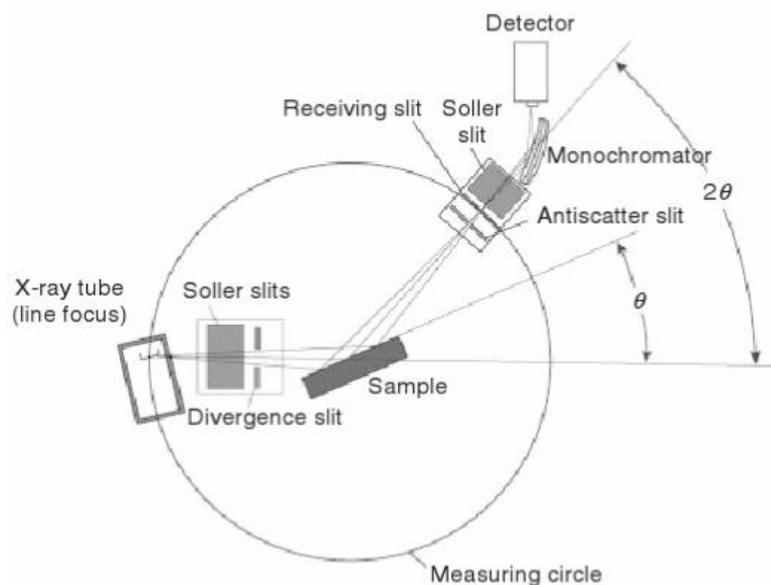
Figure 79: Geometric arrangement of X-ray diffractometer.

X-Ray diffraction technique is based on the Bragg's law:

$$n\lambda = 2d\sin\theta$$

where n is an entire number, generally 1, λ is the incident X-Ray wavelength (depending on the chosen X-Ray radiation source, usually copper Kα because of its short wavelength), θ is the incident angle and d is the distance between crystal planes reflecting the radiation.

The X-Ray Diffraction mechanisms is represented in **Figure 80** [152].

Diffraction occurs only when Bragg's law is satisfied condition for constructive interference of the interaction between the incident X photons and the atoms.

X-Rays are used as radiation to produce the diffraction pattern because they have a wavelength typically in the same order of magnitude of the spacing d between the crystal planes.
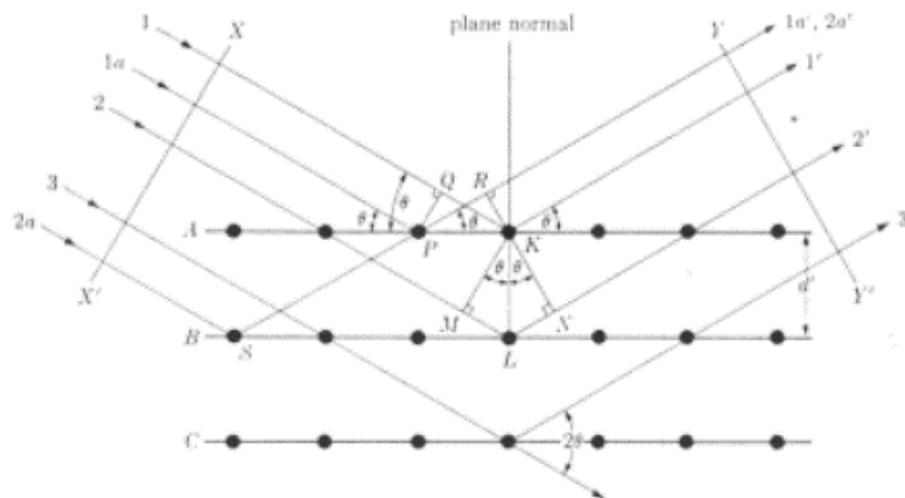
Figure 80: Bragg's law schematic explanation. Mechanism of formation of diffracted wavelength [152].

For a massive material, the measurement is influenced by its oriented crystallographic structure. In the case of a powder, if it is sufficiently fine, all possible diffracting planes can diffracting at the same time and all possible reflection are produced [150].

During this thesis, XRD was used on both powders and massive materials in order to investigate the phase composition of the different alloys and to analyze the phase evolution during the heat treatments.

The XRD instrument used in this work was a θ-2θ type Panalytical X'PERT PRO PW3040/60 diffractometer in a Bragg Brentano configuration operated at 40 kV and 40 mA.

2.4 Thermomechanical Analysis (TMA)

The principle of TMA is based on dilatation of the material induced by controlled temperature variations. The specimen is subjected to a controlled temperature ramp and its length variation is measured by an alumina probe placed in contact with the sample. TMA can be used to measure the linear thermal expansion coefficient of a material (α) in a certain temperature range and to investigate the phase transformations. Since all phase transformations cause a change in volume of the sample, it is possible to determine each phase transformation temperature by observing the peaks of displacement derivative curve versus temperature.

The used TMA apparatus is provided by a vertical graphite furnace with a cylindrical alumina tube inside. The thermocouples are placed inside this tube in a position close to the specimen. The cylindrical alumina tube can be mechanically extracted from the furnace in order to place the sample on the sample holder plate at its bottom. The probe is a mobile cylindrical tube made of a heat resistant material (alumina, silica or graphite) placed inside the cylindrical tube.

The measurements can be performed in a protective atmosphere using different type of inert gases and a water cooling system is integrated in the machine.

The machine is computer controlled by a software that allows editing the measurement programs by setting up the desired parameters such as heating rate, cooling rate, isothermal zones and the gases flows. Another software is used to acquire, elaborate and export the acquired data.

In TMA, the probe has a semi-spherical tip that is placed in contact with the upper face of the specimen. The specimens are usually small cylinders or parallelepiped having the upper and lower faces parallels in order to reduce measurement errors during the test. The sensor is a LVDT transducer (Linear Variable, Differential Transformer). The vertical hollow alumina tube allows to maintaining the transducer in suspension by means of an electromagnetic equipment and by applying to the specimen a force of about 5 g it is possible to guarantee the specimen-probe contact without obstructing the displacement [153]. The instrument used in this work and a schematic of the TMA system are represented in **Figure 81**.
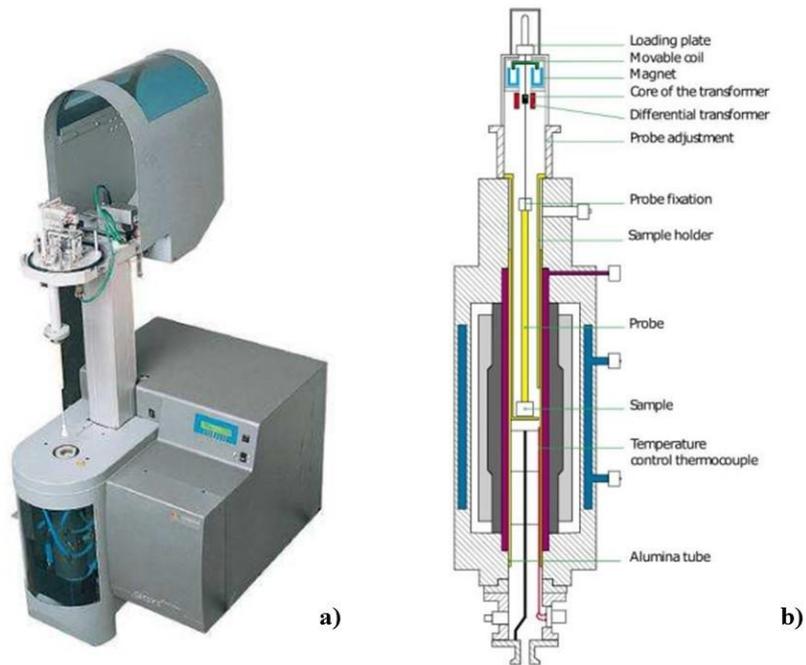
Figure 81: a) Setaram Setsys Evolution TMA instrument; b) schematic of a TMA.

During the measurement, the phase variations can be detected as slope variations in the displacement curve versus temperature. The displacement derivative can be calculated by the software at the end of the test. The peaks corresponding at the different phase variations can be observed in the displacement derivative curve and the phase transition temperatures can thus be detected. **Figure 82** shows an example of displacement curve and displacement derivative curve versus temperature [154].
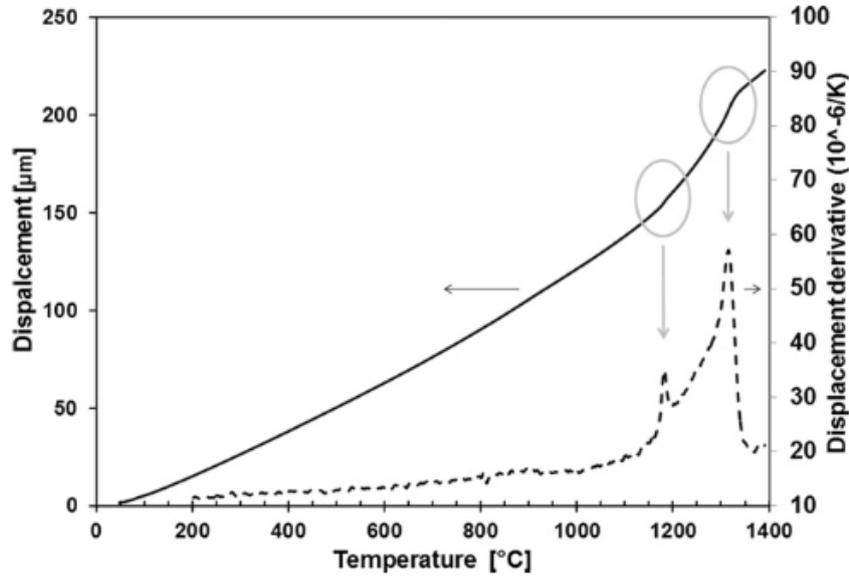
Figure 82: TMA measurement of a TiAl alloy: displacement vs. temperature (continuous line) and displacement derivative vs. temperature (dotted line) [154].

The TMA instrument used in this thesis is a Setaram Setsys Evolution having a max temperature of 1620°C, a resolution of 0.2 nm, a measuring range of ± 2 mm. The measurements were performed under an Ar flow in order to prevent oxidation. The standard test method for the linear thermal expansion coefficient measurement of solid materials by thermos mechanical analysis is provided by the ASTM E831 [155].

2.5 Sieving analysis

The powder size distribution was obtained by the sieving method according to ASTM B214-07 standard [156].

With this method, 100 ± 10 g of powder is weighed and sieved for 15 minutes. The power is divided into different fractions according to the different diameter of 180 µm, 150 µm, 106 µm, 75 µm, 63 µm, 53 µm, 45 µm thanks to the different mesh dimensions of the sequence of sieves. The different powder fractions remaining on the different sieves are weighed and the cumulative distribution can be those determined.

2.6 Flowability

The flowability of the powders was measured according to ASTM B213-11 standard [157]. The measurements were performed using a Hall Flowmeter and the time that 50 g of powder takes for flowing out from the funnel was measured. Flowability, along with other powder characteristics such as size distribution, gives important information about the processability of a powder by EBM. In particular, a powder with a not optimized flowability does not allows a proper layer distribution and raking during the EBM process. Since the flowability is strictly correlated to the powder morphology and particle size distribution, it can be improved by the tuning of these two powder characteristics.

2.7 Powder apparent density

The apparent density of the powders was measured according to ASTM B212-12 standard [158]. With this method, a Hall Flowmeter cup of 25 cm^3 is filled and weighted.

2.8 Elemental chemical analysis

The chemical analysis on massive specimens and powders were performed by ICP-OES (Inductively Coupled Plasma), by inert gas fusion infrared detection technique (IGF) and combustion infrared detection technique. The ICP was used to detect mostly of the elements contained in the alloys, the IGF detection technique has allowed the detection of the low level of oxygen and nitrogen and the combustion infrared detection technique was used to detect carbon. These analysis were performed by external laboratories according to ASTM E2371 (ICP-OES), ASTM E1941 (combustion infrared) and ASTM E1409 (IGF) standards [159] [160] [161].

2.9 Heat treatment furnace

A GERO high temperature LHTW type laboratory furnace was used to perform the heat treatments on the different alloys. The furnace consists of a stainless steel double wall and water-cooled heating chamber. The heating element is a tungsten resistance placed inside the heating chamber. The insulation is provided by a molybdenum layer and a stainless steel layer. The specimens are placed inside the chamber on a proper plate covered by a tantalum foil in order to avoid specimen contaminations during the heat treatment. The temperature is controlled by a thermocouple placed inside the chamber in a central point over the specimen plate.

With this furnace, it is possible to perform heat treatments in inert gas flow (argon) or under high vacuum (10^{-4} mbar) to avoid oxidation. **Figure 83** shows the GERO furnace and an example of specimens placed inside the furnace chamber.
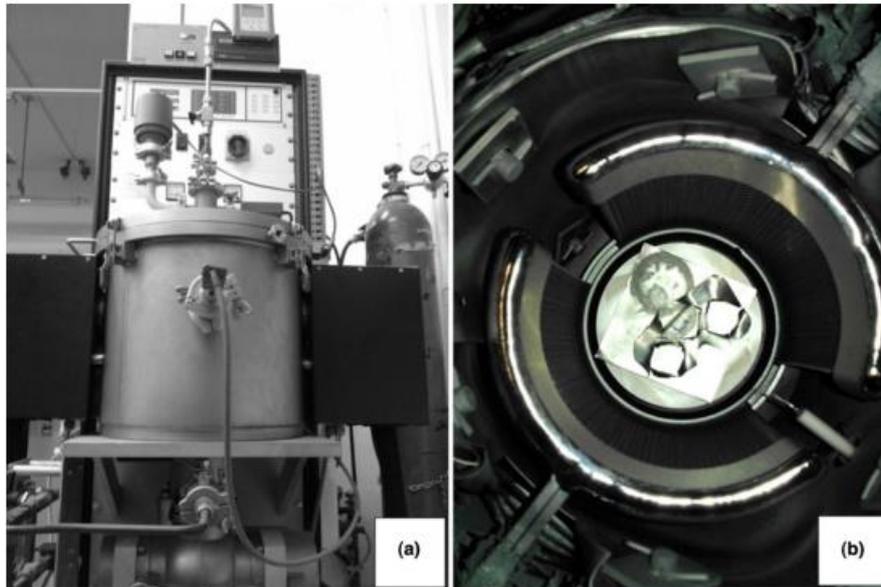
Figure 83: a) GERO furnace exterior; b) furnace chamber.

2.10 Mechanical tests

The following mechanical tests were performed by an external certified laboratory:
- *Tensile Tests* performed according to ASTM E8 (Room Temperature) [162] and ASTM E21 (High Temperature) [163] using an MTS servo-hydraulic test machine.
- *Creep Tests* performed at different temperature and stress conditions according to ASTM E139 standard [164] using an ATS test system.

2.11 Dynamic Elastic modulus determination

The Young's modulus was measured according to ASTM E 1876 [165] using an impulse excitation technique that involves the analysis of the transient natural vibration of the material (IMCE).

Chapter 3

Powders characterization

The powders used for the EBM process of Titanium aluminides are gas atomized, rapidly solidified γ-TiAl-based pre-alloyed powders.

The EBM process and the final products are strictly related to the powders characteristics and for this reason, it is necessary to spend some words about the gas atomization process for the production of TiAl powders. In gas atomization, an inert gas is used to break up a melt stream into metallic powder particles. The different types of atomization techniques used are plasma inert-gas atomization (PIGA), electrode induction melting gas atomization (EIGA), rotating-electrode process (REP), plasma rotating-electrode process (PREP), and rotating-disc atomization. The titanium gas-atomizer process (TGA), is a variation of the PIGA technique involving induction skull melting under vacuum or an inert gas prior to melt atomization [75]. The vacuum inert gas atomization (VIGA) system comprise a Vacuum Induction Melting (VIM) furnace for the melting, refining and degassing of the alloy.

In gas atomization techniques, the molten metal pass through a nozzle where the melt is disintegrated by a jet of high-velocity inert gas. During atomization, the decrease of the surface tension of the liquid metal and the increase of the atomization gas velocity lead to a decrease of the particle size. Subsequently, the atomized melt droplets fall away and thanks to the surface-tension forces the spheroidization of initially irregular shaped droplets appends. The powder characteristics are determined by the melt superheat, the cooling medium and the droplet size. A problem concerning the shape irregularity of powder particles is due

to the fact that the droplet spheroidization takes more time than the solidification. Using optimized technologies such high-pressure gas atomization (HPGA) or vacuum inert gas atomization (VIGA), it is possible to obtain a large fraction of fine and spherical powder particles [166][167]. A schematic representation of the gas atomization process is reported in **Figure 84** [168]. The TiAl powders for the EBM process used by Avio Aero are produced by the VIGA atomization method.
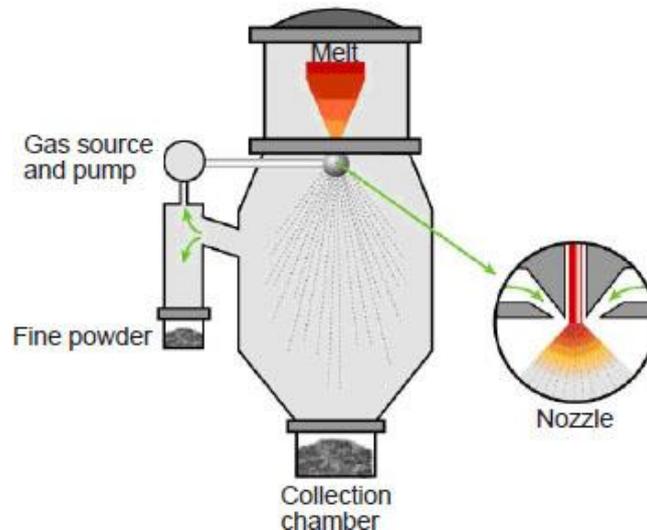
Figure 84 Schematic representation of gas atomization [168].

The atomized-powder characteristics that mainly affect the EBM process are the powder morphology, the flowability, the apparent density and the particle size distribution of the powder. Furthermore, is essential to know chemical composition of the powder in order to obtain the desired chemical composition of the final part processed by EBM. The chemical composition characterization and optimization is fundamental also to obtain the desired microstructure and consequently the best mechanical properties of the part.

3.1 Powders morphological characterization

The morphology of the powders of the different TiAl alloys considered in this research were analyzed in terms of particle shape and internal porosity in order to find any defects and irregularity. It is important to investigate such powder features because they can affect other powder characteristics and the EBM process with dramatic consequences on the final product. In fact, all the powder characteristics are in a certain manner correlated to each other, for example, the flowability of the powder depends on the powder morphology and the particle size distribution.

The technique used to analyze the powder morphology were the scanning electron microscopy (SEM) and the optical microscopy. The SEM analysis is useful to understand the morphology, shape and surface aspect of the powders. **Figure 85** shows the SEM image of a TiAl alloy powder [127].
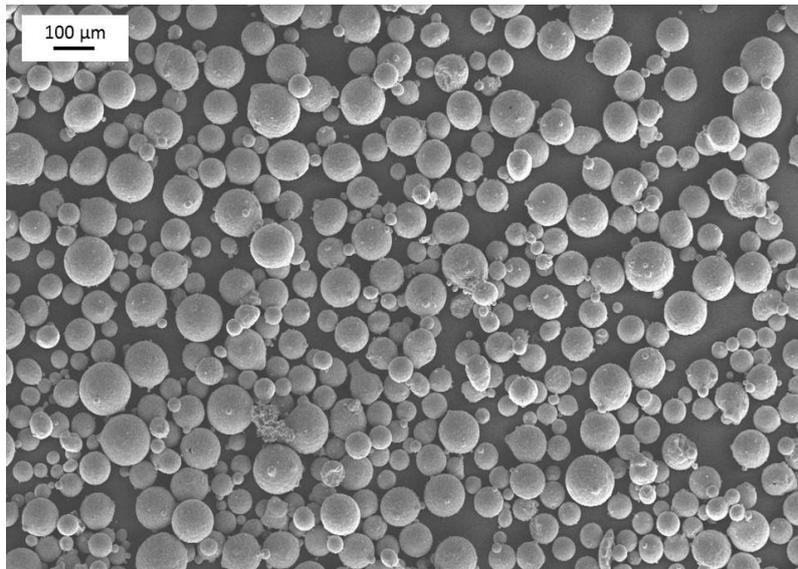
Figure 85 TiAl alloy powder morphology

As it is possible to observe, the powder shows a spherical shape and variable particles size. These features are typical of gas-atomized powders; however, some different types of defects can be detected and analyzed at higher magnifications, as shown in **Figure 86.**
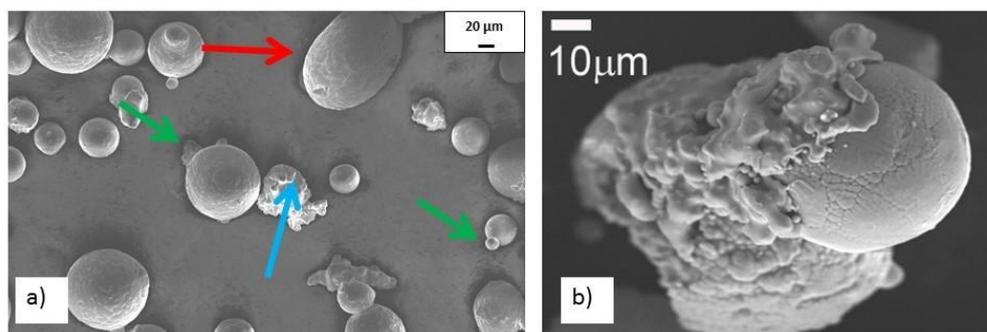
Figure 86 SEM micrographs of TiAl alloy powder indicating typical powder defects

Some elongated particles are observed (red arrow in **Figure 86 a**). The presence of satellites (green arrows in **Figure 86 a)** and agglomerated particles (blue arrow

in **Figure 86 a** and **Figure 86 b)** can also be observed. These defects are due to the impact of powder particles during the atomization process. The low amount of these defects did not affect the EBM process.

A little amount of powder is mounted and polished prior to be observed at different magnifications with an optical microscope in order to detect the possible presence of pores inside the powder particles. In **Figure 87** an example of optical micrograph of a TiAl alloy powder is reported. It is possible to observe that the amount and dimensions of the internal pores are very small (red circle).

This type of small and spherical internal porosity is typical of additive manufacturing techniques that use gas atomized powders. In fact, during the gas atomization process, a small amount of gaseous Ar can remain trapped into the solidified powder particles and in the final EBM processed part it is possible to find some spherical pores whit dimension that are comparable to those of the pores observed inside the powder particles [66].
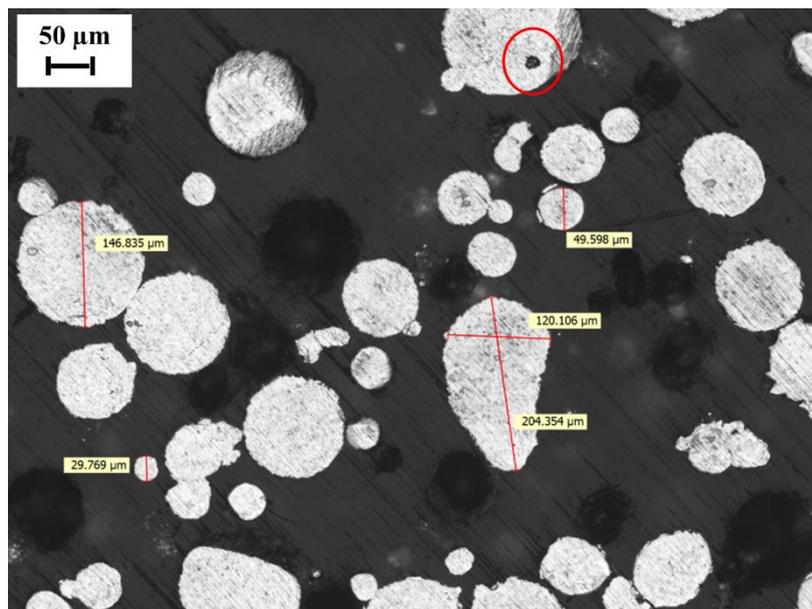
Figure 87 Optical microscopy image of TiAl alloy powder

3.2 Particle size distribution

The particle size distribution is a powder characteristic that has to be optimized in order to ensure a high packing density and a good flowability.

The particle size distribution was measured by sieving method according to the ASTM B214-07. In **Figure 88** is reported the particle size distribution of the different TiAl alloys powers.
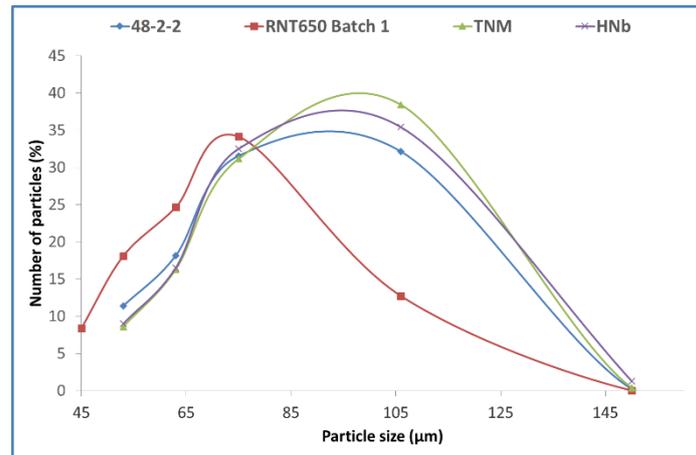
Figure 88: Particle size distribution of the different TiAl alloys powders.

The nominal particle size distribution of the powders is between 45 and 150 µm (-100/+325 mesh). The 48-2-2, TNM and high-niobium alloys powders exhibit a particle size distribution very similar between them. The RNT650 alloy powder presents a higher percent of smaller particles that brings to a lower flowability. In fact, as it will be described in the following part, using an optimized RNT650 powder (batch 2) with a fraction of larger particles added, the flowability has been improved **Figure 89**.
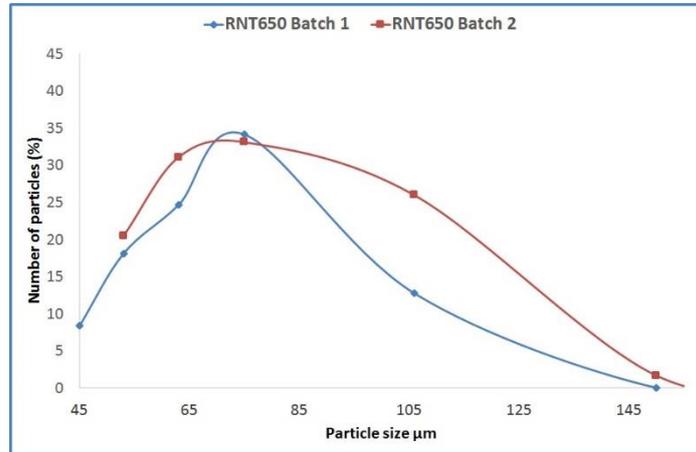
Figure 89: Particle size distribution of RNT650 batch 1 and batch 2.

As it was demonstrated by this study (**Electron Beam Melting of TiAl RNT650 alloy for automotive application**), these particle size distributions led to the successful production of massive materials by EBM.

3.3 Flowability

The flowability of the powder is critical to insure a good layer deposition by the raking system of the EBM machine. In the worst cases, the powder can remain stuck on the rake with consequence on the uniformity of the powder layers. Non-uniform powder layers can lead to the "smoke" phenomena that is highly detrimental for the EBM process.

The flowability of different TiAl alloys powders were measured according to ASTM B213-13 using the Hall flowmeter [157]. The obtained results are reported in **Table 15**.

The flowability is a powder characteristic that deeply depends on the shape regularity of the powder particles and on the particle size distribution. In fact, the presence of smaller particles can increase the friction of powders.

Table 15: Flowability of the different TiAl alloys powders

Powder	Flowability (s)
48-2-2	28 ± 1
HNb	27 ± 1
RNT650 batch 1	31 ± 1
RNT650 batch 2	24 ± 1
TNM	27 ± 1

In some cases, it was necessary to tap on the flowmeter because the powder did not start to flow spontaneously. In **Figure 90** an example of powder that remains partially adherent to the flowmeter walls is shown.

Figure 90: Powder stuck on the flowmeter walls

Regarding the RNT650 powders, the first batch has shown a lower flowability in comparison to the other alloys powders. This can be correlated to the different particle size distribution with a larger amount of finer particles. The optimized powder batch 2 exhibits a better flowability comparable to that of the other alloy powders.

3.4 Powder density

The apparent density of the powders were measured according to ASTM B212-99 [158]. **Table 16** shows the obtained values.

Table 16: Apparent density of the different TiAl alloys powders.

Powder	Apparent density (g/cm^3)
48-2-2	2.22 ± 0.03
HNb	2.31 ± 0.21
RNT650 batch 1	2.20 ± 0.00
RNT650 batch 2	2.23 ± 0.01
TNM	2.29 ± 0.03

The apparent density of the different powders was similar and this is correlated to the similar powder size distribution of the different TiAl powders.

A high powder density means a high density of the processed part and a good packing of the powder layer during the EBM process. A regular spherical shape of the powders and a proper particle size distribution lead to a good packing of the powder particles and high powder density. In fact spherical particles of bigger dimensions are packed with particles of smaller dimension filling the interstitial voids between them during the powders layers distribution in the powder bed additive manufacturing processes [169].

3.5 Chemical composition

The chemical composition was assessed by means of inductively coupled plasma (ICP-OES), inert gas fusion infrared detection technique (IGF) and combustion infrared detection technique.

Aluminum, niobium, molybdenum, silicon and chromium contents were measured using Inductively Coupled Plasma Optical Emission Spectroscopy (ICP-OES) technique according to ASTM E2371 [159]. Carbon content was evaluated by Combustion Infrared Detection Technique according to ASTM E1941, while for nitrogen and oxygen, the Inert Gas Fusion (IGF) method was used according ASTM E1409 [161].

The chemical composition analysis on the powders is fundamental in order to verify the correct nominal elemental composition on the starting material and for guarantee that the concentration of certain contaminants elements and impurities are below the specification limits for the powders.

The nominal composition for a certain alloy powder is defined considering an admitted concentration range (in at.%) for aluminum and for the different alloying elements. The nominal composition of the powder is established and optimized keeping into account of the chemical composition variations that often append during the EBM process. Due to the high temperature and the vacuum environment of the process, an evaporation of lightweight and low-melting elements is observed during the EBM. In particular, aluminum is subjected to evaporation during the EBM process and its content in the powder has to be optimized [17].

The hot vacuum environment of the EBM presents also several advantages, one of which is the degassing of impurities during the process that allows to reduce or maintain constant the presence of such impurities like oxygen that are source of defects for TiAl alloys. In section 4.1 Chemical analysis the comparison between the chemical composition of the powders and processed alloys is described [75][170].

In **Table 17** the composition of the powders chemical composition is reported. Inductively Coupled Plasma analysis (ICP-OES) was used for aluminum, chromium, niobium, molybdenum silicon; inert gas fusion infrared or thermal conductivity detection technique was used for oxygen, nitrogen and carbon.

Table 17: Elemental chemical composition of the powders.

		Chemical composition in wt.% and at.%								
		Al	Cr	Nb	Mo	Si	O	N	C	Ti
48-2-2	wt.%	34.10	2.37	4.78			0.084	0.004	0.006	Bal.
	at.%	48.83	1,76	1,99						
HNb	wt.%	31.3	2.20	17.2			0.04			
	at.%	47.99	1.75	7.66						
RNT650	wt.%	34.5	1.04	4.83		0.25	0.05	0.003	0.005	
	at.%	49.18	0.77	2		0.34	0.101	0.003	0.005	
TNM	wt.%	30.3		8.81	2.49					
	at.%	45,58		3.85	1,05					

It is worth noting that the impurities pick-up during the gas atomization process was very limited: the oxygen concentration in the powders is below the 0.1 wt. % and it is acceptable for the starting material powders.

Chapter 4

Powder recyclability investigation on Ti-48Al-2Cr-2Nb alloy

The possibility to re-use the unmelted powder instead of new powder is one of the main factor that makes the EBM extremely convenient in terms of material saving.

The study about the powder recyclability was done in collaboration with AvioAero within the EU project E-BREAK.

The EBM process begins with the preheating of the layer of powder using a moderately low beam current and a relatively high scan speed. The preheating step lightly sinters the metal powder to hold it in place during subsequent melting at higher beam powers. It also helps to reduce the thermal gradient between the melted layer and the rest of the part.

Afterward, the electron beam scans the powder surface according to the layered CAD data and melts the powder particles to a compact layer with the desired shape. Once the first layer has been melted, the build platform is lowered by one layer thickness, additional powder is spread over the below solidified layer and the process will be repeated. After the manufacturing stage, the part is cooled down either under vacuum or helium flow.

After the process, the partially-sintered particles are then removed from the part surface with a sand blasting operation. The finishing is achieved in the Powder Recovery System (PRS) using the same powder involved in the EBM process, in order to prevent contamination. The powder that is recovered from the PRS can be

sieved and mixed with new powder, in order to obtain recycled powder to be used in the following EBM cycle.

In order to evaluate the powder aging and recyclability after several EBM process, the following sampling procedure was developed:

1   six subsequent jobs with five specimens per job;
2   for the first job only new powder was used;
3   from the second to the sixth builds, recycled powder was used.

The recycled powder was obtained mixing unused powder left in the hoppers by the previous cycle, sintered powder recovered around specimens produced during the previous cycle and new powder to reach the total amount of powder needed.

At the end of the six building cycles, eight powder samples were analyzed **Table 18.** The sampling method is reported in **Figure 91**.

Table 18: Powder samples for analysis.

Sampling moment	Sample
Before 1st build (used to build A samples)	New powder
After 1st build	Sintered powder
After 1st build (used to build B samples)	Powder Recycled 1
After 2nd build (used to build C samples)	Powder Recycled 2
After 3rd build (used to build D samples)	Powder Recycled 3
After 4th build (used to build E samples)	Powder Recycled 4
After 5th build (used to build F samples)	Powder Recycled 5
After 6th build	Powder Recycled 6
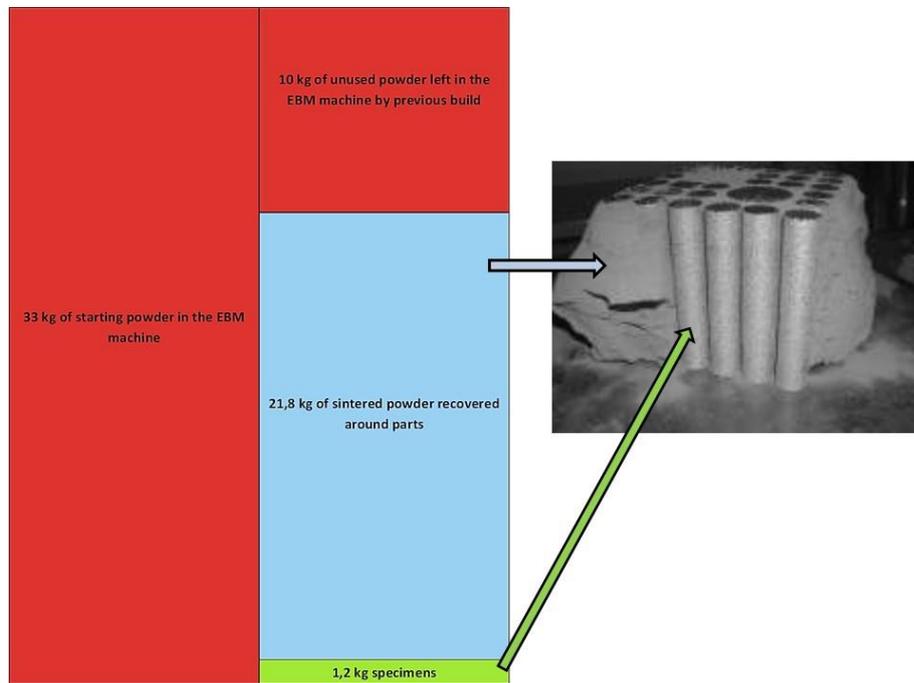
Figure 91: Powder sampling scheme.

4.1 Chemical analysis

In order to evaluate any variations of chemical composition during the different EBM cycles, in the powders and in the massive specimens produced with recycled powder, elemental chemical analysis was performed on different solid and powder samples. In particular, this type of analysis is useful to highlight any pick-up of contaminants, such as oxygen and carbon, during the powder handling and recycling cycles.

Aluminum, niobium and chromium contents were measured using Inductively Coupled Plasma Optical Emission Spectroscopy (ICP-OES) technique according to ASTM 2371. Carbon content was evaluated by Combustion Infrared Detection Technique according to ASTM E1941 while for nitrogen and oxygen, the Inert Gas Fusion (IGF) method was used according ASTM E1409. The analysis results for both powders and massive specimens are reported in **Table 19**. For Al, Cr and Nb the variation % respect to the new powder is reported instead of the chemical composition in wt.% because these data are confidential and Avio Aero property.

The chemical analysis was performed on new powder in order to obtain a chemical composition baseline, on the powder recovered around the specimens after the first job (sintered powder), on the powder recycled 1 obtained mixing

sintered powder with new powder and on powder progressively recycled six times in order to evaluate the chemical composition variations into the powder after several recycling cycles.

Table 19: Chemical analysis results for powder samples reused for different subsequent EBM builds.

	Sample	Al	Cr	Nb	O	N	C	Ti
		Composition variation % respect to the new powder			Chemical composition in wt.%			
1	**New powder**	-	-	-	0.082	0.003	0.007	
2	**Sintered powder**	0.59	-1.17	-0.82	0.077	0.002	0.007	
3	**Powder Recycled 1**	0.88	-1.17	-0.62	0.073	0.001	0.006	
4	**Powder Recycled 3**	0.59	0.39	0.41	0.083	0.002	0.006	Bal.
5	**Powder Recycled 5**	0.89	1.17	-0.21	0.100	0.005	0.005	
6	**Powder Recycled 6**	0.59	0.39	0.83	0.090	0.003	0.008	
	Uncertainties related to the test method	0.88 % 0.3 wt.%	3.12 % 0.08 wt.%	3.12 % 0.1 wt.%	0.01 wt.%	0.001 wt.%	0.001 wt.%	

Figure 92 shows the aluminum variation % for new, sintered and recycled powders.
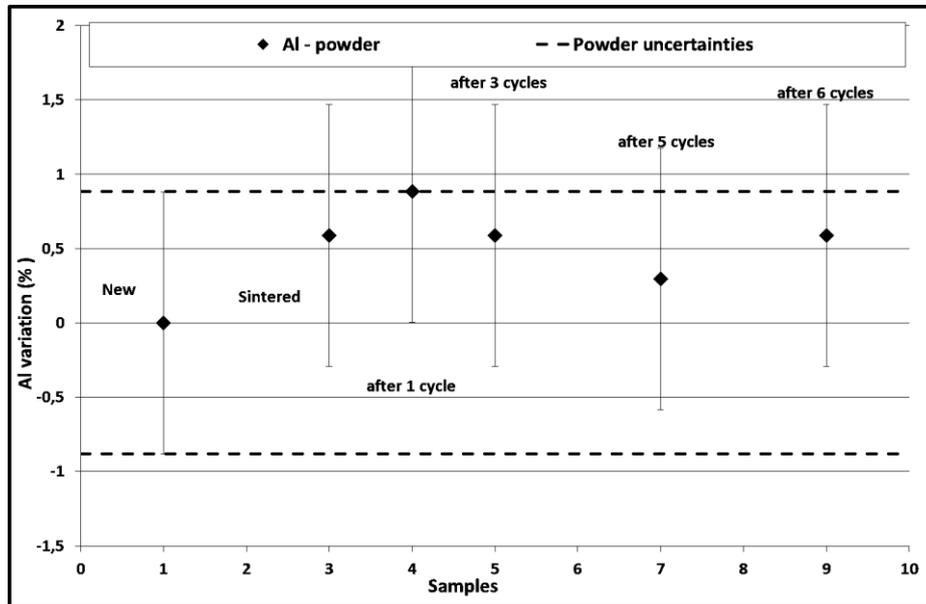
Figure 92: Aluminum variation % of powder samples; for each point the uncertainties related to the test method are reported.

It is important to point out that the hot vacuum environment may induce the evaporation of low-melting lightweight elements such aluminum.

This evaporation is governed by four distinct regimes [17][67]:

-   Mass transport of atoms from the inner of the melt to its surface;
-   Phase change to gaseous state at the surface;
-   Mass transport in the gas phase above the melt;
-   Condensation.

As it is possible to notice from the chemical analysis results above, the aluminum content of powder specimens is between the test method uncertainties lines referred to the new powder. This means that aluminum evaporation is not observed in the sintered and recycled powder.

It is also important to notice that the pick-up of contaminants such as oxygen, nitrogen and carbon by the sintered and recycled powders during the powder handling and EBM process is very limited thanks to the high vacuum environment of EBM.

However, during the recycling process of the metal powder, a slight impurities contamination can be observed. The oxygen contamination was very low and, from the chemical analysis, the maximum pick-up observed resulted to be about 0.02 wt.% $\pm$ 0.001 from the new powder and after 5 reuse (after 5 cycles) (**Figure 93**).
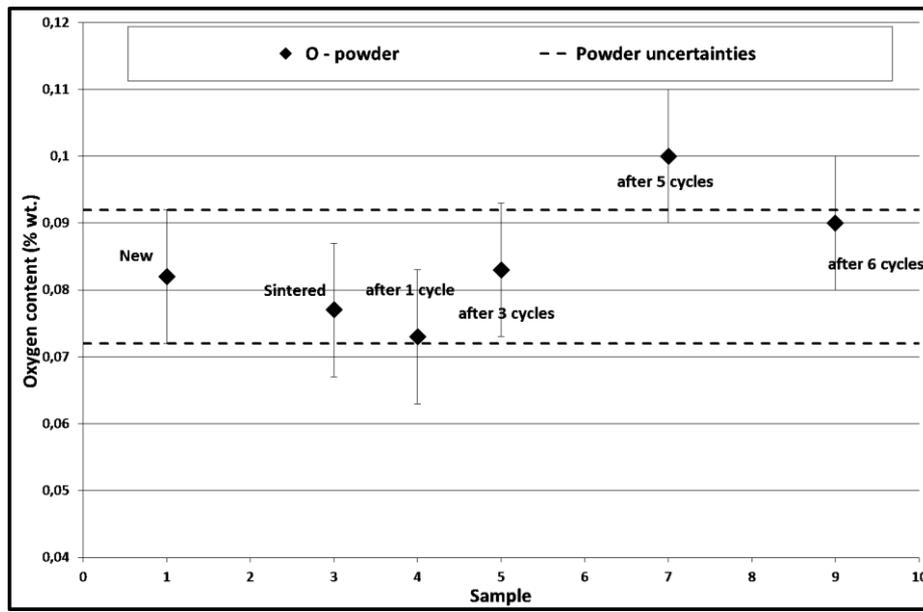
Figure 93: Oxygen content measured on powder samples; for each point, the uncertainties related to the test method are reported.

The nitrogen content seems to follow the same trend as the oxygen content. However, the nitrogen pick-up for each cycle is lower than oxygen. The maximum contamination in the powders was about 0.002 wt.% $\pm$ 0.001 during each EBM cycle (**Figure 94)**
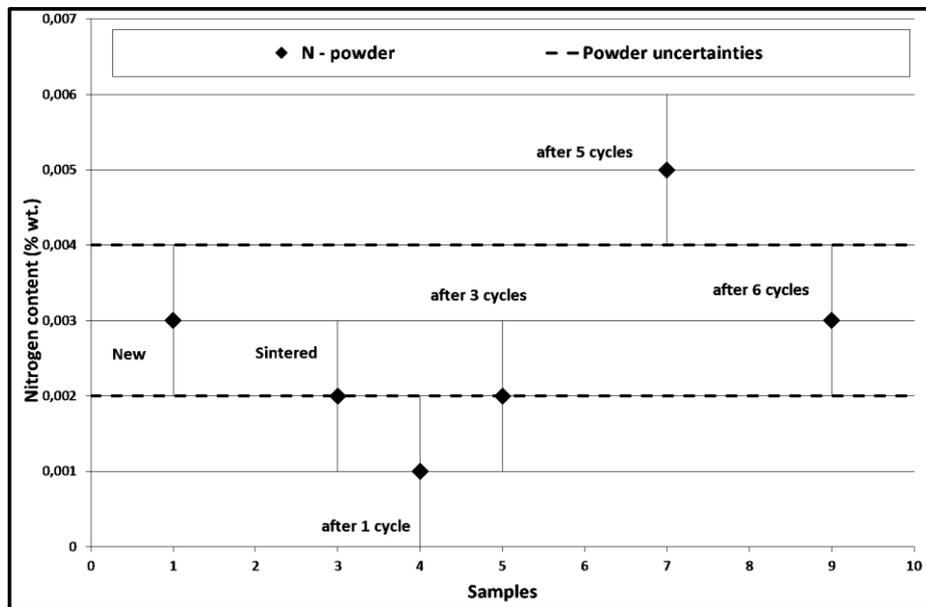
Figure 94: Nitrogen content measured on powder samples; for each point the uncertainties related to the test method are reported.

The variation in carbon content is reported in **Figure 95** and, also in this case, the contamination is very limited.
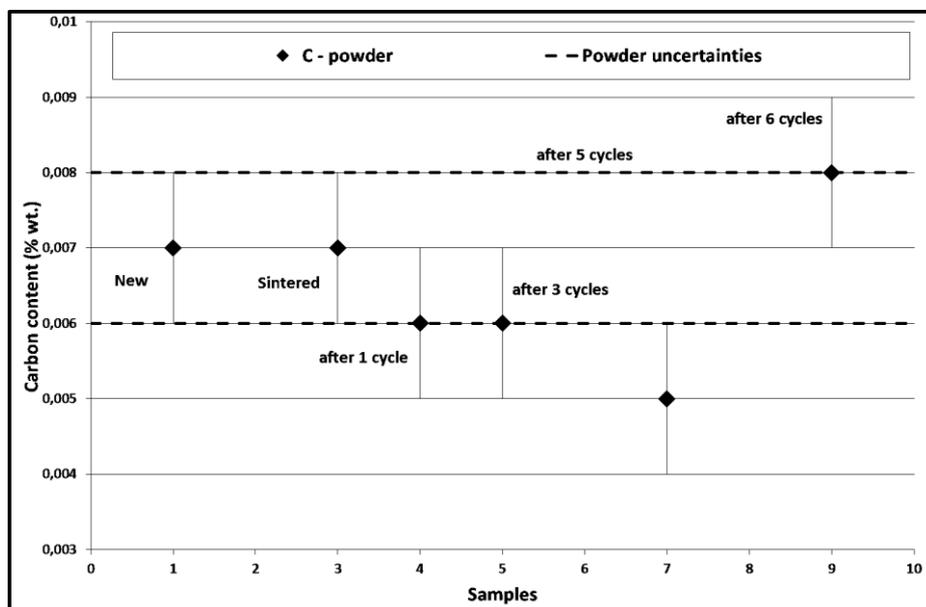
Figure 95: Carbon content measured on powder samples; for each point, the uncertainties related to the test method are reported.

The amount of the other alloying elements remains constant during the recycling cycles (**Figure 96** and **Figure 97**).
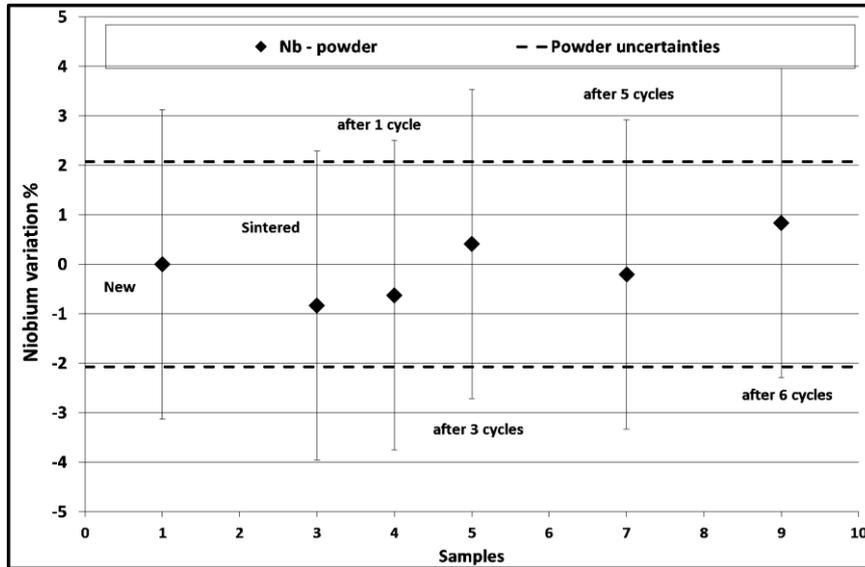
Figure 96: Niobium variation % measured on powder samples; for each point, the uncertainties related to the test method are reported.
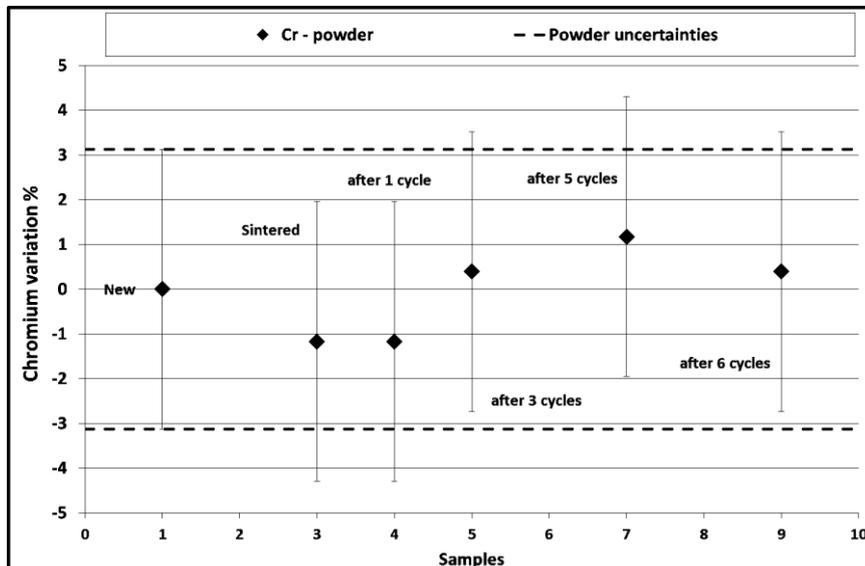
Figure 97: Chromium variation % measured on powder samples; for each point, the uncertainties related to the test method are reported.

In **Table 20** the chemical composition comparison between a specimen produced by EBM using new powder (specimen A) and a specimen produced using powder recycled six times (specimen F) is reported.

Table 20: Elemental chemical composition comparison between a specimen produced with new powder and a specimen produced with powder recycled six times.

	Sample	Al	Cr	Nb	O	N	C	Ti
		Chemical composition in wt.%						
1	**Specimen A**	32.9	2.52	4.83	0.083	0.006	0.014	Bal.
2	**Specimen F**	33.2	2.53	4.80	0.091	0.005	0.013	
	Uncertainties related to the test method	0.3	0.08	0.1	0.01	0.001	0.001	

It is interesting to observe that the chemical composition of the specimen produced with a powder after six recycles is comparable with that of the specimen produced with new powder both in terms of aluminum and impurities amount. It is possible to asses that the production of parts using TiAl powders recycled several times does not brings to a significant pick-up of contaminants because of the cleanliness of the process environment. Moreover, the aluminum content in specimen F remains acceptable because the EBM process does not produces an aluminum evaporation in the powders, in fact, the aluminum amounts of the new powder and the recycled powder used to produce these two specimen are comparable (**Table 19**). Furthermore, a limited aluminum loss, from the powder to the specimen, takes place during the EBM process. This has to be take into account in order to choose powders enriched in aluminum in order to obtain specimens with an aluminum content that fulfill the desired nominal composition.

4.2 Particle size distribution

The particle size distributions of new powder, sintered powder and powder recycled after six EBM cycles were measured according to the ASTM B214.

In **Figure 98** the cumulative size distribution comparison between the new powder, the powder removed by the machine chamber after the first EBM cycle (sintered powder) and the powder obtained mixing sintered powder with new powder (1) is reported. Sintered powder slightly lose some finer particles. However, when new powder and sintered powder are mixed and recycled after different EBM cycles, it is possible to obtain an intermediate powder.
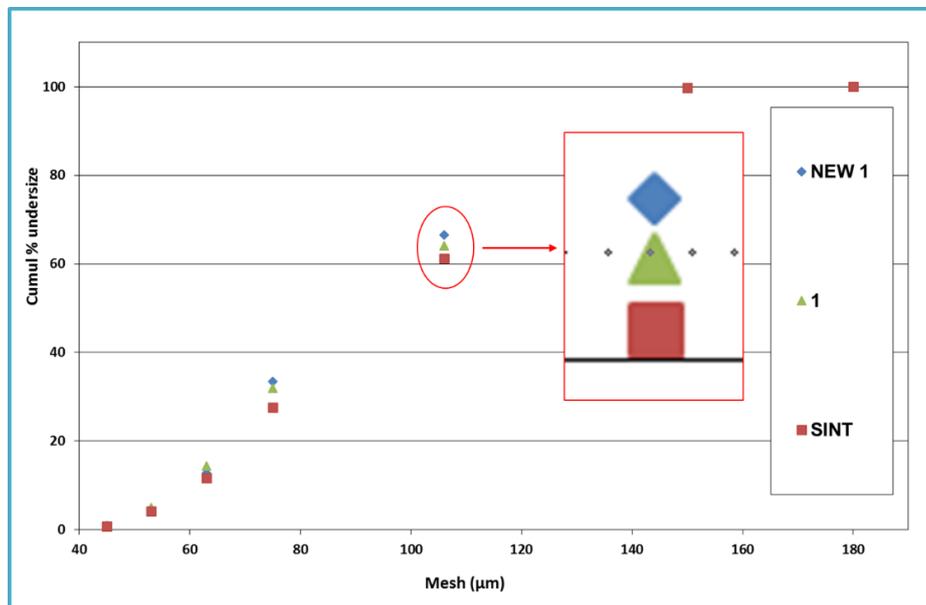
Figure 98: Cumulative particle size distribution.

It is possible to observe a slightly decrease in finer particles amount for the sintered powder. The analysis on the recycled powders shows a particle size distribution that is between the new powder and the sintered one (see detail in **Figure 98**).

In **Figure 99** it is possible to observe that also the particle size distribution of the powders recycled different times is between the new and sintered powders.
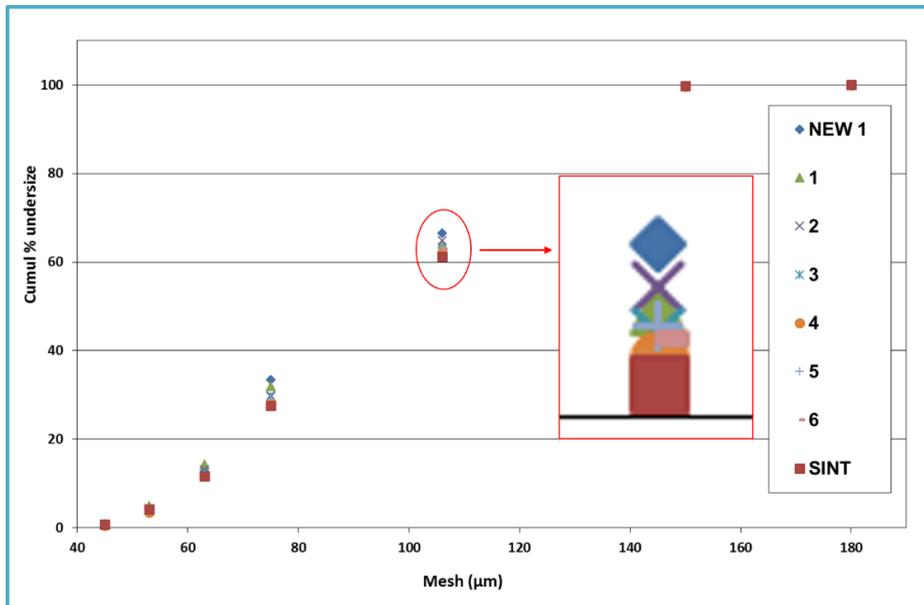
Figure 99: cumulative particle size distribution.

The histogram in **Figure 100** shows the percentage of different powders passing through the different sieves with decreasing mesh. Also from this image, it is evident that there is only a slight variation in particle size distribution between the new, sintered and recycled powders.
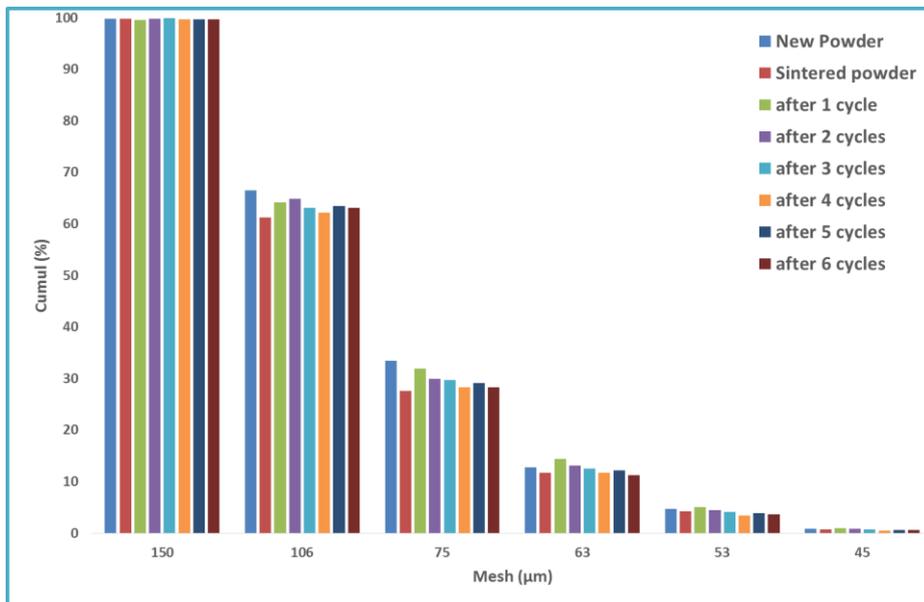
Figure 100: particle size distribution measured on different powder samples.

4.3 Flowability

The flowability of new powder, sintered powder and recycled powders after each of the six EBM cycles was measured according to ASTM B213. The sintered powder and all the recycled powders have a flowability comparable to the new powder. Moreover, the measured values are always in the average of new powder ± the measurement uncertainty. It is therefore possible to assess that the loss of a small amount of finer particles in sintered powder can be considered negligible.

Table 21: flowability measured on different powder samples.

Sample	flowability
	[sec]
New powder	28
Sintered powder	29
Powder Recycled 1	28
Powder Recycled 2	27
Powder Recycled 3	28
Powder Recycled 4	29
Powder Recycled 5	29
Powder Recycled 6	28
Uncertainty related to the test method	±1

4.4 Apparent density

The apparent density of new powder, sintered powder and recycled powders after each of the six EBM cycles was measured according to ASTM B212. Similarly to what found for the flowability, apparent density seems not be affected by the loss of small amount of finer particles; all the values stay in the range of standard deviation.

Table 22: Apparent density measured on different powder samples.

Sample	apparent density [g/cm^3]
New powder	2.23
Sintered powder	2.24
Powder Recycled 1	2.25
Powder Recycled 2	2.21
Powder Recycled 3	2.23
Powder Recycled 4	2.25
Powder Recycled 5	2.24
Powder Recycled 6	2.24
Uncertainty related to the test method	±0.02

4.5 Conclusion on powder recyclability study

In conclusion, analysis performed on powders in different recycling condition and used for several EBM cycles confirm that, for what concerns particle size distribution, flowability and apparent density, the adopted recycling process does not change the powder properties. Regarding the chemistry, it is evident that the recycling process generate a slight oxygen pick-up. The oxygen contamination was very low and, from the chemical analysis, the maximum pick-up observed resulted to be about 0.02 wt.% ± 0.001. The progressive increase of oxygen is very limited, but it has to be kept under control, especially at the time of supply of the metal powders for the EBM process, so that the final manufactured part meets the specifications requirements.

Another interesting point highlighted by the chemical analysis on specimens is that the vacuum environment of the EBM process may induce the evaporation of lightweight elements, such as aluminum. However, the aluminum loss is very limited during the EBM process. The evaporation effect is also evident in a minor amount for the other alloying elements, but for them can be negligible. Moreover, this evaporation is only observed in the manufactured parts but not in the sintered powder, which can then be recycled and reused for several subsequent EBM builds. This work has demonstrated that it is possible to reuse the EBM powder, by mixing it with new one, up to 6 EBM manufacturing cycles. Moreover, it is possible to asses that the powder reuse could be done for more than 6 cycles because, from the obtained results, the powder characteristics seem to reach a stability after a certain number of reuses.

Chapter 5

Effect of the EBM process parameters on the material

This part of the work, done in collaboration with AvioAero within the European Project E-BREAK, had the purpose to investigate the effect of the different EBM process parameters on the titanium aluminide material produced with this additive manufacturing technique. In particular, the aim of the study was to understand how the microstructure, chemical composition and material quality in terms of residual porosity of the material are affected by the variation and the combination of certain process parameters.

Sixteen specimens having form of parallelepipeds with a square base of 10x10 mm and 100 mm length were produced by AvioAereo (**Figure 101**).
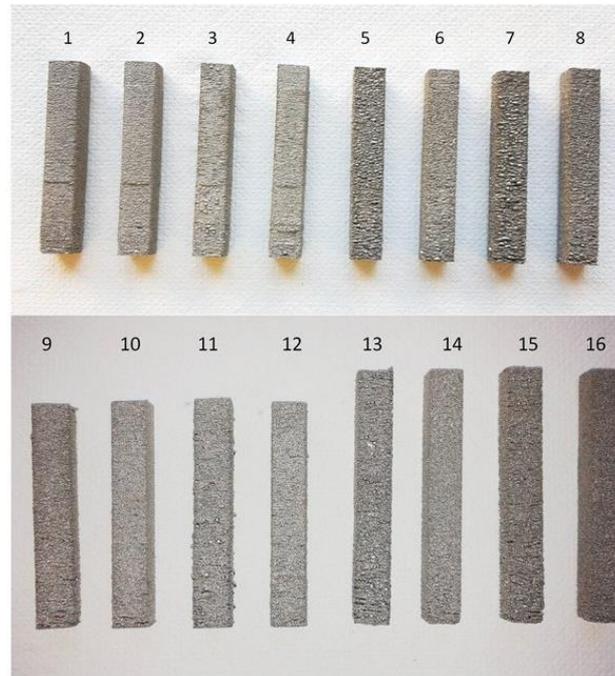
Figure 101: the 16 TiAl specimens produced by EBM.

The specimens have shown a rough external surface that is typical of the EBM process. For some specimens this surface roughness is more pronounced and with the presence of some evident defects due to a lack of fusion.

All these specimens were produced by EBM in one building job starting from a 48Al-2Cr-2Nb titanium aluminide alloy powder (**Figure 102 a)**. The building direction of the specimens (Z direction) were the longer side (100 mm) (**Figure 102 b)**.
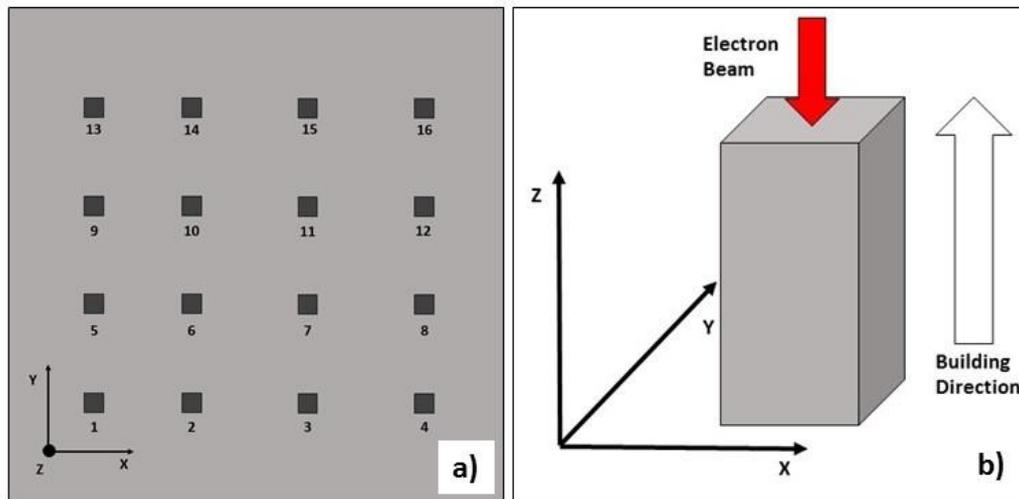
Figure 102: Representation of the EBM building job (a); specimens building scheme (b)

During the job, the specimens were produced using a different combination of process parameters for each single specimen. In particular, the 16 combinations were obtained varying between two values the speed function, the line offset, the beam current and the focus offset following a DOE (Design Of Experiment). The others building parameters were kept fixed on optimized values.

Table 23 shows the combination of the EBM building parameters associated to each specimen. The numerical values of the used parameters are confidential only and therefore replaced with letters for which is indicated which is the larger and which is the smaller.

A<B

C<D

E<F

Table 23: building parameters.

Specimen	Speed Function	Line offset	Max Beam Current	Focus offset
1	A	C	E	-
2	A	C	E	+
3	A	C	F	-
4	A	C	F	+
5	A	D	E	-
6	A	D	E	+
7	A	D	F	-
8	A	D	F	+
9	B	C	E	-
10	B	C	E	+
11	B	C	F	-
12	B	C	F	+
13	B	D	E	-
14	B	D	E	+
15	B	D	F	-
16	B	D	F	+

The speed function controls the translational speed of the electron beam during the part fabrication [148].

Line offset refers to the distance between two hatch lines.

Max beam current is the maximum current of the electron beam and it is expressed in mA.

Focus offset is the additional current running through the respective electromagnetic coil and it is reflected into an offset of the focal plane from its zero position and thus a change in beam area. A larger beam diameter during the EBM process leads to an increased beam spot but a lower energy concentration [171] [172].

The specimens produced varying the parameters were then characterized in terms of residual porosity, chemical composition and microstructure. X-Ray diffraction analysis was performed to investigate the difference in phase ratio between the samples. The specimens were then subjected to a heat treatment at 1260°C for 4 hours in order to examine the evolution of the microstructure. The final aim of this study is to allow the production of a component varying the process parameters in the different zones of the component that are subjected to different mechanical stresses, and then apply a unique heat treatment to obtain the proper microstructure for each different zone.

5.1 Porosity analysis

Residual porosity analysis was performed on the as EBM samples and on the heat-treated samples according to ASTM E 2109-01.

The aim of this analysis is to determine the degree of porosity of each sample and then correlate it to the building parameters used for its production; the goal is to detect the combination of parameters that gives the lowest residual porosity. The limit for the residual porosity is a material with less than 1% of porosity and pores dimension lower than 100 µm.

The degree of porosity calculated for each sample is reported in **Table 24**.

Table 24: Porosity % and standard deviations of the analyzed specimens.

Sample	Porosity %	Standard deviation
1	0.31	0.002
2	0.26	0.001
3	0.32	0.001
4	0.11	0.001
5	0.29	0.003
6	0.28	0.001
7	0.17	0.001
8	0.08	0.001
9	1.03	0.012
10	0.53	0.002
11	0.88	0.014
12	0.31	0.001

As it can be noticed from **Figure 103**, an increase of the porosity from the first eight samples to the successive.
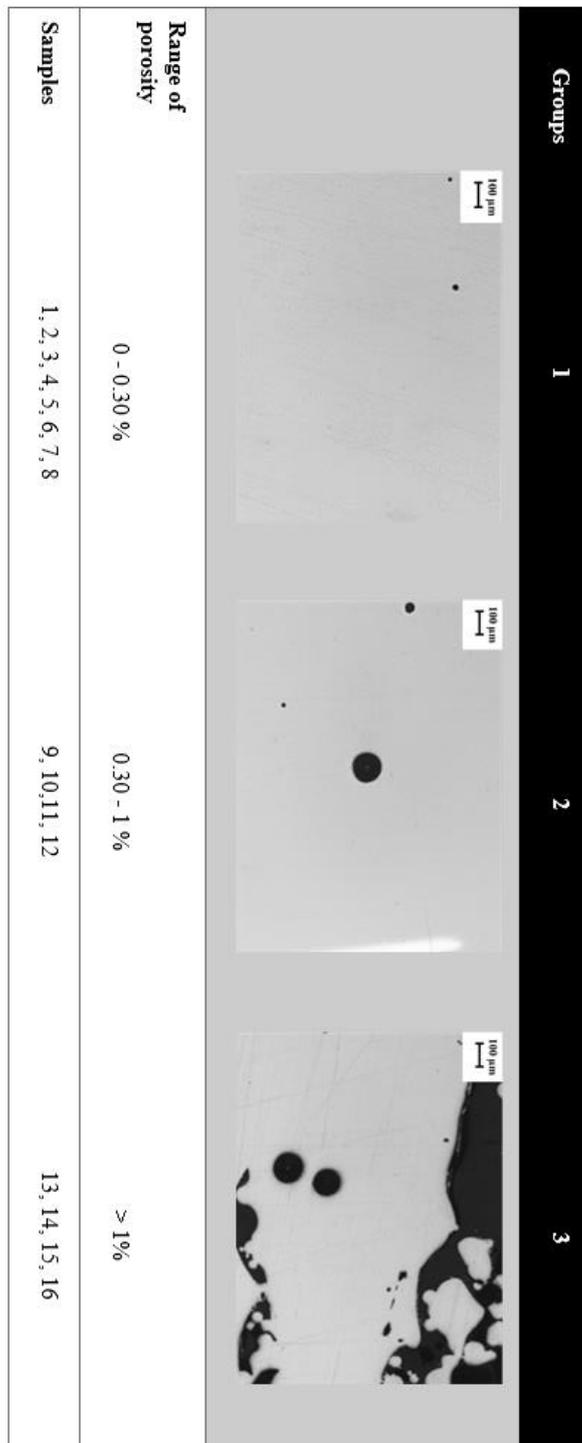
Figure 103: Specimens grouped according to their porosity.

By observing the porosity analysis results and the histogram in **Figure 104**, is possible to group the specimens into three according to the increase of the porosity.
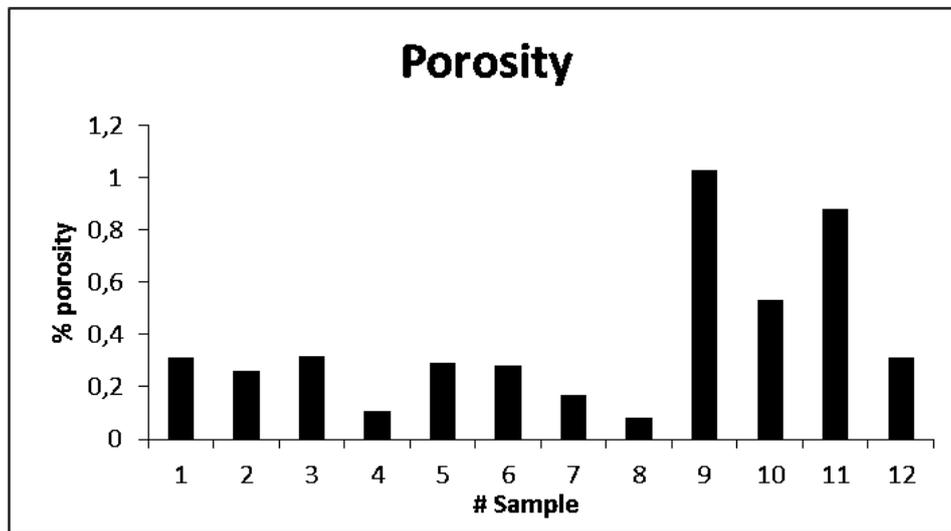
Figure 104: Porosity % of the samples from 1 to 12.

From the obtained values, it is evident that the best combination of building parameters are those applied for samples of the first group, with a residual porosity between 0 and 0.3%. This group includes most of the produced samples (from 1 to 8).

A second group consists of the samples from 9 to 12 that present a residual porosity that is still too high between 0.3 and 1%.

For these first two groups, the observed pores are mainly small and spherical. This type of porosity is due to defects already present in the powder particles that are caused by gaseous argon entrapped during the atomization process [173][66].

A third group consists of samples from 13 to 16. For these samples, the residual porosity values are not reported because of the impossibility to determine it due to the too high porosity level **Figure 105**.

Figure 105: specimens from 13 to 16 with a high defects amount

The bigger and irregular pores observed in this group of specimens, are orientated along the powder layers direction (X, Y direction), and are due to non-optimized EBM process parameters.

This suggest that the combination of high speed function and a high line offset [B/D] (first and second column in **Table 23**) is detrimental for the material gives the higher number of defects. In fact, an excessive speed of the beam does not allow the complete melting of the material and can lead to the formation of leak of fusion type defects.

Even if the speed function was also high for the second group of specimens from 9 to 12, they presented a lower amount of porosity due to the lower line offset. In fact, the combination of high speed function and low line offset is not so detrimental as the combination described before.

Furthermore, it is noticeable a decrease of porosity for samples in multiples of four. According to **Figure 104** and **Table 24**, these positions coincide to a low speed function and positive focus offset (combination [A/+] in **Table 23**)

A porosity level below the 1% and composed by only small and spherical pores can be considered acceptable because does not affect the material properties. By the other hand, the presence of a large amount of big and irregular defects can decrease the material properties and therefore cannot be acceptable.

5.2 Microstructure analysis

The microstructure was analysed for each sample in order to correlate it with the different combinations of building parameters and possibly with other analysis carried out on the material such as the DRX analysis.

Microstructure images at different magnification were taken both for the post-EBM samples that for those after the heat treatment. The resulting images have shown different microstructures grouped into two classes: some specimens exhibit a microstructure different from the others and different from the expected as-EBM microstructure.

The specimens were sectioned along the building direction, polished up to 4000 grit, etched with Kroll's solution and then observed at different magnification using optical microscopy. A macro observation was also useful to better understand the overall microstructure and its homogeneity.

5.2.1 As-EBM microstructures

By the comparison of the different macro images of the specimens microstructures (**Figure 106**), it is possible to observe a particular microstructural trend: from the samples 1 to 4 the microstructure tends to become progressively more similar to the fine γ microstructure observed in the samples from 5 to 12. By this image is also evident the high amount of porosity for specimens from 9 to 16.
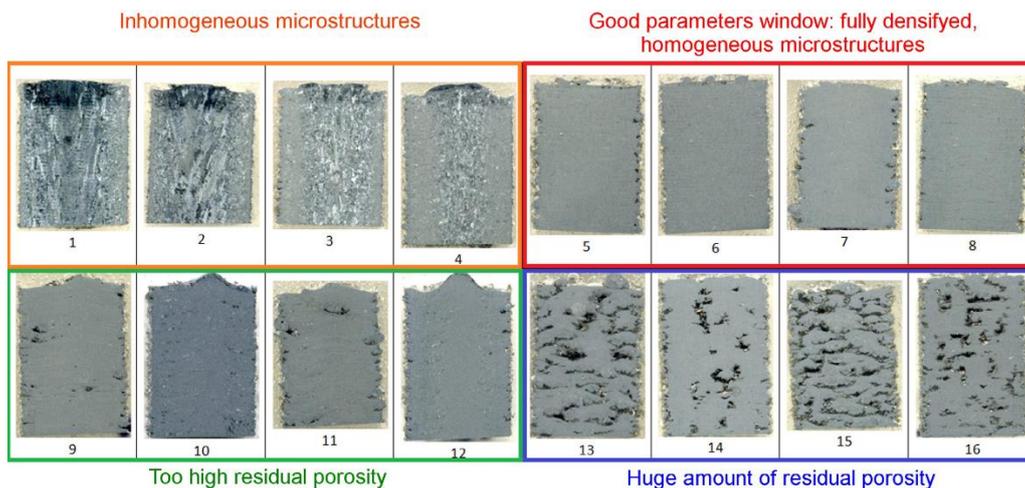
Figure 106: Microstructure of As-EBM specimens. Macro overview

By observing in detail the microstructures from optical micrographs, it is possible to notice that the samples from 5 to 12 showed the expected microstructure

for the As-EBM material (**Figure 107** and **Figure 108**). These samples exhibit a homogeneous equiaxed microstructure composed by equiaxed γ grains (less than 10 µm) [17]. The white arrow in **Figure 107** indicates the building direction of the specimen and it is the same for all the other images.
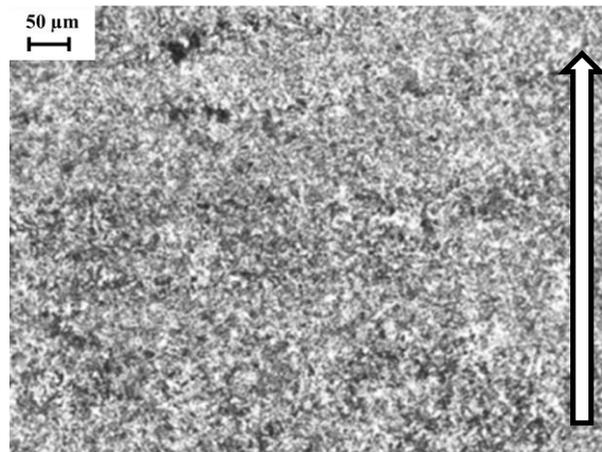
Figure 107: Microstructure of sample 8. Optical microscopy image.

From the higher magnification image in **Figure 108** it is possible to notice the presence of both fine and coarser equiaxed γ grains

Figure 108: Microstructure of sample 8. Optical microscopy image.

The samples from 1 to 4 showed different microstructures and in each samples, a microstructural variation from the lateral edges to the core was observed.

Sample 1 exhibit a completely lamellar microstructure in the centre with grains having variable dimensions (less than 50 µm). **Figure 109** and **Figure 110** show the core microstructure of the sample 1 at different magnifications.
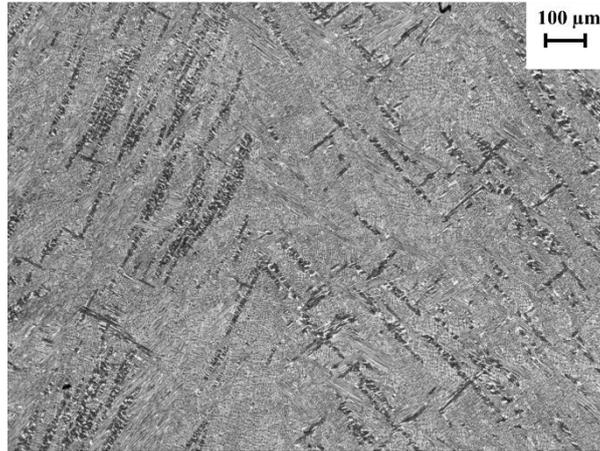
Figure 109: Core microstructure of sample 1. Optical microscopy image.
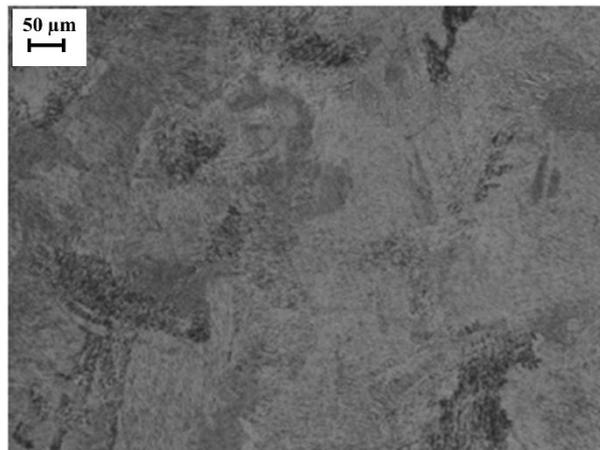
Figure 110: Core microstructure of sample 1. Optical microscopy image.

Sample 1 exhibits a different microstructure in the edge areas where an equiaxed microstructure can be observed (**Figure 111** and **Figure 112**).
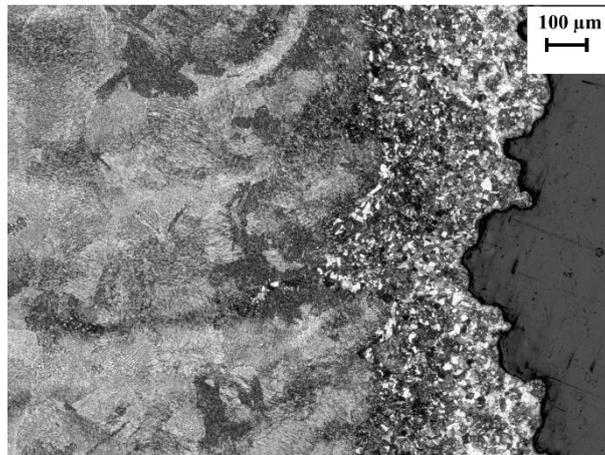
Figure 111: Edge microstructure of sample 1. Optical microscopy image.
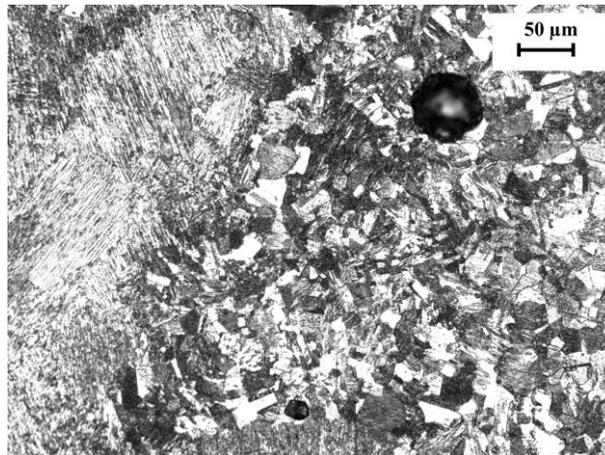
Figure 112: Edge microstructure of sample 1. Optical microscopy image.

Figure 113 shows the microstructural variation in sample 1 through the specimen section.
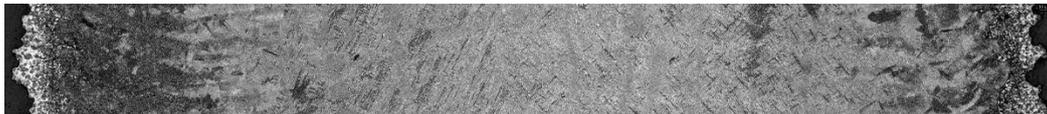
Figure 113: Cross-section of specimen 1.

Sample 2 has a completely lamellar microstructure in the core similar to sample 1 but with bigger lamellar colonies.

Figure 114 and **Figure 115** show the core microstructure of the sample 2 at different magnifications.
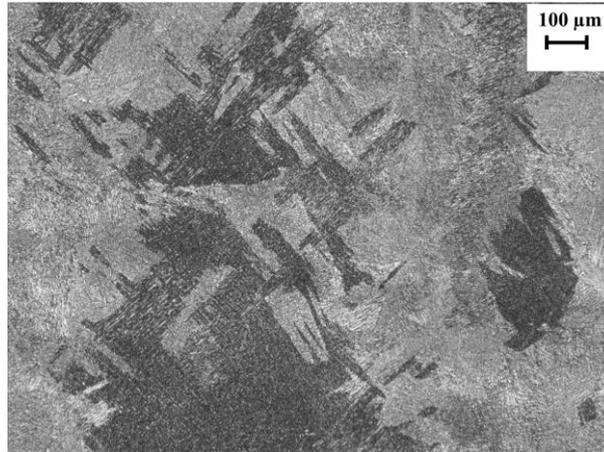
Figure 114: Core microstructure of sample 2. Optical microscopy image.
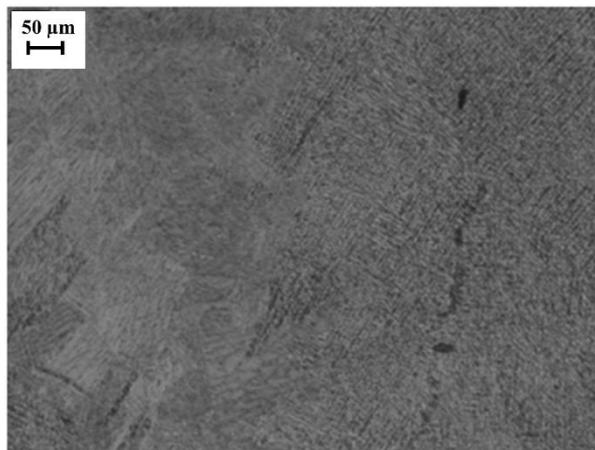
Figure 115: Core microstructure of sample 2. Optical microscopy image.

The variation from the core lamellar microstructure to the equiaxed one in the specimen edges is evident from **Figure 116** and **Figure 117**. The equiaxed area is extended for about 100 µm from the edge to the center of the sample.
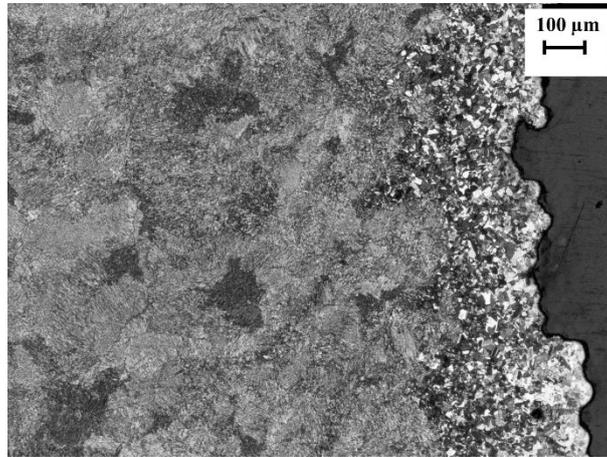
Figure 116: Edge microstructure of sample 2. Optical microscopy image.
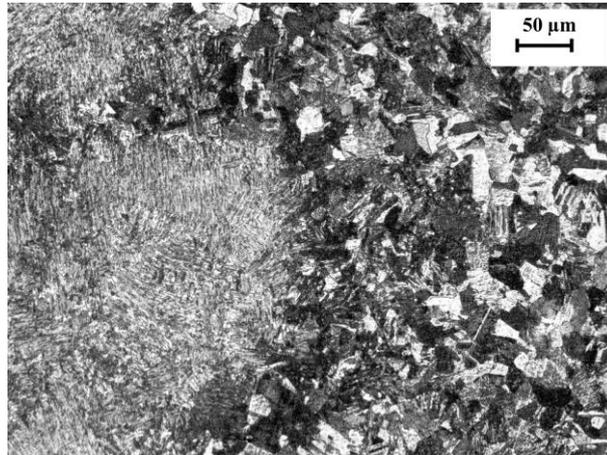
Figure 117: Edge microstructure of sample 2. Optical microscopy image.

Also for this specimen, the cross-section image in **Figure 118** highlights this microstructural variation.
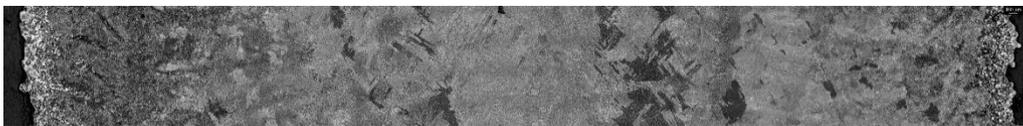
Figure 118: Cross-section of specimen 2.

Sample 3 exhibits smaller lamellar grains with some colonies of γ grains distributed along the layer deposition direction (yellow circles in **Figure 120**). An equiaxed microstructure is observed along the edges of the specimen (**Figure 121, Figure 122**).
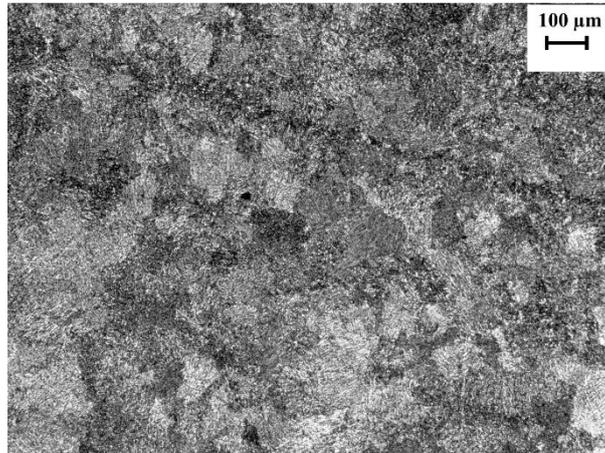
Figure 119: Core microstructure of sample 3. Optical microscopy image.
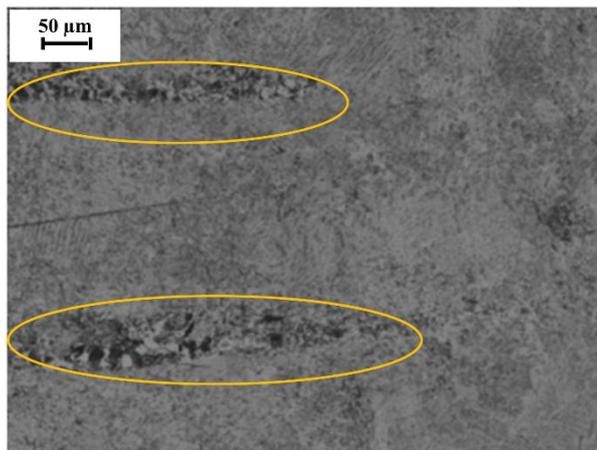
Figure 120: Core microstructure of sample 3. Optical microscopy image.
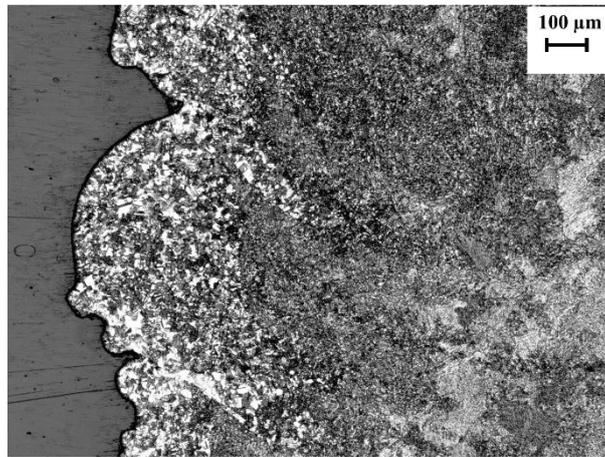
Figure 121: Edge microstructure of sample 3. Optical microscopy image.
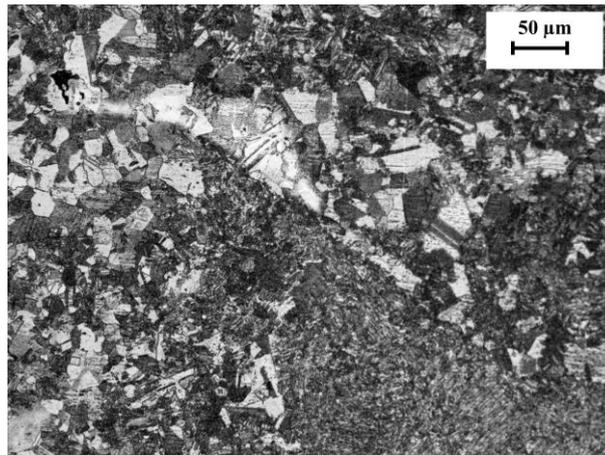
Figure 122: Edge microstructure of sample 3. Optical microscopy image.

The entire cross-section of specimen 3 is shown in **Figure 123**.

Figure 123: Cross-section of specimen 3.

Sample 4 showed a completely lamellar microstructure but with lamellar colonies of smaller dimension (about 10 µm) (**Figure 124, Figure 125**).
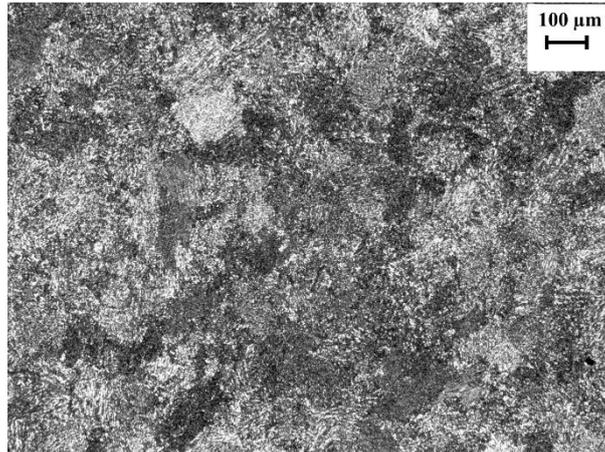
Figure 124: Microstructure of sample 4. Optical microscopy image.
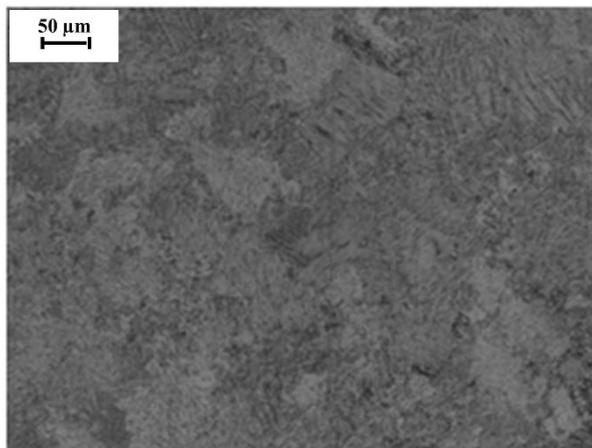
Figure 125: Microstructure of sample 4. Optical microscopy image.

By the observation of these microstructures it is possible to correlate them with the process parameters. Is possible to notice that samples from 1 to 4 were produced combining the lower speed function with the lower line offset. As a result, for this parameters combination, the powder layers are subjected to the high temperature generated by the electron beam for a longer time. The longer exposition to heat promotes the increase of the grains dimension and the high temperature produced

by the low dissipation, due to the low line offset, promotes the formation of lamellar colonies. Furthermore, the long exposition to the high temperature promotes a more remarkable aluminum evaporation as confirmed by the chemical analysis results described later in this thesis.

5.2.1 Post heat treatment microstructures

The specimens were subjected to a heat treatment at 1260°C for 4 hours simulating a Hot isostatic pressing (HIP) treatment in a high-vacuum furnace in order to examine the evolution of the microstructure [93].

This heat treatment simulated a HIP process only in terms of temperatures. In fact, the HIP process is normally conducted at high temperature at isostatic gas pressure of 170 MPa while in the case of this study the heat treatment was conducted in vacuum at 10^{-4} mbar.

For a TiAl alloy with a nominal composition of Ti-48Al-2Cr-2Nb, with the performed heat treatment, a near-γ or duplex microstructure is expected. In fact, analyzing the phase diagram it is evident that the heat treatment temperature of 1260°C is in the α+γ field, below the alpha transus transition line, that for a 48 at.% of Al is around 1350°C and the eutectoid is around 1100°C (**Figure 126**) [55].
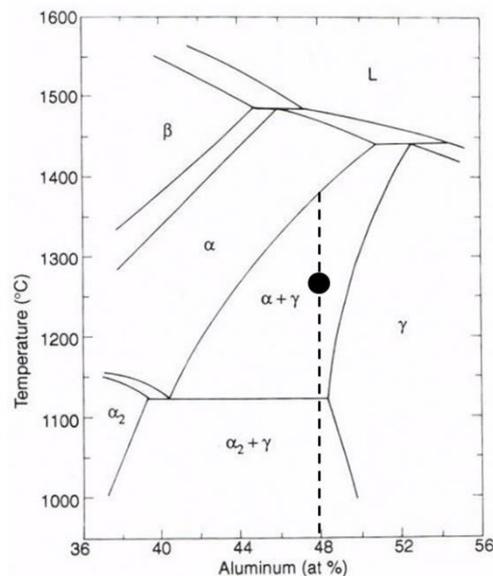
Figure 126: γ-TiAl phase diagram; the heat treatment temperature is indicated by the dot [55].

According to the work of Terner et al. [154], Thermo Mechanical Analysis (TMA) can be a useful tool to quickly identify the phase transition temperatures for γ-TiAl alloys. The derivative curve of the displacement as a function of temperature exhibit peaks in correspondence of the eutectoid transition temperature and the alpha transus temperature (**Figure 127**). These peaks correspond to the phase transformations $(\alpha_2 + \gamma) \leftrightarrow \alpha$ and $(\alpha + \gamma) \leftrightarrow \alpha$.
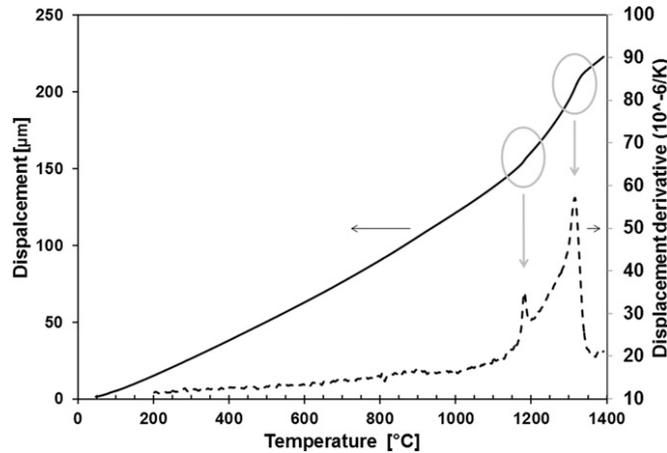
Figure 127: TMA measurement for Ti-47Al-2Cr-2Nb: displacement vs. temperature and displacement derivative vs. temperature (dotted line) [154].

The variation of the aluminum contents is reflected on a variation of the alpha transus temperature. Consequently, this have an effect on the microstructure of the heat-treated specimens. For this reason, the TMA is a reliable method to identify the transition temperature variation of specimens with different composition.

In this study, the TMA results have confirmed the microstructural variation between the different specimens and this was also explained by the chemical analysis that has shown different aluminum content for the different specimens. The chemical analysis results are described forward in this thesis.

Figure 128 shows the TMA results for specimens from 5 to 11. The peaks related to the alpha transus for these specimens are in a narrow temperature range between 1335°C and 1344°C and the eutectic between 1188 and 1192°C. This alpha transus temperature range observed is quite close to the alpha transus temperature expected for γ-TiAl alloy having the considered nominal composition. This is in a certain manner confirmed by the observed microstructure of these specimens after the EBM process and also after the heat treatment.
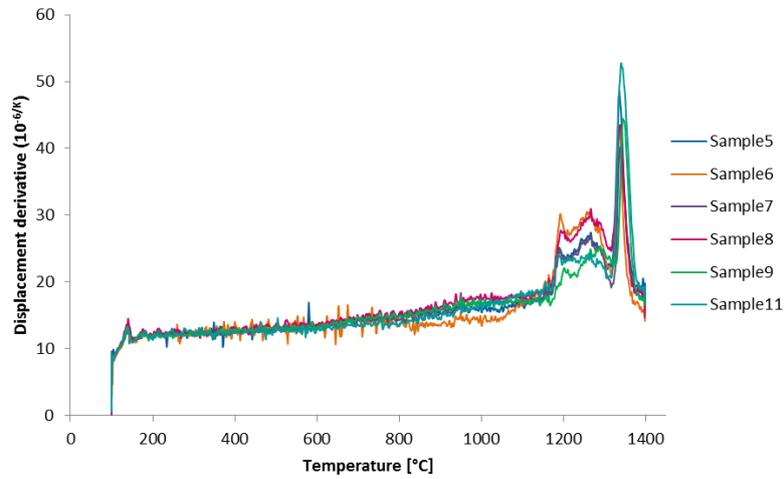
Figure 128: TMA results for specimens from 5 to 11. Displacement derivative vs. temperature.

Regarding the specimens from 1 to 4, the TMA results showed a shift toward lower temperatures with a slight increasing trend from sample 1 to sample 4 (**Figure 129** and **Table 25**). The TMA results are in agreement with the microstructural trends observed from sample 1 to sample 4.
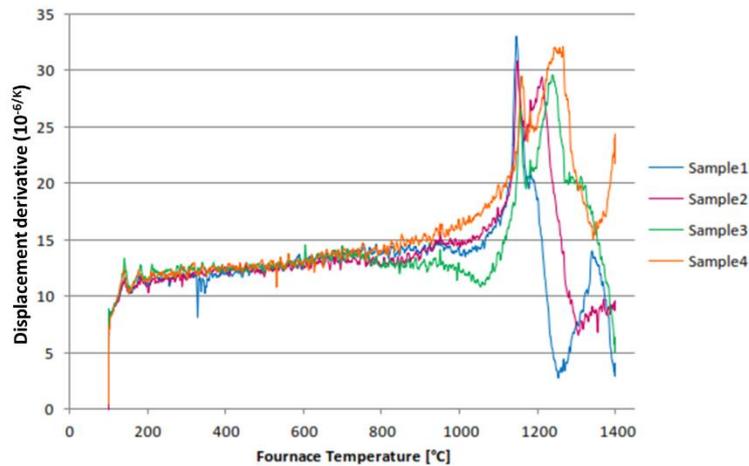
Figure 129: TMA results for specimens from 1 to 4. Displacement derivative vs. temperature.

Table 25: Phase transition temperatures measured with TMA.

Specimen	Eutectoid transition T [°C]	α-transus T [°C]
1	1145	1181
2	1147	1211
3	1155	1238
4	1158	1264
5-12	1118-1192	1335-1344

By analyzing the micrographs of the specimens, it is possible to observe a microstructural variation trend for the different specimens. By comparing the as-EBM microstructure with those after the heat treatment is possible to study the microstructural evolution caused by the heat treatment. Moreover, the effect of the different parameters combinations on the material is more evident in the heat-treated samples.

After the heat treatment at 1260°C for 4 hours, the expected near-γ microstructure was observed for specimens from 5 to 12. The obtained microstructure can be confirmed by the TMA results discussed above. In fact, their alpha transus temperature are much higher than the heat treatment temperature and this means that, for these specimens, the heat treatment was conducted in the α + γ field of the phase diagram.

Figure 130 shows a typical γ microstructure observed in samples from 5 to 12. For these samples, the observed microstructure is 100% equiaxed with an average γ grain size, evaluated with the intercept method, of 15µm. In particular, it is reported the microstructure of sample 5 where some coarser grains with maximum dimension around 80µm can be observed oriented in layers perpendicular to the building direction (**Figure 131**).
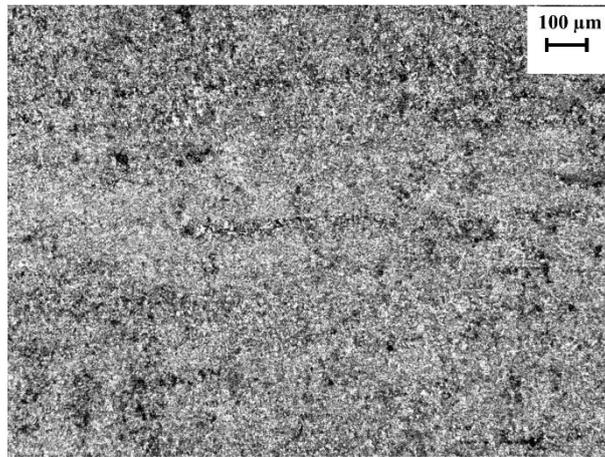
Figure 130: Micrograph of sample 5 after the heat treatment.
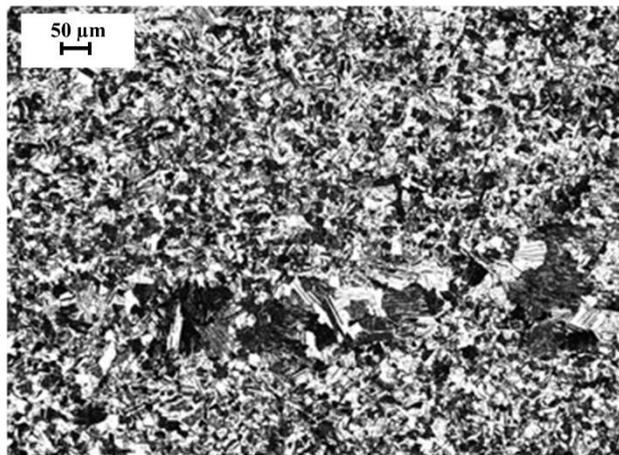
Figure 131: Micrograph of sample 5 after the heat treatment.

Specimens from 5 to 12 exhibited the same equiaxed γ microstructure observed in sample 5 above.

By the other hand, for the samples from 1 to 4 the heat treatment caused a substantial increase in the grains dimension and an evolution of lamellar colonies with a progressive increase in colonies dimensions.

By observing the macro images in **Figure 133**, it is possible to better understand the microstructural trend and observe a microstructure inhomogeneity for the first four samples. In particular, they exhibit a coarse fully lamellar or near lamellar

microstructure in the center and a finer near-γ microstructure near the outer edges. Moreover the observed microstructures differ between each samples of this family.

For sample 1, it is possible to observe three microstructural zones from the outer edges to the core (microstructural detail in **Figure 134**).

The core of specimen 1 exhibits a "basket-weave" microstructure that is not common for γ titanium aluminides (**Figure 132a**) but is the typical microstructure of titanium alloy such as Ti-6Al-4V (**Figure 132b**).
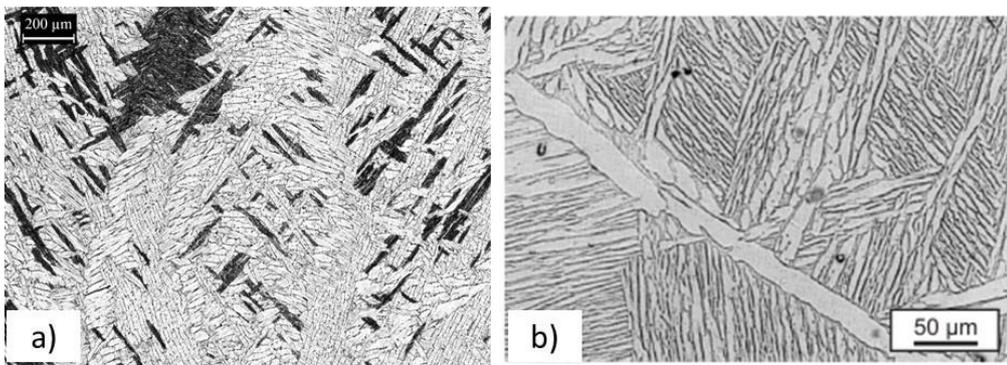
Figure 132 a): Core microstructure observed in sample 1 after the heat treatment (50X magnification); b) Ti-6Al-4V typical "basket-weave" microstructure [49]

This can be due to the combination of EBM parameters used to process this specimen. Most probably, the combination of low speed function and low line offset has produced an overheating in the central zone of the specimen bringing to a massive evaporation of aluminum during the EBM process. In this manner, sample 1 has lost the Ti-Al elemental ratio proper of TiAl intermetallics.
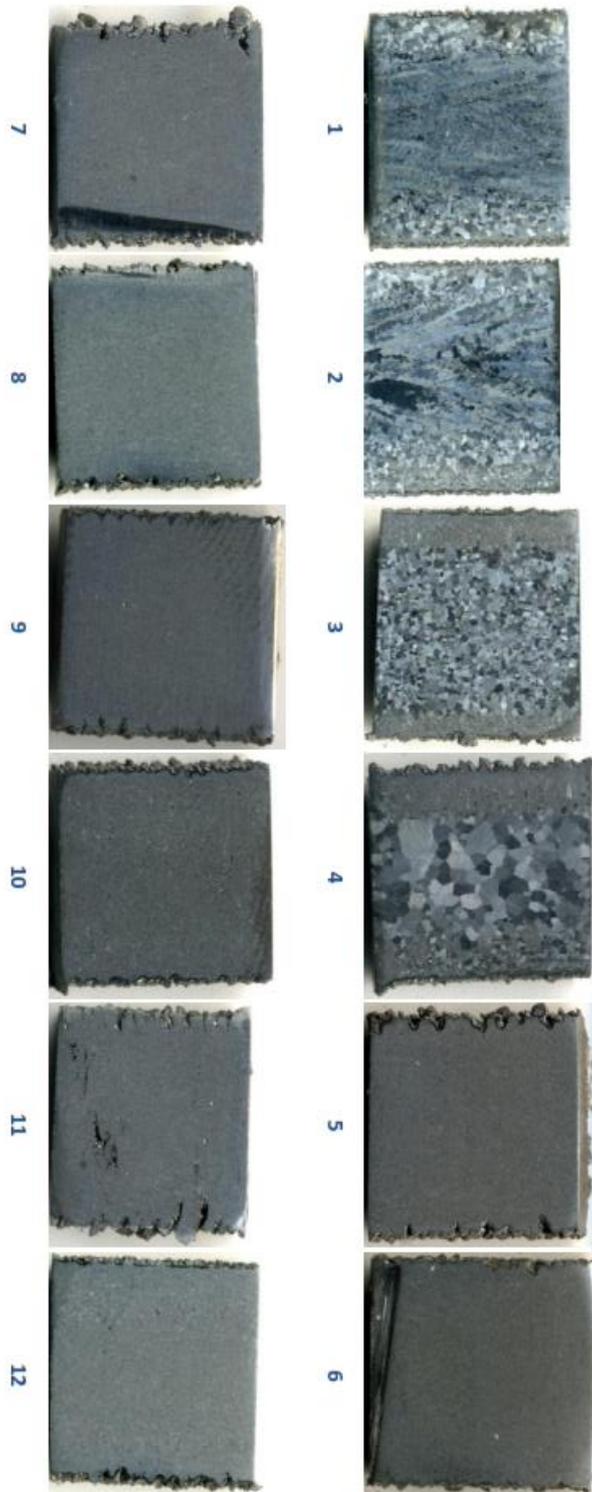
Figure 133:Post heat treatment specimens microstructure. Macro overview.
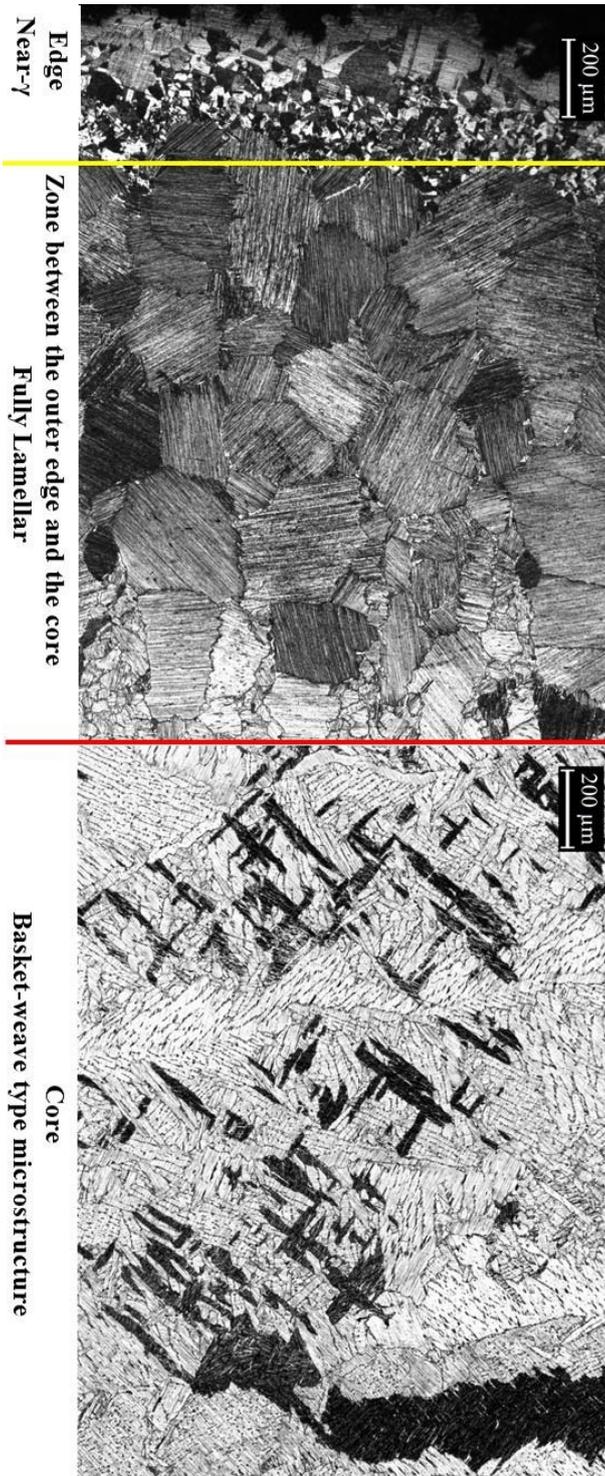
Figure 134: Three different microstructures from the outer edge to the core observed in sample 1 after the heat treatment.

In sample 2, a completely lamellar microstructure was observed in the core of the specimen (**Figure 135** and **Figure 136**). The average lamellar colonies dimension is 150µm ± 50µm with some large lamellar grains reaching a length of 800µm in the core of the specimen.
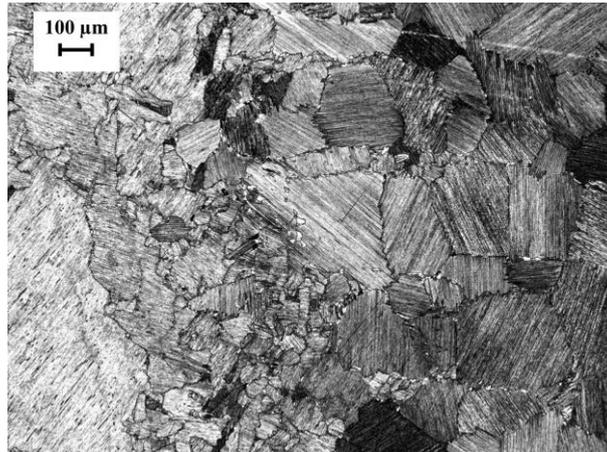
Figure 135: Core micrograph of sample 2 after the heat treatment.
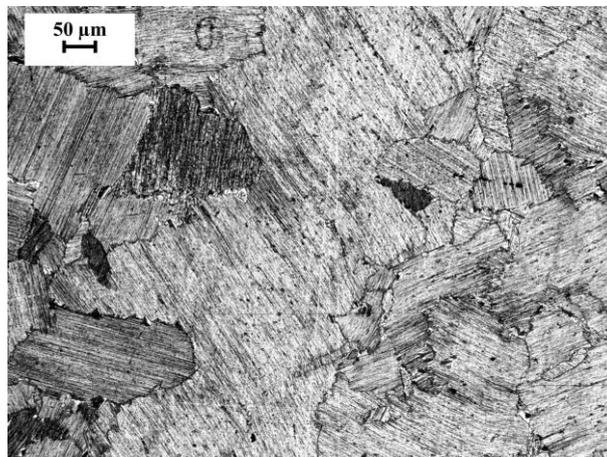
Figure 136: Core micrograph of sample 2 after the heat treatment.

Similar to what has been observed for the as-EBM specimens, a different microstructure was observed close to the lateral edges of this specimen. However, for the heat treated specimens, the edge microstructure was not a pure γ equiaxed but a near- γ with equiaxed grain size of 40µm (close to the edge) and fine duplex microstructure presenting a lamellar ratio of about 50% with average lamellar grains size of 90 µm (**Figure 137** and **Figure 138**).
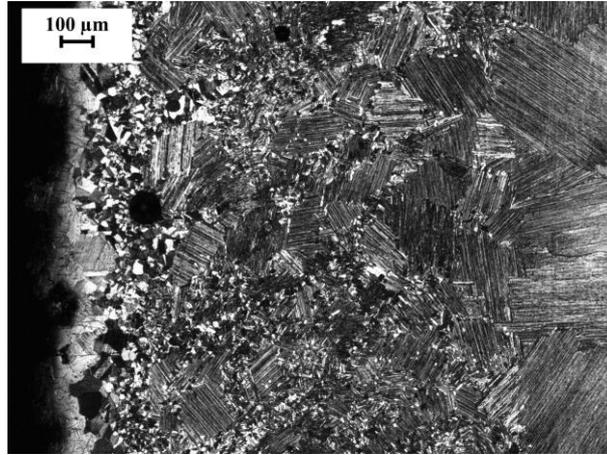
Figure 137: Edge micrograph of sample 2 after the heat treatment.
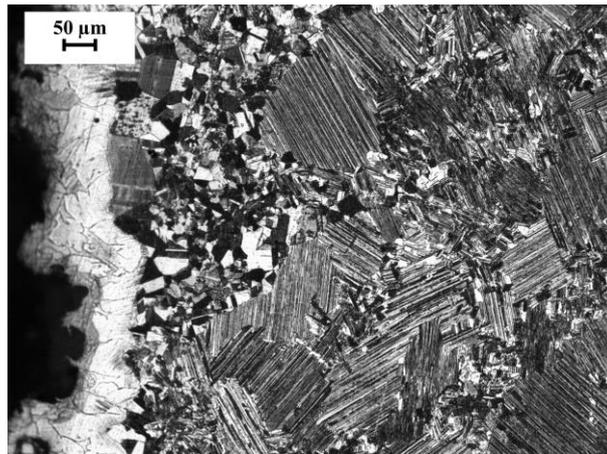
Figure 138: Edge micrograph of sample 2 after the heat treatment.

The cross-section of sample 2 reported in **Figure 139** shows the microstructural variation observed from the core of the specimen, where a coarse lamellar structure was observed to the edges that exhibited a near γ microstructure. It is also possible to notice that, passing from the core to the edges, the lamellar microstructure seems to become gradually finer.

Figure 139: Cross-section of specimen 2.

Sample 3 exhibited a microstructure similar to sample 2. In the core a completely lamellar microstructure with an average grain size of 150µm ± 20 µm with very few residual γ- grains was observed as shown in **Figure 140** and **Figure 141**.
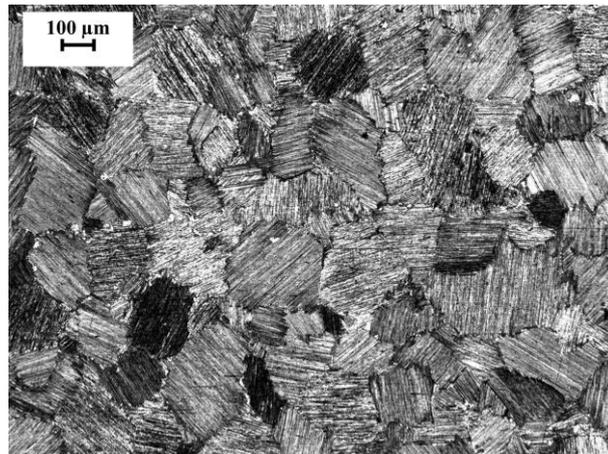
Figure 140: Core micrograph of sample 3 after the heat treatment.
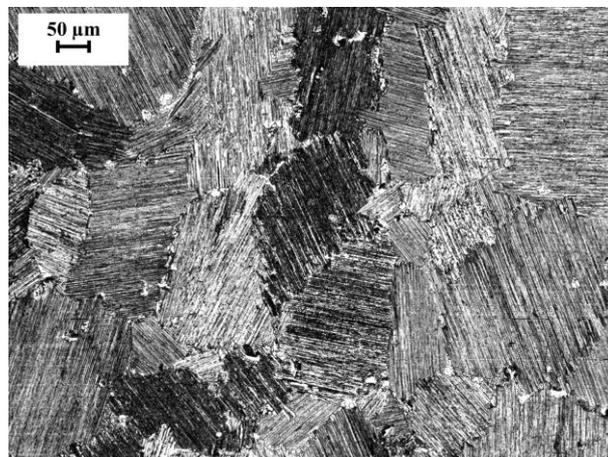
Figure 141: Core micrograph of sample 3 after the heat treatment.

A near γ microstructure was observed in the edges, as it is possible to observe from **Figure 142** and **Figure 143**.
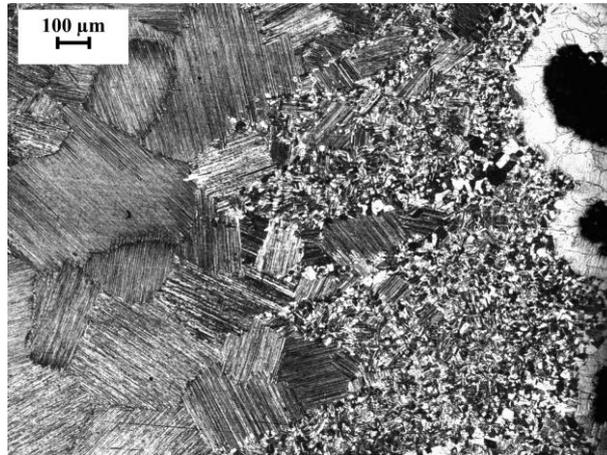
Figure 142: Edge micrograph of sample 3 after the heat treatment.
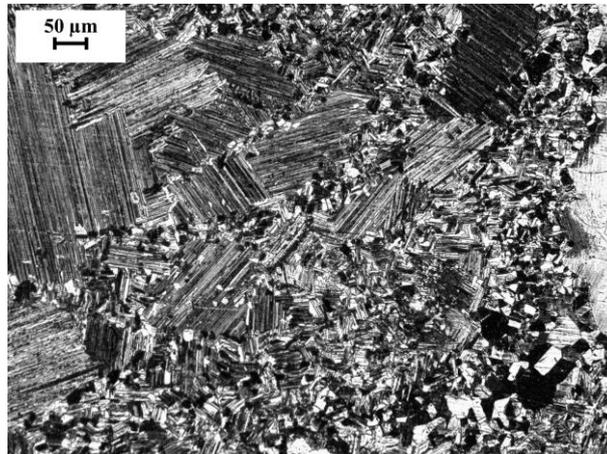
Figure 143: Edge micrograph of sample 3 after the heat treatment.

From the cross-section micrograph in **Figure 144**, it is appreciable a gradually variation from the completely lamellar microstructure composed by coarse lamellar grain of the center of the specimen to a near γ microstructure in the specimen edges.

Figure 144: Cross-section of specimen 3.

Sample 4 showed a lamellar microstructure with larger lamellar grains with average grain size of 400µm ± 80 µm in the core (**Figure 145**).
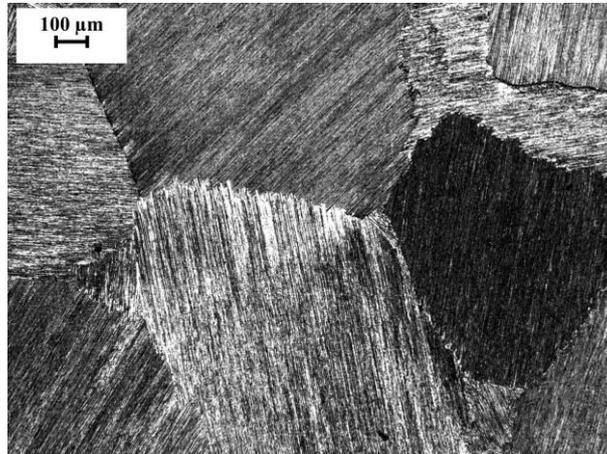
Figure 145: Core micrograph of sample 4 after the heat treatment.

An equiaxed microstructure is observed close to the specimen edge and between the center and the edges, this specimen exhibits a near γ microstructure with about 40% of lamellar grains an average lamellar grain size of 100µm ± 50µm and equiaxed grain size about 20 µm (**Figure 146** and **Figure 147**).
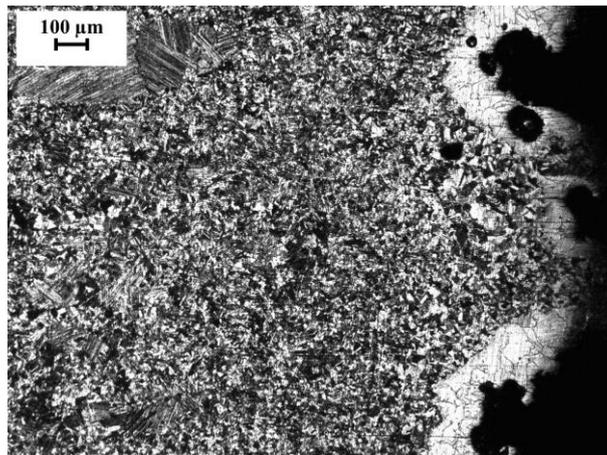
Figure 146: Edge micrograph of sample 4 after the heat treatment.
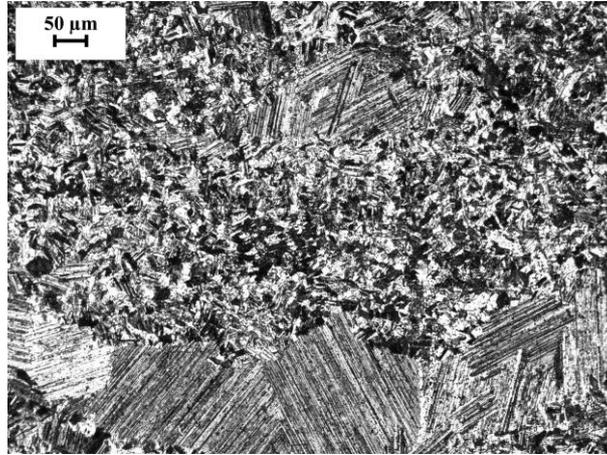
Figure 147: Edge micrograph of sample 4 after the heat treatment.

The microstructural trend inside specimen 4 can be appreciated from the cross-section in **Figure 148**.
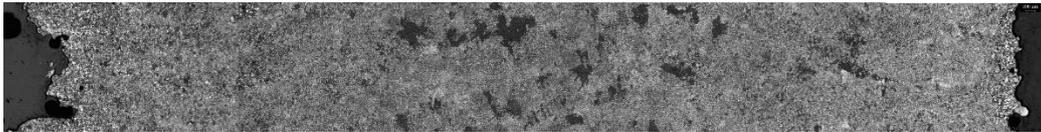
Figure 148: Cross-section of specimen 4.

5.3 X-Ray Diffraction Analysis

The X-Ray Diffraction has been performed to better understand the results obtained from previous analysis by examining the phases composition and ratio between the different samples.

In **Figure 149** the diffractograms of the samples are shown. The diffractograms of the samples from 5 to 12 are similar in terms of phases present and phase ratio. In fact, these samples can be classified in the same group according to the previous analysis.
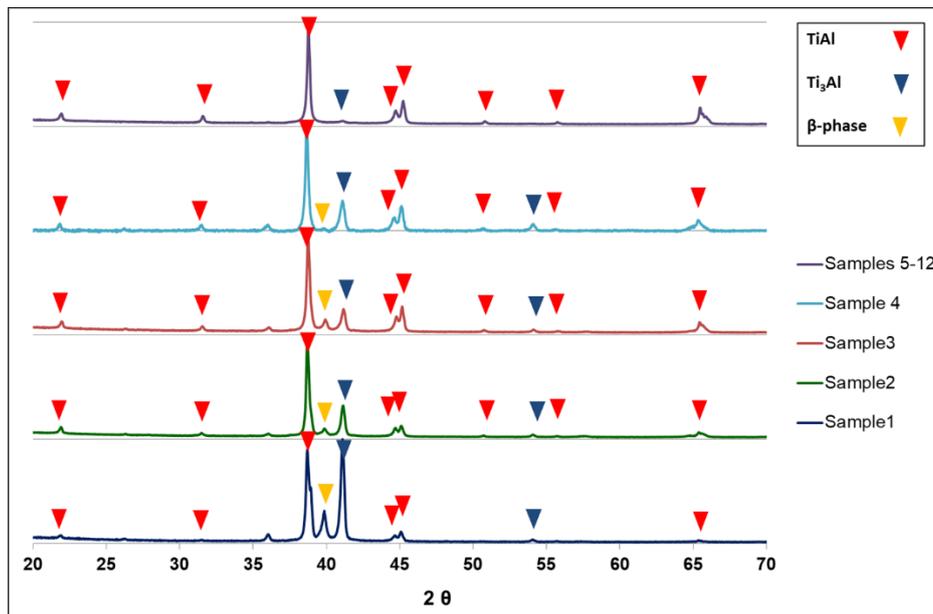
Figure 149: X-Ray diffractogram of the specimens from 1 to 5 and 5 to 12; the different phases are indicated by colored arrows.

The peak with the higher intensity is that at $2\Theta = 38.7°$, corresponding to the γ-TiAl phase, present in higher percentage. For the samples from 1 to 4 the peaks related to the α_2-Ti$_3$Al phase and the peaks related to the β-Ti phase are observed.

Starting from sample 1 a trend in phase ratio variation can be observed: from sample 1 to sample 4 the α_2-Ti$_3$Al and the β-Ti phases decrease, tending to disappear in sample 5 and the following. Regarding the γ-TiAl phase, an increase in the phase amount is observed from sample 1 to sample 4.

For the sample 1, the higher intensity peak is the one related to the γ-TiAl phase, this could indicate an aluminium loss due to a prolonged exposure to a high temperature, according to the microstructure analysis. The presence of the β phase in the first four samples can be correlated to the building parameters, in particular to the low speed function and the low line offset. It is possible that the combination of these two parameters results in an increase in temperature that causes the formation of the β phase; it is also possible that the high temperature causes the evaporation of aluminum resulting in a composition variation with a higher titanium content.

To confirm this composition variation between the different samples, a chemical analysis was performed.

5.4 Chemical composition analysis

Chemical analysis was performed to know the elemental composition of the as-built material. In this analysis, the amount of the constituent elements, titanium, aluminum, chromium, niobium were determined by using the ICP-OES technique. This gives an indication both on the degree of purity maintained by the production processes and on the aluminum evaporation degree during the fusion. This evaporation obviously leads to a component having a different aluminum composition respect to the powder. For this reason, once chosen and properly fixed the EBM parameters, the chemical composition has to be adjusted in order to reach the desired aluminum composition in the final part.

The elemental chemical composition of the as-EBM samples from 1 to 12 is reported in **Table 26**.

Table 26: Chemical composition of the different specimens.

		Al	Cr	Nb	Ti
		Chemical composition in wt.% and at.%			
Sample 1	wt.%	28.30	2.30	5.20	
	at.%	42.10	1.78	2.25	
Sample 2	wt.%	29.30	2.35	5.18	
	at.%	43.60	1.82	2.24	
Sample 3	wt.%	30.30	2.43	5.00	
	at.%	45.10	1.88	2.16	
Sample 4	wt.%	30.70	2.45	5.00	
	at.%	45.70	1.89	2.16	
Sample 5	wt.%	32.40	2.53	4.85	Balance
	at.%	48.20	1.96	2.10	
Sample 10	wt.%	32.30	2.50	4.91	
	at.%	48.10	1.93	2.12	
Sample 11	wt.%	32.80	2.52	4.84	
	at.%	48.80	1.95	2.09	
Sample 12	wt.%	32.60	2.54	4.90	
	at.%	48.50	1.96	2.12	
Uncertainties	wt.%	0.25	0.10	0.15	

The reported chemical compositions confirms what supposed analyzing the result of X-Ray diffraction microstructure analysis, which is a progressive loss in aluminum from sample 4 to sample 1. By comparing this information with the DOE

table, is noticeable that these specimens were built applying the lower speed function and the lower line offset. This leads to a high amount of energy transmitted and to a low heat dissipation; so the temperature rapidly increases and decreases very slowly, giving the time to aluminum to evaporates.

The diagram in **Figure 150** shows the trend of aluminum content in at.% from sample 1 to sample 12. It is possible to notice an increasing trend from sample 1 to 4, then there is a step of about 2 at.% from sample 4 to the next specimens that has shown an aluminum content that remains more or less constant confirming the near-γ microstructure observed in these specimens.

The aluminum evaporation causes a progressive increase of the α_2 and β phases and a decrease of the γ phase as observed by the X-Ray diffractograms.
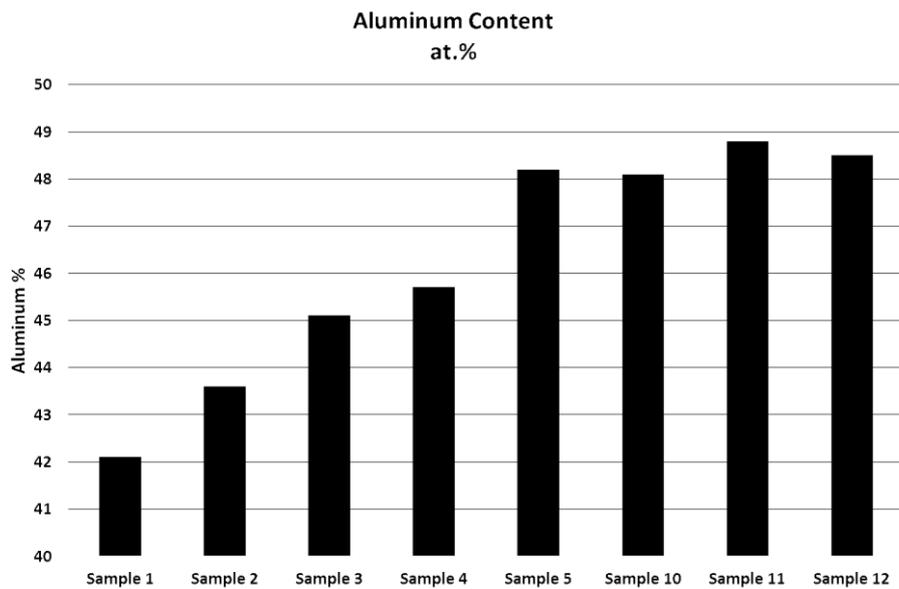
Figure 150: Aluminum content trend in at.% from sample 1 to sample 12

5.4.1 EDS Analysis

A further investigation was done using the EDS analysis in order to quantify the aluminum variations trough the different microstructural zones observed in the first four samples. In particular, the investigation has focused on the interface between the specimen edges with an equiaxed or near γ microstructure and the specimens bulk presenting a lamellar microstructure. For this purpose, EDS elemental profile, EDS punctual analysis and elemental maps were performed on specimen 1 in both as-EBM and heat treated condition. Specimen 1 was chosen as representative of the first group, composed by specimens from 1 to 4, where this microstructural difference between the edges and the bulk was observed. Moreover, these analysis were conducted also on specimen 5 in order to do a comparison with a specimen of the second group having an homogeneous equiaxed microstructure.

5.4.1.1 Sample 1 As-EBM

The EDS elemental profiles tracked along the cross-section of sample 1, from the edge toward the core for about 300 µm, highlighted a decrease in aluminum amount and an increase in titanium in the first zone of about 100 µm. This area corresponds to the microstructural zone with an equiaxed microstructure observed by the optical microscopy images and it can also be distinguished from the SEM image where it appears darker. Regarding chromium and niobium, their concentrations don't present a significant variation through the analyzed profile. **Figure 151 a** shows the optical microscopy image of sample 1 edge, **Figure 151 b** shows the SEM image of the analyzed zone of the specimen and in **Figure 151 c** the EDS elemental profiles measured through this zone are reported.
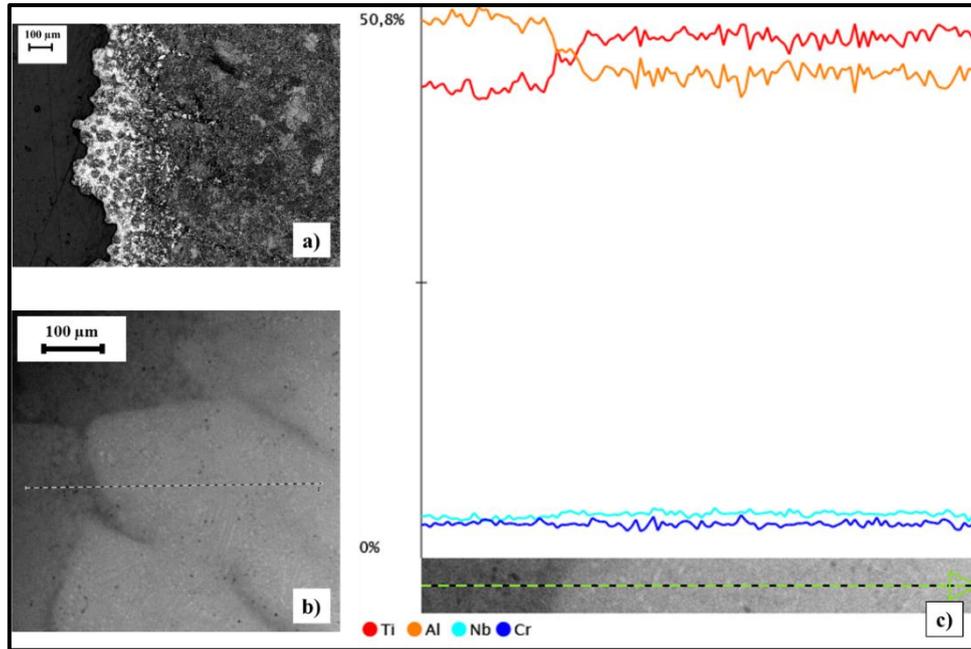
Figure 151: EDS elemental profiles analysis of sample 1 as-EBM; a) optical micrograph of the area of interest; b) SEM micrograph of the analyzed cross-section; c) EDS elemental profiles.

The punctual EDS and elemental mapping performed on this area, have confirmed this trend in aluminum and titanium variation from the edges to the core. In fact, as it is possible to see from **Table 27** and **Table 28**, the measured aluminum amount in the equiaxed edge area is 50.44 at.% while its concentration measured in the bulk is 45.37 at.% that is closer to that measured by the ICP analysis on this sample. **Figure 152 a** shows the SEM image with the points where EDS analysis was performed (yellow: edge area, blue: bulk) and **Figure 152 b** represent the EDS elemental map for aluminum and titanium. It is quickly clear from the EDS map that the darker edge zone in SEM image is richer in aluminum than the brighter bulk zone that presents more titanium.
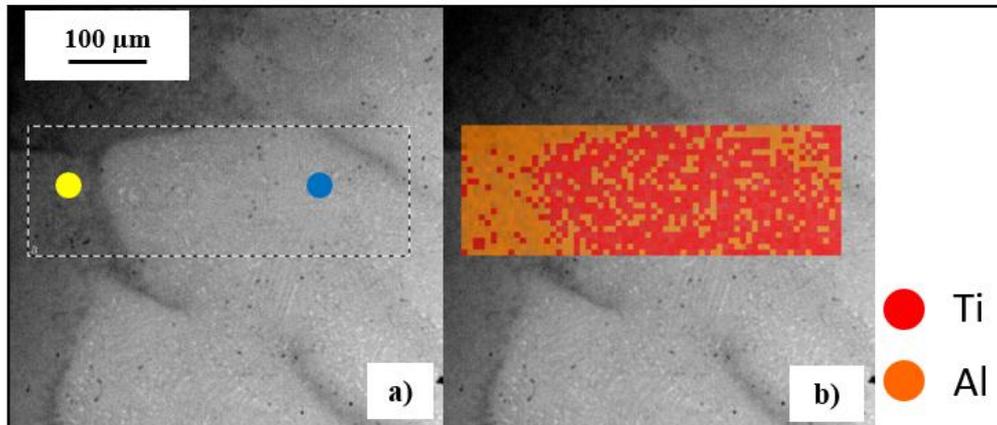
Figure 152: EDS elemental analysis of sample 1 as-EBM; a) punctual EDS; b) Elemental map.

The elemental chemical compositions measured in the two points indicated in **Figure 152 a** are reported in **Table 27** and **Table 28**.

Table 27: EDS elemental composition of the edge area of sample 1 as-EBM.

⬤	Atomic Concentration %	Weight Concentration %
Ti	45.64	56.84
Al	50.44	35.41
Nb	2.30	5.57
Cr	1.61	2.18

Table 28: EDS elemental composition of the bulk area of sample 1 as-EBM.

●	Atomic Concentration %	Weight Concentration %
Ti	50.61	61.11
Al	45.37	30.88
Nb	2.66	6.22
Cr	1.36	1.79

The EDS elemental composition analysis and elemental mapping were performed in a more central area of sample 1 in order to do a comparison with the area closer to the edge described before. The obtained results reported in **Figure 153** and in **Table 29** show a further decrease in aluminum amount (43.14 at.%) that is very similar to that obtained from the ICP analysis (42.10 at.%).
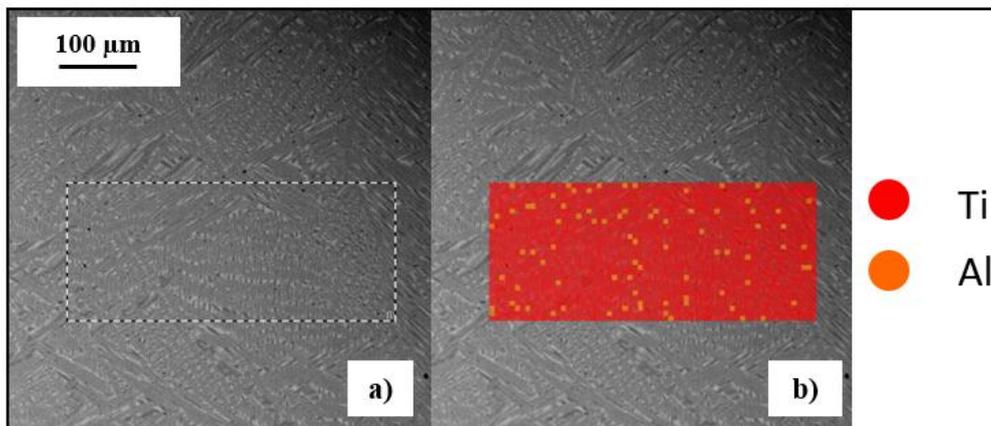
Figure 153: EDS elemental analysis of the central zone of sample 1 as-EBM; a) punctual EDS; b) Elemental map.

Table 29: EDS elemental composition of the central of sample 1 as-EBM.

	Atomic Concentration %	Weight Concentration %
Ti	52.70	62.94
Al	43.14	29.05
Nb	2.57	5.95
Cr	1.59	2.07

5.4.1.2 Sample 1 heat treated

The same analysis were performed on sample 1 in heat treated condition. **Figure 154 a** shows the optical microscopy image of sample 1 edge, **Figure 154 b** shows the SEM image of the analyzed zone of the specimen and in **Figure 154 c** the EDS elemental profiles measured through this zone are reported.
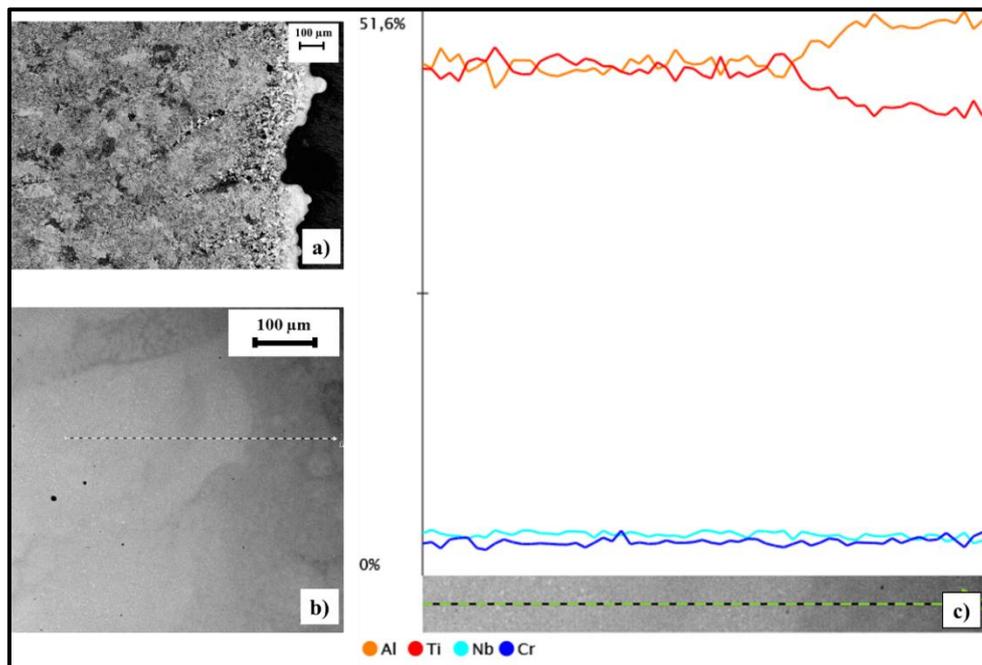
Figure 154: EDS elemental profiles analysis of sample 1 heat treated; a) optical micrograph of the area of interest; b) SEM micrograph of the analyzed cross-section; c) EDS elemental profiles.

Also in this case, it is possible to observe an aluminum increase and a titanium decrease through the area close to the sample edge.

EDS analysis and elemental maps highlight this phenomena as it is possible to see in **Figure 155 a** and **Figure 155 b** and in **Table 30** and **Table 31**.
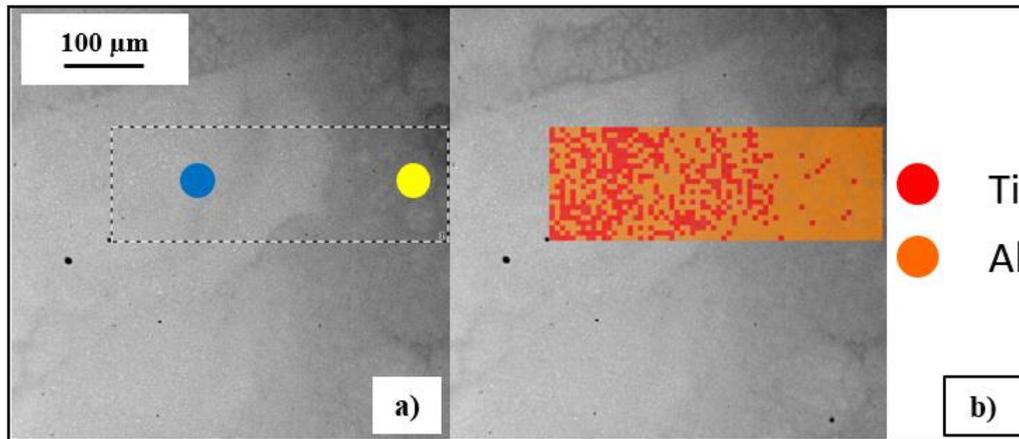
Figure 155: EDS elemental analysis of sample 1 heat treated; a) punctual EDS; b) Elemental map.

Table 30: EDS elemental composition of the edge area of sample 1 heat treated..

🟡	Atomic Concentration %	Weight Concentration %
Ti	45.05	56.23
Al	50.96	35.85
Nb	2.35	5.69
Cr	1.65	2.23

Table 31: EDS elemental composition of the bulk area of sample 1 heat treated.

●	Atomic Concentration %	Weight Concentration %
Ti	49.26	59.88
Al	46.60	31.93
Nb	2.62	6.19
Cr	1.51	2.00

What it is possible to notice from the elemental map and the elemental composition measured in the edge area of sample 1 heat treated, is that the aluminum amount tends to remains slightly higher through the analyzed area respect to the sample in the as-EBM condition. This could means that aluminum tends to diffuse for a certain distance toward the bulk of the specimen during the heat treatment [174].

Furthermore, a central area of the specimen was analyzed and the obtained results are reported in **Figure 156** and **Table 32**.
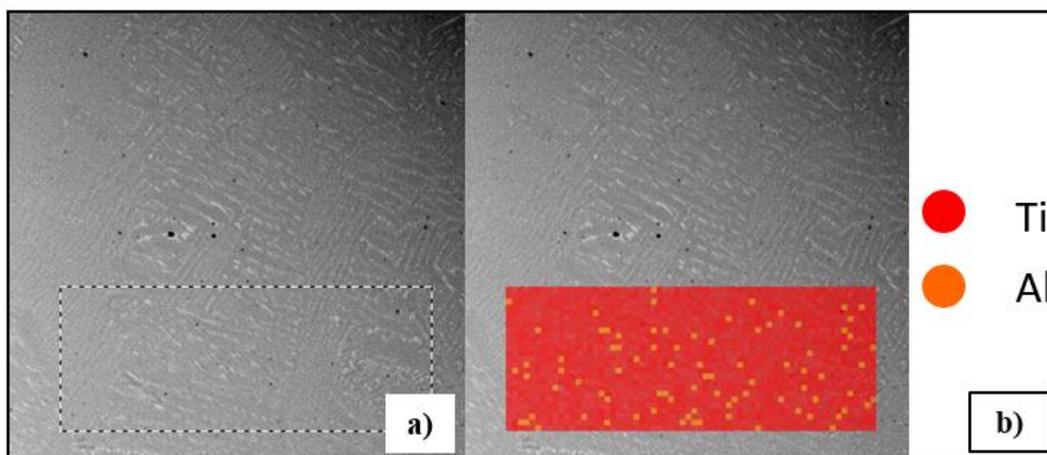
Figure 156: EDS elemental analysis of the central zone of sample 1 heat treated; a) punctual EDS; b) Elemental map.

Table 32: EDS elemental composition of the central of sample 1 heat treated.

	Atomic Concentration %	Weight Concentration %
Ti	52.60	62.86
Al	43.21	29.10
Nb	2.55	5.91
Cr	1.64	2.13

The obtained results in the core of sample 1 heat treated are in line with what observed in the as-EBM sample and ICP analysis in terms of aluminum content. This means that the aluminum content does not varies during the heat treatment.

5.4.1.3 Sample 5 As-EBM

The EDS profile analysis, elemental mapping and punctual elemental analysis were further performed on sample 5, considered representative of the second group of specimens (5-12) where an homogeneous equiaxed microstructure was observed without any microstructural variation from the edges to the bulk of the specimens. These analysis have confirmed an homogeneous distribution of the elements, in particular aluminum and titanium, in the different zones of the specimen.

In fact, as it is possible to see from the elemental profiles in **Figure 157**, an aluminum and titanium variation through the cross-section close to the edge is not observed.
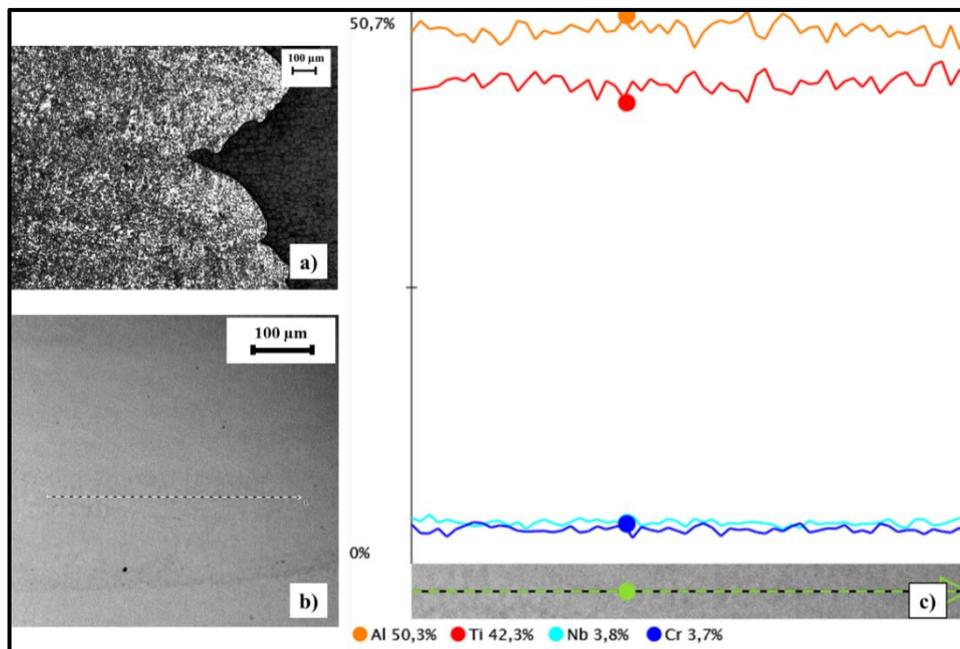
Figure 157: EDS elemental profiles analysis of sample 5 as-EBM; a) optical micrograph of the area of interest; b) SEM micrograph of the analyzed cross-section; c) EDS elemental profiles.
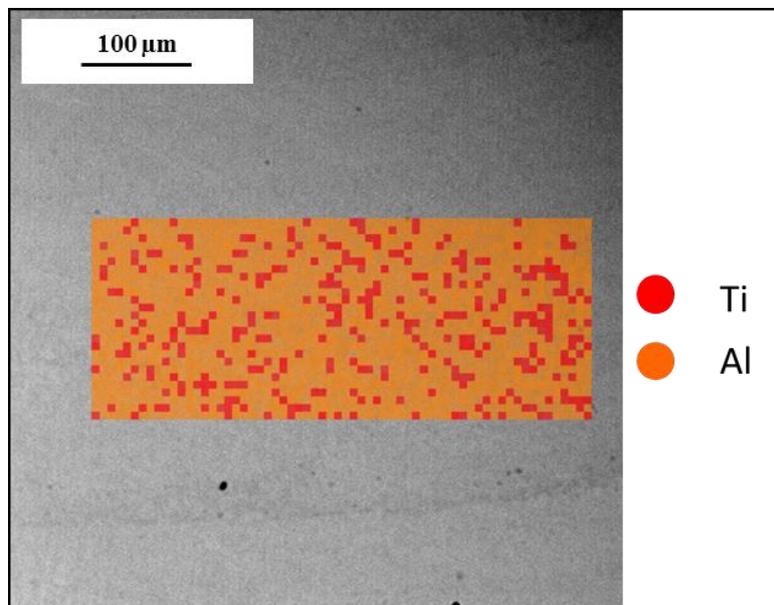
Figure 158: EDS elemental maps for Al and Ti of the edge area of sample 5 as-EBM.

The elemental maps of the sample region close to the edge for aluminum and titanium in **Figure 158** demonstrates a uniform distribution of those two elements in the analyzed area.

Table 33: EDS elemental concentration in the edge area of sample 5 as-EBM.

	Atomic Concentration %	**Weight Concentration %**
Ti	46.48	57.70
Al	49.48	34.67
Nb	2.13	2.14
Cr	1.85	2.49

5.4.1.4 Sample 5 heat treated

The results of the analysis performed on sample 5 after the heat treatment are very similar to those of sample 5 in as-EBM condition (**Figure 159, Figure 160** and **Table 34**: EDS elemental concentration in the edge area of sample 5 heat treated.).
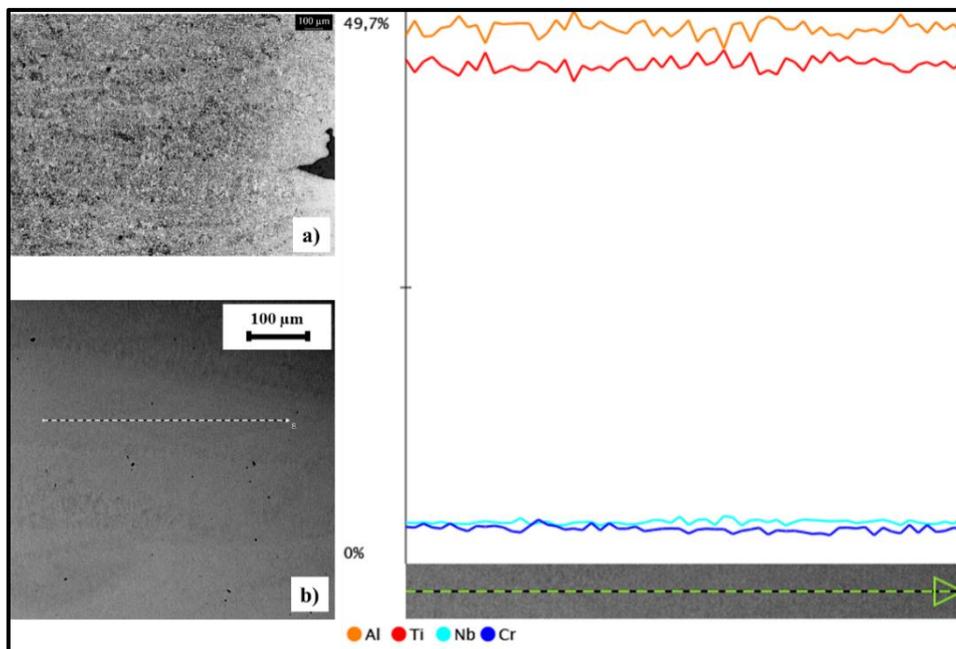
Figure 159: EDS elemental profiles analysis of sample 5 heat treated; a) optical micrograph of the area of interest; b) SEM micrograph of the analyzed cross-section; c) EDS elemental profiles.
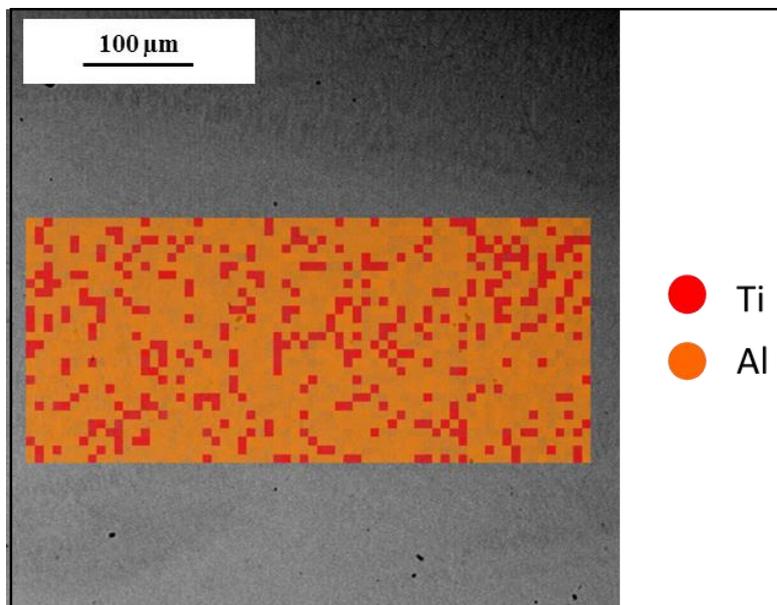
Figure 160: EDS elemental maps for Al and Ti of the edge area of sample 5 heat treated.

Table 34: EDS elemental concentration in the edge area of sample 5 heat treated.

	Atomic Concentration %	**Weight Concentration %**
Ti	46.79	57.99
Al	49.31	34.46
Nb	2.17	5.22
Cr	1.73	2.33

During the heat treatment, a variation in aluminum concentration is not observed.

5.5 Correlation of the observed microstructures and chemical compositions with a Finite Element (FE) thermal model of EBM process

Other interesting results, are reported in the work done by E. Galati et. al.: "FE Thermal Model of EBM process to investigate different experimental microstructures for TiAl" [175]. In this study, an FE thermal model of the EBM process was applied to investigate the differences in microstructure obtained during the process. With the FE thermal model was possible to know the temperatures and the thermal cycles to which the material is subjected before and after the EB scan. The thermal cycles lead to a first temperature raise before the EB scan, and then several re-melting of the same tracks. This brings to the evaporation of different amounts of aluminum depending to the used building parameters.

This study was organized according to the following experimental sequence:

- DOE matrix with the different combination of EBM building parameters used to produce the investigated specimens (see **Table 23**). In particular, the parameters that were kept fixed are the beam diameter, the preheating temperature, the scanning strategy (see **Figure 161**) and the layer thickness.

  The parameters varied to perform the two simulations according the DOE table for sample are the speed function index, the line offset, the max beam current and the focus offset. Moreover, the parameter used to study and compare the different heat phenomena was the line offset.
- Numerical modelling built considering the material properties and heat transfer analysis [176].
- Microstructure and aluminum composition analysis of the produced specimens (described before).
- Analysis of the numerical results obtained and their correlation with the effect of process parameters in terms of microstructure and aluminum content.
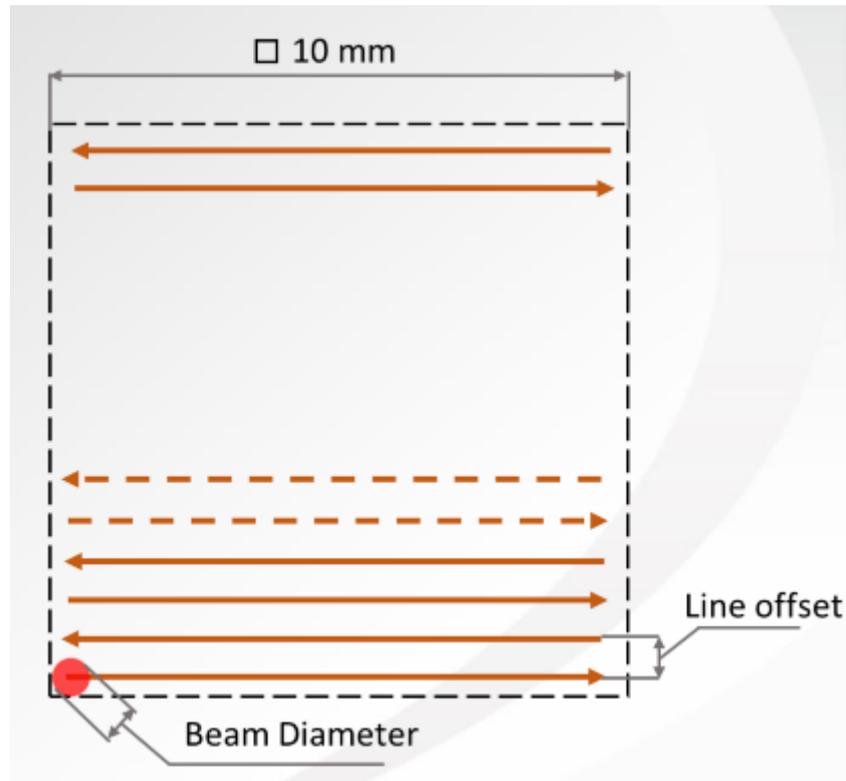
Figure 161: Scan strategy used.

This study focused on the comparison of sample 1 and sample 5 and the combination of the building parameters used for these two specimens were applied to build the respective FE thermal models.

The aims of the thermal model performed for these two specimens was the followings:

- In **Sample 1**: investigate the heat phenomena, produced by the considered line offset, causing a different aluminum evaporation from the edges to the bulk of the specimen.
- In **Sample 5**: investigate the effect of line offset on the heat phenomena producing the uniform aluminum content and homogeneous equiaxed microstructure observed in this specimen.
- Comparisons between the numerical results, heat phenomena and experimental observation between the two samples.

By applying the FE thermal model to samples, using the lower and higher line offset, the numerical results indicated the reached temperature and the resident time in melting phase and showed that the material is subjected to numerous thermal

cycles before and after the EB scan, leading to a first temperature raise before the EB scan, and then several remelting events.

In sample 1, the lower line offset produced a longer exposure of the melting phase to high temperature (above the aluminum evaporation temperature), in particular for the inner zones of the specimen, that can be correlated to the difference in aluminum content and microstructural variation from the edges to the bulk observed during the material characterization (**Figure 162**).
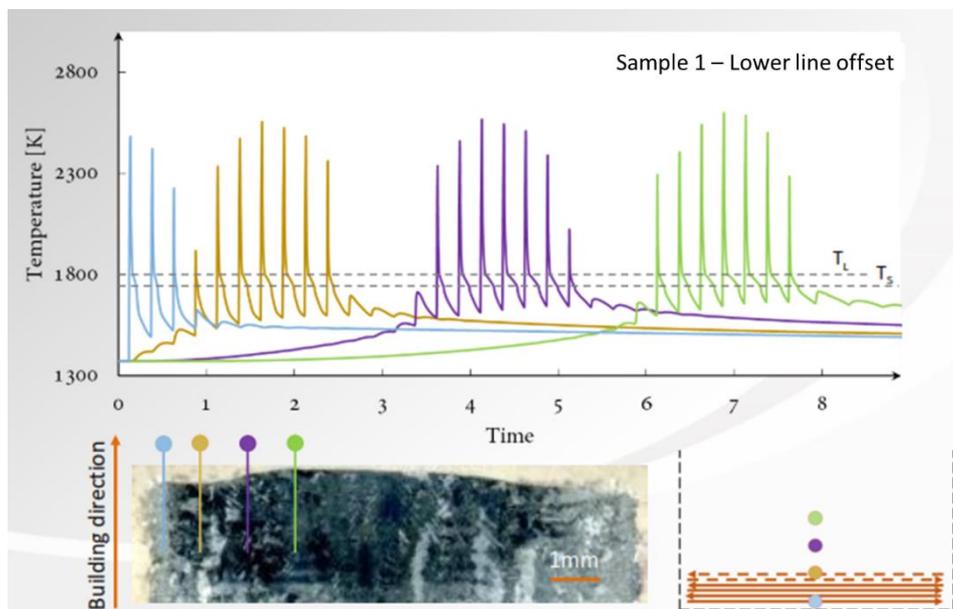
Figure 162: Thermal envelopes for the different zones through the cross section of specimen 1.

In sample 5, the higher line offset reduces the number of thermal cycles for a certain period of time and a certain zone and thus the exposure of the melting phase to high temperature is reduced respect to what observed in sample 1. In other words, a certain zone considered in the model (indicated by the different colors in **Figure 162**) is subjected to high temperature for a shorter time and this reduce the amount of aluminum that evaporates during the EBM process. It is also possible to observe for sample 5, that the exposure time at high temperature is equivalent between the different zones and this explain the uniform equiaxed microstructure through the cross section of the specimen (**Figure 163**).
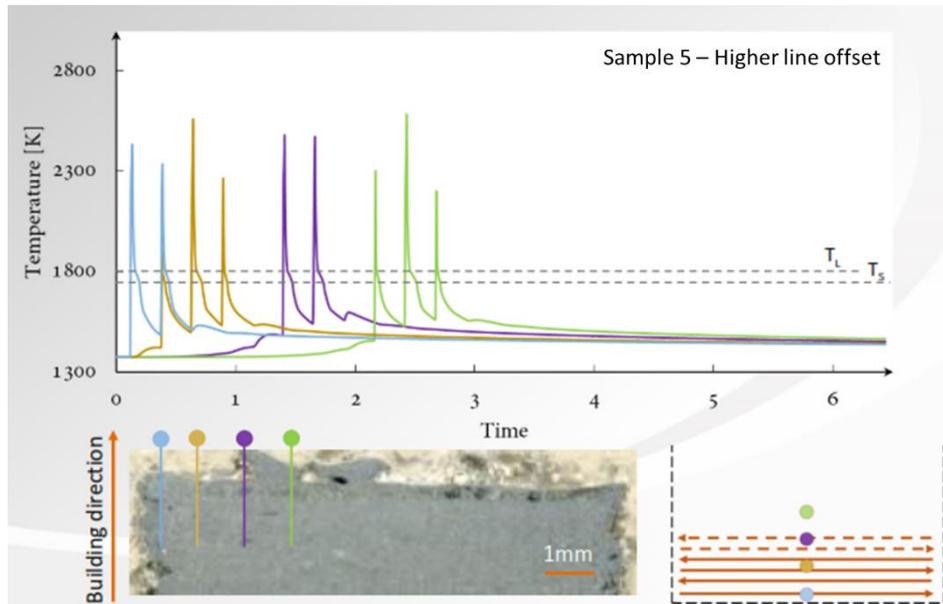
Figure 163: Thermal envelopes for the different zones through the cross section of specimen 5.

The lower exposure time at higher temperature in sample 5 is clearly visible by the comparison in **Figure 164**, where the temperature envelopes of equivalent inner zones of sample 1 and sample 5 are superimposed.
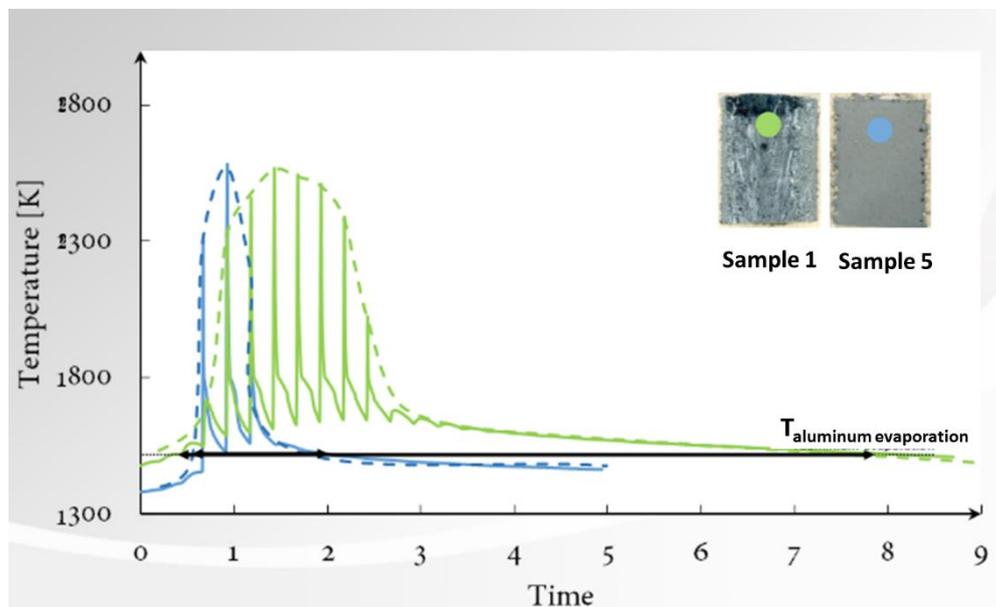
Figure 164: Thermal envelopes comparison between an inner zone of sample 1 and an equivalent inner zone of sample 5.

By observing **Figure 165**, it is possible to asses that the thermal envelope of the edge area of sample 1 is comparable to those of the central area of sample 5. This confirms the equiaxed microstructure, due to the lower aluminum evaporation, observed in the edges of the first group of four specimens and both in the edges and bulk in the second group of specimens.
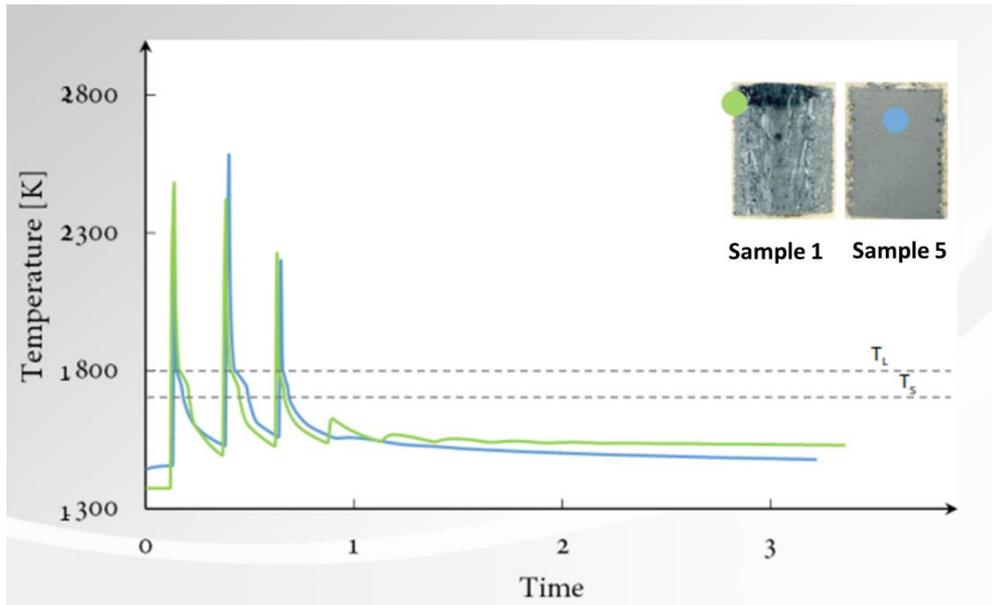
Figure 165: Thermal envelopes comparison between the edge zone of sample 1 and an inner zone of sample 5.

5.6 Conclusions on the effect of the EBM process parameters on the material

The analysis performed on the different samples had the purpose of determine the variation of the material characteristics, in terms of porosity, microstructure, phases distribution, chemical composition, with the variation of the combination of four building parameters (speed function, line offset, max beam current, focus offset).

Regarding the material defect, the observed level of residual porosity was acceptable for a certain parameters window, after the optimization of the process parameters, in particular, the combination bringing to the higher level of porosity is the use of high line offset combined to high speed function.

With the overview of the different results obtained in this study, is possible to correlate them to a very influential factor that is the aluminum content. The different combination of the EBM parameters applied to build each specimen had mainly an effect on the aluminum evaporation during the process and this produced the observed variations in terms of microstructure, phase transition temperature and phase composition.

As conclusion, in order to build components using different process parameters for the different zones to obtain the microstructural properties more suitable for different stress distributions, this study could be the starting point for further research aimed to optimize the building process. According to the obtained results, it is reasonable to focus the research on the shaping of the parameters between the range of values used for sample 4 – 5; in this way, it might be possible to obtain a duplex microstructure, with fine grains, optimizing also the heat treatments and maintaining an uniform and sufficiently high aluminum concentration.

Chapter 6

Electron Beam Melting of TNM TiAl alloy for aircraft engine application

This part of the work was done in collaboration with AvioAero within the European Project E-BREAK [13].

Advanced TiAl alloys, such as β-solidifying TNM alloys, which contains Nb and Mo addictions in the range of 3-7 atomic percent as well, in certain case, as small addictions of B and C, are complex multi-phase alloys.

The main advantages of this alloy are a low density, a high specific elastic modulus and a high specific tensile yield strength. This material class also exhibits excellent oxidation resistance at service temperatures up to 800°C due to high content of Al and Nb.

Recent publications underline the enormous potential and huge demand for novel β-solidifying multi-phase γ-TiAl based alloys for structural components like turbine blades. Forging can be considered the main processing route for this alloy since the higher volume fraction of high-temperature β-TiAl (disordered bcc structure) phase enhance the hot workability. With post-forging heat treatment, the volume fraction of β-TiAl phase can be minimized and this provides balanced properties at room and service temperatures [177]. These alloys can also be

processed by ingot or powder metallurgy as well as precision casting methods [178][179][92].

However, the EBM, that is the most advanced manufacturing method for this alloy has been considered in this work [144][17][125][126].

Regarding the elemental composition, the β-stabilized TNM alloy (TNM = TiAl-Nb-Mo) has a nominal composition range of Ti-(42-45)Al-(3-5)Nb-(0.1-2)Mo-(0.1-0.2)B (at.%) with a preferred composition of Ti-43.5Al-4Nb-1Mo-0.1B [71][180].

For this study, the chosen nominal composition was Ti-44Al-4Nb-1Mo (at.%) and the material was produced by AvioAero using the Electron Beam Melting technology.

The Aluminum content was increased in order to counteract an aluminum loss typical of the EBM process, in addition boron was not inserted because it acts a role of keeping fine grains but finer grained microstructure is already a feature characteristic of EBM process [17] [125] [126].

A first part of the work was the material characterization in terms of residual porosity and as-built microstructure analysis in order to evaluate the material quality after the EBM process. The characteristics phase transition temperatures for this alloy were also investigated as the starting point for the heat treatment set up performed in order to obtain the best microstructure bringing to the desired mechanical properties for the aircraft engine application, in particular for the LPT blades production.

The state-of-the-art considered as a starting point for the heat treatment set up was based on several studies found in literature. In these works a cast/HIP TNM alloy with a nominal composition of Ti-43.5Al-4Nb-1Mo-0.1B (at.%) was considered as a reference material [92].

6.1 Porosity analysis

14 TNM cylindrical specimens were produced by EBM by AvioAero and provided to Politecnico di Torino for the material characterization (**Figure 166**).
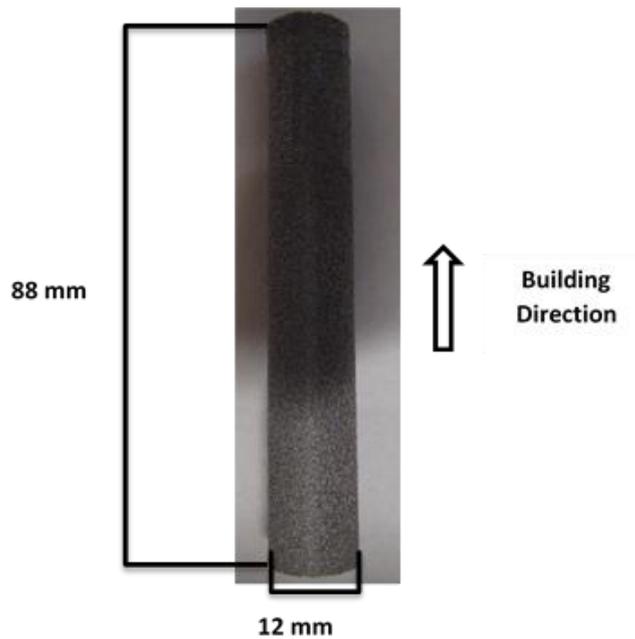
Figure 166: TNM specimen produced by EBM.

The specimens were sectioned as shown in **Figure 167** in order to characterize the material along the EBM building direction.

By observing the material perpendicularly to the building direction, it is possible to detect any residual defects such as elongated pores parallel to the powder layers that are typical of a not optimized EBM process.
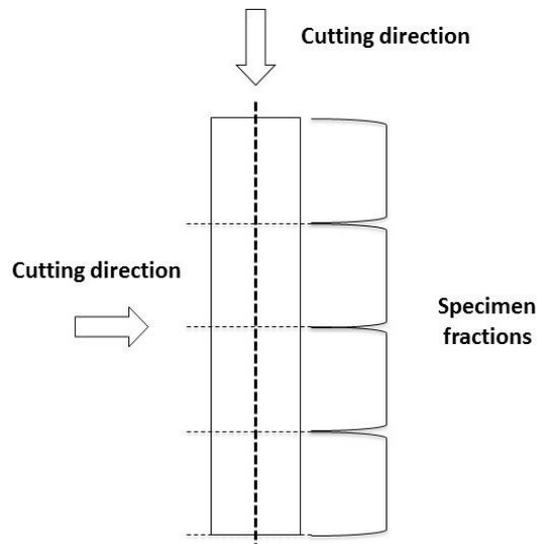
Figure 167: specimen sampling for porosity and microstructural evaluation.

For the residual porosity analysis, two bars were sectioned and 20 optical microscopy images for each section were analyzed according to ASTM E 2109-01 [149].

The average residual porosity, measured for the as-EBM material, was around 0.3% and all the detected pores were spherical and small. The biggest pores observed were lower than 100 µm.

As already described in section 3.1 Powders morphological characterization, this type of small and spherical pores are not caused by the EBM process, but are typical of additive manufacturing techniques that use gas atomized powders. In fact, during the gas atomization process, a small amount of gaseous Ar can remain trapped into the solidified powder particles and in the final EBM processed part it is possible to find some spherical pores whit dimension that are comparable to those of the pores observed inside the powder particles [66].

In agreement with AvioAero and with previous work on EBM materials [17] [125] [126], the as-EBM material was considered acceptable from the porosity point of view.

Some images, showing characteristic residual pores observed, are reported in **Figure 168** and **Figure 169**.
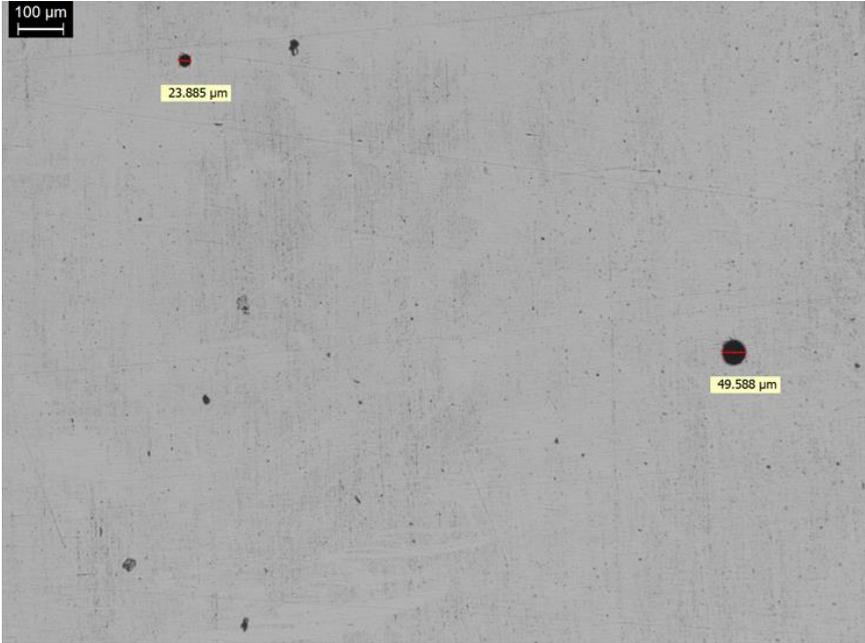
Figure 168: optical microscopy images of material porosity and pores dimensions.
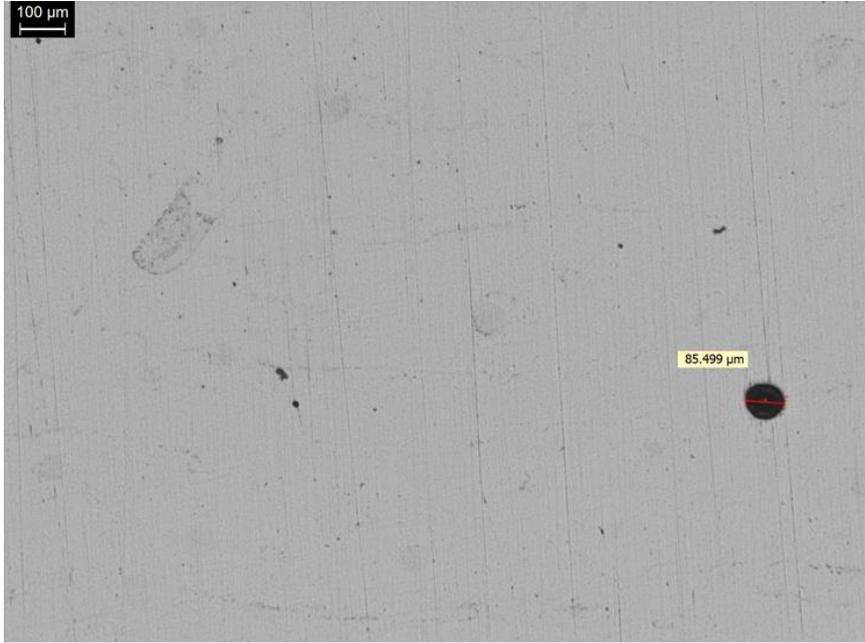
Figure 169: optical microscopy images of material porosity and pores dimensions.

6.2 Chemical analysis

The elemental chemical analysis was performed on the TNM powder and on the material processed by EBM by means of inductively coupled plasma (ICP) for Al, Nb, Mo and Fe, combustion - infrared adsorption and/or thermal conductivity detection for C and inert gas fusion infrared detection for N and O.

The chemical analysis results are reported in **Table 35**.

Table 35: Elemental chemical composition of the TNM powder and material processed by EBM.

		Al	Nb	Mo	Fe	O	N	C	Ti
		Chemical composition in wt.% and at.%							
Powder	wt.%	30.30	8.81	2.49	0.02	0.101	0.003	< 0.005	Bal.
	at.%	45.49	3.84	1.05	0.01	0.256	0.009	< 0.017	
As-EBM	wt.%	28.80	8.86	2.48	0.04	0.085	0.003	0.019	
	at.%	43.68	3.90	1.06	0.03	0.217	0.008	0.0648	

The measured chemical composition was considered acceptable since it was conform to the chemical composition range required by the specification.

6.3 As-EBM microstructure and phase analysis

The microstructure of the material processed by EBM was evaluated using the Field Emission Scanning Electron Microscopy technique (FE-SEM). Optical microscopy evaluation is difficult for this type of alloy because of the too fine microstructure. In particular, the secondary electron mode and backscattered electron mode were adopted in order to better appreciate the different phases having different densities

and this give them different contrast that helps to distinguish the phases during the analysis.

The as-EBM microstructure observed at different magnifications is reported in **Figure 170** and **Figure 171**.
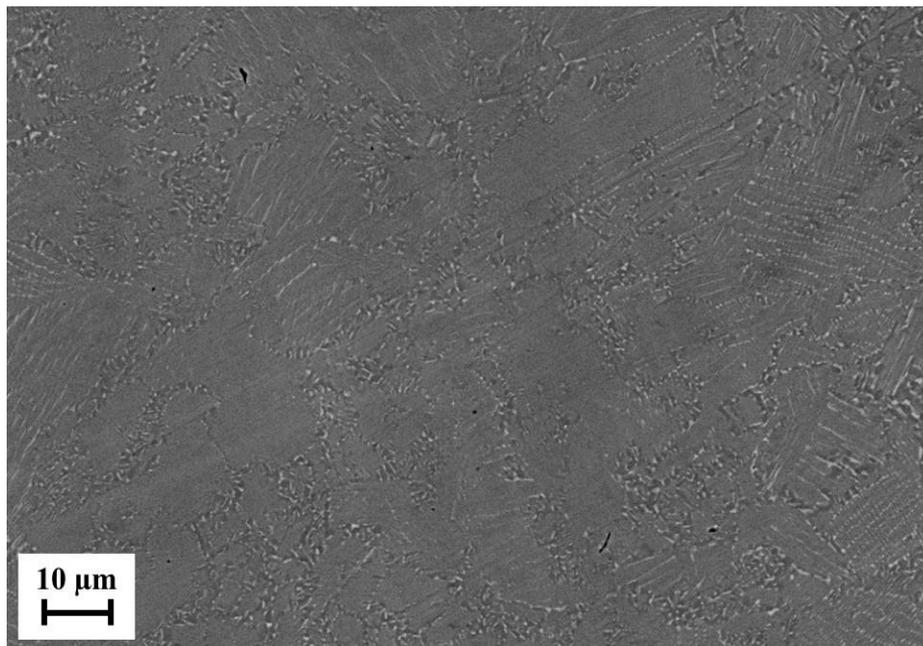
Figure 170: SEM image of the as-EBM TNM alloy.
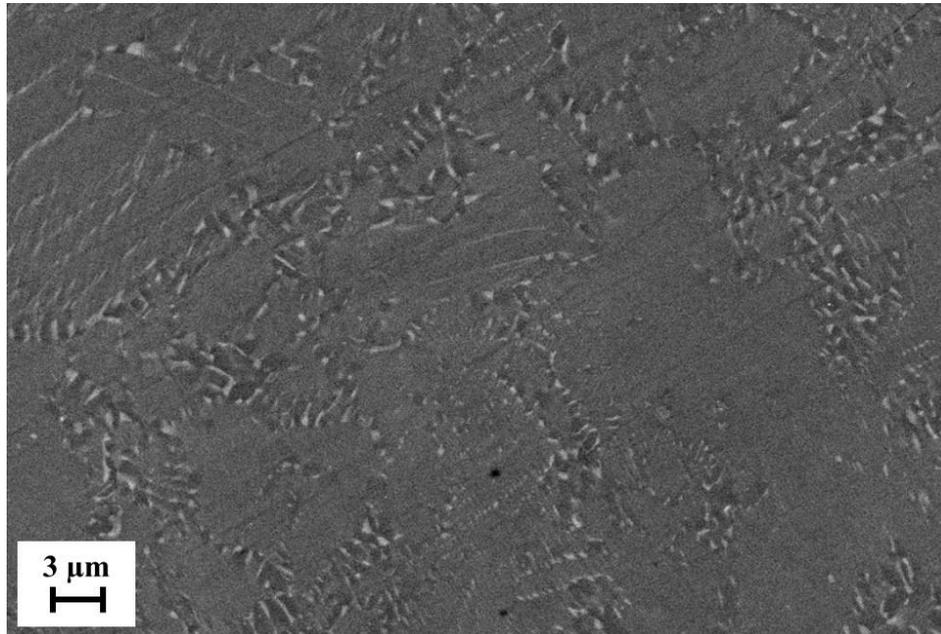
Figure 171: SEM image of the as-EBM TNM alloy.

An elemental chemical analysis of the different phases observed in the FE-SEM micrographs was attempted by the Energy-Dispersive X-ray spectroscopy technique (EDX) and the results in wt.% and at.% are shown in **Table 36**. The obtained values are to be considered taking in account of a consistent measurement uncertainty because the EDX analysis spot was bigger than the analyzed grains.

Table 36: EDX analysis results. Different phase compositions.

As-EBM	EDX elemental composition wt.%				EDX elemental composition at.%			
	Al	Ti	Nb	Mo	Al	Ti	Nb	Mo
γ-grains	30.21	57.89	10.03	1.87	45.59	49.21	4.40	0.79
β-phase	25.76	58.94	10.84	4.45	40.66	52.40	4.97	1.98
α₂/γ colonies	28.61	59.08	9.71	2.60	43.72	50.86	4.31	1.12

The main differences in elemental composition between the phases are that the β-phase is richer in Mo, that is the β stabilizer element, and the γ-grains present a slightly higher Al content respect to the other phases. The elemental composition of the α₂/γ colonies is the closer to the elemental chemical composition of the alloy (**Table 35**). This suggest that the As-EBM microstructure is composed by a

considerable α₂/γ colonies fraction, as it is also possible to observe from the FE-SEM images, that was quantified about 75%, with average lamellar dimension of 10µm. The volume fraction of β-phase in the as-EBM microstructure resulted 4%, determined by image analysis method.

The analyzed phases having different elemental composition are indicated in the FE-SEM image at higher magnification (**Figure 172**). The three different phases that can be distinguished also for their different contrast are:

1. Small and dark grains → globular γ-grains, with average dimension around 1µm;
2. Coarse lamellar grains → α₂/γ colonies;
3. Small and bright grains located at the grains boundaries between the other phases → β-phase.
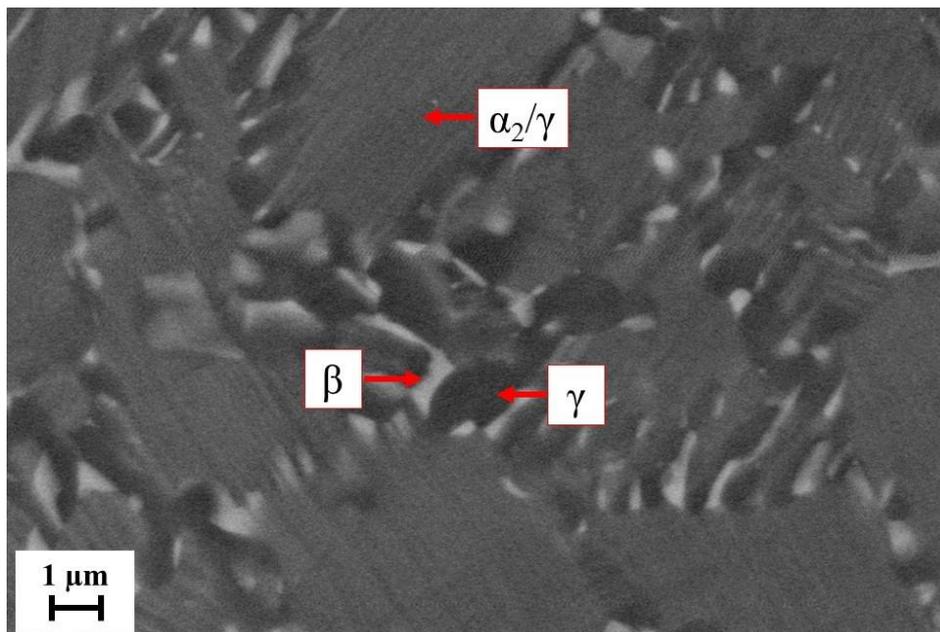
Figure 172: SEM image of the as-EBM TNM alloy. The three different phases are indicated.

The phases investigated by FE-SEM analysis can be compared with some literature on TNM alloy [71] [178] [92].

6.4 Thermomechanical Analysis (TMA) and phases evolution investigation

Similarly to what was done for the 48-2-2 alloy, the thermomechanical analysis (TMA) was performed on a TNM alloy specimen in order to investigate and get indications about the phase transformations for this alloy [154].

The obtained result is shown in **Figure 173**.
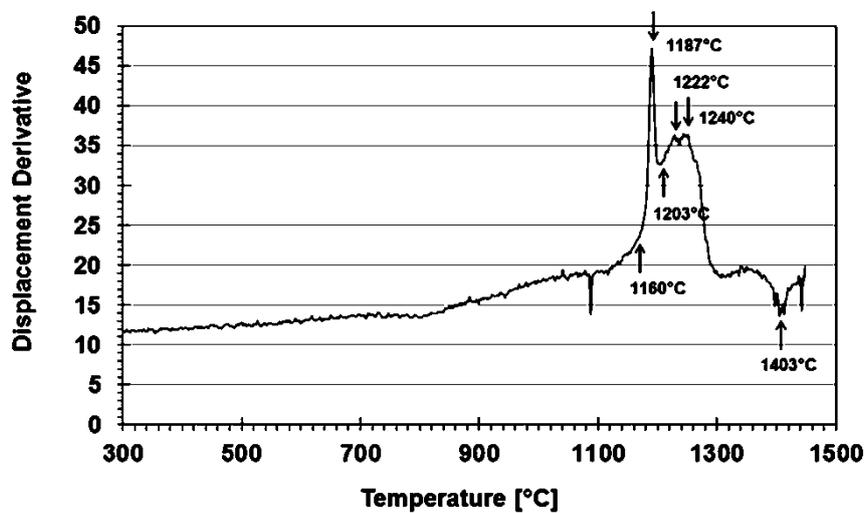
Figure 173: TMA measurement for TNM alloy: displacement derivative vs temperature. The phase transition peaks are indicated.

The result was compared with literature data, for a TNM alloy with a composition of Ti-43.67Al-4.08Nb-1.02Mo-0.1B [92] [181].

In the work of Schwaighofer E. et al. [92], the phase fraction evolution was determined by in-situ HEXRD experiments and confirmed by DSC experiments on cast/HIP material. The quaternary phase diagram was also estimated by means of thermodynamic calculations in order to obtain additional information on phase transition temperatures (**Figure 174**).
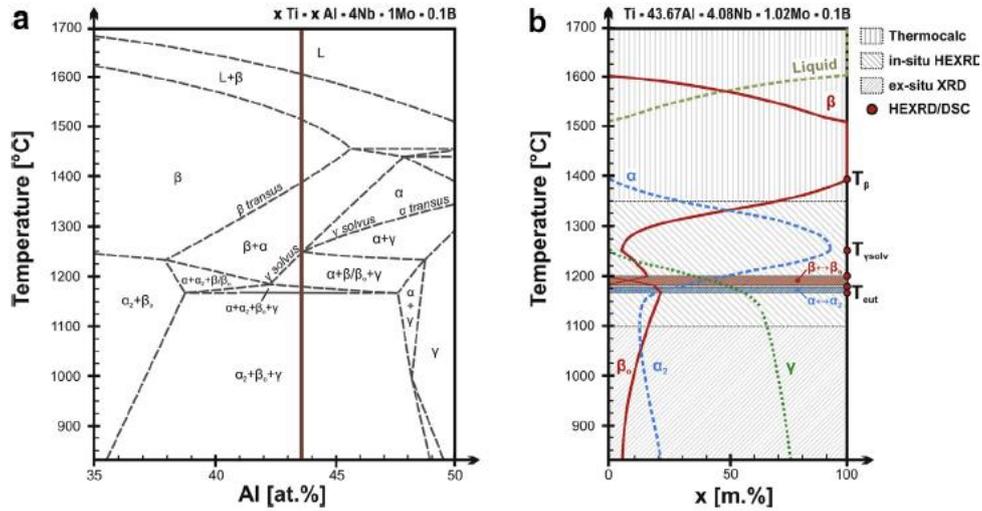
Figure 174: a) Experimental quasi-binary section through the TNM alloying system. The Al-content of the investigated alloy is indicated as a vertical line. b) Course of phase fractions with temperature for the investigated alloy composition Ti-43.67Al-4.08Nb-1.02Mo-0.1B [92].

The literature phase transition temperatures are reported in **Table 37**.

Table 37: phase transition temperatures for TNM alloy from HEXRD and DSC [92].

Phase transitions	**Phase transition temperatures from HEXRD and DSC [°C]**
T_{eut}	1160
$T_{\alpha2 \to \gamma}$	1160-1175
$T_{\beta0 \to \beta}$	1175-1205
$T_{\gamma solv}$	1255
T_{β}	1405

In accordance to the literature results and the experimental Ti-Al quaternary phase diagram for TNM alloy [92], the observed TMA peaks were thus correlated to the corresponding phase transitions of our TNM alloy and the temperatures and temperature ranges for the different phase transitions are resumed in **Table 38**.

Table 38: Experimental phase transitions temperatures determined by TMA.

Phase transitions	Experimental phase transition temperatures from TMA [°C]
T_{eut}	1160
$T_{\alpha2 \rightarrow \gamma}$	1160-1187
$T_{\beta0 \rightarrow \beta}$	1187-1203
$T_{\gamma solv}$	1240
T_{β}	1403

It is possible to observe that the phase transitions determined by means of TMA are comparable with those from literature. However, from the displacement derivative versus temperature diagram, two peaks are observed in the temperature range from 1203°C to 1240°C, in particular at 1222°C and at 1240°C. From the comparison with literature data, the peak that could be attributed to the γ solvus transition temperature is that at 1240°C. The slight differences in transition temperatures between literature and experimental TMA results could be attributed to the difference in the alloys composition; in fact, as described in section 1.5 The binary Ti-Al phase diagram the variations in alloying elements and their amount have a strong influence on the phase transformation temperatures.

The information given by the TMA analysis was also useful for the heat treatment set up, because it was possible to decide the heat treatment temperature in order to obtain the desired microstructure, according to the phase transition temperatures identified with this technique.

6.5 Post-HIP microstructure and phase analysis

Hot Isostatic Pressing (HIP) treatment was performed by AvioAero on the post-EBM material in order to homogenize the post-EBM microstructure and to reduce or eliminate any residual porosity in the material.

In **Figure 175** a FE-SEM of the microstructure obtained after the HIP process is shown. The different phases identified are indicated in the image.
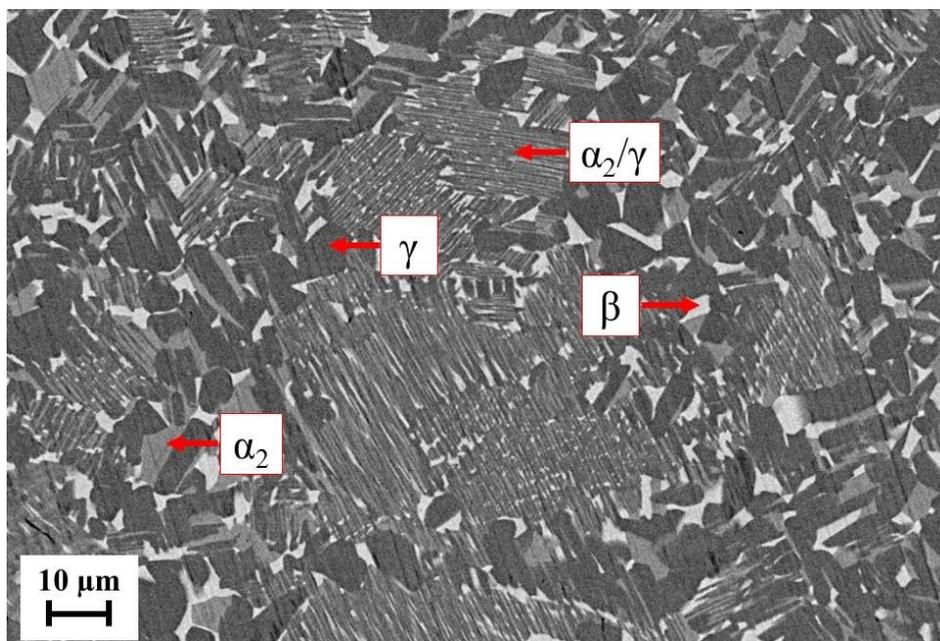
Figure 175: BSE FE-SEM image of the TNM microstructure after the HIP.

The different phase observed are:

1. Small and dark grains → globular γ-grains,;
2. Coarse lamellar grains → α_2/γ colonies;
3. Small and bright grains located at the grains boundaries between the other phases → β-phase.
4. Small and grey grains which are in between globular γ-grains and the β-phase → α_2 phase

The phases observed are the same of the as-EBM material except for the small and brighter grains that in some cases seems to be part of the γ-grains. This phase can be identified as the α_2 Ti_3Al phase.

Figure 176 shows the comparison between the post-HIP microstructure and the as-EBM microstructure.
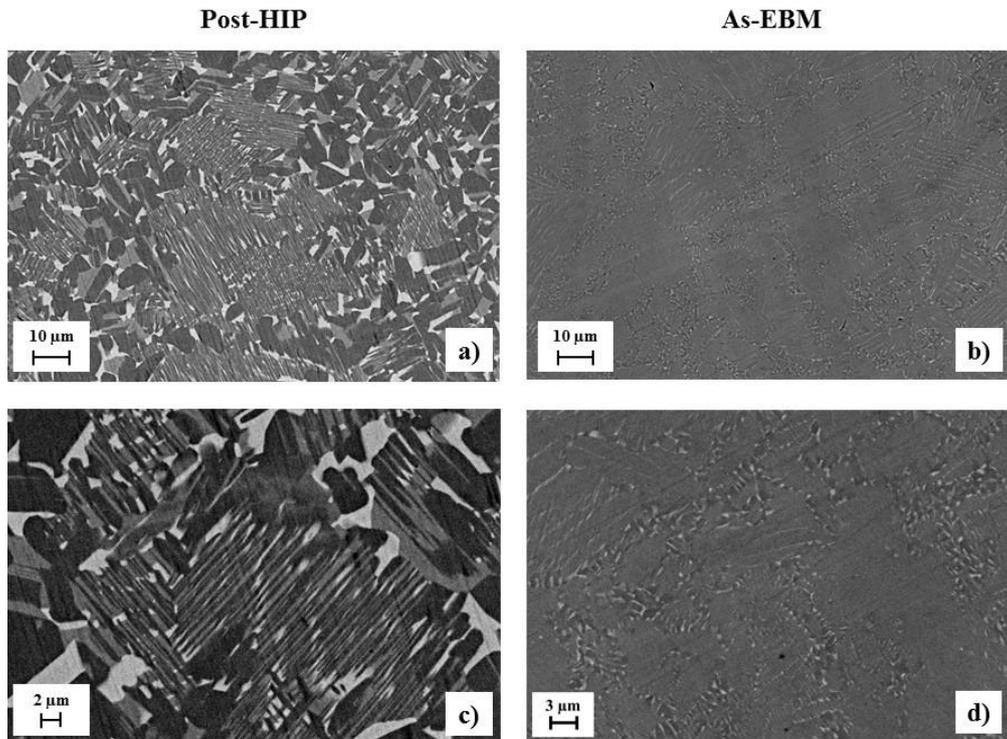
Post-HIP   As-EBM

Figure 176: post-HIP and as-EBM microstructures comparison. 7a) and 7c): post-HIP microstructure at different magnifications; 7b) and 7c): as-EBM microstructure different magnifications.

According to Shwaighofer et al., during the HIP process, a decomposition reaction within the α_2/γ – colonies according to $\alpha \rightarrow \beta + \gamma$ takes place. This produces an increase in γ lamellae thickness and the formation of secondary precipitates of the β_0 – phase within the α_2/γ – colonies. The microstructure changes because of a strong phase imbalance of the as-EBM microstructure. During HIP the material undergoes also a recrystallization [92].

It is possible to observe from the micrographs that the HIP process increase the average dimension of the globular γ grains (about 8µm) and the lamellar colonies (18µm). However, the overall microstructure after the HIP process is still fine. Lamellar colonies, with volume fraction of 65% on the overall phases, reach a maximum length of about 20-30 µm as it is possible to observe from the comparison in **Figure 176**.

The microstructure obtained after the HIP process is quite similar if compared to the post-HIP microstructure obtained for a TNM alloy produced by casting. The main difference is that the EBM process brings to a finer microstructure with a lamellar colonies maximum length of about 20-30 µm versus about 150 µm of the HIP material and the EBM material presents a lower amount of β-phase (about 8%). **Figure 177** shows SEM images from literature at different magnifications of post-HIP microstructure of the TNM material produced by casting [92].
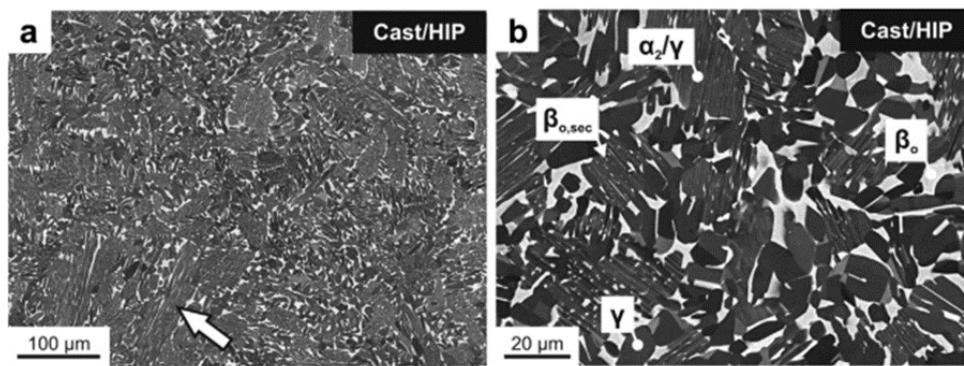
Figure 177: Reference microstructure determined by SEM in BSE mode: a) As-cast and hot-isostatically pressed (cast/HIP) starting condition. The white arrow indicates a coarse α2/γ-colony. Coarse α2/γ-colonies have a typical dimension of 150 µm in length and 30 mm [92].

The fine duplex microstructure after the HIP process was considered acceptable as the starting condition for the ensuing heat treatment set up.

6.6 Heat treatment set-up

According to the TMA results and to some literature (see 1.10 Alloy development and generations of γ-TiAl alloys"), because of the similarity with the cast material which is already proved to have good mechanical properties, the material processed by EBM and HIPped, was subjected to five different heat treatments. The heat treatment set up was necessary in order to understand the microstructural evolution of the TNM alloy and to select the heat treatment conditions bringing to the most suitable microstructure for the turbine blade aircraft application.

The performed heat treatments and the obtained microstructure are shown in the following.

The exact heat treatment temperatures are not given in this thesis because they are of industrial interest and confidential only.

- **HT1**

The first heat treatment was conducted at a temperature just below the γ-solvus temperature. For all the heat treatments, after the annealing, a stabilization treatment for six hours near service temperatures was performed.

The microstructure obtained with the HT 1 is shown in **Figure 178** and **Figure 179**.

It is possible to observe that, with the HT 1, a microstructure with a large amount of lamellar colonies, about 78%, presenting big dimensions (average dimension of 25µm, and maximum lamellar colonies dimension about 80 µm) is obtained. It is also possible to notice that the lamellar thickness is very low and in comparison to the post-HIP microstructure, there is a decrease of the β-phase (6% vs 8% of the HIPped). The average equiaxed γ-grains dimension is around 7µm.
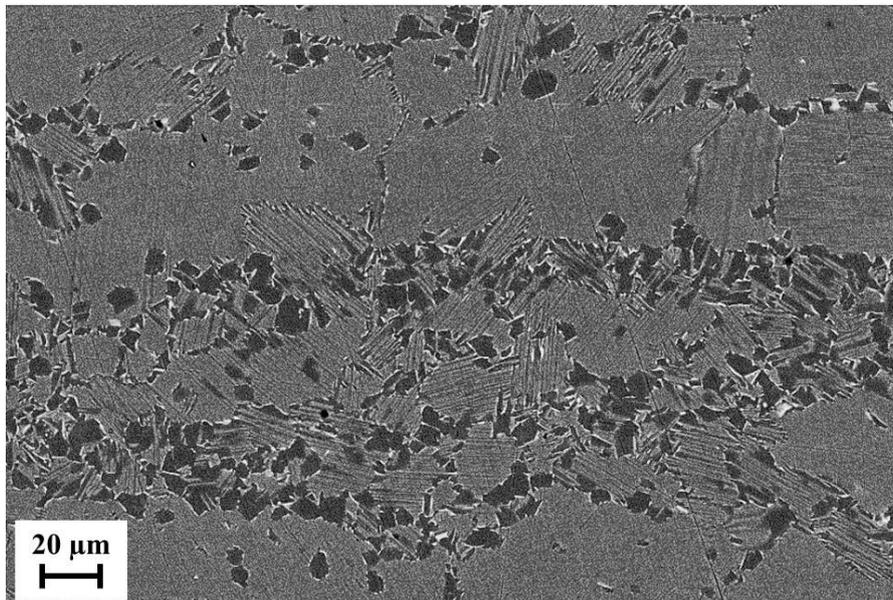
Figure 178: Microstructure after HT 1.
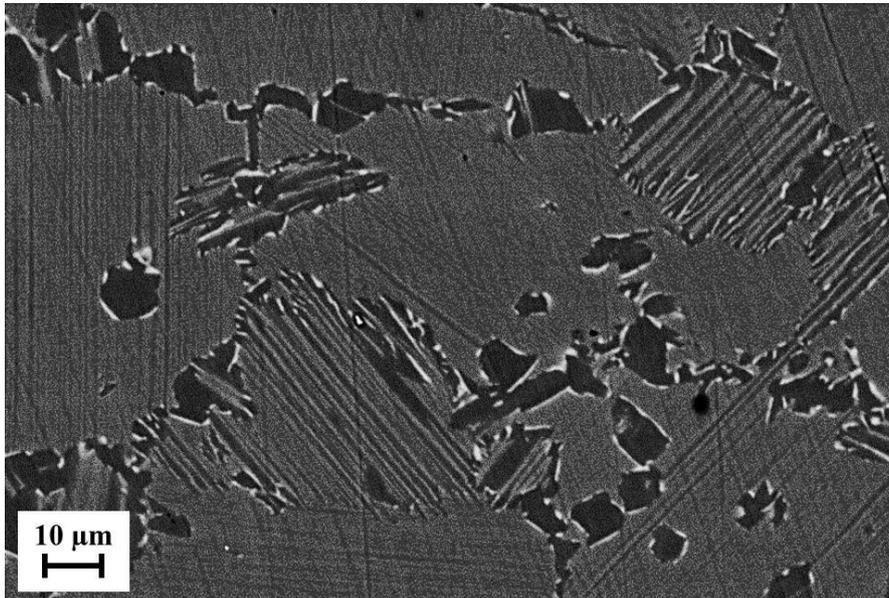
Figure 179: Microstructure after HT 1.

In order to better understand the microstructural evolution around the γ-solvus temperature, a fine-tuning of the heat treatment was performed treating the post-HIP material at:

- 10°C below the HT1 → HT1'
- 10°C above the HT1 → HT1"

- **HT1'**

In **Figure 180**, **Figure 181** and **Figure 182**, the microstructure obtained with the HT1' is shown.
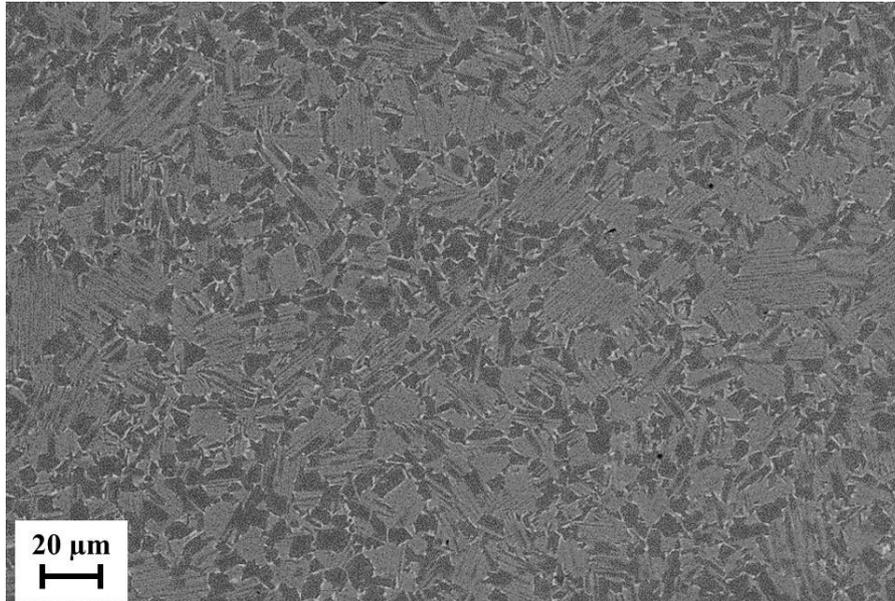
Figure 180: Microstructure after HT 1'.
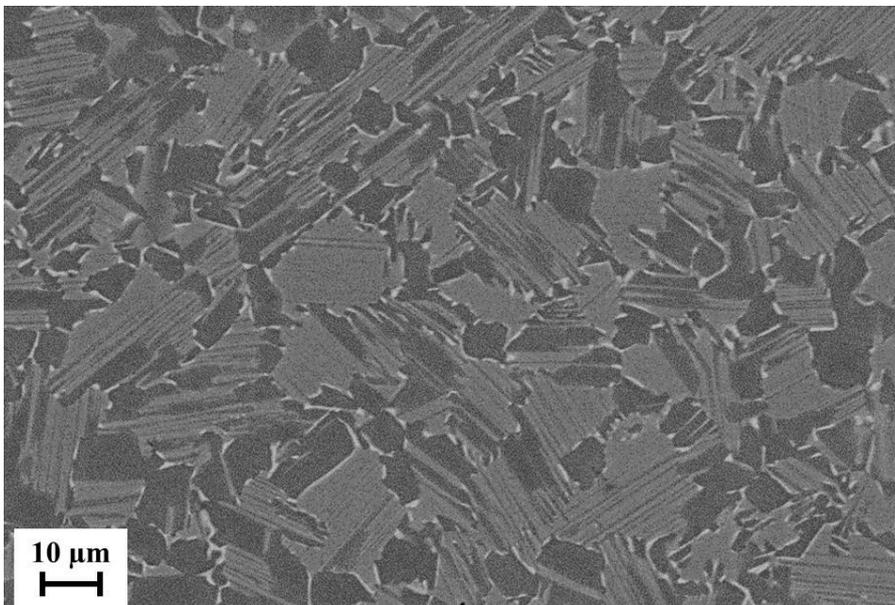
Figure 181: Microstructure after HT 1'.
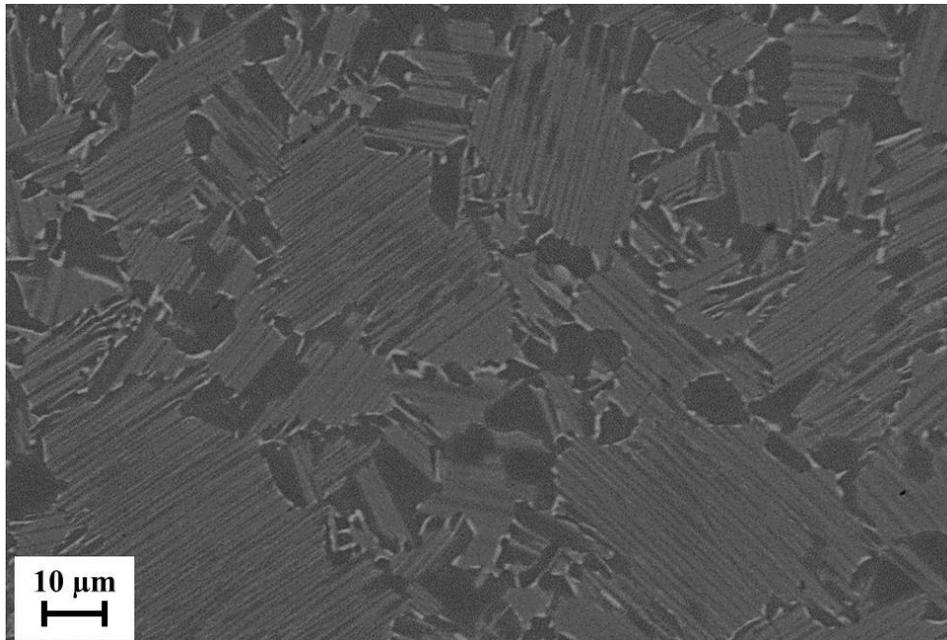
Figure 182: Microstructure after HT 1'.

The microstructure obtained with the HT1' is a duplex microstructure presenting a lower amount of lamellar colonies (65%) with smaller dimensions, compared to HT1 microstructure. The lamellar width ranges from about 10 µm to a maximum of 40 µm with an average grain size of 15µm. The equiaxed grains dimension is similar to that of HT1 (6µm) Also for this microstructure, it is possible to appreciate a small amount of β phase at the grain boundaries (5%).

- **HT1"**

HT1" was performed at 10°C above the HT1. In **Figure 183**, **Figure 184** and **Figure 185** the microstructure obtained with this heat treatment is shown.
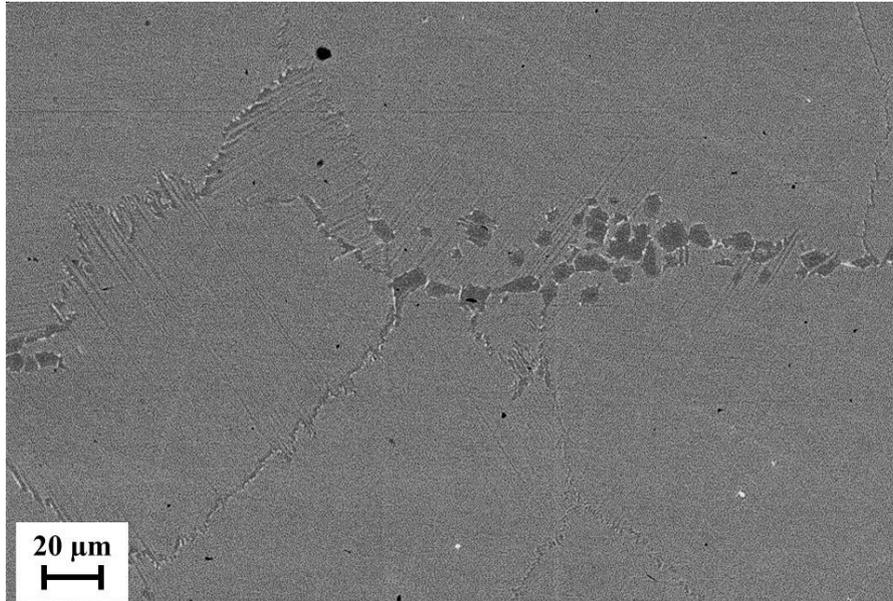
Figure 183: Microstructure after HT 1".
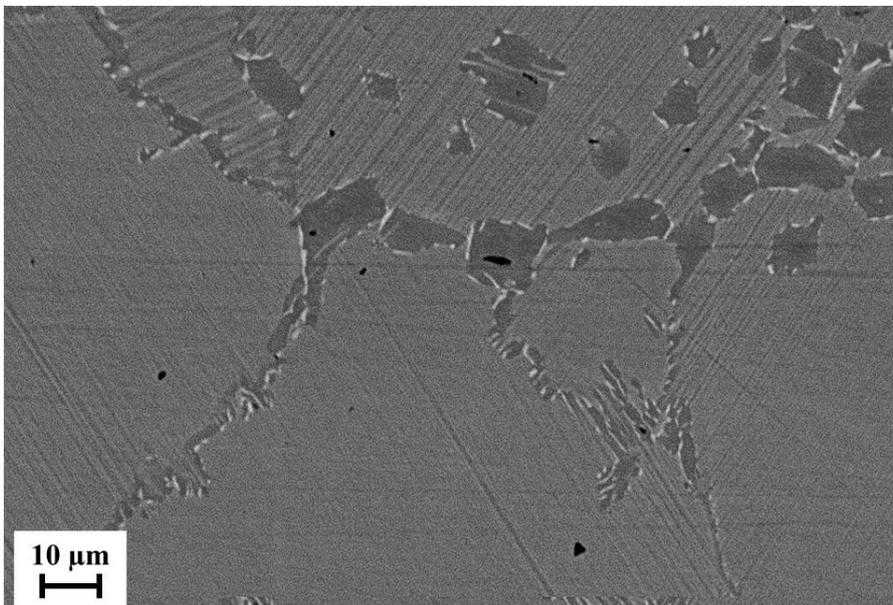
Figure 184: Microstructure after HT 1".
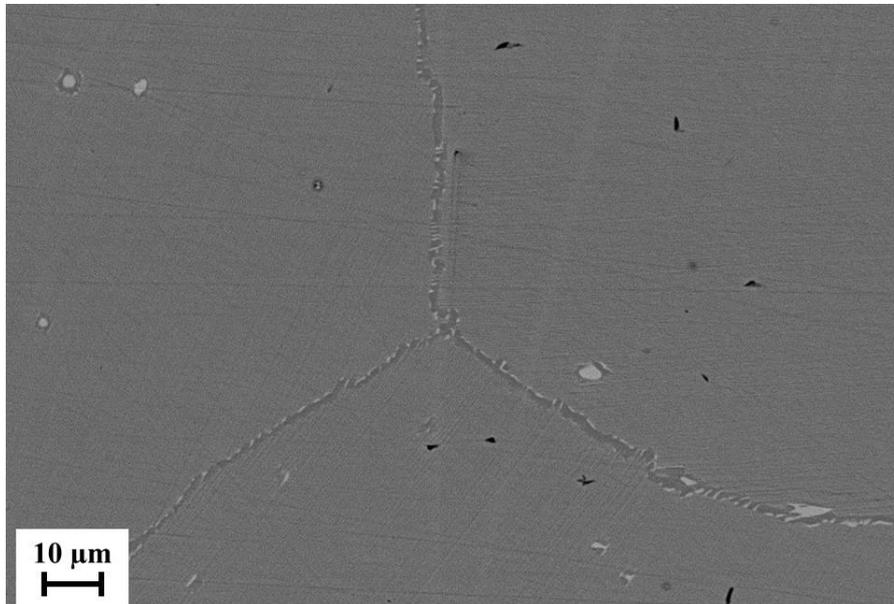
Figure 185: Microstructure after HT 1''.

With the HT1", the obtained microstructure was a near lamellar microstructure (NL) presenting a larger amount of lamellar colonies, about 94% volume fraction, having bigger dimensions and a small amount of γ-phase confined at the grain boundaries, with γ- grains ranging from 2 to 10µm. The average lamellar colonies dimension is 50µm, with some large colonies up to 100 µm width and the spacing between them is very low. With this heat treatment, the β-phase amount is further reduced (1.5%) compared to the first two heat treatment.

In order to investigate other microstructures bringing to a material with higher creep resistance and good tensile properties, two other heat treatments at higher temperatures (HT2 and HT3) were evaluated.

- **HT2**

This heat treatment was performed at a higher temperature, far above the γ-solvus temperature, in the β-phase region.

The microstructure obtained with the HT2 is shown in **Figure 186**, **Figure 187** and **Figure 188**.

Because of the coarser colonies produced by this heat treatment, the microstructural evaluation was possible by using lower magnifications.
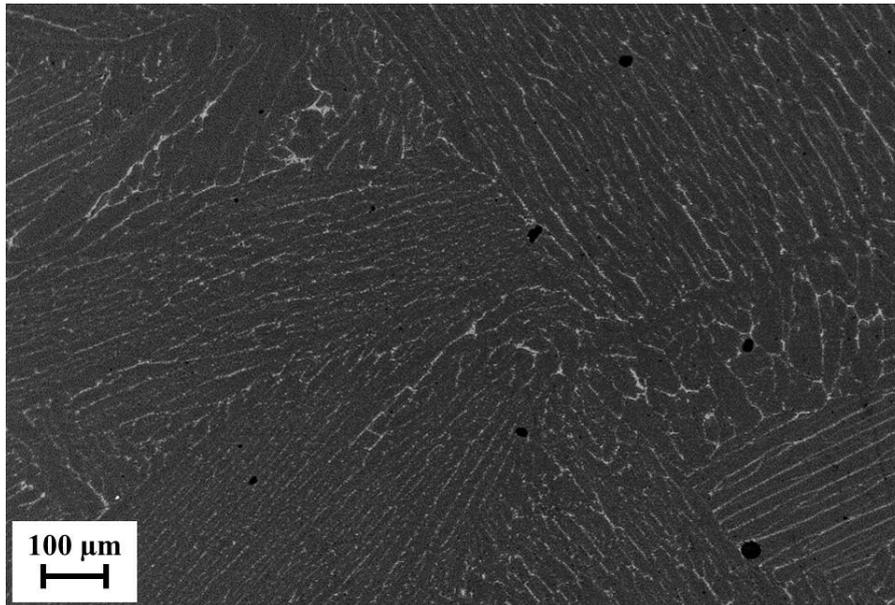
Figure 186: Microstructure after HT2.
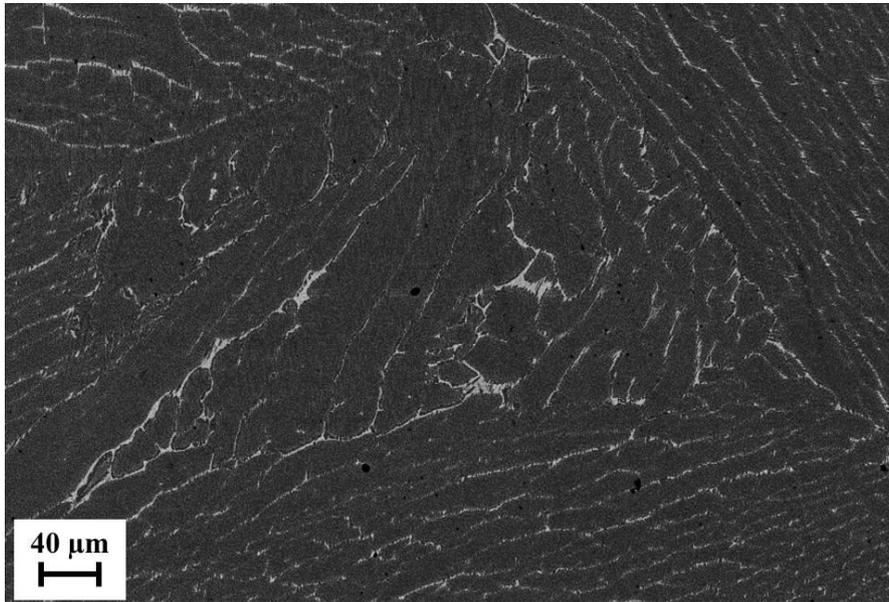
Figure 187: Microstructure after HT2.
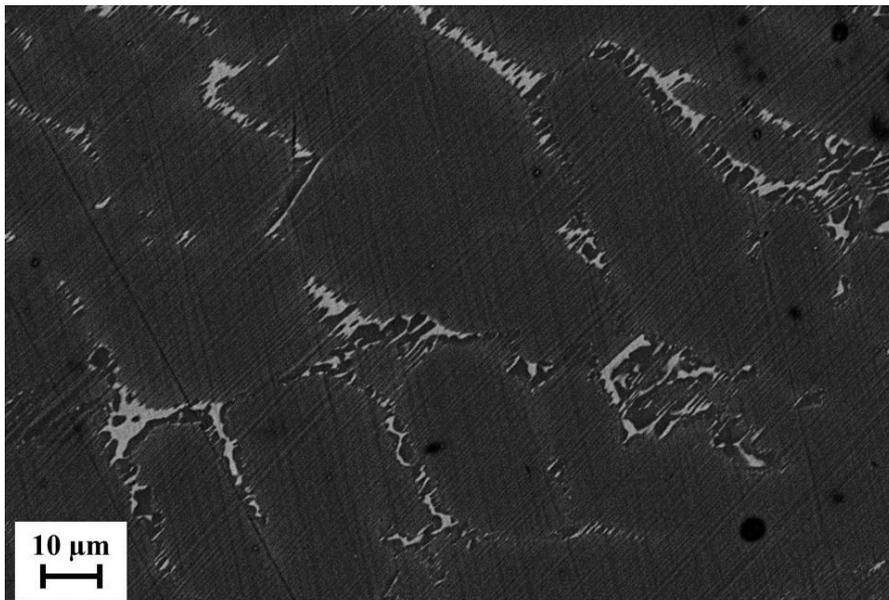
Figure 188: Microstructure after HT2.

With HT2, a near lamellar microstructure, presenting the 90% of lamellar colonies, was obtained. From the lower magnification images, it is possible to appreciate extended lamellar colonies with average dimension of 50µm, with grains oriented in different directions. The spacing between lamellar grains is higher

compared to the other microstructures and, from higher magnification images (**Figure 188**), it is possible to appreciate the presence of small globular γ-grains, ranging from 1 to 8µm, and a volume fraction of 4% of β-phase at the lamellar grains boundaries.

- **HT3**

With HT3, a solution annealing was performed at the same annealing temperature of HT2, than, after a cooling at room temperature, a second annealing at a temperature around the γ-solvus temperature, in the range of the β – phase minimum was performed in order to adjust an almost fully lamellar microstructure. Also for this heat treatment, the stabilization treatment was performed.

The microstructure obtained with this heat treatment are shown in **Figure 189**, **Figure 190** and **Figure 191**.
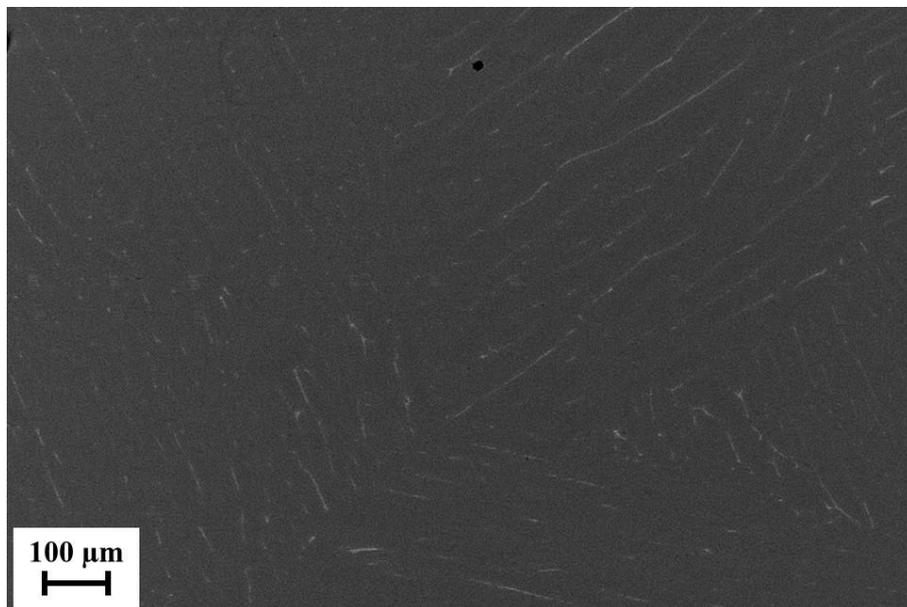
Figure 189: Microstructure after HT3.
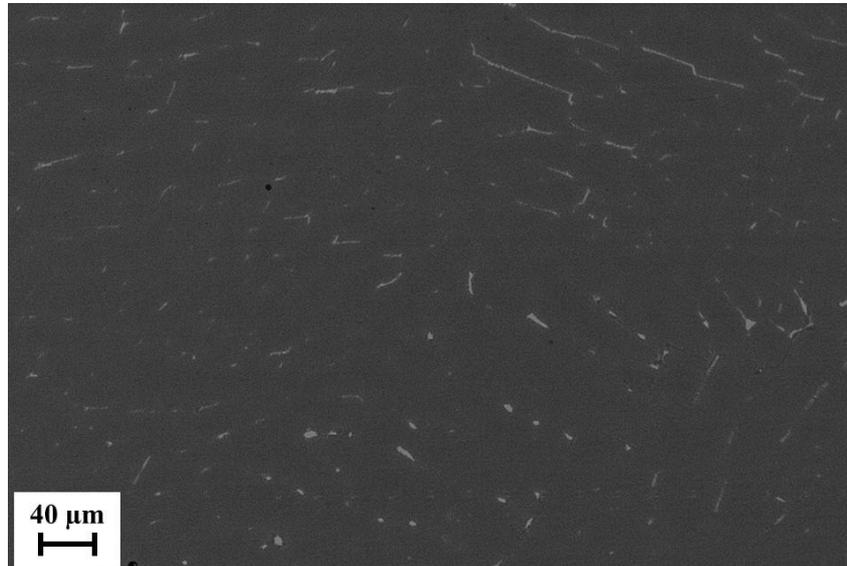
Figure 190: Microstructure after HT3.
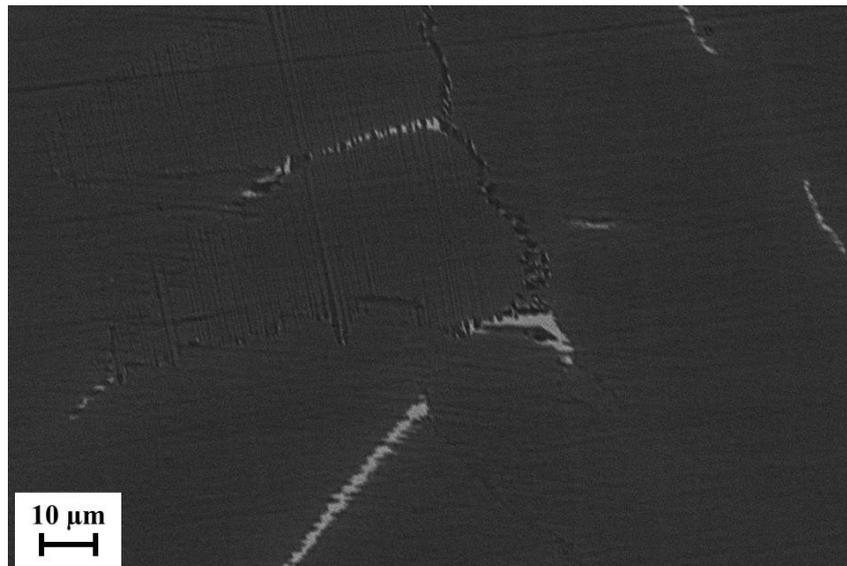
Figure 191: Microstructure after HT3.

As expected, this heat treatment has produced an almost fully lamellar microstructure (95% of lamellar colonies), similar to the one obtained with HT2 but with a very small amount of small globular γ-grains, about 2%, with small dimension about 2µm, confined at the lamellar grain boundaries. However, some β-phase (2%) can be observed between the lamellar colonies.

6.7 X-Ray diffraction analysis

The observed microstructures after the EBM process, after the HIP treatment and after the different heat treatments, were also confirmed in terms of phase composition by the X-Ray diffraction analysis.

In **Figure 192** the diffractograms of the TNM specimen in the different heat treatment condition are shown.
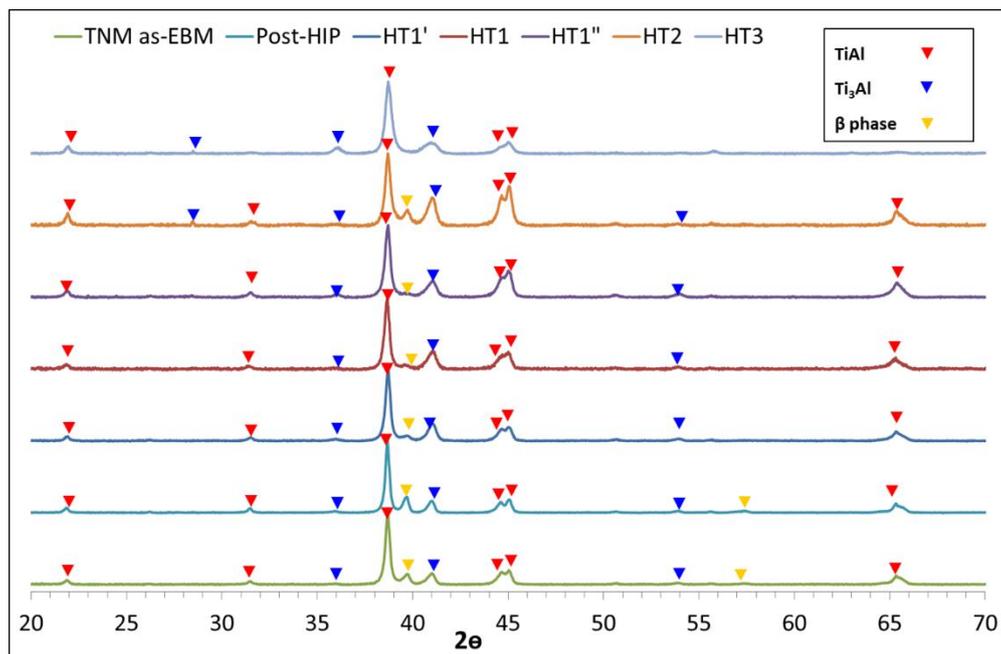
Figure 192: X-Ray diffractogram of as-EBM, post-HIP and heat treated specimens; the different phases are indicated by colored arrows

The X-Ray diffraction analysis has highlighted the presence of the γ-TiAl phase (red arrow), the α_2-Ti$_3$Al phase (blue arrow) and the β phase (yellow arrow). There is a correlation between the observed microstructures and the X-Ray diffractograms where it is possible to notice a reasonable increase of the α_2-Ti$_3$Al phase for the specimens treated at higher temperatures. The β phase peaks are more evident for the as-EBM, post-HIP and post-HT2 specimens, in agreement to what observed from the FE-SEM micrographs. This phase compositions was also pointed out by the EDX analysis for the as-EBM and post-HIP material.

6.8 Conclusions on Electron Beam Melting of TNM TiAl alloy for aircraft engine application

The studies on the TNM TiAl alloy produced by EBM have demonstrated the possibility to process this alloy by the EBM technology and to obtain a desired microstructure after a proper heat treatment in order to improve the mechanical properties of the material.

The residual porosity after EBM was acceptable in terms of pores size and number of defects.

The chemical composition of the TNM alloy is in the required nominal chemical composition range.

The HIP process is necessary to close or shrink any bigger residual defects and to homogenize the microstructure after EBM.

The microstructure obtained after the HIP treatment was the starting point for the heat treatment set up and the thermomechanical analysis (TMA) was adopted for the phase transition temperature investigation.

The analysis of the microstructures obtained with the different heat treatments, has demonstrated that the most promising heat treatment are the HT1' and HT2.

The HT1' has been considered the most promising in terms of good room temperature ductility, tensile properties and with sufficient creep properties. The limited amount of β phase acts as a grain growth suppressor and improve the high-temperature ductility. The room temperature ductility is improved by the presence of globular γ-grains. It is worth notice that the boundary structures between the grain colonies strongly influence mechanical properties. As demonstrated by Leitner et al., the fracture toughness strongly depends on structure and phase arrangement at the boundaries and can be enhanced by thick boundary areas consisting of unconnected β_0 and γ grains. On the contrary, a connected β_0-phase at the colony boundaries that provide lamellae parallel to the subsequent fracture surface reduce the fracture toughness [182].

Moreover, the observed α_2/γ-lamellar colonies are not preferentially oriented and present small size with a small lamellar spacing. These α_2/γ-lamellar colonies features are expected to give good strength, HCF fatigue properties and ductility.

However, if the microstructure obtained with the HT1' will reveals some weakness in creep resistance, HT2 can be considered because the microstructure obtained with it should lead to a higher creep resistance without a considerable decrease in tensile properties. In fact, a lower amount of globular γ-grains and the presence of bigger α_2/γ-lamellar colonies is expected to improve the creep resistance of the material.

A comparisons between mechanical properties and microstructures can be based on literature data for the TNM alloy produced by casting and forging [179] [92] [136] [75] [177] [182].

Some mechanical tests (tensile, creep, fatigue and fatigue crack growth), were performed by Avio during the SP5 part of the E-Break project on the heat-treated EBM material. These tests have shown promising mechanical properties for this material compared to the same material produced by casting and the TiAl 48-2-2 alloy produced by both casting and EBM. However, the results cannot be disclosed in this thesis because the data are of industrial properties.

Chapter 7

Electron Beam Melting of TiAl RNT650 alloy for automotive application

The application of new high-performance titanium aluminide alloys within turbochargers has been confirmed by numerous spin and engine tests and in at least one successful low volume production automotive application in Japan where the TiAl wheels were produced by investment casting [44] [32] [58]. The improvement in vehicles performance will come through higher boost levels and reduced turbo lag due to the higher allowable operating temperatures and the lower mass moments of inertia of the TiAl wheel shaft assemblies compared with Ni based wheel shaft assemblies. Despite the excellent technical properties of TiAl turbo chargers such as a lower weight leading to an engine efficiency and acceleration improvement, this type of alloy is not currently used in mass production turbine wheel assemblies.

The two major reasons why TiAl turbochargers are still not produced in an industrial scale are that the turbine wheel manufacturing process (casting) suffers from high failure rates, low productive efficiency related to the high cost and the technology required to join TiAl turbine wheels to standard steel shafts is not flexible or reliable enough to be used for mass production. Another considerable drawback is the low workability of TiAl alloys due to the brittleness of these materials.

A great effort is made to develop new TiAl alloys with higher properties fitting the automotive engine requirements. Next generation turbo chargers that using improved TiAl alloys will could be able to operate at higher temperature ranges, comparable to those of superalloys turbochargers, and it will increase the engines performance levels. This will significantly contribute towards the reduction of CO_2 emissions in passenger vehicle through the market introduction of turbo chargers into diesel and petrol engine powered vehicles as well as improving the efficiency in all turbocharged engines utilizing this technology.

In this thesis work, the activities related to the TiAl material development for turbocharger application were carried out within the European project TIALCHARGER.

The overall objectives of the TIALCHARGER program, are the processing of titanium aluminide turbocharger turbine wheels by Electron Beam Melting (EBM) and the production of a wheel-shaft assembly prototype in order to demonstrate joining feasibility [14].

In this part of the work, TiAl-based powder of Ti-48Al-2Nb-0.7Cr-0.3Si (at.%) (RNT650 alloy), was used to fabricate specimens and prototypes of turbocharger turbines by Electron Beam Melting (EBM).

TiAl turbochargers have to resist to extreme operating environments hence this particular TiAl alloy has been used to produce the considered components for automotive application. The presence of silicon was demonstrated to be effective for enhancing creep strength and to increase the oxidation resistance [115] [44]. The alloy having the same chemical composition of the RNT650 alloy is named DAT-TA1 and it was developed by DAIDO steel CO. LTD [116].

The TiAl RNT650 alloy test specimens (cylinders and cubes with a volume of 1000 mm^3) and turbocharger wheels were produced via EBM by the Fraunhofer Institute for Manufacturing and Advanced Materials in Dresden. Thanks to the freedom in design given by EBM, hollow turbine wheels were produced bringing to a further reduction of the component weight.

In **Figure 194** an exemplary samples placement for the EBM fabrication of prototype wheels is shown. In order to increase productivity, the wheels can be produced stacked in different process layers. To avoid the distortion of components

during the EBM process, different support structures were tested for single and stacked samples.

The additional cylindrical samples were built together with the wheels to improve the temperature homogeneity inside the building chamber during the EBM process and also to be used as representative test specimens for material characterization.

Part of this study about the RNT650 alloy was published on Intermetallics [127].

Figure 193: preliminary RNT650 test specimens produced by EBM
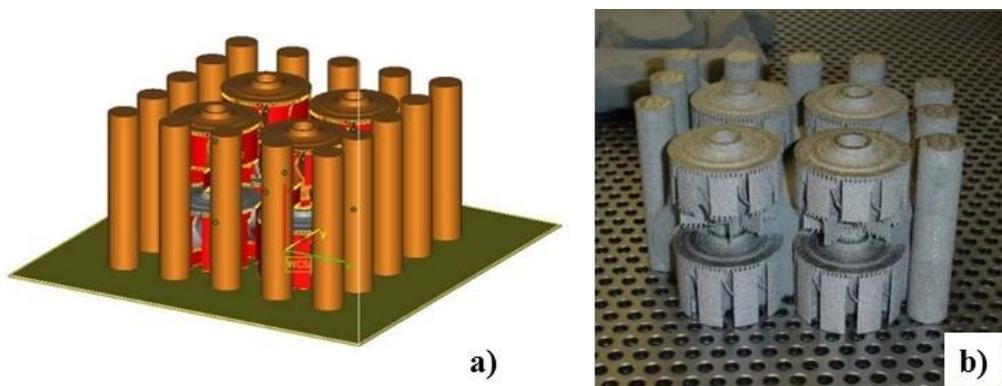
Figure 194: a) samples placement scheme within the EBM built chamber; b) Rotor wheels produced by EBM (the image represent the exact placement inside the building chamber).

The specimens and components produced with RNT650 TiAl powder with the optimized particle size distribution (batch 2) described in paragraph 3.2 Particle size distribution were characterized in terms of residual defects and they resulted appropriate in terms of both overall residual porosity and maximum defect size.

The chemical composition of RNT650 powders and massive materials was analyzed. A loss in Al content was observed, while the levels of impurities was very low and comparable between the powder and the parts.

Furthermore, the microstructure of the as produced material was investigated and the heat treatments were set up in order to obtain the better microstructure for the application. This is an indispensable point for these materials because their mechanical properties are extremely sensitive to microstructure.

Mechanical tests were performed on the heat treated samples and the results were in well agreement with literature data for this TiAl alloy produced by casting for the automotive turbocharger application.

Furthermore, some brazed joints between steel and TiAl processed by EBM were produced by TWI. These samples were then tested and characterized in terms of residual defects, microstructure and elemental distribution through the junction region.

7.1 Porosity analysis of specimens

After the optimization of EBM process for this alloy, the porosity was quantified according to ASTM E 2109-01 [149] on cylindrical specimens produced during the same job of the wheels.

The only porosity observed on the specimens processed by EBM, using the optimized powder (batch 2), consisted of small spherical pores.

This type of porosity is not caused by the process itself but it is due to defects already present in the powder particles as already explained in paragraphs 3.1 Powders morphological characterization and 5.1 Porosity analysis of this thesis [173] [66].

The total amount of residual porosity resulted to be $0.07 \pm 0.06\%$, indicating a full densification of the samples. The observed defects are spherical pores and the biggest pore observed reaches the dimension of about 50 µm. (**Figure 195**)

This low amount of residual porosity was considered not detrimental for the material as it was below 1% and pores smaller than 100µm [66].
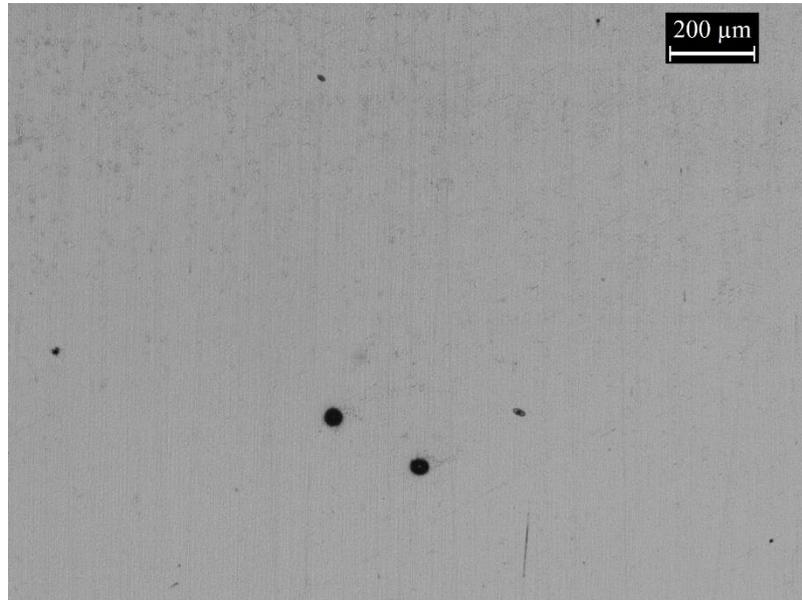
Figure 195: Optical microscopy image of residual pores observed on the specimens processed by EBM.

7.2 Chemical characterization

The chemical compositions of the RNT650 specimens and of the prototype wheels processed by EBM, using the optimized powder (batch 2), were analyzed and compared with the chemical composition of the powder reported in 3.5 Chemical composition and with the chemical composition of a reference RNT650 wheel produced by casting.

For the production of specimens, the nominal chemical composition of the powder was increased in aluminum to avoid its loss during the EBM process. Therefore, the chosen nominal composition of the starting powder was Ti-(34-34.5)Al-4.8Nb-1Cr-0.2Si (wt.%).

Table 39 shows the comparison in terms of chemical composition of the RNT650 powder and specimen produced by EBM [127].

Table 39: Chemical composition of the powder and specimen.

	Al	Cr	Nb	Si	O	N	C	Ti
	Chemical composition in wt.%							
RNT650 powder	34.5	1.04	4.83	0.25	0.05	0.003	0.005	Bal.
RNT650 specimen	32.8	1.04	4.69	0.24	0.05	0.004	0.005	
RNT650 wheel casting	32.6	1.07	5.55	0.22	-	-	-	

As foreseen, thanks to the previous experiences by Biamino et al. [17] and Terner et al. [125], and as previously described in this thesis for the 48-2-2 alloy and for the TNM alloy, an aluminum loss lower than 2 wt.% occurs during the EBM process.

Thanks to the vacuum environment, the pickup of impurities such as oxygen, nitrogen and carbon was very limited during the process. The final amount of oxygen (500 ppm) and nitrogen (40 ppm) were well below the values considered problematic for ductility reduction (around 1000 ppm for oxygen and 600 ppm for nitrogen) [114] [183].

7.3 X-Ray diffraction analysis

The X-Ray diffraction analysis was performed on RNT650 specimen after the EBM process.

In **Figure 196** the diffractogram of the as-EBM RNT650 alloy is compared to Ti-48Al-2Cr-2Nb alloy as reference material.
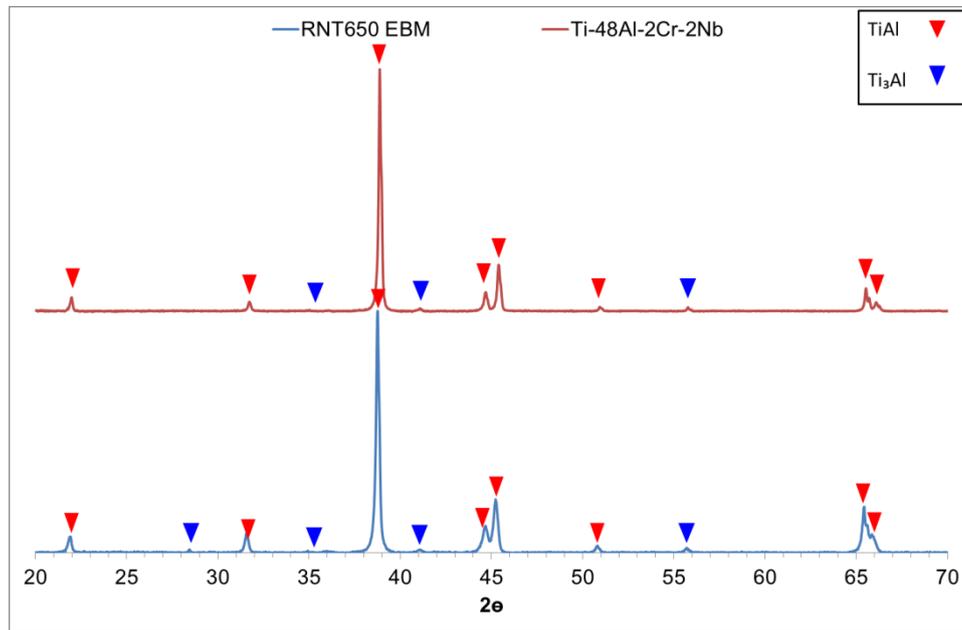
Figure 196: X-Ray diffractogram of Ti-48Al-2Cr-2Nb and RNT650 alloys as-EBM; the
different phases are indicated by colored arrows.

The X-Ray diffraction analysis has highlighted the presence of the γ-TiAl phase
(red arrow) and the α₂-Ti₃Al phase (blue arrow). This phase composition is very
close to that of the 48-2-2 TiAl alloy and typical for the as-EBM material, since the
γ-phase is the main phase observed.

7.4 As-EBM microstructure

The microstructure of the material observed after the EBM process is shown in **Figure 197**.
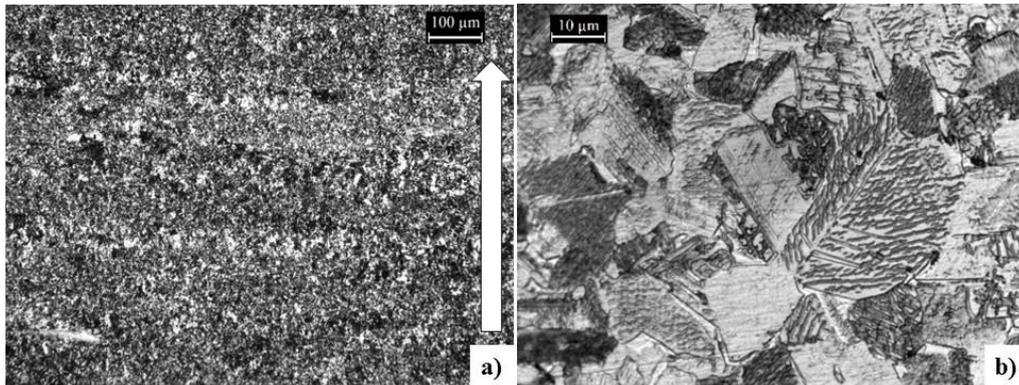
Figure 197a) and b): as-EBM microstructure of the RNT650 TiAl alloy; 5a): lower magnification image, 5b): higher magnification detail of the equiaxed γ-grains.

The as-EBM microstructure is made of very fine equiaxed γ-grains with some bands of coarser grains organized along the powder layers. The white arrow in **Figure 197 a)** indicates the building direction of the EBM process. The morphology of the equiaxed γ-grains can be better appreciated from the optical microscopy images at higher magnification (**Figure 197 b)**. This type of microstructure is typical of TiAl alloys processed by EBM because of the small melt pool and the rapid cooling. On the other hand, the coarser grains are probably due to local overheating and heat diffusion phenomena during the melting of the new powder layer, and the re-melting of a portion of the underlying powder layer.

This fine and homogeneous γ-microstructure was considered acceptable for this material because it is the typical microstructure obtained after the EBM process for the γ-TiAl alloys [17]. This type of microstructure, together with the low amount of porosity observed, has also proved the validity of the material and has confirmed the optimization of the EBM process for the RNT650 alloy.

The obtained as-EBM microstructure was the starting point for the heat treatment setup.

The bottom parts of the specimens in contact to the EBM building platform have shown the presence of defects as reported in **Figure 198**.
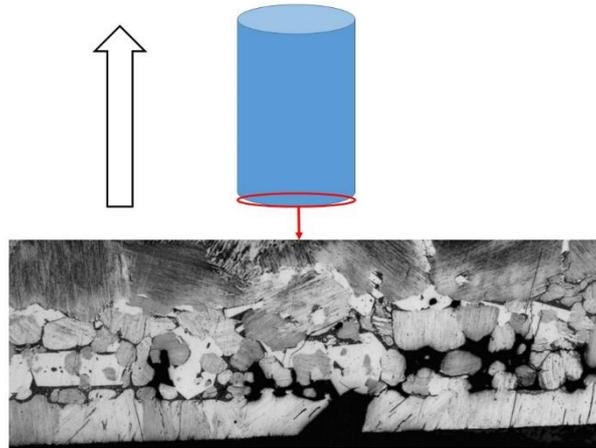
Figure 198: microstructure of the contaminated layer; the white arrow indicates the building direction.

The cause of the contamination was the EBM start plate that is made of high-temperature stable steel that can release a slight amount of iron into the TiAl material during the melting. In fact, the presence of iron in the lower region of the specimens (thickness about 1 mm), in a concentration of about 3.5 wt.%, was confirmed by the EDX analysis performed on this interested area of a specimen.

7.5 Heat Treatment setup

Once the EBM process has been optimized and the quality of the as-EBM material was established, a series of heat treatments were performed in order to investigate the microstructural evolution of the RNT650 material and to obtain the desired near lamellar microstructure for the automotive application. The reference near lamellar microstructure was chosen in accordance to the works of Tetsui and Ono (1999) [58], Tetsui (2002) [32] and Koyanagi et al. (2011) [116].

In a similar way to the other γ-TiAl alloys considered in this thesis, TMA analysis was a useful tool to quickly know the phase transition temperatures for this alloy and consequently, select the starting temperatures for the heat treatment setup. The TMA diagram for the Ti-48Al-2Nb-0.7Cr-0.3Si alloy, reporting the displacement derivative versus temperature is shown in **Figure 199**.
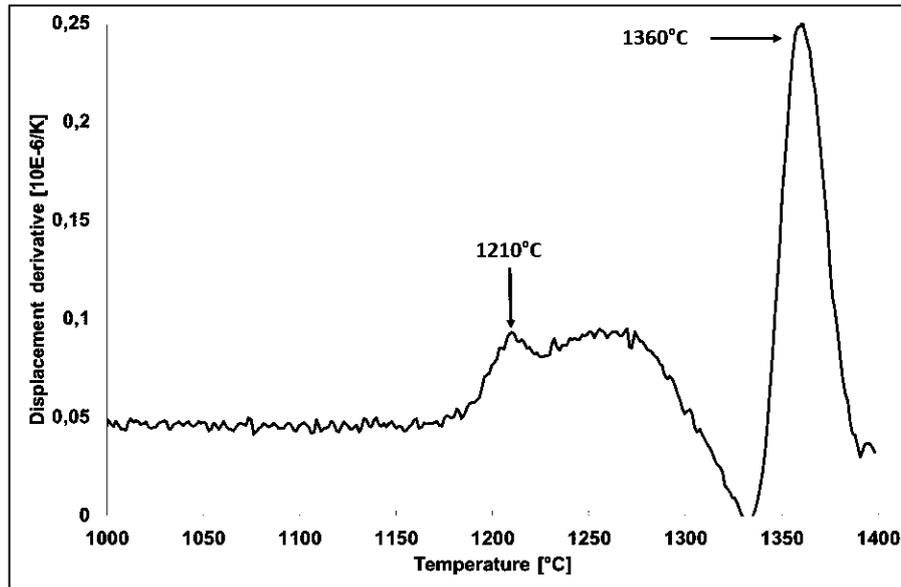
Figure 199: TMA displacement derivative versus temperature diagram of RNT650 alloy.

The α-transus temperature, corresponding to the transformation $\alpha + \gamma \leftrightarrow \alpha$, can be correlated to the peak at 1360°C.

The performed heat treatments and the obtained microstructure are reported below:

HT at 1300°C for 2 hours

The first heat treatment was performed at a temperature of 1300°C for 2 h followed by furnace cooling.

With this annealing temperature, far below the alpha transus temperature, the obtained microstructure was almost totally equiaxed. As it is possible to observe in **Figure 200 a, b** and **c**, only a few lamellar grains below 100 µm began to grow. These grains seem to be originated from the coarser grains observed in the as-EBM microstructure.
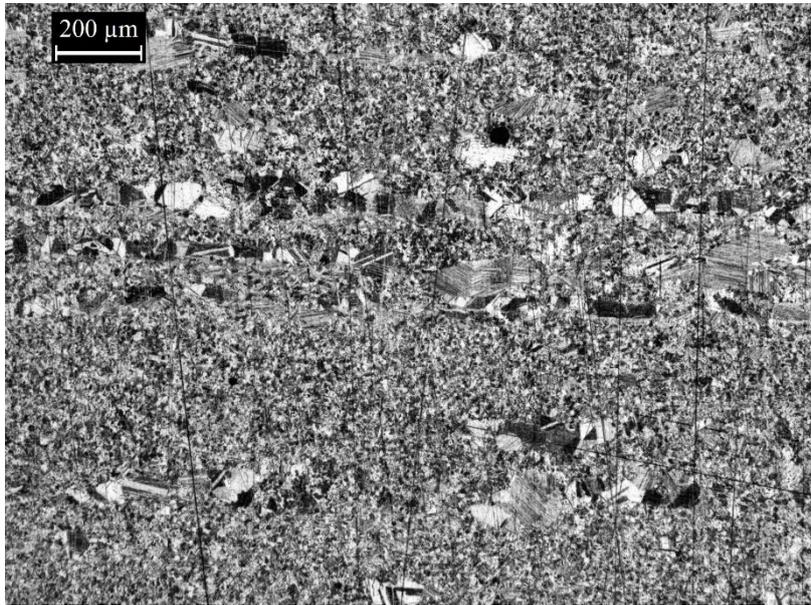
Figure 200a: microstructure after heat treatment at 1300°C for 2 h.
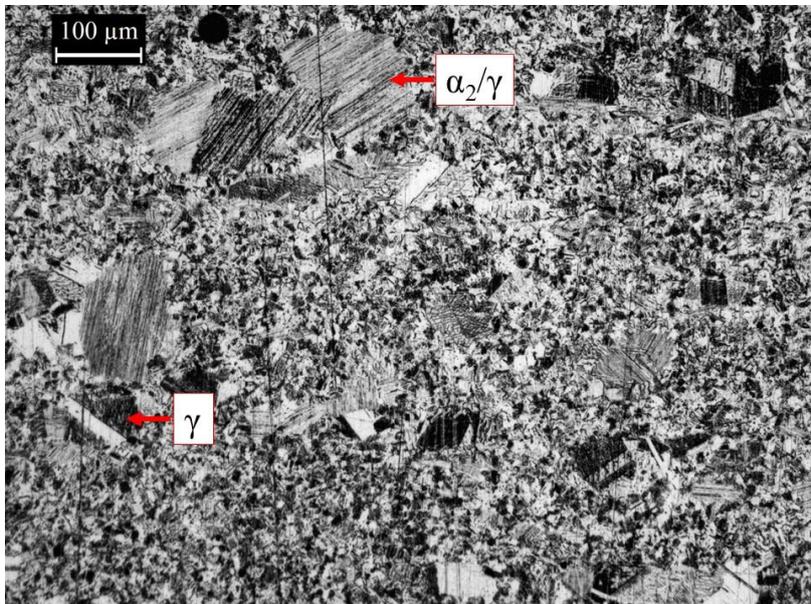
Figure 200b: microstructure after heat treatment at 1300°C for 2 h.
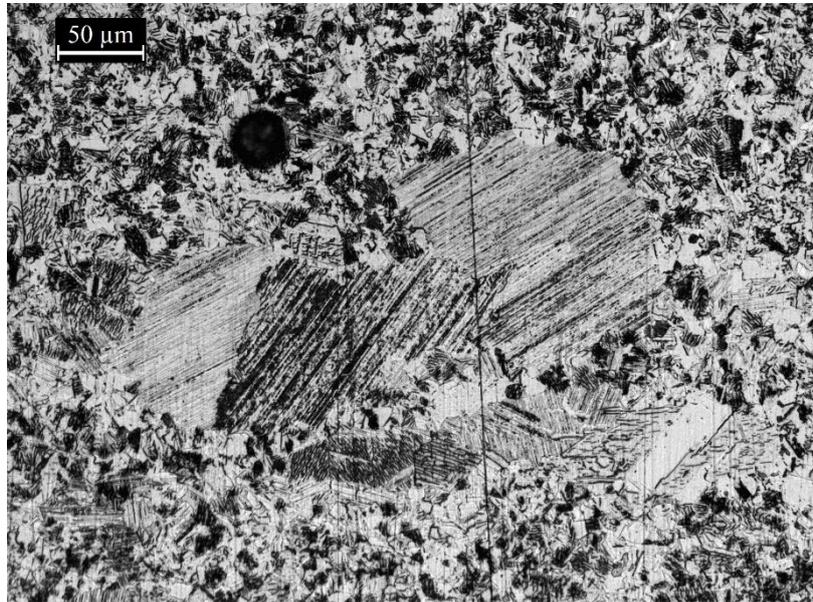
Figure 200c: microstructure after heat treatment at 1300°C for 2 h; lamellar colonies detail.

When the microstructure is near gamma, the formation of the first lamellar colonies follows the banded structure of the as-EBM microstructure. The lamellar colonies are organized in bands that are parallel to the powder layer deposition direction that replicates the previous location of the coarser γ-grains.

Heat treatments at higher temperatures were performed to obtain microstructures with more lamellar colonies and less equiaxed γ-grains.

HT at 1350°C for 2 hours

With this heat treatment, a duplex microstructure was obtained.

From **Figure 201** it is possible to observe a considerable increase of the lamellar grains to about 200 µm length.
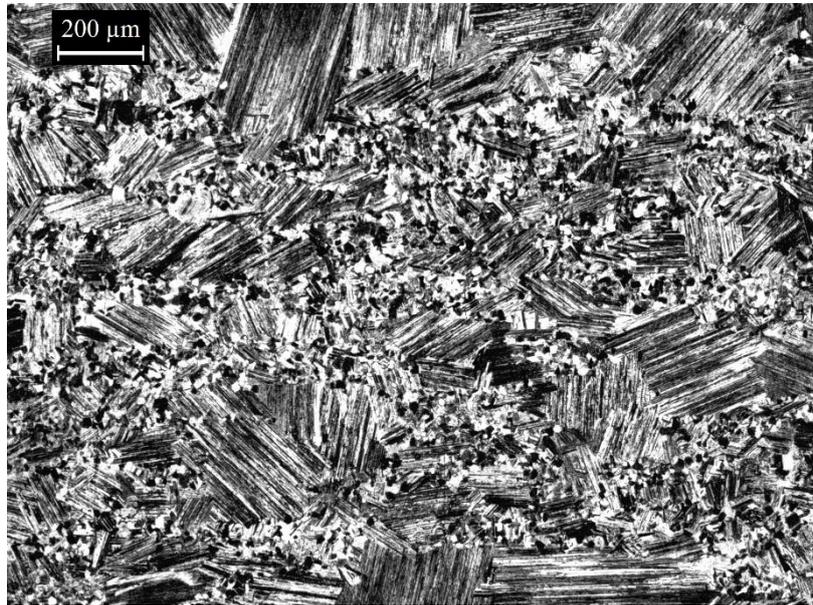
Figure 201: duplex microstructure after heat treatment at 1350°C for 2 h.
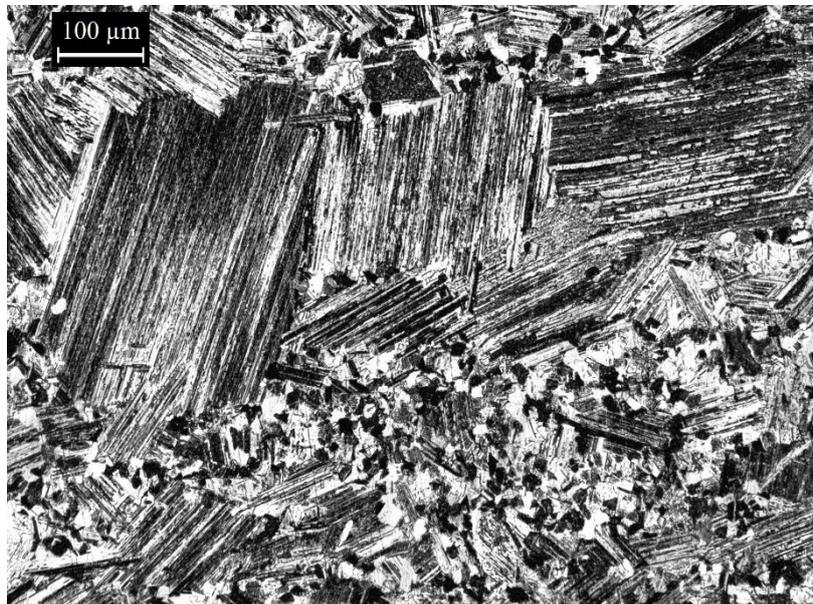
Figure 201b: duplex microstructure after heat treatment at 1350°C for 2 h.
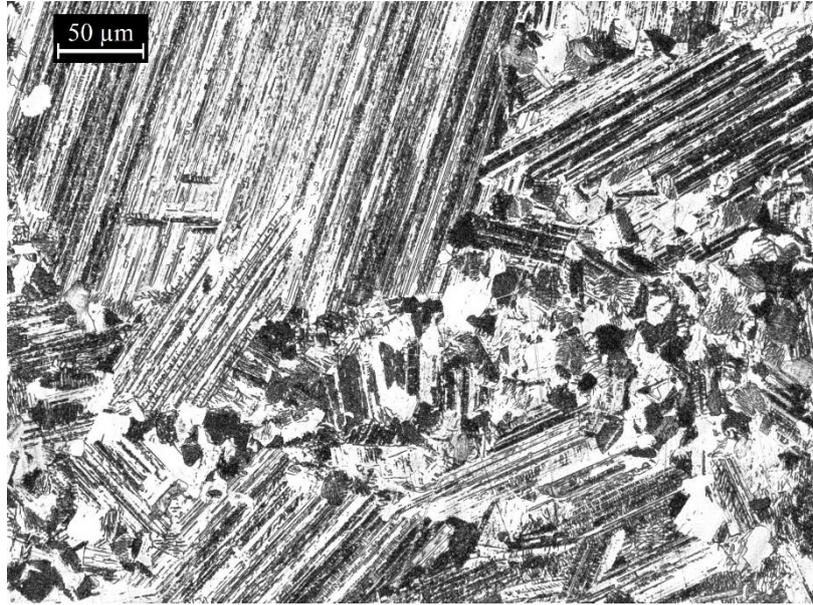
Figure 201c: duplex microstructure after heat treatment at 1350°C for 2 h.

The duplex microstructure is expected to exhibits sufficient room temperature ductility and good strength, but for automotive application, high temperature properties such as creep and fatigue resistance are desirable [75][62][55][44]. For this reason, further heat treatments at higher temperatures were performed in order to obtain near lamellar and fully lamellar microstructures.

HT at 1360°C for 2 hours

With this third heat treatment, the evolution from a duplex to a near lamellar microstructure was observed. From **Figure 202** it is possible to notice as the increase in temperature has promoted the formation and growth (> 200 µm) of the α_2/γ lamellar colonies. It is also possible to notice a small amount of globular γ-grains that remain confined between the lamellar colonies.
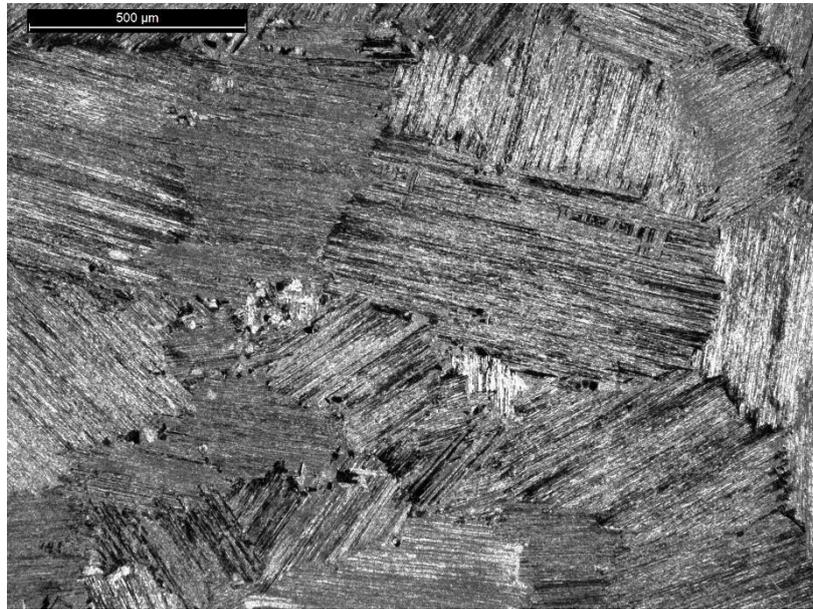
Figure 202a: near lamellar microstructure after heat treatment at 1360°C for 2 h.
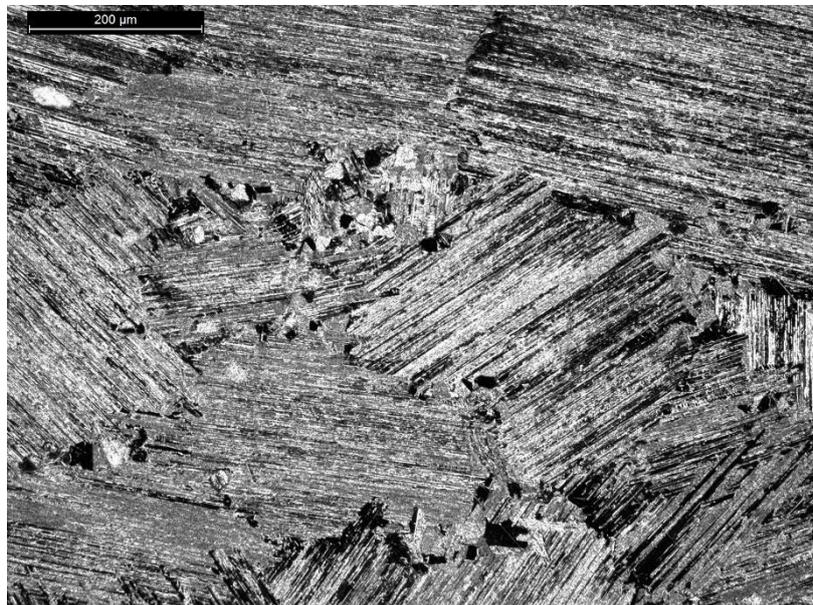
Figure 202b: near lamellar microstructure after heat treatment at 1360°C for 2 h.
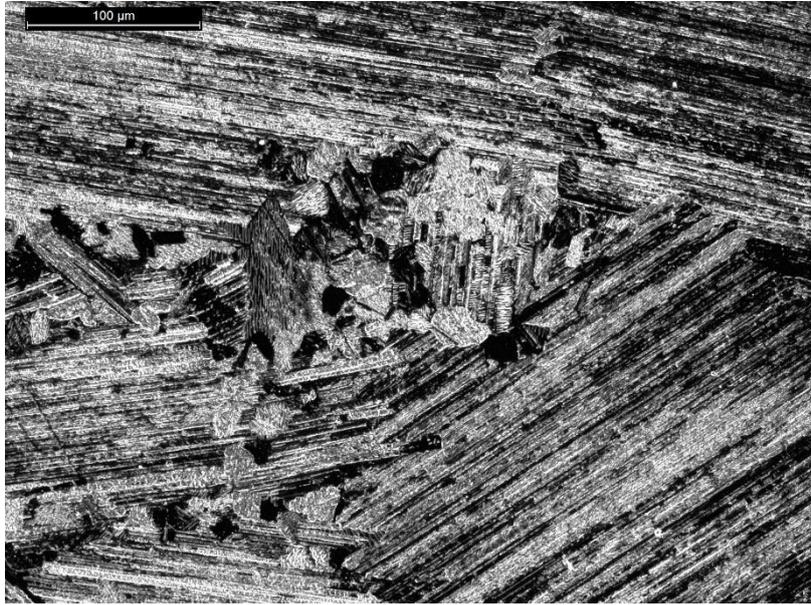
Figure 202c: near lamellar microstructure after heat treatment at 1360°C for 2 h.

In order to analyze a consistent formation of the lamellar colonies and the decrease of the residual γ-phase, a further heat treatment at 1365°C for 2 h was conducted.

HT at 1365°C for 2 hours

With this heat treatment, a fully lamellar microstructure is obtained. As it is possible to notice from **Figure 203** a non-total cohesion between lamellar grains is observed and there is the presence of few residual globular γ-grains at the grain boundaries of lamellar colonies.
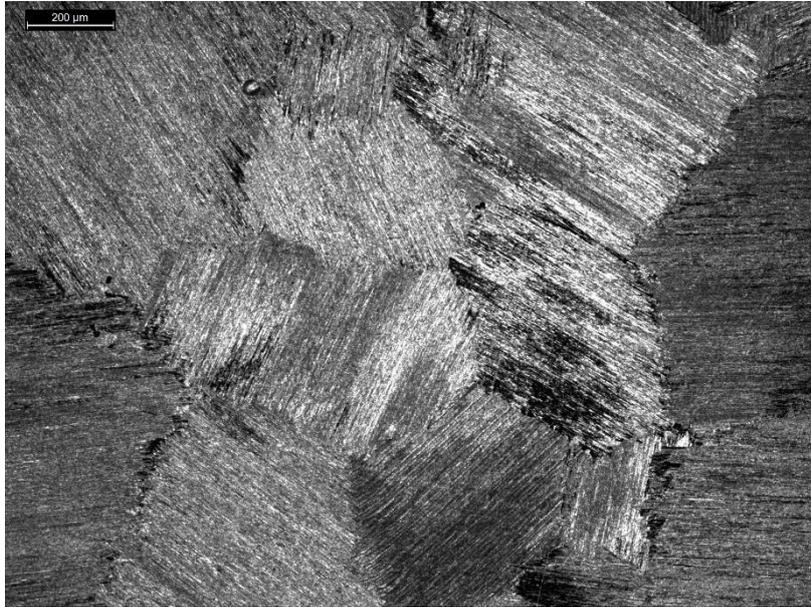
Figure 203a: near fully lamellar microstructure after heat treatment at 1365°C for 2h.
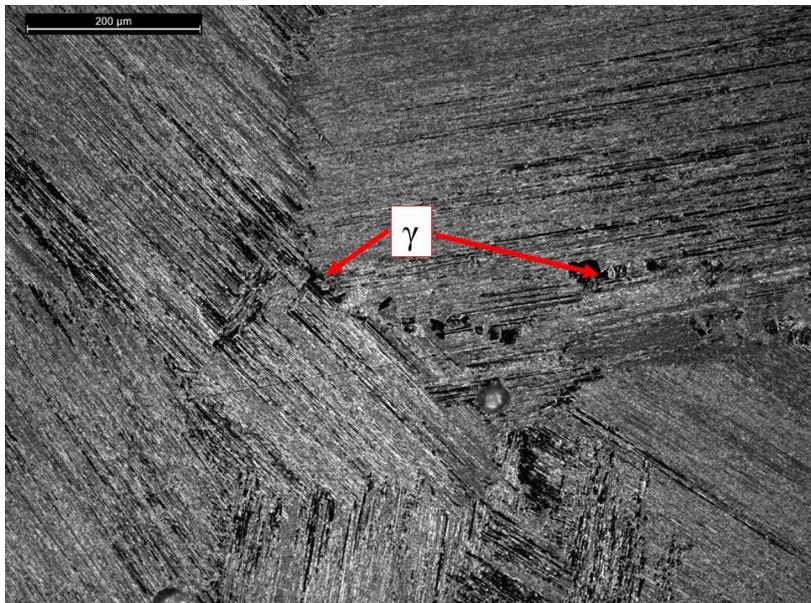
Figure 203b: near fully lamellar microstructure after heat treatment at 1365°C for 2h.
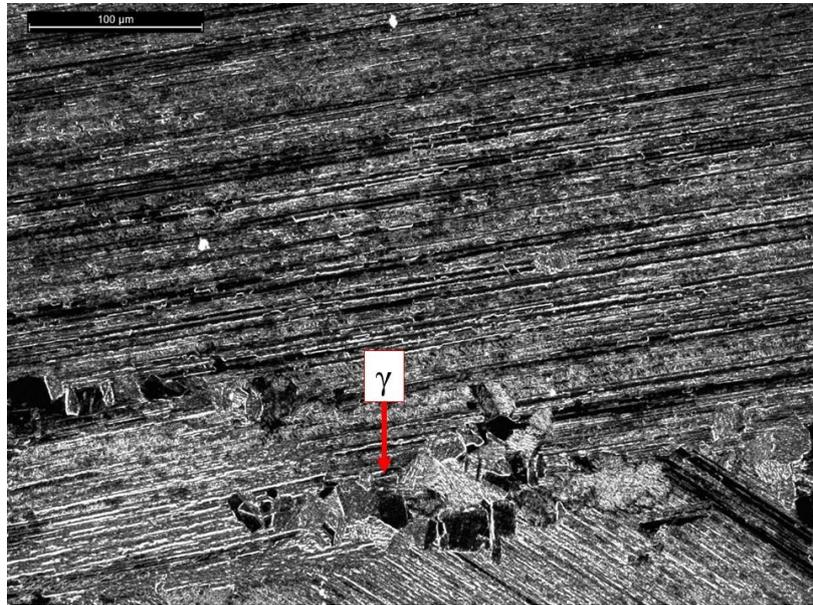
Figure 203c: near-fully lamellar microstructure after heat treatment at 1365°C for 2h; residual γ-grains detail.

In order to obtain a fully lamellar microstructure without any equiaxed grains, another heat treatment at 1370°C for 2 hours was performed.

HT at 1370°C for 2 hours

By treating the material at this high annealing temperature, there was no residual globular γ-phase left and the growth of α_2/γ phase lamellar colonies up to 1000 µm has been produced. This growth of lamellar colonies caused the complete adhesion between the grains (**Figure 204**).
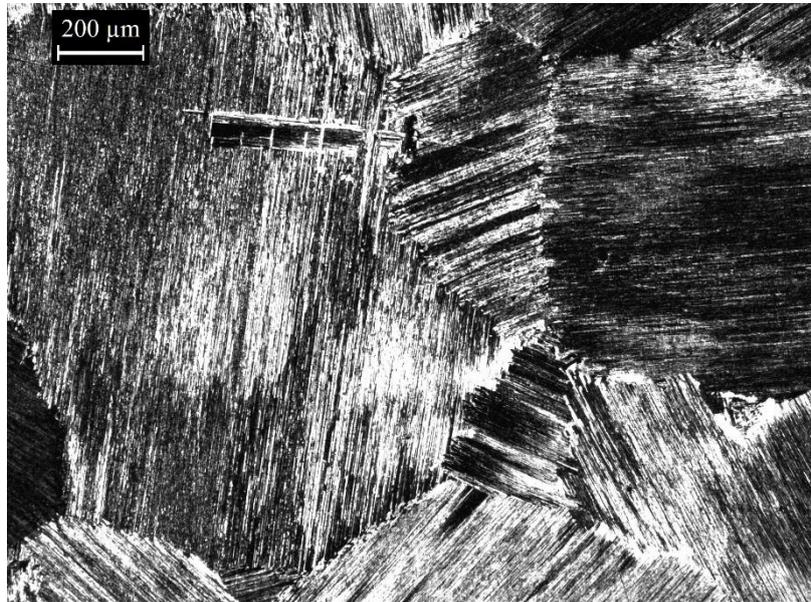
Figure 204: fully lamellar microstructure after heat treatment at 1370°C for 2h.

Regarding the material properties related to the different microstructures obtained with the different heat treatment, the fully lamellar microstructure obtained with the HT at 1370°C for 2 h is expected to enhances good high temperature properties such as creep and fatigue resistance [46][32][113][72]. However, a fully lamellar microstructure with coarser grains presents a low room temperature ductility and, for this reason, a microstructure with smaller lamellar colonies size and with some globular γ-grains is most desirable for the application. In fact, by performing a heat treatment in the near lamellar range (HT at 1360°C for 2 hours), it was possible to obtain a near lamellar microstructure with lamellar colonies surrounded by fine equiaxed grains. The room temperature ductility of this microstructure is lower than duplex microstructure but better than a fully lamellar one thanks to the equiaxed γ-grains at the lamellar colonies grains boundaries (**Figure 205**) [70].
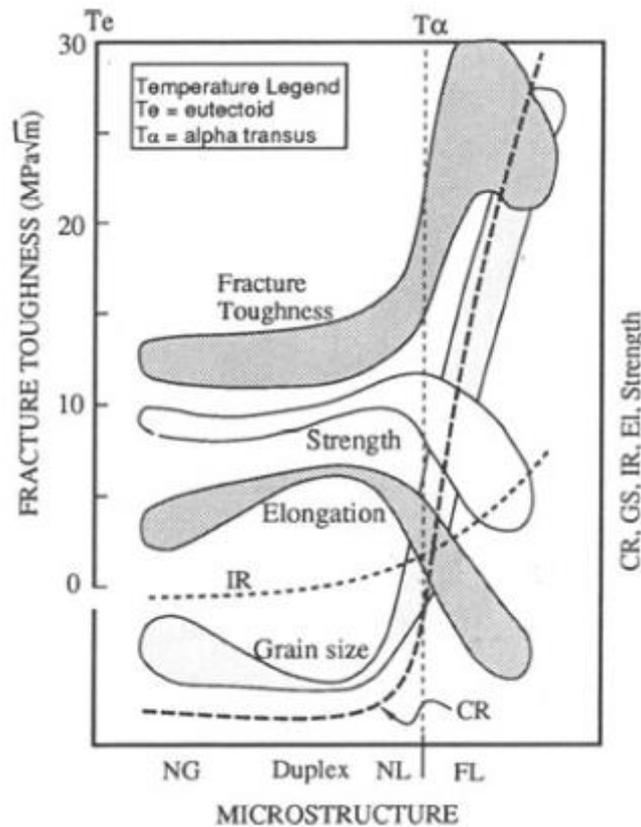
Figure 205: Schematic relationships between microstructure and grain size (GS) and mechanical properties [70].

According to the work of Kothari et al., with this microstructure, an improvement in both ductility and strength is expected [55].

Since this near lamellar microstructure was considered promising for the automotive application, the HT at 1360°C for 2 hours has been chosen to treat the cylindrical specimens for mechanical testing.

7.6 Mechanical characterization

The room temperature dynamic elastic modulus (Young's modulus) was measured by impulse excitation technique (IMCE) according to ASTM E 1876-09 [165] on specimens heat treated at 1360°C for 2 h and it resulted to be 168 ± 2 GPa.

The specimens for creep and tensile tests were obtained by machining blanks heat treated with the HT at 1360°C for 2 hours.

7.6.1 Tensile test

The tensile tests were performed on three specimens at room temperature according to ASTM E 8 [162] and three specimens were tested at 800°C according to ASTM E 21 [163] by using an MTS servo hydraulic test machine.

The tensile tests results are reported in **Table 40**.

Table 40: Tensile test results [127].

Temperature	Modulus [GPa]	Stress at offset yield (0.02%) [MPa]	Peak stress UTS [MPa]	Elongation %	Peak stress UTS [MPa] [116]
Room	166 ± 2	253 ± 13	336 ± 26	0.27 ± 0.1	410
800°C	132 ± 2	149 ± 15	426 ± 22	1.96 ± 0.5	430

It is possible to notice that the ultimate tensile strength (UTS) at room temperature was lower than that measured at 800°C. This typical behavior of γ-TiAl with a near lamellar or a fully lamellar microstructure can be explained since at the higher test temperatures, the higher fracture strength arises from the larger ductility. More precisely, this is due to the brittle to ductile transition that occurs at a certain temperature. The specific strength obtained with the HT at 1360°C for 2 hours was comparable to that of superalloys and to the results from the study of Koyanagi et al. on the similar material produced by casting [116].

The room temperature static Young's modulus was comparable to the dynamic one measured by the IMCE technique.

7.6.2 Creep test

The creep tests were performed at 800°C with constant applied stresses of 200 MPa and 300 MPa according to ASTM E139 [164] using an ATM test system.

The creep tests were performed only on one specimen for each condition because of the limited number of available specimens. However, this was enough to do a preliminary analysis of the material creep behavior. In **Table 41** the obtained results are reported.

Table 41: creep test result; LM = Larson-Miller parameter [116].

Stress [MPa]	Final creep %	Elongation %	Rupture [h]	LM parameter $(T(20+\log t_r))$ $T = K; t_r = h$	LM parameter $(T(20+\log t_r))$ $T = K; t_r = h;$ [116]
200	5.72	6.8	372	24.22	24.3
300	8.32	9.8	23.7	22.93	23.1

Also for creep, the obtained results are comparable with those obtained by
Koyanagi et al. [116]. However, the difference observed between these results and
the literature results is due to the fact that the microstructure considered in this work
is a near lamellar and the material of the work of Koyanagi et al. presented a fully
lamellar microstructure.

7.7 Comparison with TiAl RNT650 turbocharger wheel produced by casting and further HT investigation

In order to compare the microstructure obtained on the RNT650 alloy processed by
EBM with the typical microstructure for the same alloy produced by casting, an
RNT650 turbine wheel produced by casting was supplied by a partner of the
TIALCHARGER project.

The chemical composition of the casted wheel was evaluated and compared
with the composition of the RNT650 processed by EBM. As it is possible to observe
from **Table 39** in paragraph 7.2 Chemical characterization, the two chemical
compositions are comparable.

The casted wheel was sectioned and the microstructure was observed. In **Figure
206**, the section of the wheel subjected to the etching with Kroll's solution in order
to highlight the TiAl microstructure is shown.
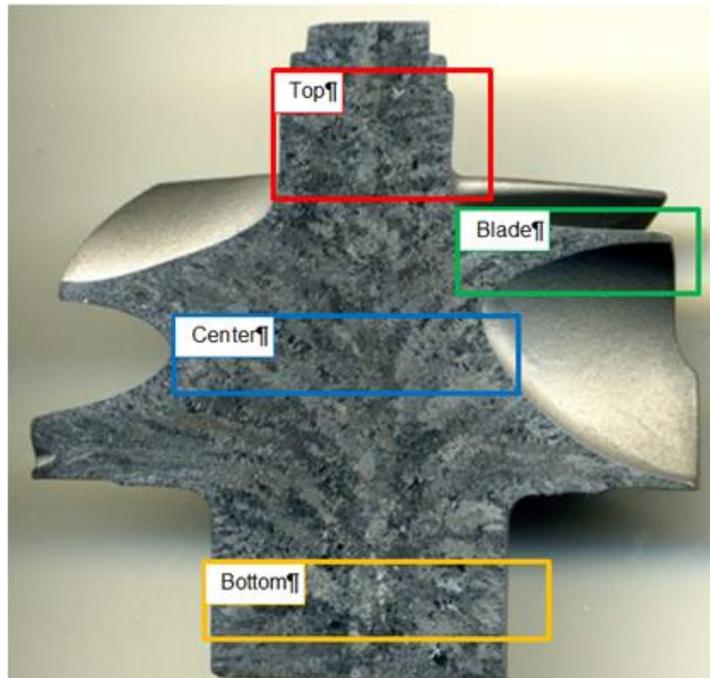
Figure 206: Reference RNT650 casted turbochargher section.

As it is possible to observe from the macrostructure in **Figure 206**, the casted
wheel exhibits coarse and preferentially oriented lamellar grains. This big columnar
lamellar structure is typical of the casting process due to solidification through the
α path and slow cooling rates. Since the preferential crystal growth is parallel to the
c axis and there are no other orientations equivalent to it in the hcp α phase, the α
crystals tent to form columnar grains along the direction of heat extraction during
solidification [56] [184]. **Figure 207** shows a section of a casted wheel produced
by DAIDO steels by the levitation melting and casting (Levicast) process, where a
similar columnar structure is also evident [116].
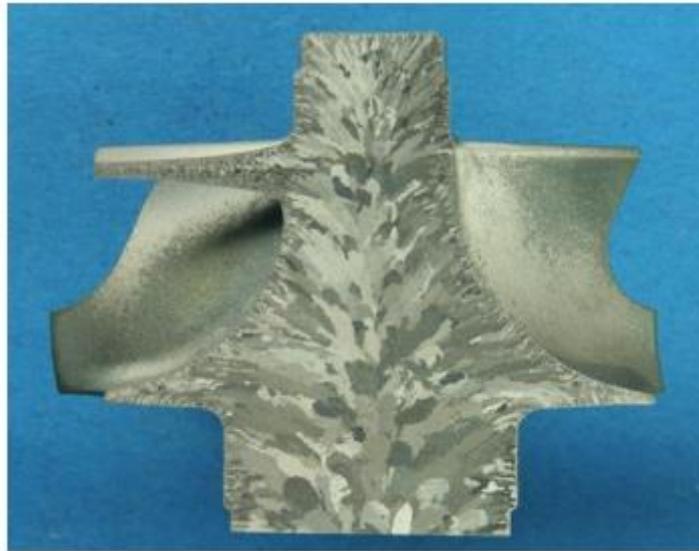
Figure 207: Macrostructure of the wheel produced by DAIDO steels.

In the next images the microstructure observed in the different zones of the reference cast wheel are shown. The microstructure of the wheel is almost completely lamellar with lamellar colonies oriented from the external part to the bulk and angulated versus the bottom of the component.
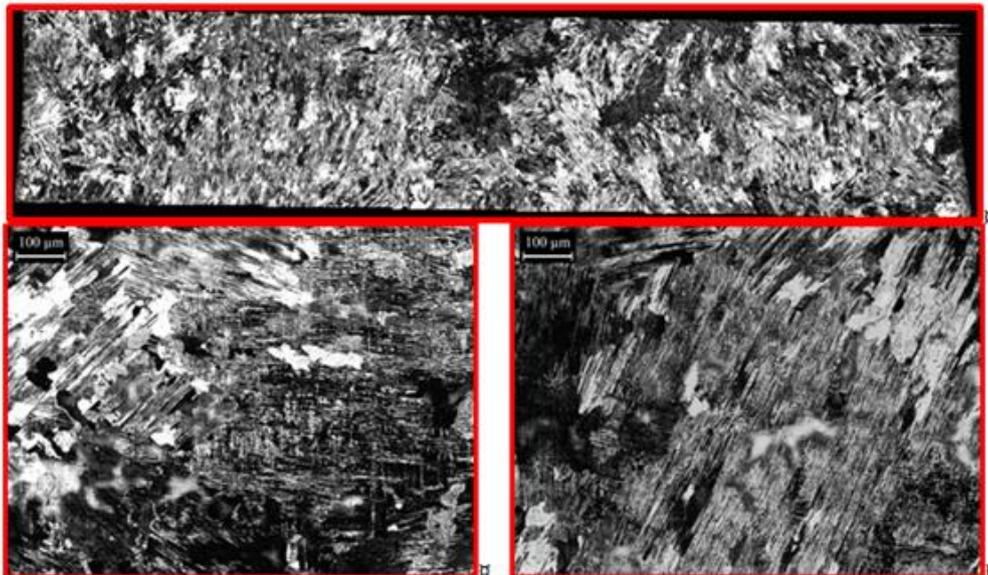
Figure 208: microstructure observed in the top part of the wheel.
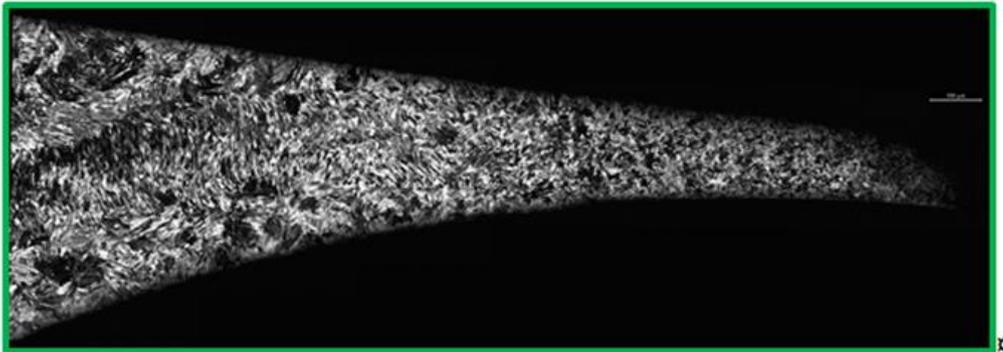
Figure 209: microstructure observed in the blade of the wheel
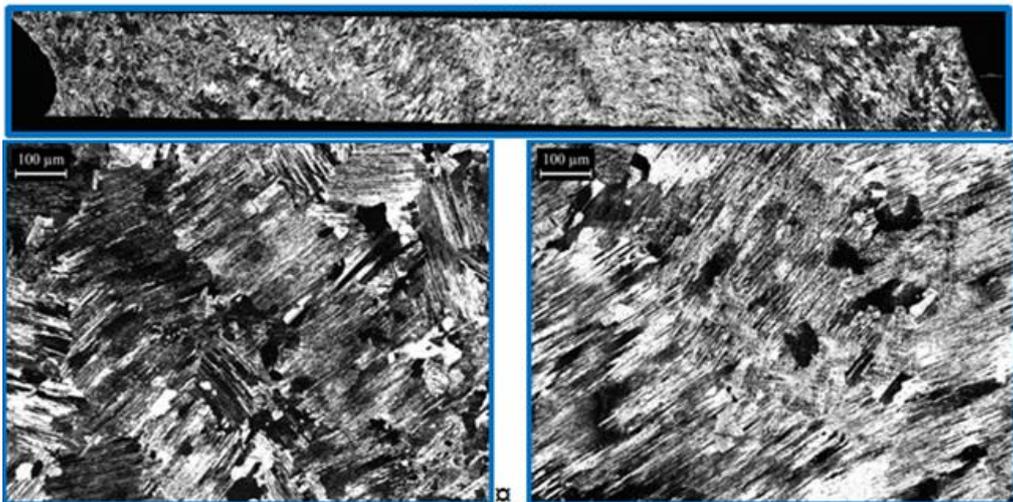
Figure 210: microstructure observed in the central section of the wheel.
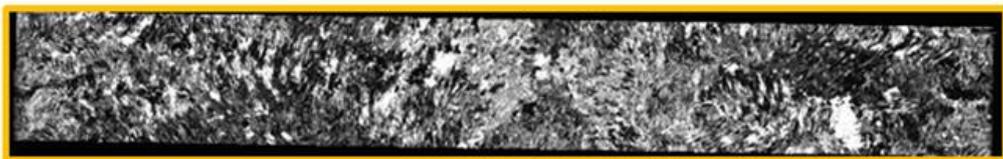
Figure 211: microstructure observed in the bottom part of the wheel.

HT at – 1360°C for 1 hours

Once assessed the good mechanical properties of the near-lamellar microstructure material obtained with the heat treatment at 1360°C for 2 hours, a further heat treatment at 1360°C was performed lowering the annealing holding time from 2 hours to 1 hours. The purpose was to investigate the microstructural variations caused by the shorter heat treatment time.

After this heat treatment some more equiaxed γ-grains remained along the lamellar grain boundaries and the lamellar colonies presented a smaller size (100 – 200 µm) (**Figure 212a, b** and **c**) in comparison with the HT at 1360°C for 2 hours (**Figure 202**). Since with this heat treatment the microstructure resulted too equiaxed, the microstructure obtained with the heat treatment at 1360°C for 2 hours was considered the most desirable one.

Figure 212 a: near lamellar microstructure after heat treatment at 1360°C for 1 h.
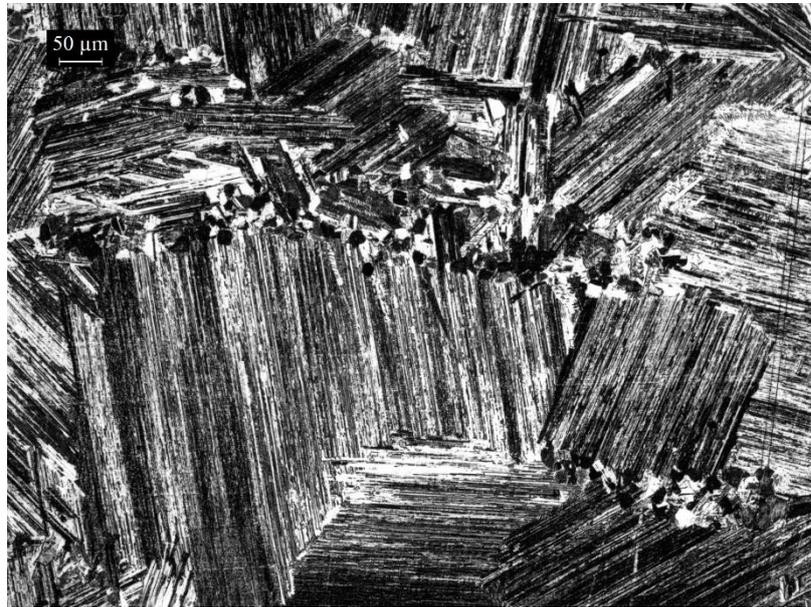
Figure 2132 b: near lamellar microstructure after heat treatment at 1360°C for 1 h.
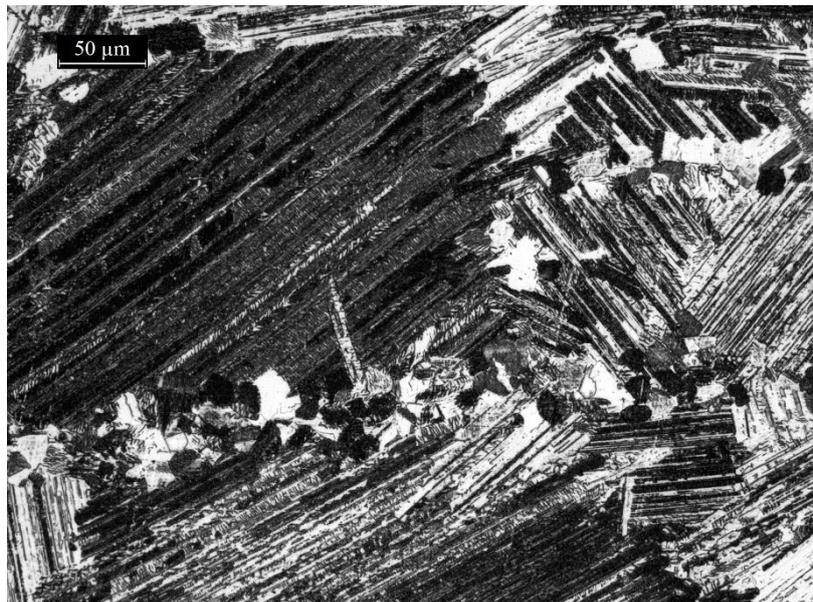
Figure 212 c: near lamellar microstructure after heat treatment at 1360°C for 1 h.

7.8 Turbocharger wheels characterization

Some turbocharger wheel prototype were produced by IFAM by EBM using optimized powder (batch 2) of Ti-48Al-2Nb-0.7Cr-0.3Si alloy (RNT650).

Some wheels were produced to optimize the EBM process for the component production, to improve the design, in particular for the hollow turbocharger wheel prototypes, and for material characterization, other wheels with the final optimized design were used as demonstrator for the EU project TIALCHARGER [14].

The design of hollow turbocharger wheels was developed by several partners within a particular WP of the project.
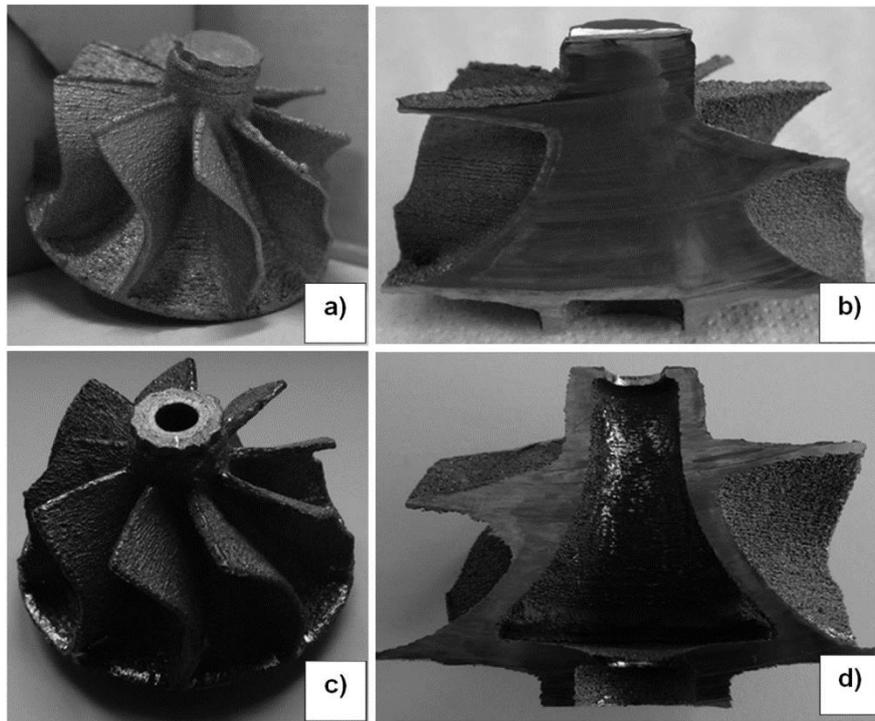
Figure 214: a) and b): full turbocharger wheels; c) and d): hollow turbocharger wheels.

The production feasibility of the hollow wheel was possible thanks to the freeform capability of EBM process. Thanks to this innovative design, a further component weight reduction can be obtained.

This design was developed and improved by FEM-calculated design, based on stress levels at elevated temperatures. The holes at the top and the bottom are used for the removal of surplus powder that remain after the EBM process.
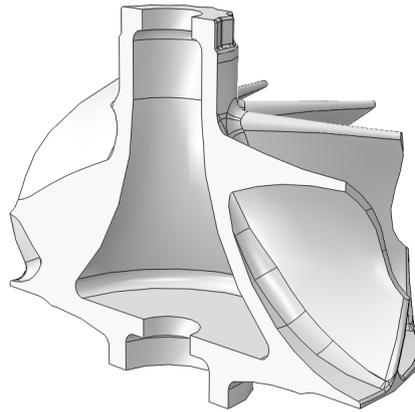
Figure 215: hollow turbocharger wheel section

The wheels were built top-down in the EBM chamber (**Figure 194**) and the deposition of a first powder layer between the EBM plate and the wheels has been used to avoid contamination of the component. Such contamination was already observed during the previous test specimen building (**Figure 198**).

After the production by EBM of a certain number of turbocharger wheel prototypes, some of them were subjected to a material characterization in terms of residual porosity, as-EBM and post-heat treatment microstructure, roughness evaluation and dimensional analysis. The material characterization results are reported in the following part.

7.8.1 Porosity and defects analysis

For the porosity analysis and investigation to observe the presence of any manufacturing defects, a turbocharger wheel was sectioned as shown in **Figure 214**.

The overall residual defects observed and measured using optical microscopy and image analysis software, resulted to be $0.17 \pm 0.24\%$. The observed defects were spherical pores with a maximum size of about 60 µm (**Figure 216**). As described in the previous parts, this low percentage of small and spherical porosity

can be considered acceptable because it will not affect the mechanical properties of the material and indicates a fully densification of the part during the EBM process.

In **Figure 216 a** and **b** two examples of pores with bigger dimension are shown.
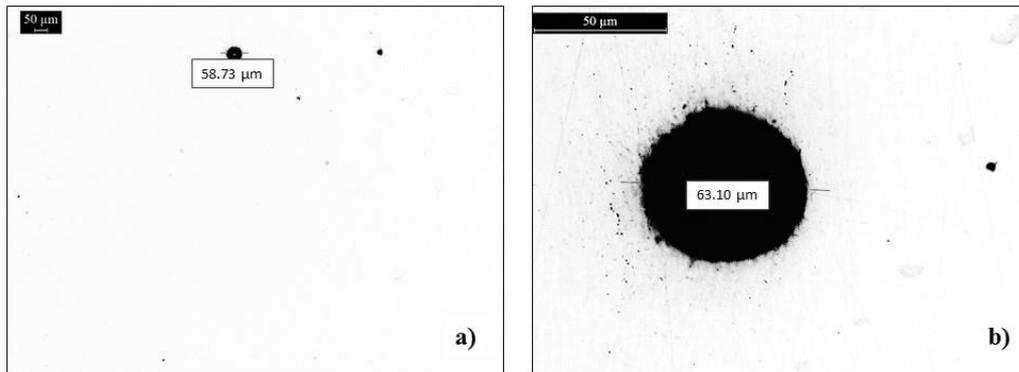
Figure 216: two examples of spherical pores observed; b) pore detail.

7.8.2 As-EBM microstructure analysis

As expected, the as-EBM microstructure of the turbocharger wheels was comparable to that of the RNT650 specimens. **Figure 217 a** and **b** show the equiaxed γ-microstructure of the RNT650 turbocharger wheels.
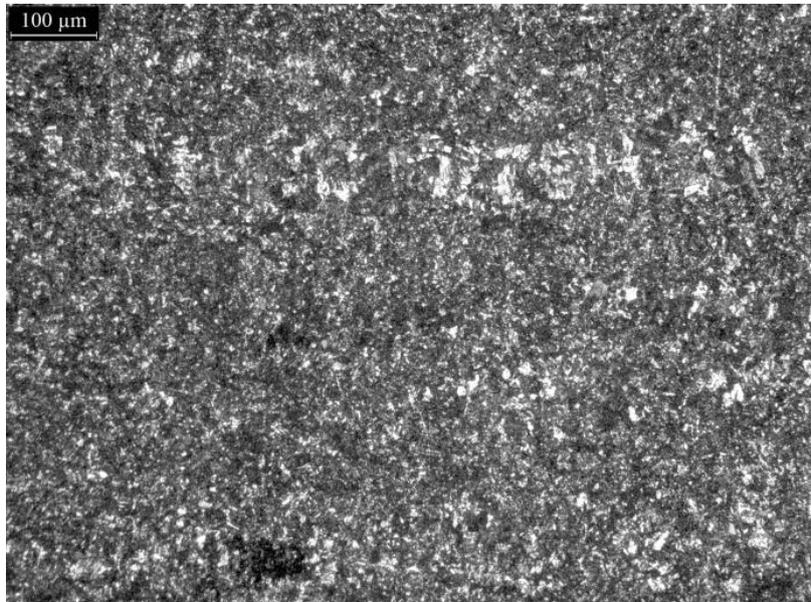
Figure 217 a: As-EBM microstructure of the turbocharger wheel.
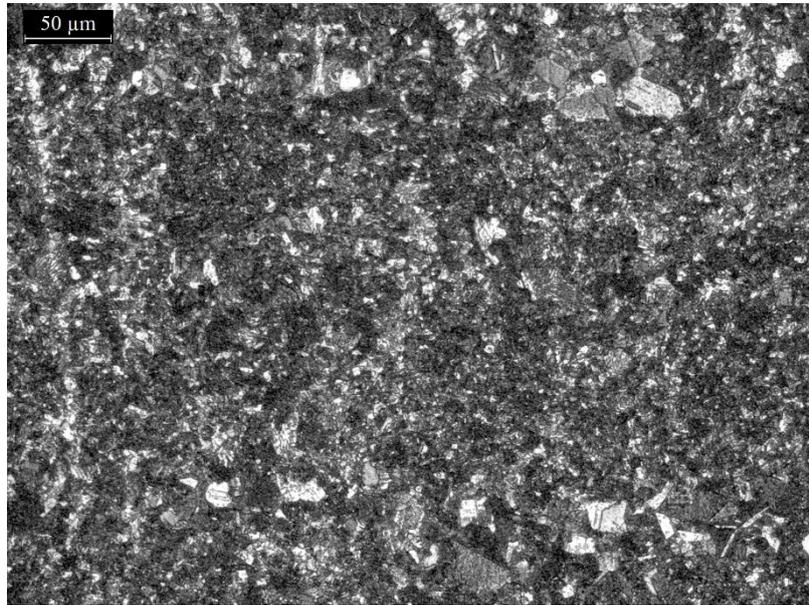
Figure 217 b: As-EBM microstructure of the turbocharger wheel.

Also in this case, some coarser equiaxed γ-grains organized in bands are observed.

7.8.3 Post-heat treatment microstructure analysis

Heat treatment at 1360°C for 1 hour

A heat treatment at 1360°C for 1 hour was performed on a section of turbocharger wheel cut along the building direction as shown in **Figure 218**. The chosen heat treatment corresponds to the HT described before. According to the heat treatment setup and mechanical tests results, the choice of this heat treatment was done in order to obtain the desired near lamellar microstructure. The holding time of 1 hour instead of 2 hour was motivated by the thinner section of material exposed to the heat treatment in the case of the hollow turbocharger wheel respect to the cylindrical test specimens. 1 hour of annealing was expected to be sufficient to allow the almost complete phase transformation from the as-EBM near-γ microstructure to a near lamellar one.

Figure 218 shows the microstructure observed in the different zone of the wheel section after the heat treatment at 1360°C for 1 hour.
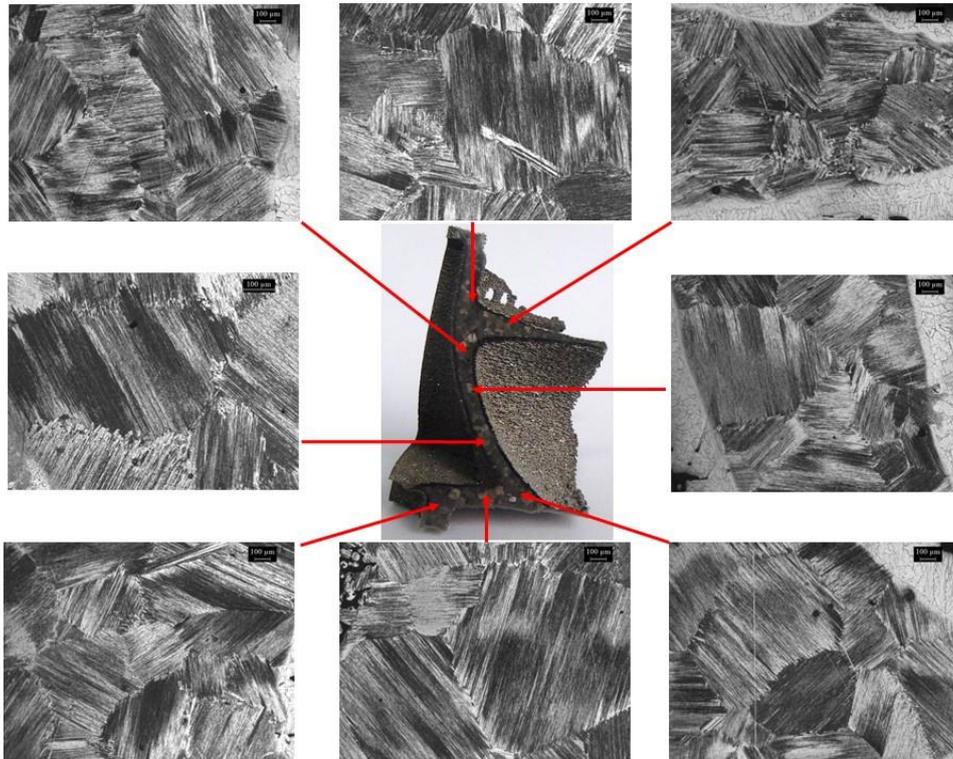
Figure 218: section of a turbocharger wheel after the heat treatment at 1360°C for 1 h and micrograph of the microstructure in the different zones.

As it is possible to observe from **Figure 218**, the wheel after the heat treatment at 1360°C for 1 hour exhibits a fully lamellar microstructure in almost all of the zones excepts for the blade, where a near lamellar microstructure can be observed. This difference can be due to the lower thickness of the blade respect to the other zones and this leads to different heat phenomena between the thinner parts and the core during the EBM process. In particular, a lower cooling rate is expected for the thicker zones or bulk and this promote the lamellar microstructure formation. This also cause a more pronounced Al evaporation in certain parts of the component and it is reflected in a microstructural difference [137].

As it is possible to observe from the micrographs in **Figure 218** and in more detail in the next image, the heat treated wheels exhibit an outer layer of about 200 µm with a different microstructure (see also paragraph 5.2 Microstructure analysis). The observed basketweave microstructure is due to the higher Al evaporation on the surface caused by the heat treatment in vacuum. However, an overstock material

is considered for the wheels design since a post machining or finishing of the wheels is performed also to remove the surface roughness caused by the EBM process.
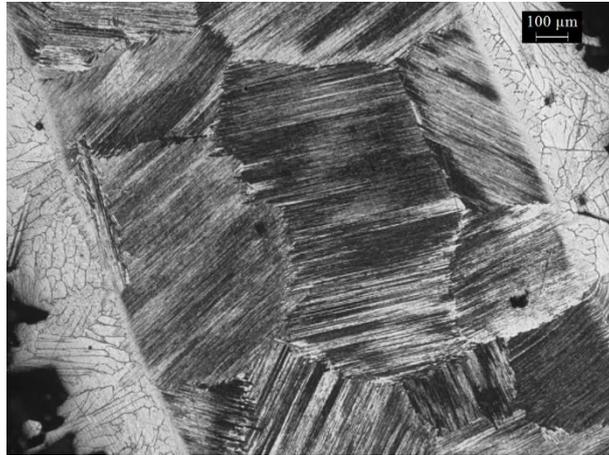
Figure 219: microstructural detail of the outer layer presenting the basketweave microstructure and surface roughness.

With this heat treatment, a near lamellar microstructure was expected in according to the microstructure obtained from the heat treatment setup in (HT at 1360°C for 2 hours and 1 hours). On the other hand, the microstructure of γ-TiAl is very sensitive to slight changes in temperatures, especially around the α-transus temperature, and variations of 5°C can produce a slight microstructural modification such as what observed there.

Since the control of the actual temperature in the GERO furnace used for the heat treatments is critical, a regular and periodic calibration is needed, and the difference between the set point temperature and the actual temperature has to be determined. Thus, temperature variations of about 5°C for the heat treatment are hard to be identified.

In order to obtain the desired near lamellar microstructure obtained with the HT at 1360°C for 2 hours during the heat treatment setup, a fine microstructural tuning was done performing a further heat treatment at 5°C below.

Heat treatment at 1355°C for 1 hour.

As expected, the wheel section subjected to the heat treatment at 1355°C for 1 h exhibits a near lamellar microstructure comparable to that obtained with HT at 1360°C for 2 hours during the heat treatment setup. In **Figure 220** it is possible to

observe the post heat treatment microstructure of the different zones of the wheel section.
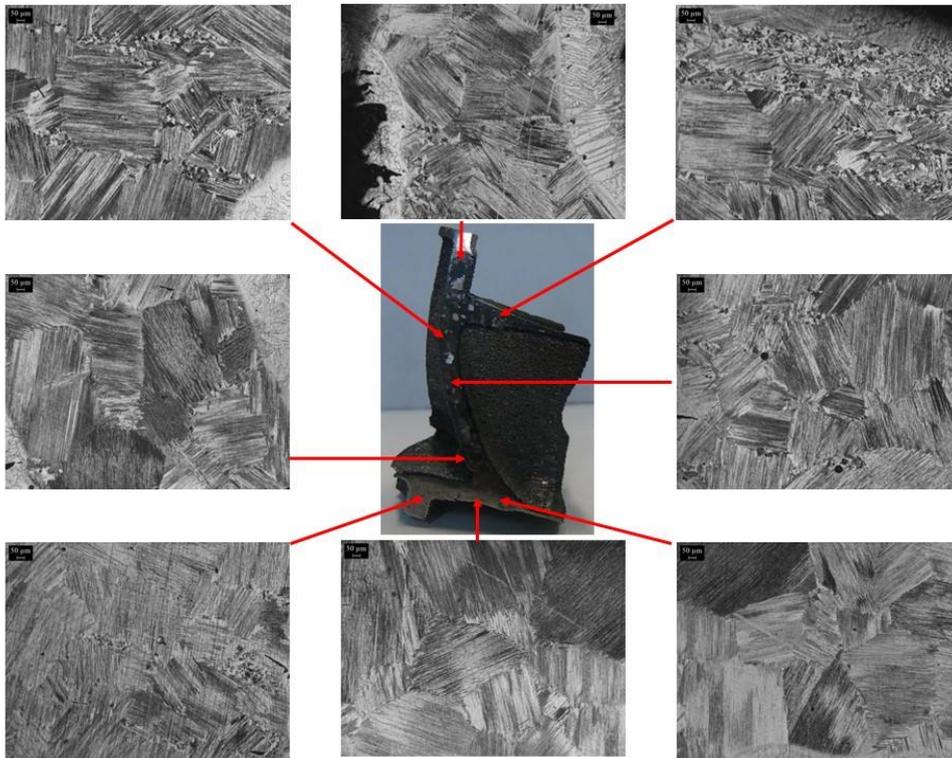
Figure 220: section of a turbocharger wheel after the heat treatment at 1355°C for 1 h and micrograph at 50X magnification of the microstructure in the different zones.

The overall microstructure was near lamellar characterized by lamellar colonies with an average dimension over 200 µm length with some residual γ-grains at the lamellar grain boundaries (**Figure 221**).

Moreover, for the zone inside the thinner blade, the observed microstructure was more equiaxed with a higher presence of residual γ-phase (**Figure 222**). This difference in microstructure between the bulk zones and the blade could be originated by heat phenomena during the EBM process as described for the wheel treated at 1360°C for 1 h.

However, the presence of a higher amount of γ-grains in these thinner zones can be considered acceptable since it is expected to do not have a significant and negative impact on the mechanical properties of the material.
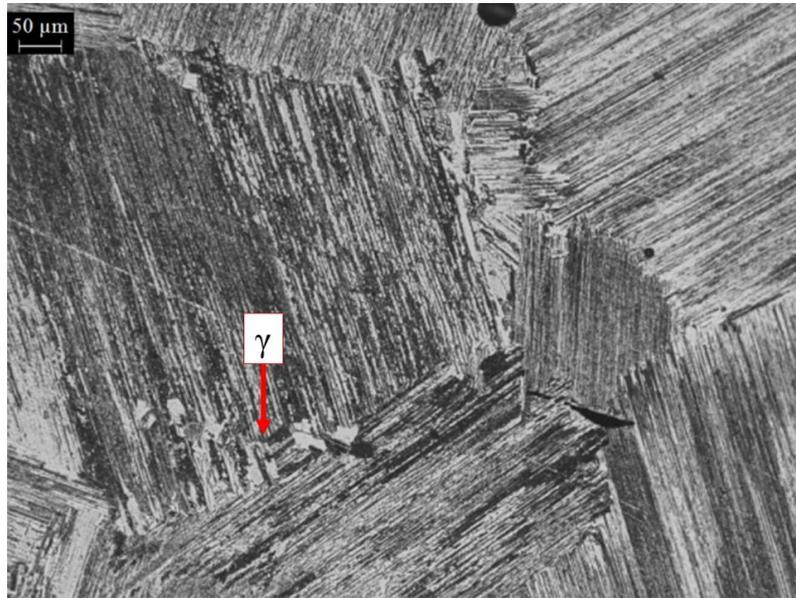
Figure 221: Near lamellar microstructure of the wheel after the heat treatment at 1355°C for 1 h.

Figure 222: Duplex microstructure of the wheel thinner blade after the heat treatment at 1355°C for 1 h.

The heat treatment at 1355°C for 1 hours is considered the best one for the hollow wheels produced by EBM because it produce the most near lamellar microstructure desirable for application.

7.8.4 Dimensional stability evaluation

In order to evaluate the effect of the heat treatment on the dimensional stability of the wheels, some measurements were performed on the wheels before and after the heat treatment. These measurements were done by both a dimensional measurement using a caliper and by a laser 3D scan measurement.

From the 3D scan image in **Figure 223** it is possible to notice that no significant distortion or dimensional variation were observed.
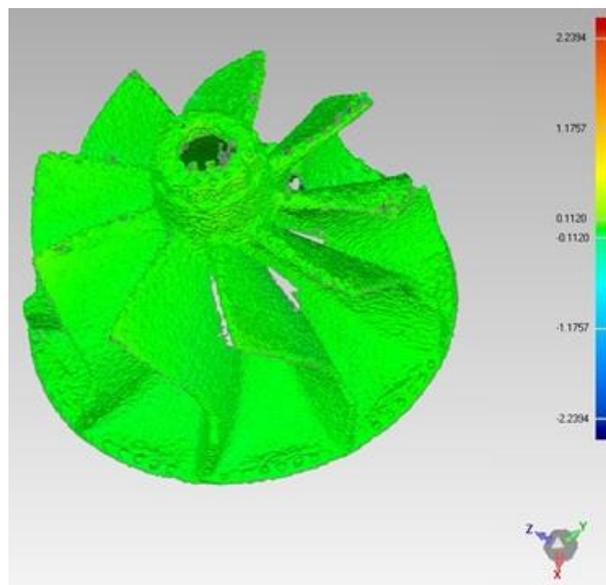
Figure 223: 3D scan image.

From these results, it is possible to asses that the RNT650 turbocharger wheels processed by EBM present a high dimensional stability and the heat treatment does not affects the shape and the dimension of the components.

7.8.5 Roughness considerations

The average roughness of the RNT650 specimen after EBM was measured using a profilometer and it resulted to be around 30-40 µm in terms of Ra.

This result suggests that machining operations after EBM or the optimization of the EBM process parameters are needed in order to decrease the surface roughness and meet the component requirements for application. Surface roughness is a well known issue of the EBM process, in fact, with this additive manufacturing technology it is impossible to reach, directly from the process, acceptable roughness

values on the manufactured parts. Moreover, adjusting the EBM parameters to decrease roughness, could not be a convenient solution because it has the consequence to decrease productivity if machining will be necessary anyway.

Since machining is needed, an accurate sizing of the wheel during its design is needed in order to guarantee the presence of the necessary overstock material. This allows to obtain the correct component dimension after machining.

The main factors causing surface roughness are:

- Partially sintered powder that remains attached to the surface for the effect of heat diffusion (**Figure 224 a**);
- Effect of the single layer melting during EBM. The material has shown a periodic inharmonic mountain-valley structure and the grooves, having dimensions of the same order of magnitude of the powder layer thickness used in the EBM process, are parallel to the powder layers [66][185].
    Figure 224 b shows the cross section of a specimen where this mountain-valley feature is clearly evident.
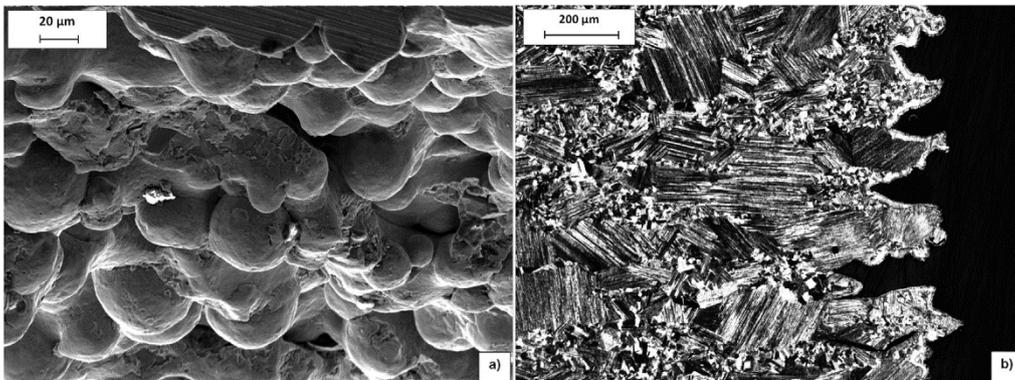
Figure 224: a) SEM image of a specimen showing the typical surface roughness composed by partially sintered powder particles; b) mountain-valley structure visible in a cross section of a specimen cut along the building direction.

The post process machining is thus necessary to improve the surface quality of the component removing such types of defects. During the TIALCHARGER project, different machining processes were tried and evaluated in order to demonstrate the feasibility, in terms of costs and technology, of finished RNT650 turbocharger wheels processed by EBM.

In **Figure 225** a detail of the surface of a wheel as-EBM and after finishing operation.
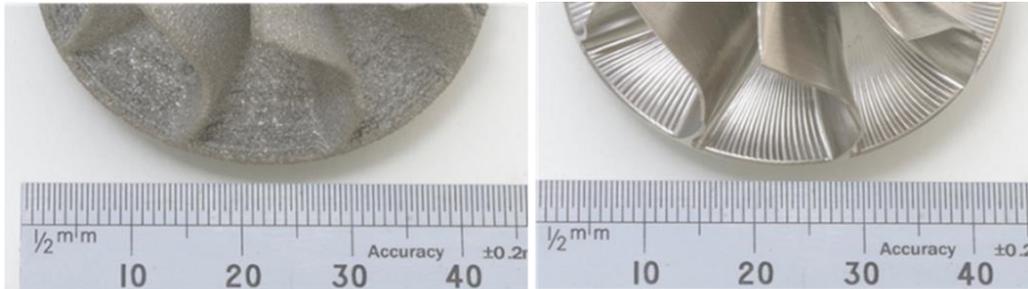
Figure 225: EBM turbocharger wheel surface detail before and after the surface finishing.

7.9 Brazed joints characterization

In order to demonstrate the effectiveness of producing titanium aluminide turbocharger wheels by EBM, it was necessary to produce a wheel/shaft assembly, which requires joining a steel shaft to a TiAl EBM wheel. For a Ni alloy wheel, this is quite straight forward and, traditionally, either rotary friction or EB (Electron Beam) welding is used to make serial production of turbocharger rotors assemblies. In recent times, EB welding has become the most common method due to the accuracy of the process eliminating the need for post welding machining, removal of excessive material for balancing and the minimal metallurgical disturbance caused to the high temperature Ni alloy. The use of TiAl as a wheel material presents a greater challenge as both Ti and Al form brittle intermetallic compounds when alloyed with iron, potentially leading to a risk of welds being produced with little ductility and severe cracking.

During TIALCHARGER project, the EB brazing process has been optimized and a procedure for joining EBM TiAl rotors to the CrMo steel shaft has been developed.

The brazing was achieved through the use of a localized, diffuse, heat source provided by a defocused EB positioned either side of the braze line thereby locally heating the steel and TiAl parts above the braze liquidus, melting the braze foil by conduction and forming a brazed joint at the planar interface at the end of the rotor wheel. The brazing process was carried out by TWI Ltd.

In order to develop the brazing process and perform a metallurgical assessment for of the TiAl/shaft assemblies, some brazed joints were produced using EBM RNT650 TiAl cylindrical specimens and steel shaft. Then, further brazing tests were necessary to transfer the brazing procedure to the rotor wheel/shaft joints, due to the differences in thermal mass and geometry of the wheel assemblies especially when considering the hollow wheel design.

In **Figure 226** a schematic representation and a photo of the brazed joints are shown.
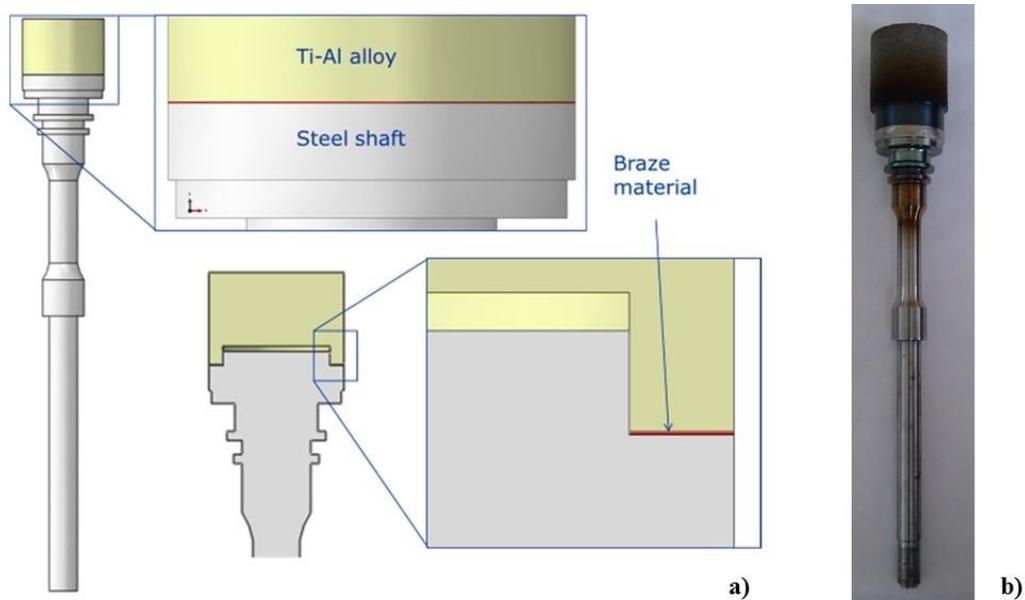
Figure 226: a) schematic representation of a brazed joint with junction details; b) TiAl cylinder/steel shaft brazed joint.

The composition of the three base materials employed for the joint is reported in **Table 42**.

Table 42: Chemical composition of the parts of the joint.

Composition wt%										
	Ti	Al	Nb	Cr	Si	Ni	B	C	Fe	Mo
(TiAl alloy) RNT 650	Bal	33.5	4.8	1	0.2	-	-	-	-	-
(brazing material) METGLAS® MBF-30	-	-	-	-	4.5	Bal	3.2	0.06	-	-
(steel shaft) JIS SCM435H	-	-	-	1.06	-	-	-	0.35	Bal	0.25

The choice of brazing derived from the need to connect two different materials with different coefficients of thermal expansion: the nickel-based alloy was selected because it ensures a stable joining having intermediate thermal features between those of steel and titanium aluminide [186]. In addition, the adoption of EBW was dictated by the possibility to heat and melt only the precise location of the braze alloy, reducing in this way the deformations of the heat treated zones and the thermal residual stresses [187][188].

A cylindrical TiAl part/steel shaft specimen was then characterized in terms of junction quality, by checking the presence of any defects at the junction level and assessing the complete adhesion of the parts. Metallographic analysis was performed in order to verify the presence of any microstructural anomalies caused by the brazing process and EDS elemental distribution mapping was also performed to investigate the elements distribution in the junction zone.

7.9.1 Metallurgical analysis and junction quality investigation

7.9.1.1 Optical microscopy analysis

A TiAl coupon – steel shaft joint produced by TWI was subjected to metallurgical investigation.

The TiAl part was joined to the steel shaft in the as-EBM condition and after a proper machining of the welded part in order to obtain a low roughness level, which is an essential condition for a successful EB welding.

For the metallographic preparation of the specimen, the junction has been cut perpendicularly in order to appreciate a planar surface of the junction region.

The sections were then mounted, polished up to 4000 grit and subjected to the optical metallographic analysis.

The obtained optical microscopy images are reported below.
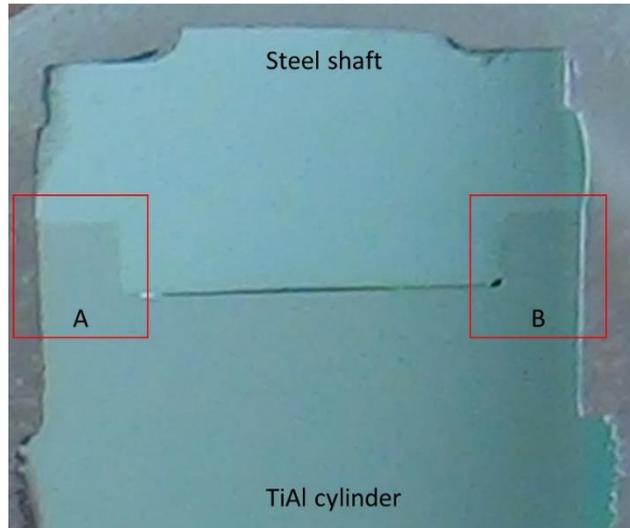
Figure 227: Joint section analyzed.
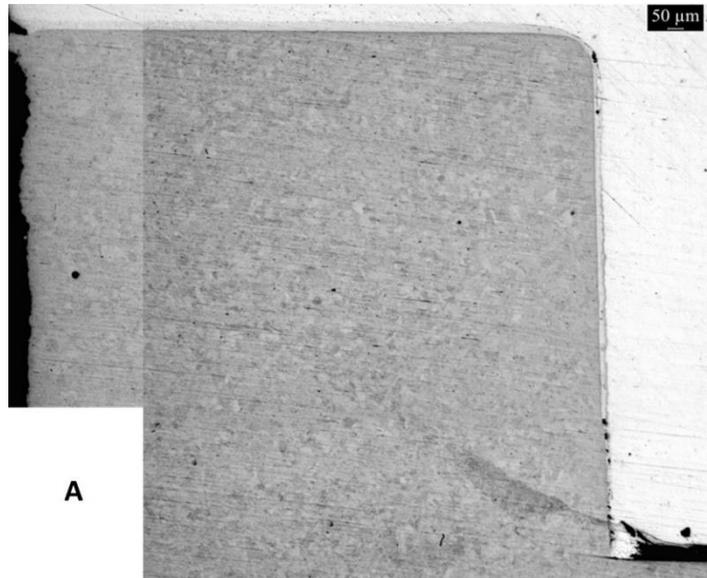
Figure 228: Optical micrograph of the junction region A.
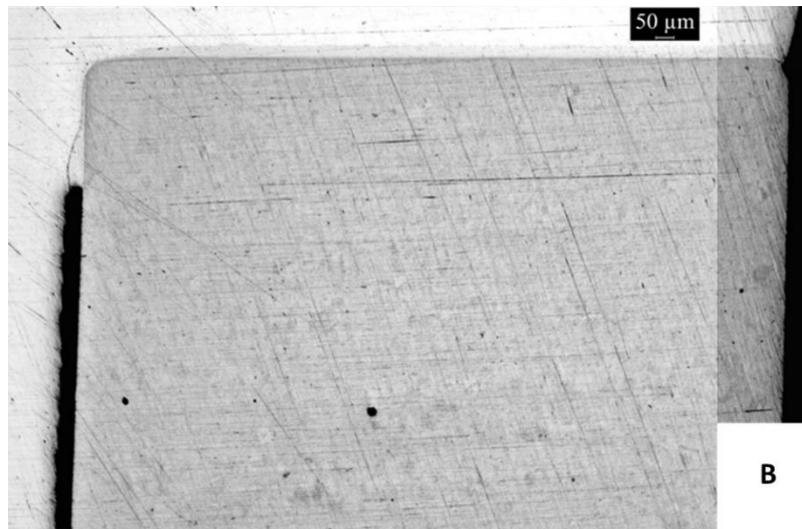
Figure 229: Optical micrograph of the junction region B.
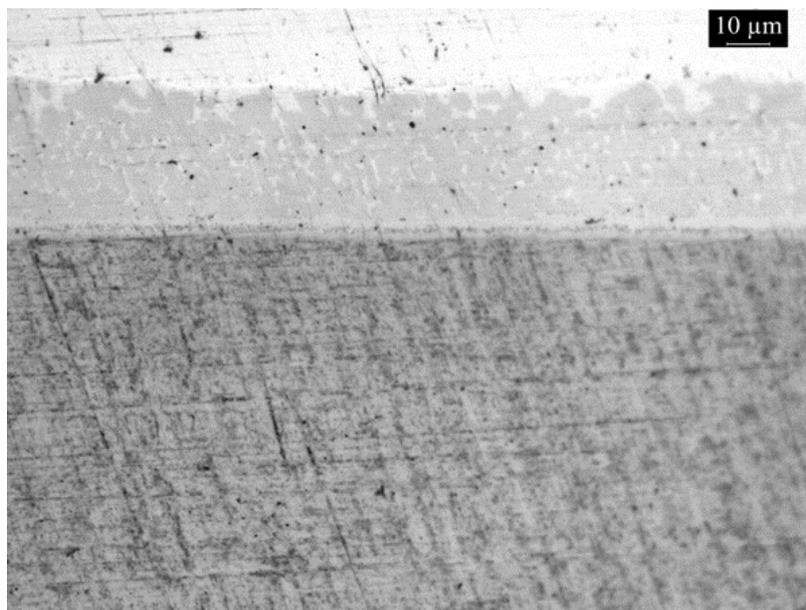
Figure 230: Optical micrograph detail of the junction region.

From the optical micrograph above (**Figure 228** - **Figure 230**), it is possible to assess a good junction quality.

From the lower magnification image (**Figure 228, Figure 229**) the overview of the entire junction region can be evaluated. From these images, no particular defects are observed. From the higher magnification images (**Figure 230**, **Figure 231**) it is

possible to analyze more in detail the junction and also from these image the good quality of the junction, in terms of adhesion between TiAl part – Brazing material – Steel shaft, and in terms of pores and defects can be assessed. However, some defects can be observed, in particular some pores between the brazing layer and the steel part (**Figure 231**). These defects are mainly present in the sides of the junction region and this can be considered acceptable because the brazing material is only deposited in the horizontal contact area during the brazing (**Figure 226 a**). The presence of brazing material also in the side area is mainly due to its diffusion in this zone during its melting and can be considered a normal phenomenon for this process. Moreover, the dimension of these defects is very low and are expected to not affect the mechanical properties of the joints.
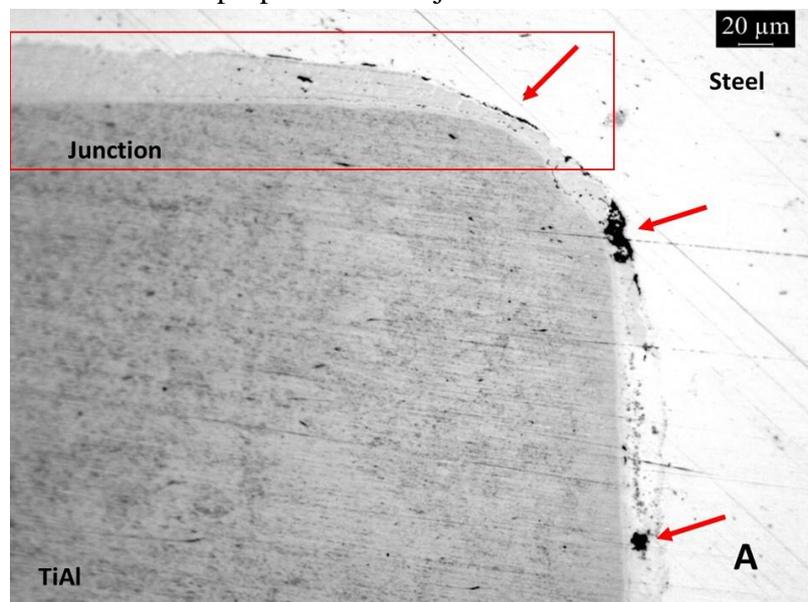
Figure 231: Junction detail. The defects are highlighted by the red arrows and the junction region is framed in red.

In order to better evaluate the junction quality for an extended brazed region, few millimeters of the external part of the junction has been polished and characterized (**Figure 232**).

Figure 232: polished junction.

In **Figure 233** the interface between the steel shaft and TiAl cylinder is shown with particular attention both in the central part (red) and the external parts (yellow).
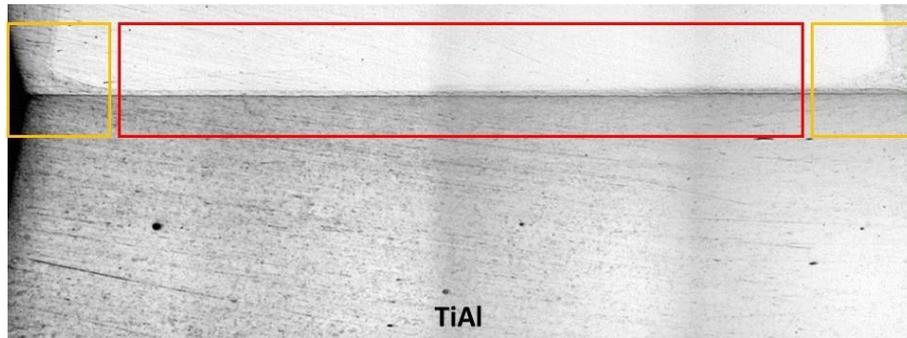
Figure 233: polished junction micrograph overview.

From this image appears that the junction presents a good quality without the presence of significant defects.

In **Figure 234** the optical micrograph of the external part and the higher magnification detail of the external part is reported. Some cracks in the brazing material and defects are highlighted by the red arrow.
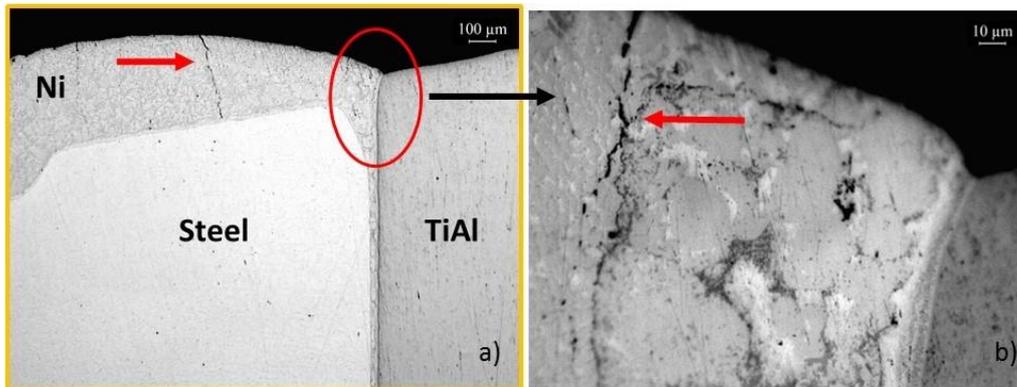
Figure 234: a) micrograph of the external part of the junction; b) higher magnification detail with cracks highlighted by the red arrow.

Figure 235 and **Figure 236** show the optical micrograph of the central part of the junction at different magnifications.
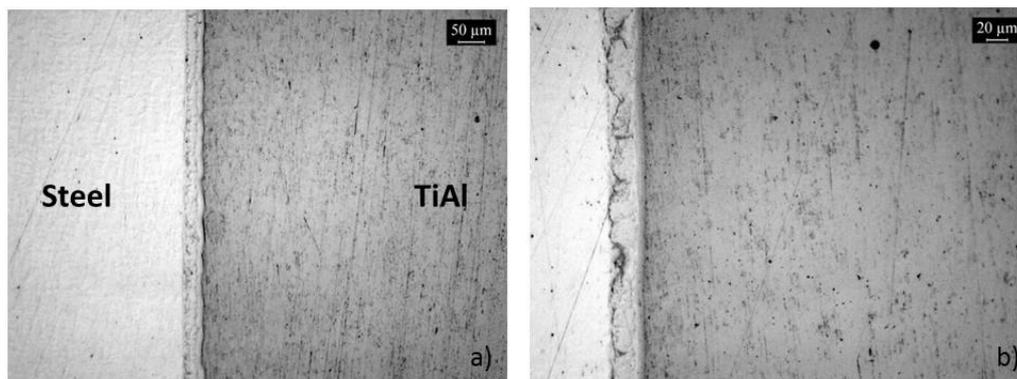
Figure 235: micrographs at different magnification of the central part of the junction.

Figure 236: detail of the central part of the junction.

Also in the central area, the junction presents a good adhesion between the parts. However, some defects were detected at the interface between the steel shaft and Ni brazing material.

By observing the junction nickel layer, it is possible to appreciate a sort of inhomogeneity showing the presence of brighter spots (**Figure 237**).
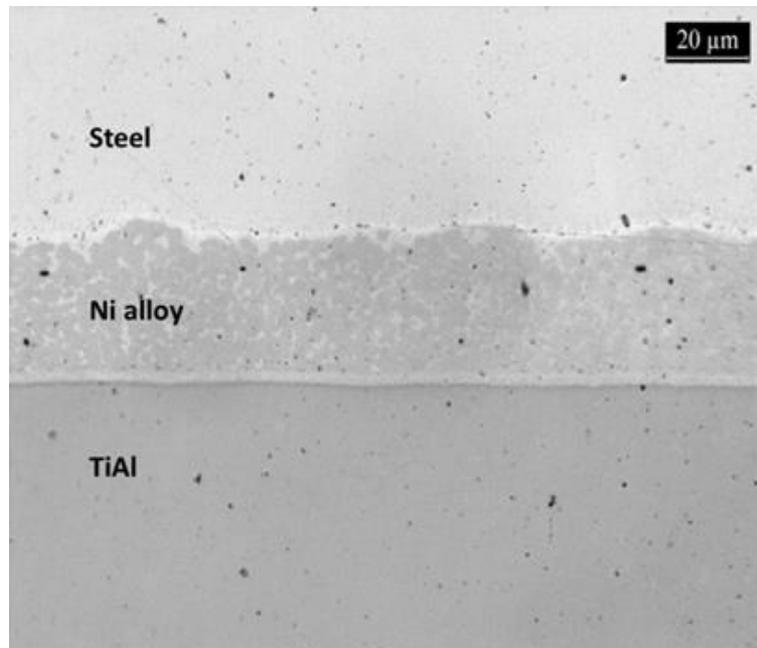
Figure 237: optical microscope image of the joint. joining layer detail

In order to evaluate the microstructure of the TiAl part and to check if it was eventually affected by the temperature reached during the brazing, the polished specimen was etched with Kroll's solution and analyzed by optical microscopy.

The resulting microstructure is shown in **Figure 238**. The steel part appears completely black because of the etching and the TiAl part has shown a fine near gamma microstructure (microstructure detail in **Figure 239**) and therefore, it is possible to asses that it was not affected during the brazing process.

Again, some cracks in the Ni brazing material can be identified in this image (red arrow) but also some residual defects in the TiAl material, in particular some elongated pores parallel to the powder layers (green arrows) and some small spherical pores (yellow arrows).
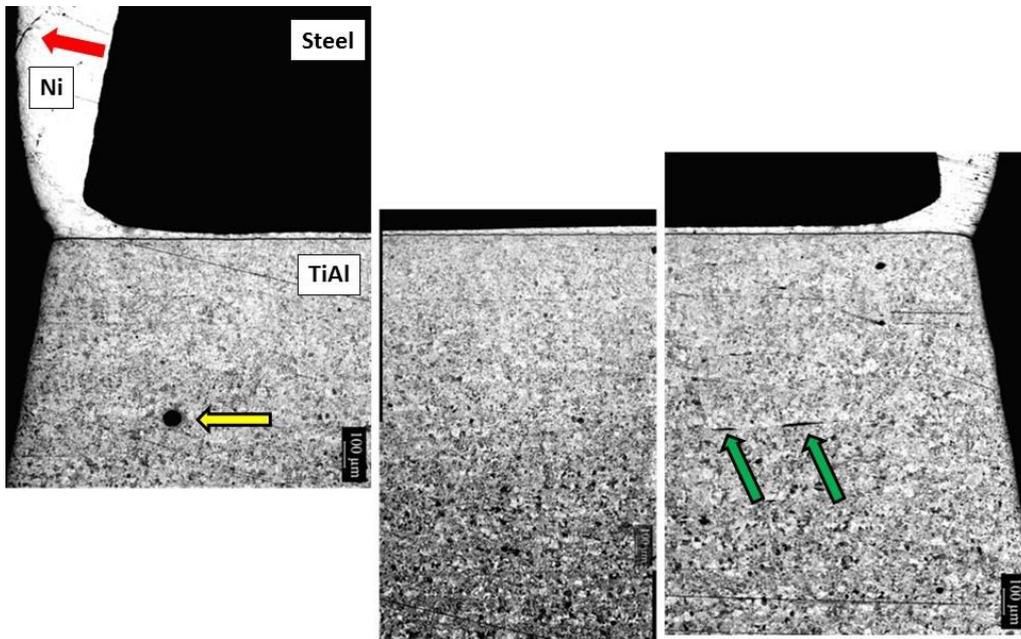
Figure 238: Optical microscopy images of the etched sample for the microstructural evaluation. The red arrow indicates a micro crack observed in the Ni, the yellow arrow points a typical spherical porosity in the TiAl cylinder and the green arrows highlight some elongated pores.
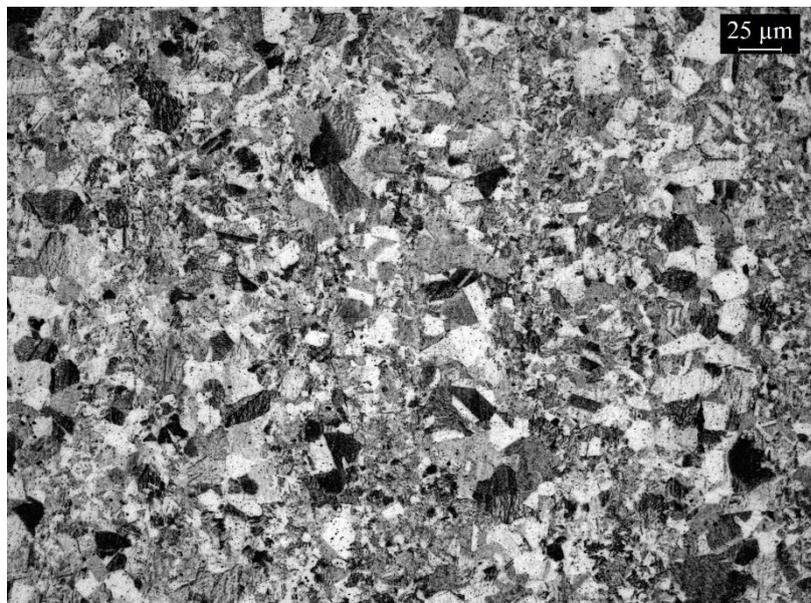
Figure 239: Optical micrograph detail showing the gamma microstructure of the TiAl part of the joint.

A further investigation was done on the polished joint using the SEM technique. With this technology, the morphology and the elemental distribution maps were investigated and the results are reported in the following part.

7.9.1.2 Electron Microscopy analysis

The FE-SEM analysis was used to better appreciate the quality of the junction from the morphological point of view, to investigate the presence, diffusion and distribution of the different elements through the junction region and also to check the presence of any new phases and precipitates formed during the brazing. The elemental distribution mapping was done using the EDS technology.

Some SEM images of the central region are reported below (**Figure 240**). This area generally exhibits a good junction quality however, some defects can be observed in particular at higher magnifications (**Figure 241**).
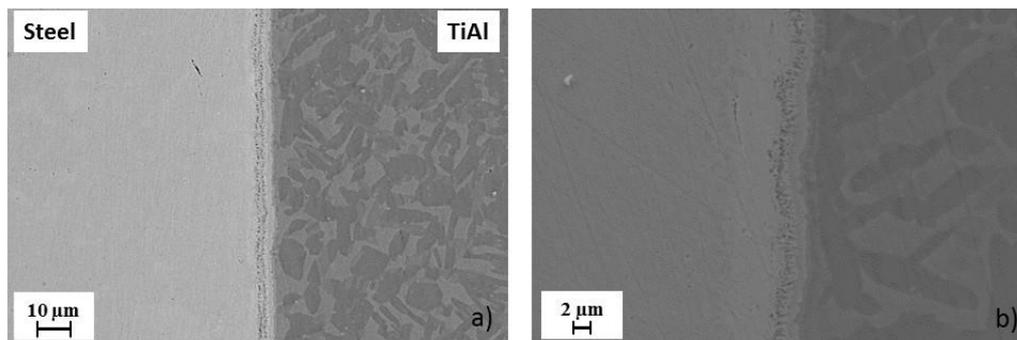
Figure 240: SEM image of the central junction region.
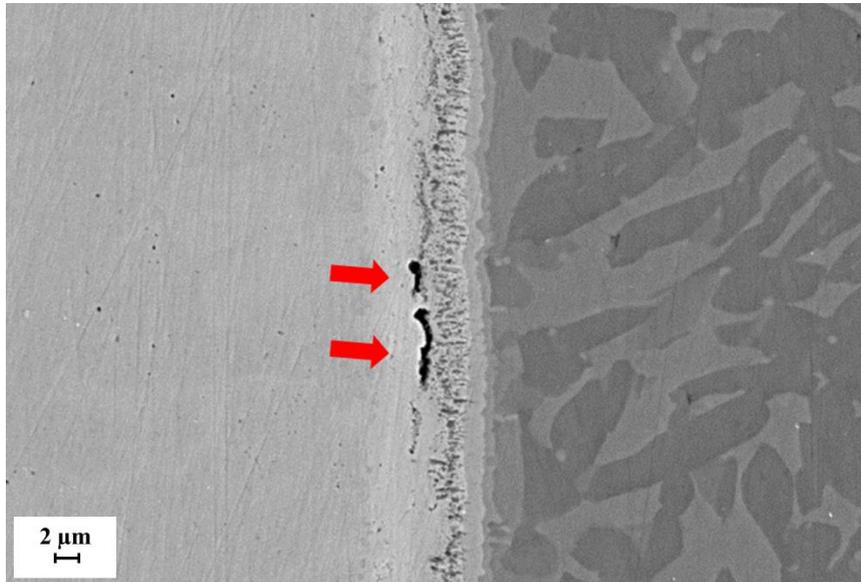
Figure 241: detail of the defects between the steel shaft and the Ni alloy.

The elemental distribution maps for the central junction region of the trial were performed at 5000X magnification as represented in the images below.
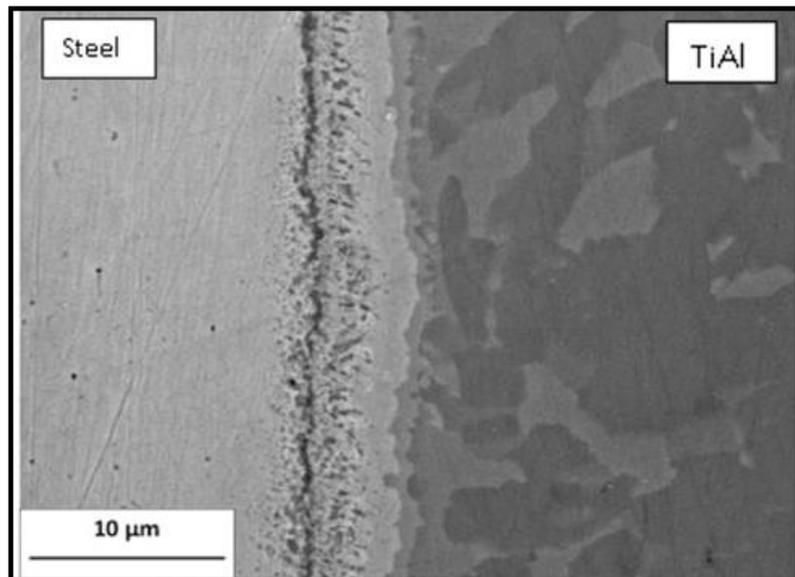
Figure 242: SEM image of the analyzed central junction area.
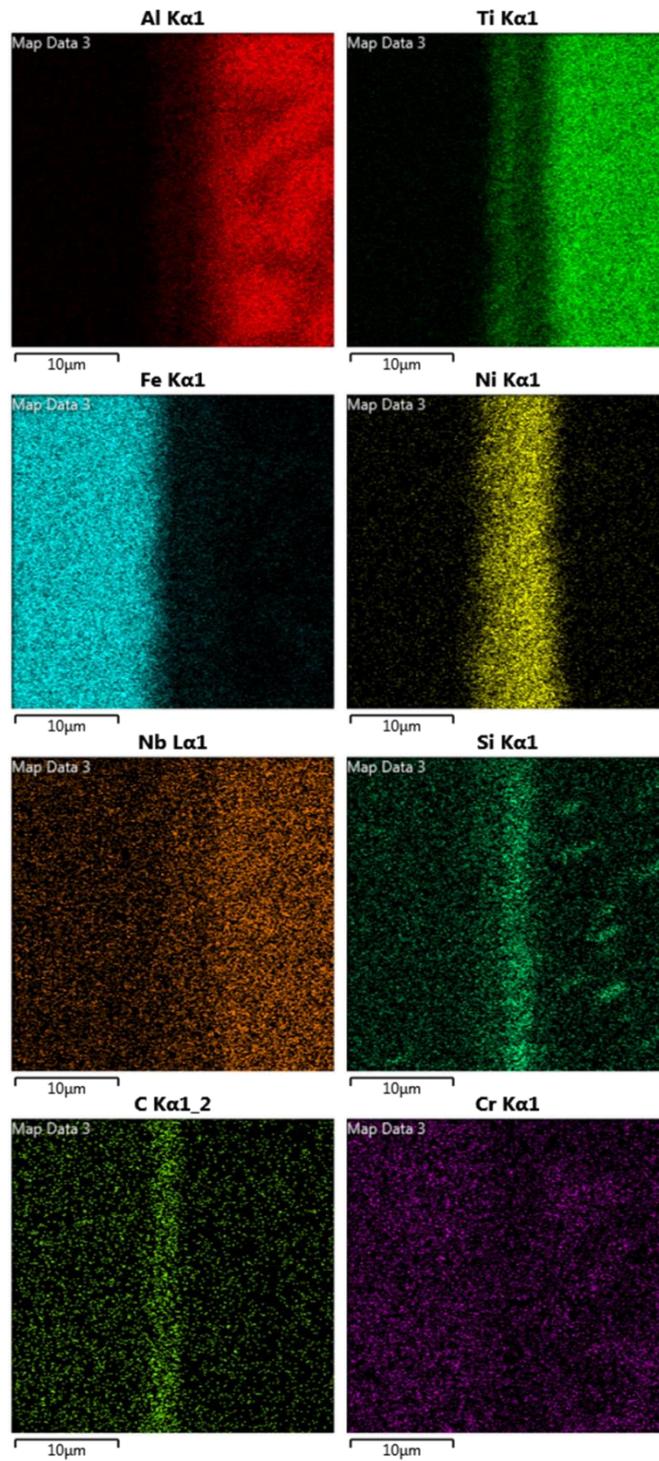
Figure 243: Elemental distribution maps of the different elements in the central part of the junction region.

The layered images of the maps helps to understand the distribution of the different elements for the central area.
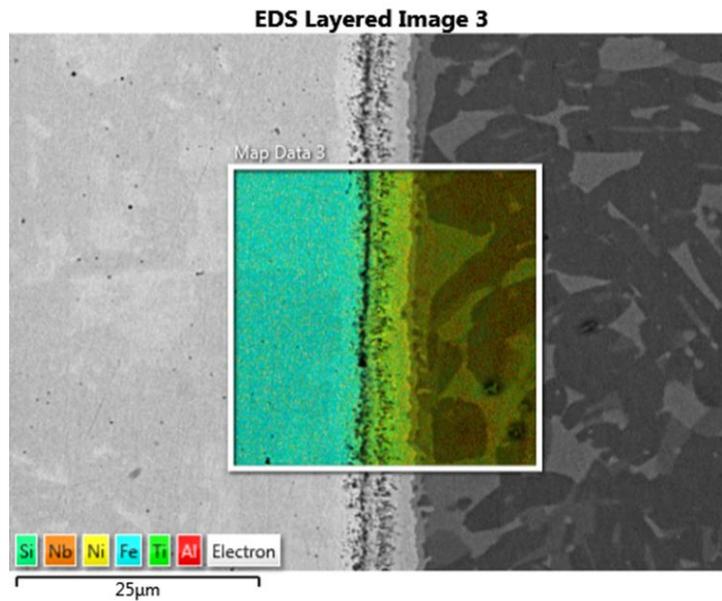
Figure 244: Layered image of elemental distribution maps for the central junction region.
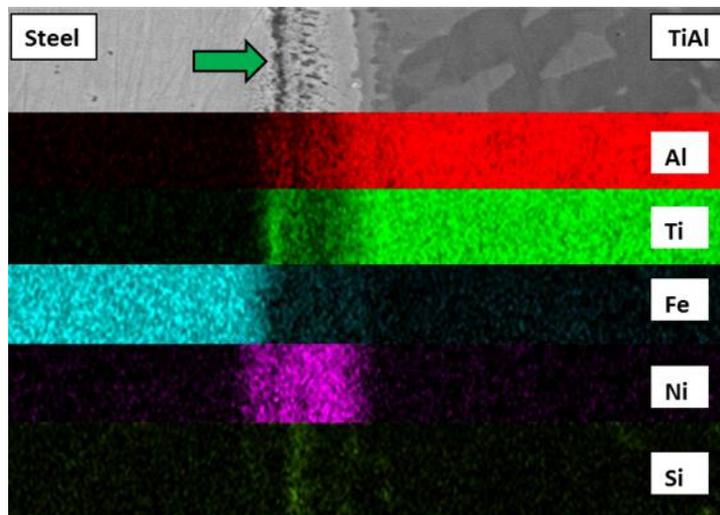
Figure 245: Graphic processing of the SEM and the elemental maps images at the central part of the junction. By this way is possible to associate the element distributions to the different layers.

From the elemental distribution maps and in particular from the layered image of the maps in **Figure 245**, it is possible to observe that both Al and Ti present in the TiAl part tend to diffuse inside the Ni junction layer. In a similar way, Fe from the steel part diffuses inside the junction layer.

The dark grey layer, appreciable from the morphology SEM image and highlighted by the green arrow, exhibit a considerable presence of Ti while the brighter gray layer presents a dotted morphology and it is rich in Si. It is important to point out that the nickel-based brazing alloy present an amount of about 4,5 wt.% of Si in its composition.

The formation of different phases and precipitates in this area, could in part explains the presence of certain types of defects observed in SEM micrograph in the junction. More precisely, harder phases, such as precipitates or clusters of precipitates, tend to detach from the substrate, leaving holes and pores that can be noticed from the morphology images.

The presence of Si-rich areas is confirmed by the EDS line and map analyses performed on the nickel junction layer (**Figure 246** and **Figure 247**).
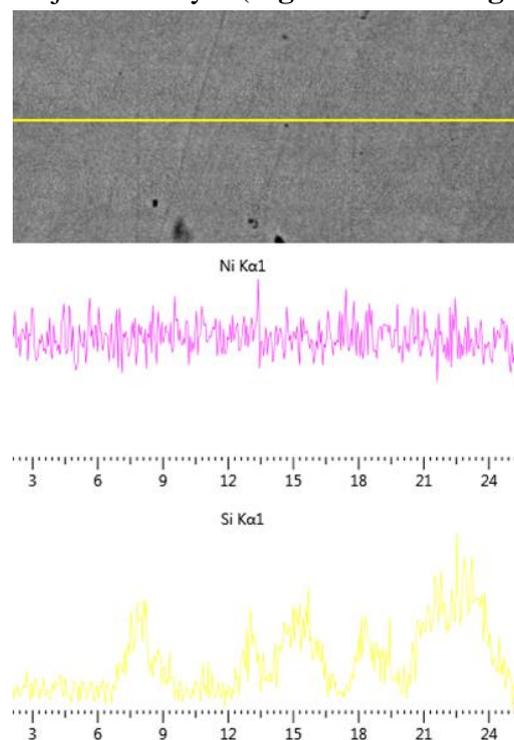
Figure 246: EDS line along the Ni alloy braze region.

The EDS line result above shows some Si peaks that correspond to the in-homogeneities in the nickel braze alloys. The Si-rich areas are also highlighted by the EDS map in **Figure 247** (pink areas).
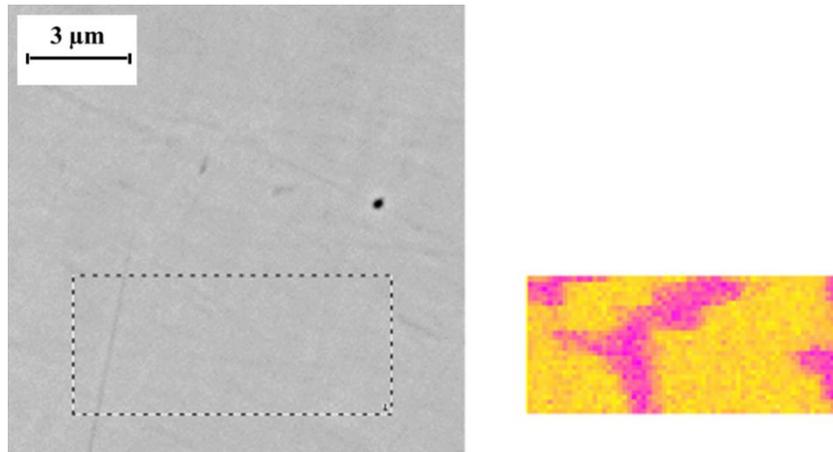
Figure 247: EDS map of the Ni braze alloy region.

The diffusive interfaces generated during the brazing were then deeply investigated with back-scattered SEM at higher magnification (**Figure 248**).
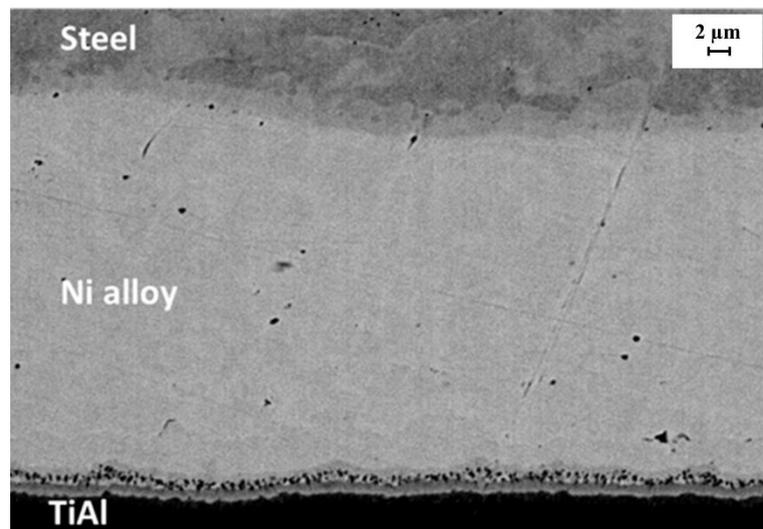
Figure 248: SEM backscattered electrons image. It is possible to distinguish the three materials forming the joint, in particular, different phases have been generated at the TiAl-Ni interface.

On the steel side, the diffusive phenomena seems not to have generated any additional phases. On the other hand, it is possible to observe several phases produced at the diffusive interface between TiAl and Ni alloy (detail in **Figure 249**). This type of morphology and layers observed are also confirmed by the works of Tetsui [187] and Liu J et al [186].
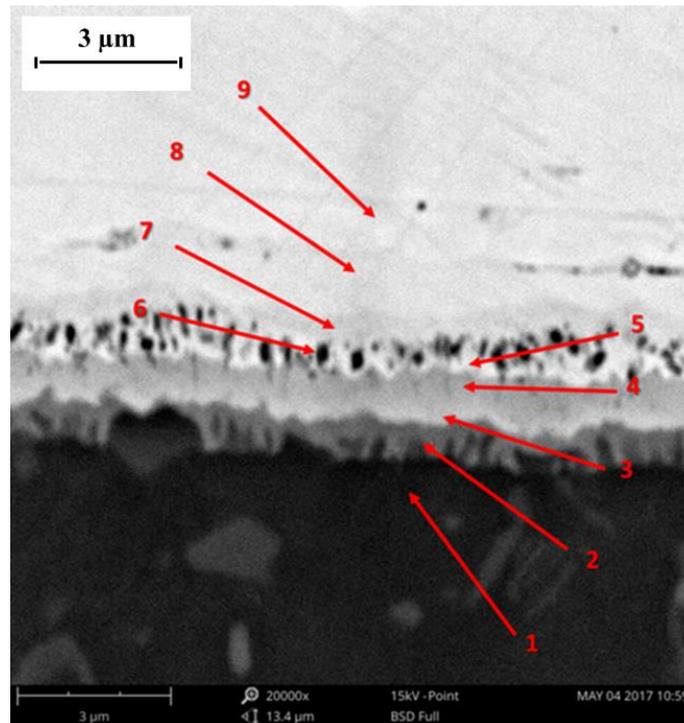
Figure 249: Higher magnification detail of the diffusive interface between TiAl and Ni braze alloy. The different phases and zone of the junction are indicated.

To better understand the nature of these phases and the distribution of the single elements, punctual, linear and EDS map analysis of the diffusive interface (**Figure 250**) have been executed [189].

The different layers observed and observed phases, indicated in **Figure 249** are reported below:

1. TiAl RNT650 alloy;
2. continuous grey layer which could be approximated to the TiAl alloy. In particular it can be observed an enrichment in titanium (**Figure 250b**) compatible with the Ti_3Al phase, also recognized in the work of Tetsui T [187];
3. continuous phase with sawtooth morphology. The EDS analysis pointed out the increase of nickel concentration in the composition of this phase. The

fringes could be due to the diffusion of nickel through the TiAl alloy at high temperatures during the brazing procedure. In the work of Liu J. et al [186], when joining TiAl to Ti_3SiC_2 with pure nickel brazing material, a similar morphology was found and it has been identified as Al_3NiTi_2. In accordance with the line EDS (**Figure 250b**) and the punctual EDS, there is an elemental proportion between Al:Ni:Ti of 3:1:2 approximately, for this reason this phase could correspond to Al_3NiTi_2;
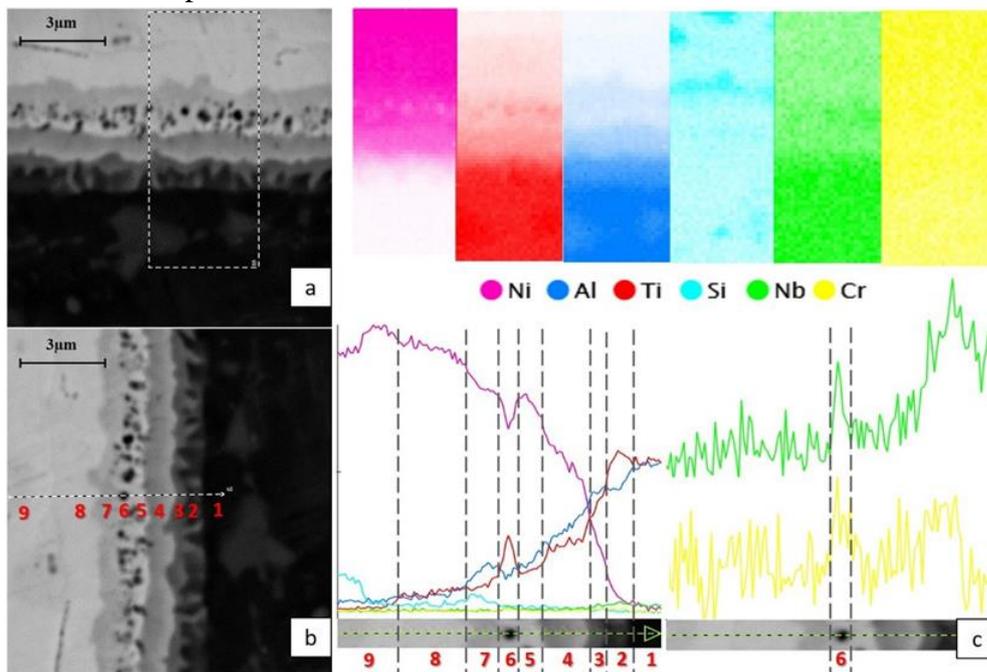
Figure 250: a)EDS map along the TiAl-Ni braze interface; b) EDS line; c) EDS line details for Cr and Nb.

4. continuous grey phase due to the diffusion of the TiAl alloy elements toward the brazing alloy. The concentrations of Al, Ti and Ni 26.7%, 22.6% and 48.4% respectively suggest that this phase could be associated to $AlNi_2Ti$, similarly to what observed by Tetsui T.[187];

5. continuous white phase richer in Ni. Also this morphology is confirmed by the work of Tetsui [187];

6. black spherical precipitates within the fifth layer. As showed by the map in **Figure 250a** and the line in **Figure 250b** and **c**, they seem to be rich respectively in titanium, niobium and chromium. According to literature, Tetsui T. [187] reported these precipitates as borides, on the contrary Liu et al [186] identifies them as carbides. Ti, Nb and Cr have a high affinity with both

     C and B, however, the higher amount of boron respect to carbon in the brazing alloy suggest that, in our case, the formation of borides is more probable;

7. grey continuous phase containing a higher concentration of silicon. Si comes from both TiAl and nickel-based alloy. According to Liu J. et al [186], Si displays a high migration activity, for this reason they can promote the bonding of materials reacting with the other elements;

8. lighter grey continuous phase where there are some traces of the TiAl diffusion, even if the composition is almost the same of the nickel alloy;

9. nickel braze alloy, whose composition are reported previously. In **Figure 250a**, and **b** it is possible to appreciate the silicon rich regions discussed previously.

7.10 Conclusion on the Electron Beam Melting of TiAl RNT650 alloy for automotive application

The characterization of test samples made of alloy Ti-48Al-2Nb-0.7Cr-0.3Si produced by Electron Beam Melting highlighted a fully densification of the part during EBM with only a minor amount of build flaws (residual porosity $0.07 \pm 0.06\%$).

The chemical composition analysis has shown an Al loss lower than 2 wt.% during the EBM process. Nevertheless, Al loss can be overcome using a starting powder enriched in Al. The amount of impurities detected in the specimens after EBM was very low and comparable between the powder and the part indicating the cleanliness of the process.

The X-Ray diffraction analysis has highlighted the prevalence of γ-TiAl phase and the presence α_2-Ti$_3$Al phase also. This phase composition is very close to that of the 48-2-2 TiAl alloy and typical for the as-EBM material.

The microstructure of the specimens after EBM was a fine and homogeneous γ-microstructure and it was considered acceptable for this material. This type of microstructure, together with the low amount of porosity observed, has proved the validity of the material and has assessed the validity of the EBM process for the RNT650 alloy.

With a subsequent heat treatment at 1360°C for 2 hours, the as-EBM gamma microstructure can be transformed into a near fully lamellar one that is expecting to presents properties bringing to promising performances for the application in turbocharger wheels.

Some mechanical tests (tensile tests and creep tests) were performed on heat treated specimens and the obtained results were comparable with literature data for Ni based superalloys and with the similar alloy produced by casting [116].

Some turbocharger wheels prototype were produced by the Fraunhofer Institute of Dresden as demonstrator for the EU project TIALCHARGER. With EBM technique was possible to produce turbocharger wheels with an innovative lightweight hollow design exploiting the freeform capability of EBM process in order to further reduce component weight.

The material characterization performed on as-EBM wheel has shown a low amount of residual defects (residual porosity $0.17 \pm 0.24\%$) and a typical fine and homogeneous near gamma microstructure.

A heat treatment was performed to reach the desired near fully lamellar microstructure using the same parameters necessary to obtain this microstructure in RNT650 specimens. Furthermore, a fine heat treatment tuning was necessary because of the different shape of the component presenting both thinner and massive parts respect to the test specimens. Therefore, a heat treatment at 1355°C for 1 hour was necessary to obtain a near fully lamellar microstructure.

The heat treated wheel presented a good dimensional stability during the heat treatment

The measured surface roughness of about 30-40 µm in terms of Ra suggests that machining operations after EBM is needed in order to decrease the surface roughness and meet the component requirements for application.

Some RNT650 TiAl cylinder/shaft joints were successfully produced by TWI Ltd using Electron Beam brazing technique. Joint trials produced using different brazing parameters was characterized and the results have pointed out a promising junction quality.

The elemental distribution mapping was also performed in order to investigate the distribution and diffusion of the different elements through the junction. This analysis has highlighted that some elements presents in the TiAl part and in the steel part tend to diffuse and segregate in particular zones of the interfaces. EDS line and EDS punctual analysis were used to deeper investigate the diffusion phenomena and it was possible to highlight and partially explain the formation of precipitates during the brazing process.

The microstructure observed in the TiAl part of the joint was the typical near gamma equiaxed microstructure and it means that the EB brazing process did not affect the TiAl microstructure. It is necessary to point out that these joints were prod66uced using TiAl part in its as-EBM condition and, for applications, would be necessary to produce the joints using heat treated TiAl part and heat treated steel shaft because performing the heat treatment after the joining process will affect the properties of the different part of the assembly.

Finally, it is possible to assess that the joints are very promising for application, and some wheel/shaft assemblies were successfully produced as demonstrators (**Figure 251**). However, in order to validate the quality of the junction for the component application, it would be necessary to evaluate the impact of the observed defect such as pores and precipitates on the mechanical properties of the component. A preliminary evaluation could be done by microhardness test across the joint interface, used to evaluate the performance of reaction products correlating

the results to the mechanical properties of the joint in terms of ductility and ability to resist deformation.

The joint strength could be then evaluated by means of tensile tests using particular tensile specimens having the joined parts in the gauge length. Also the fatigue performance of the joint could be subsequently evaluated by proper fatigue tests.

Generally, as reported in literature, by means of the reaction between TiAl and brazing fillers, the brazed portion becomes brittle but high-temperature strength is improved. When high temperature strength is required for a brazed TiAl joint, hardness should be adjusted by controlling the amounts of the hardening elements (Cu, Ni, Au) in brazing fillers according to the application and using temperature [187].

The impact of the precipitates observed in a particular area of the junction should not be too negative on mechanical performance considering their small dimensions, however, their high concentration in thin area extended along all the junction could bring to an embrittlement of the component under stress conditions with the risk of failure and delamination. The mechanical tests indicated above can be useful to assess the impact of the precipitates.

The residual stresses generated in the interface region during the cooling stage of the brazing can degrade the joining properties giving rise to a severe crack tendency. For this reason is important to select a proper brazing temperature and control the brazing parameters [186].

Improvement of the joint quality and performance could be obtained focusing on the design, for example introducing a spacer into the joint design to control the thickness of braze in the joint and hence increasing the consistency of the assemblies in terms of run-out and length, on the selection of brazing material and brazing parameter. In particular, the critical process control parameters for the production of the analyzed joint were the heat distribution between the TiAl and the steel parts (governed by the deflection pattern) and soak time.

Further endurance tests using a particular test rig simulating the operation condition of a turbocharger assembly would be an essential step to ensure the required run-out requirements.

Figure 251: wheel/shaft assembly demonstrator produced within the TIALCHARGER project.

Chapter 8

Conclusions and Perspectives

The aims of this work were the characterization of different γ-TiAl alloys powders for aerospace and automotive applications and parts processed by EBM, the heat treatment setup to produce the best microstructure for application of the different alloys and the characterization of turbocharger wheels produced by EBM and wheel-shaft assemblies trials. The powders characterization is an essential step to ensure a good success of the additive manufacturing process. The characterization of massive specimens and parts consolidated by EBM in terms of residual porosity/defects, chemical composition and microstructure it is necessary to assess the feasibility of the process for a certain alloy. Moreover, the characterization helps the EBM process improvement by modifying the process parameters in order to obtain a defect-free material with an optimal as-EBM homogeneous microstructure.

The main results obtained in this work are:

- The powders characterization has shown that the used powders of Ti-48Al-2Cr-2Nb (at.%), HNb, RNT650 and TNM alloys presented a proper morphology without the presence of defects. The particle size distribution, flowability and apparent density were optimal for the EBM process and regarding the RNT650 alloy a modification of the particle size distribution has been done in order to improve the flowability and, consequently, ensure the powder deposition process during EBM.

  The chemical analysis demonstrated that the presence of impurities, in particular oxygen, was very limited. It was also performed to check the nominal elemental composition of the powders and, by comparing it with that observed in the EBM processed specimen, was possible to know the amount of Al lost due to EBM and consequently optimize the

powder chemical composition in order to reach the proper nominal composition of the specimens and parts.

- The investigation carried out on the possibility to reuse the Ti-48Al-2Cr-2Nb (at.%) TiAl powder for several EBM cycles has demonstrated that it is possible to reuse it for subsequent EBM manufacturing cycles. In any case, it is possible to mix the recycled powder with new one in order to obtain a final powder with proper characteristics. The possibility to reuse the powder leads to a considerable advantage in terms of material and cost saving in addition to the advantages of the EBM technique itself.

- The study about the effect of the EBM building parameters variation on the Ti-48Al-2Cr-2Nb (at.%) material characteristics has shown that, by using a proper parameters combination, it is possible to obtain specimens with a very low amount of residual porosity, an elemental composition in the range of the desired nominal composition and the desired microstructure. In particular, it is fundamental to control the aluminium content that is very sensitive to the parameters variation. Since the microstructure is strictly correlated to the aluminium content, a further technological development could be to obtain particular microstructures in different zones of a component, leading to combinations of material properties, by varying the building parameters between the different zones,. In this way, the component capability to resist different types of stresses applied on its different areas could be improved.

- The activity on the TNM (Ti-44Al-4Nb-1Mo (at.%)) alloy for aircraft engine application produced by EBM has demonstrated the possibility to process this alloy by the EBM technology and to obtain a desired microstructure after a proper heat treatment in order to improve the mechanical properties of the material. The fine and homogenous microstructure after the HIP treatment was the starting point for the heat treatment set up. After the heat treatment setup, two particular microstructure have been selected for the aircraft low-pressure turbine blade application. These microstructures are expected to produce a proper combination of strength, ductility, creep and fatigue resistance. In fact, the mechanical tests performed by Avio during the SP5 part of the E-Break project on the heat-treated EBM material have shown promising mechanical properties compared to the same material produced by casting and the TiAl 48-2-2 alloy produced by both casting and EBM.

- Regarding the Ti-48Al-2Nb-0.7Cr-0.3Si (at.%) (RNT650) alloy for the automotive application in turbochargers, it has been assessed the possibility to produce lightweight hollow wheels by EBM. With the selected heat treatment it has been possible to obtain a near fully lamellar microstructure that has demonstrated to give good mechanical properties and, consequently, high component performances. The characterization of wheel-shaft assembly prototype has shown that the Electron Beam brazing technique is well suitable to produce promising component assemblies.

  This activity done within the European project TIALCHARGER has bring to very satisfactory results. In fact, thanks to the capability of additive manufacturing techniques like EBM to build components with complex shapes, it is possible to have more freedom in components design. The particular hollow design of the EBM processed wheels together with the low weight and good specific mechanical properties of TiAl alloy, might lead to a significant improvement of the engine performance with also a decrease in fuel consumption and emissions. However, the need for a post processing machining or surface finishing of the components processed by EBM has not allowed to meet the costs established by the project. A further efficient and low cost surface finishing optimization shall be necessary to make this technological application competitive on an industrial scale.

The achievements obtained in this thesis have well confirmed the great potential of the EBM additive manufacturing technology to process various γ-TiAl alloys for both automotive and aerospace applications. Considering that the γ-TiAl alloys, studied and processed by AM until now, were designed mainly for conventional manufacturing methods such as casting, the study and production of new generation γ-TiAl alloys, conceived for the EBM technique, would be a great technological improvement both in terms of processability and material properties.

On the additive manufacturing side, the companies are increasingly developing advanced technologies and they are working together with material scientists in order to improve the processability of materials by shaping the additive machines parameters in a targeted way for each new developed material. In particular, for γ-TiAl alloys, it is essential to be capable to obtain fully densified parts, without defects and with homogeneous microstructure in order to have isotropic mechanical properties in the components and avoid structural weaknesses.

Big effort has been made on the alloys development in order to satisfy the ever stricter requirements for aircraft engine and automotive engine components, and also, to push the material to higher performance in more extreme environmental conditions such as higher temperature and oxidizing or corrosive environments. To do that, it is fundamental to know how to modify the elemental composition of the alloys according to the material properties needed for a particular application. One of the main challenge is to minimize the brittleness of this class of materials that is a considerable drawback for their application. Moreover, there is a big interest in increasing the γ-TiAl operating temperature by playing on the alloys composition and microstructure in order to enhance oxidation resistance and high temperature mechanical properties such as creep, high temperature strength and fatigue resistance.

In conclusion, the progresses in additive manufacturing technologies and materials development are pushing the aerospace and automotive industry forward to a new concept of components design and advantageous manufacturing strategies. This will lead to an exponential technological growth with also an emphasis on the environmental and energy problem.

References

[1]   G. W. Meetham, "High -Temperature materials - a general review," *J. Mater. Sci.*, vol. 26, no. 4, pp. 853–860, 1991.

[2]   J. D. Venables, "HIGH TEMPERATURE STRUCTURAL MATERIALS," *EOLSS*. .

[3]   "Intergovernment Panel on Climate Change." [Online]. Available: http://www.ipcc.ch/.

[4]   "The IATA Technology Roadmap Report," 2009.

[5]   "EUROPEAN AERONAUTICS : A VISION FOR 2020," 2001.

[6]   "Flightpath 2050 Europe's Vision for Aviation," 2011.

[7]   "Nasa   N+3."   [Online].   Available: http://www.aeronautics.nasa.gov/nra_awardees_10_06_08.htm.

[8]   W. R. Graham, C. A. Hall, and M. V. Morales, "The potential of future aircraft technology for noise and pollutant emissions reduction," *Transp. Policy*, vol. 34, pp. 36–51, 2014.

[9]   "Reducing CO2 emissions from passenger cars." [Online]. Available: http://ec.europa.eu/clima/policies/transport/vehicles/cars/index_en.htm.

[10]   "Official Journal of the European Union L 145," *Off. J. Eur. Union*, vol. 54, 2011.

[11]   *Aeronautics and Air Transport Research 7 th Framework Programme 2007-2013*, vol. 3. European Commision, 2013.

[12]   "ATAG   Air   Transport   Action   Group."   [Online].   Available: http://www.atag.org/.

[13]   "E-BREAK: Engine Breakthrough Components and Subsystems." [Online]. Available: http://www.e-break.eu/.

[14]   "TiAlCharger - Titanium Aluminide Turbochargers." [Online]. Available: http://www.tialcharger.de/.

[15] J. Guedou, "MATERIALS EVOLUTION IN HOT PARTS OF AERO-TURBO-ENGINES," in *27th international congress of the aeronautic science*, 2010.

[16] R. Parker, "Green Aeroengines," 2011.

[17] S. Biamino, a. Penna, U. Ackelid, S. Sabbadini, O. Tassa, P. Fino, M. Pavese, P. Gennaro, and C. Badini, "Electron beam melting of Ti-48Al-2Cr-2Nb alloy: Microstructure and mechanical properties investigation," *Intermetallics*, vol. 19, no. 6, pp. 776–781, 2011.

[18] J. D. Mattingly, *Elements of Propulsion: Gas Turbine And Rockets*. AIAA Education Series. American Institute of Aeronautics and Astronautics, 2006.

[19] N. Cumpsty, *Jet Propulsion - A Simple Guide to the Aerodynamic and Thermodynamic Design and Performance of Jet Engines*. Cambridge University Press, 2003.

[20] H. Cohen, G. F. C. Rogers, and H. I. H. Sovranamuttoo, *Gas Turbine Theory*. Pearson Education, 2001.

[21] "Turbofan." [Online]. Available: https://en.wikipedia.org/wiki/Turbofan.

[22] "GE Aviation, GE Aviation Engines." [Online]. Available: http://www.geae.com/engines/index.html.

[23] "Rolls-Royce Engines." [Online]. Available: http://www.rolls-royce.com/products-and-services/civil-aerospace/products/civil-large-engines.aspx.

[24] "Pratt & Whitney Canada." [Online]. Available: http://www.pwc.ca/.

[25] P. Walsh and P. Fletcher, *Gas Turbine Performance, Second Edition*, 2nd ed. Blackwell Science Limited, 2004.

[26] M. Gholamrezaei, "High-bypass Ratio Turbofan Engine Simulation," 2007.

[27] A. Gianpaolo, *Gas turbine handbook: principles and practices*, 3rd ed. The Fairmont Press, 2009.

[28] J. D. Mattingly, *Elements of gas turbine propulsion*. McGraw-Hill, 1996.

[29] J. E. Allen, F. W. Armstrong, and R. M. Denning, "Evolution of aviation and propulsion systems: the next fifty years," *J. Aerosp. Eng.*, pp. 15–33, 1995.

[30] V. H. Monir, R. Salehi, H. Salarieh, and A. Alasty, "Real-time estimation of

the volumetric efficiency in spark ignition engines using an adaptive sliding-mode observer," *J. Automob. Eng.*, vol. 229, no. 14, pp. 1925–1933, 2015.

[31] T. K. Garret, K. Newton, and W. Steeds, "Turbocharging and supercharging," in *Motor Vehicle*, 13th ed., Butterworth Heinemann, 2000, pp. 556–589.

[32] T. Tetsui, "Development of a TiAl turbocharger for passenger vehicles," *Mater. Sci. Eng. A*, vol. 331, pp. 582–588, 2002.

[33] "How Turbocharger Works," 2012. [Online]. Available: http://conceptengine.tripod.com.

[34] L. Eriksson and L. Nielsen, "Turbocharging Basics and Models," in *Modelling and Control of Engines and Drivelines*, 1st ed., no. September, John Wiley & Sons. Ltd, 2016.

[35] D. Samoilenko and H. M. Cho, "Improvement of combustion efficiency and emission characteristic of IC diesel engine operating on ESC cycle applying variable geometry turbocharger (VGT) with vaneless turbine volute," *Int. J. Automot. Technol.*, vol. 14, no. 4, pp. 521–528, 2013.

[36] J. M. Lujàn and J. R. Bermùdez, "Test Bench for Turbocharger Groups Characterization," *SAE Tech. Pap.*, vol. 200201–016, 2002.

[37] D. Naundorf, H. Bolz, and M. Mandel, "Design and Implementation of a New Generation of Turbo Charger Test Benches Using Hot Gas Technology," *SAE Int.*, vol. 2001–01–02, 2001.

[38] A. D. Kumar, S. Sathyanarayanan, S. Gupta, and M. Rao, "Gas Turbine Materials- Current status and its Developmental Prospects-A Critical Review." .

[39] *Coatings for High-Temperature Structural Materials: Trends and Opportunities*. The National Academic Press, 1996.

[40] J. P. Angus, "Aero engine ceramics - the vision, the reality and the progress," *J. Aerosp. Eng.*, pp. 83–96, 1993.

[41] P. W. Schilke, "Advanced Gas Turbine Materials and Coatings," 2004.

[42] "AMG Advanced Metallurgy Group." [Online]. Available: http://www.amg-nv.com.

[43] Y. Okazaki, N. Matsudaira, and M. Matsuda, "Ceramic Turbine Wheel

Developments for Mitsubishi Turbocharger," *SAE Int.*, vol. 850312, pp. 21–29, 1985.

[44] T. Noda, "Application of cast gamma TiAl for automobiles," *Intermetallics*, vol. 6, no. 7–8, pp. 709–713, 1998.

[45] "Advances in Turbocharger Impeller Materials," *Cummins Turbo Technologies*.

[46] T. Tetsui and S. Ono, "Endurance and composition and microstructure effects on endurance of TiAl used in turbochargers," *Intermetallics*, vol. 7, no. 6, pp. 689–697, 1999.

[47] N. R. Muktinutalapati, "Materials for Gas Turbines – An Overview," in *Advances in Gas Turbine Technology*, InTech, 2011, pp. 293–314.

[48] M. Whittaker, "Titanium in the Gas Turbine Engine," in *Advances in Gas Turbine Technology*, InTech, 2011, pp. 316–336.

[49] M. Peters and C. Leyens, *Titanium and Titanium Alloys*. Wiley-VCH, 2003.

[50] "Rolls-Royce, high temperature materials." [Online]. Available: http://www.rolls-royce.com/about/technology/material_tech/high_temperature_materials.jsp.

[51] J. B. Wahl and K. Harris, "Advanced Ni base superalloys for small gas turbines," *Can. Metall. Q.*, vol. 50, no. 3, pp. 207–214, 2011.

[52] C. Reed, Roger, *The Superalloys - Fundamentals and Applications*. Cambridge University Press, 2006.

[53] E. Campo and V. Lupinc, "High temperature structural materials for gas turbines.pdf," *Metall. Sci. Technol.*, vol. 11, no. 1, pp. 31–47, 1993.

[54] G. Sauthoff, *Intermetallics*. New York Weinheim, 1995.

[55] K. Kothari, R. Radhakrishnan, and N. M. Wereley, "Advances in gamma titanium aluminides and their manufacturing techniques," *Prog. Aerosp. Sci.*, vol. 55, pp. 1–16, 2012.

[56] J. Lapin, "TiAl-BASED ALLOYS : PRESENT STATUS AND FUTURE," *Metal*, vol. 19, pp. 1–12, 2009.

[57] M. Terner, S. Biamino, G. Baudana, A. Penna, P. Fino, M. Pavese, D. Ugues, and C. Badini, "Initial Oxidation Behavior in Air of TiAl-2Nb and TiAl-8Nb Alloys Produced by Electron Beam Melting," *J. Mater. Eng. Perform.*, vol.

24, no. 10, pp. 3982–3988, 2015.

[58] T. Tetsui, "Gamma Ti aluminides for non-aerospace applications," *Curr. Opin. Solid State Mater. Sci.*, vol. 4, no. 3, pp. 243–248, 1999.

[59] X. Wu, "Review of alloy and process development of TiAl alloys," *Intermetallics*, vol. 14, no. 10–11, pp. 1114–1122, 2006.

[60] Y. Y. Chen, H. B. Yu, D. L. Zhang, and L. H. Chai, "Effect of spark plasma sintering temperature on microstructure and mechanical properties of an ultrafine grained TiAl intermetallic alloy," *Mater. Sci. Eng. A*, vol. 525, pp. 166–173, 2009.

[61] T. Cheng and M. McLean, "Characterization of TiAl intermetallic rods produced from elemental powders by hot extrusion reaction synthesis (HERS)," *J. Mater. Sci.*, vol. 32, pp. 6255–6261, 1997.

[62] K. Kothari, R. Radhakrishnan, N. M. Wereley, and T. S. Sudarshan, "Microstructure and mechanical properties of consolidated gamma titanium aluminides," *Powder Metall.*, vol. 50, no. 1, pp. 20–27, 2007.

[63] A. Bartels, H. Kestler, and H. Clemens, "Deformation behavior of differently processed g -titanium aluminides," *Mater. Sci. Eng. A*, vol. 331, pp. 153–162, 2002.

[64] G. Wegmann, R. Gerling, and F. Schimansky, "Temperature induced porosity in hot isostatically pressed gamma titanium aluminide alloy powders," *act*, vol. 51, pp. 741–752, 2003.

[65] R. Gerling, A. Bartels, H. Clemens, and H. Kestler, "Structural characterization and tensile properties of a high niobium containing gamma TiAl sheet obtained by powder metallurgical processing," *Intermetallics*, vol. 12, pp. 275–280, 2004.

[66] L. E. Murr, S. M. Gaytan, a. Ceylan, E. Martinez, J. L. Martinez, D. H. Hernandez, B. I. Machado, D. a. Ramirez, F. Medina, S. Collins, and R. B. Wicker, "Characterization of titanium aluminide alloy components fabricated by additive manufacturing using electron beam melting," *Acta Mater.*, vol. 58, no. 5, pp. 1887–1894, 2010.

[67] D. Cormier, O. Harrysson, T. Mahale, and H. West, "Freeform Fabrication of Titanium Aluminide via Electron Beam Melting Using Prealloyed and Blended Powders," *Res. Lett. Mater. Sci.*, vol. 2007, pp. 1–5, 2007.

[68] H. Clemens and S. Mayer, "Intermetallic titanium aluminides in aerospace

applications – processing , microstructure and properties," *Mater. High Temp.*, vol. 33, pp. 560–570, 2016.

[69] McCullough and Valencia, "Phase equilibria and solidification in Ti-Al alloys," *Acta Metall. 37*, vol. 37, no. 5, 1989.

[70] Y.-W. Kim and D. M. Dimiduk, "Progress in the understanding of gamma titanium aluminides," *Jom*, vol. 43, no. 8, pp. 40–47, 1991.

[71] B. H. Clemens, W. Wallgram, S. Kremmer, V. Güther, and A. Otto, "Design of Novel β -Solidifying TiAl Alloys with Adjustable β / B2-Phase Fraction and Excellent Hot-Workability," *Adv. Eng. Mater.*, vol. 10, no. 8, pp. 707–713, 2008.

[72] S. Bystrzanowski, A. Bartels, H. Clemens, R. Gerling, F. P. Schimansky, G. Dehm, and H. Kestler, "Creep behaviour and related high temperature microstructural stability of Ti-46Al-9Nb sheet material," *Intermetallics*, vol. 13, no. 5, pp. 515–524, 2005.

[73] J. P. Lin, X. J. Xu, Y. L. Wang, S. F. He, Y. Zhang, X. P. Song, and G. L. Chen, "High temperature deformation behaviors of a high Nb containing TiAl alloy," *Intermetallics*, vol. 15, pp. 668–674, 2007.

[74] J. P. Lin, L. L. Zhao, G. Y. Li, L. Q. Zhang, X. P. Song, F. Ye, and G. L. Chen, "Effect of Nb on oxidation behavior of high Nb containing TiAl alloys," *Intermetallics*, vol. 19, pp. 131–136, 2011.

[75] F. Appel, J. D. H. Paul, and M. Oehring, *Gamma Titanium Aluminide Alloys: Science and Technology*. Wiley-VCH, 2011.

[76] M. Charpentier, A. Hazotte, and D. Daloz, "Lamellar transformation in near-gamma TiAl alloys — Quantitative analysis of kinetics and microstructure," *Mater. Sci. Eng. A*, vol. 491, pp. 321–330, 2008.

[77] S. R. Dey, A. Hazotte, and E. Bouzy, "Crystallography and phase transformation mechanisms in TiAl-based alloys – A synthesis," *Intermetallics*, vol. 17, no. 12, pp. 1052–1064, 2009.

[78] X. Wu and D. Hu, "Microstructural refinement in cast TiAl alloys by solid state transformations," *Scr. Mater.*, vol. 52, pp. 731–734, 2005.

[79] X. D. Zhangp, S. Godfrey, M. Weavers, and M. Strangwood, "THE MASSIVE TRANSFORMATION IN Ti-Al MECHANISTIC OBSERVATIONS," *Acta Mater.*, vol. 44, no. 9, pp. 3123–3134, 1996.

[80] M. Yamaguchi, H. Inui, and K. Ito, "HIGH-TEMPERATURE STRUCTURAL INTERMETALLICS," *Acta Mater.*, vol. 48, 2000.

[81] A. Denquin and S. Naka, "Phase Transformation Mechanisms Involved in Two-Phase TiAl-Based Alloys. Lamellar Structure Formation," *Acta Mater.*, vol. 44, no. 1, pp. 343–352, 1996.

[82] S. R. Dey and A. Hazotte, "Development of Widmanstatten laths in a near-γ TiAl alloy," *Acta Mater.*, vol. 53, pp. 3783–3794, 2005.

[83] Y.-W. Kim and W. Smarsly, *Gamma Titanium Aluminide Alloys*. Wiley-VCH, 2014.

[84] J. Jeon, A. B. Godfrey, P. A. Blenkinsop, W. Voice, and Y. Hahn, "Recrystallization in cast 45-2-2 XD ^{TM} titanium aluminide during hot isostatic pressing," *Mater. Sci. Eng. A*, vol. 271, pp. 128–133, 1999.

[85] A. Godfrey, D. Hu, and M. H. Loretto, "Properties and microstructure of TiAl-based alloys," *Mater. Sci. Eng. A*, vol. 240, pp. 559–563, 1997.

[86] R. V Ramanujan, "Phase transformations in γ based titanium aluminides," *Int. Mater. sreviews*, vol. 6608, no. February, 2017.

[87] U. Habel and B. J. Mctiernan, "HIP temperature and properties of a gas-atomized γ-titanium aluminide alloy," *Intermetallics*, vol. 12, pp. 63–68, 2004.

[88] S. L. Semiatin, V. Seetharaman, D. M. Dimiduk, and K. H. G. Ashbee, "Phase Transformation Behavior of Gamma Titanium Aluminide Alloys during Supertransus Heat Treatment," *Metall. Mater. Trans. A Phys. Metall. Mater. Sci.*, vol. 29, no. January, pp. 7–18, 1998.

[89] W. Szkliniarz, A. Ko, and B. Serek, "Microstructure and chemical composition of phases in Ti – 48Al – 2Cr – 2Nb intermetallic alloy," *Mater. Chem. Phys.*, vol. 81, pp. 438–442, 2003.

[90] Y. Wang, "Grain refinement of a TiAl alloy by heat treatment through near gamma transformation," *J. Mater. Sci.*, vol. 6, pp. 4465–4468, 2001.

[91] S. U. Meike, Z. Lijing, L. Zebao, Y. A. N. Jie, and Z. Hu, "Microstructural evolution of a PM TiAl alloy during heat treatment in α + γ phase field," *rare Met.*, vol. 31, no. 5, pp. 424–429, 2012.

[92] E. Schwaighofer, H. Clemens, S. Mayer, J. Lindemann, J. Klose, W. Smarsly, and V. Güther, "Microstructural design and mechanical properties

of a cast and heat- treated intermetallic multi-phase g -TiAl based alloy," *Intermetallics*, vol. 44, pp. 128–140, 2014.

[93] A. Penna, "γ -TiAl Fabricated by EBM as Innovative Material for Aerospace Applications with Low Environmental Impact," Politecnico di Torino, 2013.

[94] M. Terner, "Innovative materials for high temperature structural applications: 3rd Generation gamma-TiAl fabricated by Electron Beam Melting," Politecnico di Torino, 2014.

[95] Y. Kim, "Strength and ductility in TiAl alloys," *Intermetallics*, vol. 9795, no. 98, 1998.

[96] K. S. Chan and Y. Kim, "Effect of lamellar spacing and colony size on the fracture resistance of a fully-lamellar TiAl alloy," *acta Met. mater.*, vol. 43, no. 2, pp. 439–451, 1995.

[97] R. Porizek, S. Znam, and V. Vitek, "Atomistic Studies of Dislocation Glide in gamma- TiAl," in *Proceedings of materials research symposium. Department of materials science and engineering. University of Pennsylvania*, 2002, vol. 753, no. December.

[98] W. T. Marketz, F. D. Fischer, and H. Clemens, "Deformation mechanisms in TiAl intermetallics — experiments and modeling," *Int. J. Plast.*, vol. 19, pp. 281–321, 2003.

[99] Y.-W. Kim, "Ordered Intermetallic Alloys, Part III: Gamma Titanium Aluminides (Overview)," *TMS*, pp. 30–39, 1994.

[100] C. Tönnes, J. Rösler, R. Baumann, and M. Thumann, "Structural Intermetallics," in *TMS*, p. 241.

[101] Y. Kim, "Effects of microstructure on the deformation and fracture of γ-TiAl alloys," *Intermetallics*, vol. 193, pp. 519–533, 1995.

[102] A. Gloanec and G. He, "Fatigue properties of TiAl alloys," *Intermetallics*, vol. 13, pp. 543–558, 2005.

[103] L. Sastry and H. Lipsitt, "Fatigue deformation of TiAl base alloys," *Met. Trans A*, vol. 8, pp. 299–308, 1977.

[104] J. Larsen, "Assuring reliability of gamma titanium aluminides in long-term service," *TMS*, pp. 463–472, 1999.

[105] M. Filippini, S. Beretta, L. Patriarca, and S. Sabbadini, "Effect of the

microstructure on the deformation and fatigue damage in a gamma-TiAl produced by additive manufacturing," in *Gamma Titanium Aluminide Alloys 2014*, no. October, 2014.

[106] M. Filippini, S. Beretta, L. Patriarca, G. Pasquero, and S. Sabbadini, "Defect tolerance of a gamma titanium aluminide alloy," *Procedia Eng.*, vol. 10, pp. 3677–3682, 2011.

[107] V. Recina and B. Karlsson, "HIGH TEMPERATURE LOW CYCLE FATIGUE PROPERTIES OF Ti-48Al-2Cr-2Nb GAMMA TITANIUM ALUMINIDES CAST IN DIFFERENT DIMENSIONS," *Scr. Mater.*, vol. 43, pp. 609–615, 2000.

[108] V. Recina and B. Karlsson, "High temperature low cycle fatigue properties of Ti-48Al-2W-0.5Si gamma titanium aluminide," *Mater. Sci. Eng. A*, vol. 262, pp. 70–81, 1999.

[109] L. Patriarca, M. Filippini, and S. Beretta, "Digital image correlation-based analysis of strain accumulation on a duplex γ -TiAl," *Intermetallics*, vol. 75, pp. 42–50, 2016.

[110] V. Recina, "High temperature low cycle fatigue properties of two cast gamma titanium aluminide alloys with refined microstructure," *Mater. Sci. Technol.*, vol. 0836, no. March, 2017.

[111] R. C. Feng, "IMPROVED METHOD OF FATIGUE LIFE ASSESSMENT FOR TiAl ALLOYS," vol. 46, no. 2, pp. 183–189, 2014.

[112] H. Kitagawa and S. Takahashi, "Applicability of fracture mechanics to very small cracks or the cracks in the early stage," in *American Society for Metals; Second international conference on mechanical behavior of materials*, 1976, pp. 627–631.

[113] F. Appel, M. Oehring, and R. Wagner, "Novel design concepts for gamma-base titanium aluminide alloys," *Intermetallics*, vol. 8, no. 9–11, pp. 1283–1312, 2000.

[114] M. Lamirand, J. L. Bonnentien, G. Ferrière, S. Guérin, and J. P. Chevalier, "Effects of interstitial oxygen on microstructure and mechanical properties of Ti-48AI-2Cr-2Nb with fully lamellar and duplex microstructures," *Metall. Mater. Trans. A Phys. Metall. Mater. Sci.*, vol. 37, no. 8, pp. 2369–2378, 2006.

[115] T. Noda, M. Okabe, S. Isobea, and M. Sayashib, "Silicide precipitation

strengthened TiAl," *Mater. Sci. Eng.*, vol. 193, pp. 774–779, 1995.

[116] Y. Koyanagi, S. Ueta, and T. Noda, "Development of TiAl alloy with high creep strength and manufacturability for a turbine wheel," *4th Int. Work. Titan. Alum.*, pp. 1–15, 2011.

[117] C. T. Liu and P. J. Maziasz, "Microstructural control and mechanical properties of dual-phase TiAl alloys," *intermetallics*, vol. 9795, no. 98, 1998.

[118] V. A. C. Haanappel, R. Hofman, W. Glatz, H. Clemens, and M. F. Stroosnijder, "The Influence of Microstructure on the Isothermal and Cyclic , Oxidation Behavior of Ti-48A1-2Cr at 800 ° C," *Oxid. Met.*, vol. 48, 1997.

[119] V. A. C. Haanappel, J. D. Sunderko, and M. F. Stroosnijder, "The isothermal and cyclic high temperature oxidation behaviour of Ti - 48Al - 2Mn - 2Nb compared with Ti - 48Al - 2Cr - 2Nb and Ti - 48Al - 2Cr," *Intermetallics*, vol. 7, 1999.

[120] P. Raluca, S. Friedle, and M. Schütze, "Oxidation protection of g -TiAl-based alloys e A review," *Intermetallics*, vol. 56, 2015.

[121] A. Donchev, B. Gleeson, and M. Schu, "Thermodynamic considerations of the beneficial effect of halogens on the oxidation resistance of TiAl-based alloys," *Intermetallics*, vol. 11, pp. 387–398, 2003.

[122] S. Friedle, N. Laska, R. Braun, H. Zschau, M. C. Galetz, and M. Schütze, "Oxidation behaviour of a fluorinated beta-stabilized gamma-TiAl alloy with thermal barrier coatings in H2O- and SO2-containing atmospheres," *Corros. Sci.*, 2014.

[123] B. P. J. Masset and M. Schütze, "Thermodynamic Assessment of the Alloy Concentration Limits for the Halogen Effect of TiAl Alloys," *Adv. Eng. Mater.*, no. 177, pp. 666–674, 2008.

[124] T. Tetsui, "TiAl intermetallic compound-based alloy," 6,294,132 B1, 2001.

[125] M. Terner, S. Biamino, P. Epicoco, A. Penna, O. Hedin, S. Sabbadini, P. Fino, M. Pavese, U. Ackelid, P. Gennaro, F. Pelissero, and C. Badini, "Electron beam melting of high niobium containing TiAl alloy: Feasibility investigation," *Steel Res. Int.*, vol. 83, no. 10, pp. 943–949, 2012.

[126] M. Terner, S. Biamino, A. Penna, O. Hedin, S. Sabbadini, P. Fino, M. Pavese, and U. Ackelid, "Material properties of TiAl alloy with high Nb content produced by the additive manufacturing technology of Electron Beam Melting," in *Euro PM*, 2012, pp. 3–8.

[127] G. Baudana, S. Biamino, B. Kl, A. Kirchner, B. Kieback, M. Pavese, D. Ugues, P. Fino, T. Weißg, and C. Badini, "Electron Beam Melting of Ti-48Al-2Nb-0 . 7Cr-0 . 3Si : Feasibility investigation," *Intermetallics*, vol. 73, pp. 43–49, 2016.

[128] S. C. Huang, "TMS Warrendale PA," in *Structural Intermetallics*, p. 299.

[129] Y. Shen, X. Ding, and F. Wang, "High temperature oxidation behavior of Ti-Al-Nb ternary alloys," *J. Mater. Sci.*, vol. 39, pp. 6583–6589, 2004.

[130] G. Chen, Z. Sun, and X. Zhou, "Oxidation and mechanical behavior of intermetallic alloys in the T i-Nb-Al ternary system," *Mater. Sci. Eng. A*, vol. 153, pp. 597–601, 1992.

[131] D. Pilone, F. Felli, and A. Brotzu, "High temperature oxidation behaviour of TiAl - Cr - Nb - Mo alloys," *Intermetallics*, vol. 43, pp. 131–137, 2013.

[132] W. Jiang, Hui-ren, Wang, Zhong-lei, Ma, "Effects of Nb and Si on high temperature oxidation of TiAl," *Trans. Nonferrous Met. Soc. China*, vol. 18, pp. 512–517, 2008.

[133] "GE Aviation GEnx engine." [Online]. Available: https://www.geaviation.com/commercial/engines/genx-engine.

[134] "CFM LEAP engine." [Online]. Available: https://www.cfmaeroengines.com/engines/leap/.

[135] "GE Aviation GE9x engine." [Online]. Available: https://www.geaviation.com/commercial/engines/ge9x-commercial-aircraft-engine.

[136] H. Clemens and S. Mayer, "Design, processing, microstructure, properties, and applications of advanced intermetallic TiAl alloys," *Adv. Eng. Mater.*, vol. 15, no. 4, pp. 191–215, 2013.

[137] S. Franzèn Fager and J. Karlsson, "γ -Titanium Aluminide Manufactured by Electron Beam Melting," Chalmers University of Technology, 2010.

[138] "The library of manufacturing. Investment casting." .

[139] "The library of manufacturing. Centrifuge casting." .

[140] J. Gardan, "Additive manufacturing technologies: state of the art and trends," *Int. J. Prod. Res.*, vol. 54, no. 10, 2016.

[141] I. Gibson, W. Rosen, and B. Stucker, *Additive manufacturing technologies*. Springer, 2010.

[142] G. Baudana, S. Biamino, D. Ugues, M. Lombardi, P. Fino, M. Pavese, and C. Badini, "Titanium aluminides for aerospace and automotive applications processed by Electron Beam Melting: Contribution of Politecnico di Torino," *Met. Powder Rep.*, vol. 00, no. 00, pp. 2–8, 2016.

[143] "Arcam AB." [Online]. Available: http://www.arcam.com/.

[144] L. E. Murr, S. M. Gaytan, D. A. Ramirez, E. Martinez, J. Hernandez, K. N. Amato, P. W. Shindo, F. R. Medina, and R. B. Wicker, "Metal Fabrication by Additive Manufacturing Using Laser and Electron Beam Melting Technologies," *J. Mater. Sci. Technol.*, vol. 28, no. 1, pp. 1–14, 2012.

[145] J. Schwerdtfeger and C. Körner, "Selective electron beam melting of Ti-48Al-2Nb- 2Cr: Microstructure and aluminium loss," *Intermetallics*, vol. 49, pp. 29–35, 2014.

[146] A. Klassen, T. Scharowsky, C. Körner, A. Klassen, V. E. Forster, C. Körner, M. Courtois, M. Carin, P. Le, and K. Carolin, "Fundamental consolidation mechanisms during selective beam melting of powders," *Model. Simul. Mater. Sci. Eng.*, vol. 21, 2013.

[147] M. Sigl and J. Milberg, "Electron beam sintering of metal powder," *Prod. Eng. Res. Devel.*, vol. 2, pp. 117–122, 2008.

[148] S. P. B. Cheng, X. Gong, and J. Lydon, "Speed Function Effects in Electron Beam Additive Manufacturing," in *ASME 2014 International Mechanical Engineering Congress and Exposition IMECE2014*, 2014.

[149] "ASTM E2109 - Standard Test Methods for Determining Area Percentage Porosity in Thermal Sprayed Coatings." ASTM International, 2014.

[150] Y. Leng, *Materials Characterization*. John Wiley & Sons. Ltd, 2013.

[151] H. Luth, *Surfaces and interfaces of solid materials*, 3rd ed. Springer, 1995.

[152] B. D. Cullity, *Elements of X-ray diffraction*, 2nd ed. Reading: Addison - Wesley, 1978.

[153] M. E. Brown, *Thermomechanical analysis (TMA)*. Springer, 1988.

[154] M. Terner, S. Biamino, D. Ugues, S. Sabbadini, P. Fino, M. Pavese, and C. Badini, "Phase transitions assessment on gamma-TiAl by Thermo

Mechanical Analysis," *Intermetallics*, vol. 37, pp. 7–10, 2013.

[155] "ASTM E831 - Standard Test Method for Linear Thermal Expansion of Solid Materials by Thermomechanical Analysis." ASTM International, 2014.

[156] "ASTM B214 - Standard Test Method for Sieve Analysis of Metal Powders." ASTM International, 2016.

[157] "ASTM B213 - Standard Test Methods for Flow Rate of Metal Powders Using the Hall Flowmeter Funnel." ASTM International, 2013.

[158] "ASTM B212 - Standard Test Method for Apparent Density of Free-Flowing Metal Powders Using the Hall Flowmeter Funnel." ASTM International, 2013.

[159] "ASTM E2371 - Standard Test Method for Analysis of Titanium and Titanium Alloys by Direct Current Plasma and Inductively Coupled Plasma Atomic Emission Spectrometry (Performance-Based Test Methodology)." ASTM International, 2013.

[160] "Standard Test Methods for Determination of Carbon, Sulfur, Nitrogen, and Oxygen in Steel, Iron, Nickel, and Cobalt Alloys by Various Combustion and Fusion Techniques." ASTM International, 2011.

[161] "ASTM E1409 - Standard Test Method for Determination of Oxygen and Nitrogen in Titanium and Titanium Alloys by Inert Gas Fusion." ASTM International, 2013.

[162] "ASTM E8 - Standard Test Methods for Tension Testing of Metallic Materials." ASTM International, 2016.

[163] "ASTM E21 - Standard Test Methods for Elevated Temperature Tension Tests of Metallic Materials." ASTM International, 2009.

[164] "ASTM E139 - Standard Test Methods for Conducting Creep, Creep-Rupture, and Stress-Rupture Tests of Metallic Materials." ASTM International, 2011.

[165] "ASTM E1876 - Standard Test Method for Dynamic Young's Modulus, Shear Modulus, and Poisson's Ratio by Impulse Excitation of Vibration." ASTM International, 2015.

[166] M. Palm, "Advanced Intermetallic-Based Alloys for Extreme Environment and Energy Applications," in *MRS Proceeding*, 2009.

[167] N. Ashgriz, *Handbook of Atomization and Sprays - Theory and Applications*. Springer US, 2011.

[168] R. M. German, *Powder Metallurgy Science*, 2nd ed. Metal Powder Industry, 1994.

[169] H. H. Zhu, J. Y. H. Fuh, and L. Lu, "The influence of powder apparent density on the density in direct laser-sintered metallic parts," *Int. J. Mach. Tools Manuf.*, vol. 47, pp. 294–298, 2007.

[170] A. Lasalmonie, "Intermetallics : Why is it so difficult to introduce them in gas turbine engines ?," *Intermetallics*, vol. 14, pp. 1123–1129, 2006.

[171] M. L. Blackmore, W. Zhang, and I. Todd, "The Origin of Microstructural Diversity , Texture , and Mechanical Properties in Electron Beam Melted Ti-6Al-4V," *Metall. Mater. Trans. A Phys. Metall. Mater. Sci.*, vol. 41A, 2010.

[172] S. Tammas-williams, H. Zhao, F. Léonard, F. Derguti, I. Todd, and P. B. Prangnell, "Materials Characterization XCT analysis of the in fl uence of melt strategies on defect population in Ti – 6Al – 4V components manufactured by Selective Electron Beam Melting," *Mater. Charact.*, vol. 102, pp. 47–61, 2015.

[173] R. Gerling, R. Leitgeb, and F. Schimansky, "Porosity and argon concentration in gas atomized γ -TiAl powder and hot isostatically pressed compacts," *Mater. Sci. Eng. A*, vol. 252, pp. 239–247, 1998.

[174] Y. Mishin and C. Herzig, "DIFFUSION IN THE Ti - Al SYSTEM," *Acta Mater.*, vol. 48, no. 136, 2000.

[175] M. Galati, G. Baudana, A. Salmi, E. Atzeni, S. Biamino, P. Fino, and L. Iuliano, "FE Thermal Model of EBM process to investigate different experimental By means of the advantages of the numerical simulation," in *1st International Conference on Electron Beam Additive Manufacturing*, 2016.

[176] M. Galati, L. Iuliano, A. Salmi, and E. Atzeni, "Modelling energy source and powder properties for the development of a thermal FE model of the EBM additive manufacturing process," *Addit. Manuf.*, vol. 14, pp. 49–59, 2017.

[177] M. S. Dahar, S. A. Tamirisakandala, and J. J. Lewandowski, "Fatigue crack growth and fracture behavior of as-cast Ti-43 . 5Al-4Nb-1Mo- 0 . 1B (TNM) compared to Ti-48Al-2Nb-2Cr (4822)," *Intermetallics*, vol. 91, no. August, pp. 158–168, 2017.

[178] T. Schmoelzer, K. Liss, C. Kirchlechner, S. Mayer, A. Stark, M. Peel, and H. Clemens, "An in-situ high-energy X-ray diffraction study on the hot-deformation behavior of a b -phase containing TiAl alloy," *Intermetallics*, vol. 39, pp. 25–33, 2013.

[179] E. Schwaighofer, M. Schloffer, T. Schmoelzer, H. Clemens, A. Stark, P. Staron, T. Lippmann, S. Mayer, M. Testing, M. Leoben, and H. Geesthacht, "Phase fraction evolution in a multi-phase intermetallic γ -TiAl based alloy."

[180] S. Mayer, C. Sailer, T. Schmoelzer, H. Clemens, T. Lippmann, and P. Staron, "On Phase Equilibria and Phase Transformations in β / γ -TiAl Alloys – A Short Review," *BHM*, vol. 156, no. 11, pp. 438–442, 2011.

[181] M. Schloffer, F. Iqbal, H. Gabrisch, E. Schwaighofer, F. Schimansky, S. Mayer, A. Stark, T. Lippmann, M. Göken, F. Pyczak, and H. Clemens, "Microstructure development and hardness of a powder metallurgical multi phase γ -TiAl based alloy," *Intermetallics*, vol. 22, pp. 231–240, 2012.

[182] T. Leitner, M. Schloffer, S. Mayer, J. Eßlinger, H. Clemens, and R. Pippan, "Fracture and R -curve behavior of an intermetallic beta-stabilized TiAl alloy with different nearly lamellar microstructures," *Intermetallics*, vol. 53, pp. 1–9, 2014.

[183] H. S. Cho, S. W. Nam, J. H. Yun, and D. M. Wee, "Effect of 1 at.% nitrogen addition on the creep resistance of two phase TiAl alloy," *Mater. Sci. Eng. A*, vol. 262, no. 1–2, pp. 129–136, 1999.

[184] W. Yan, L. I. U. Yong, Y. Guang-yu, L. I. Hui-zhong, and T. Bei, "Microstructure of cast γ -TiAl based alloy solidified from β phase region," *Trans. Nonferrous Met. Soc. China*, vol. 21, no. 2, pp. 215–222, 2010.

[185] A. Safdar, "A Study on Electron Beam Melted Ti-6Al-4V," Faculty of Engineering, Lund University, 2012.

[186] J. Liu, J. Cao, X. Song, Y. Wang, and J. Feng, "Evaluation on diffusion bonded joints of TiAl alloy to Ti 3 SiC 2 ceramic with and without Ni interlayer : Interfacial microstructure and mechanical properties," *J. Mater.*, vol. 57, pp. 592–597, 2014.

[187] T. Tetsui, "Effects of brazing filler on properties of brazed joints between TiAl and metallic materials," *Intermetallics*, vol. 9, pp. 253–260, 2001.

[188] M. S. Węglowski, S. Blacha, and A. Philips, "Electron beam welding - Techniques and trends - Review," *Vacuum*, vol. 130, pp. 72–92, 2016.

[189] G. Basile, G. Baudana, G. Marchese, M. Lorusso, M. Lombardi, D. Ugues, P. Fino, and S. Biamino, "Characterization of an Additive Manufactured TiAl Alloy — Steel Joint Produced by Electron Beam Welding," *Materials (Basel).*, vol. 11, no. 1, pp. 3–11, 2018.